



Laboratory Astrophysics:  
Investigating the mystery of low  
charge states of Si and S in the  
HMXB Cyg X-1

Master Thesis of

**Natalie Hell**

performed at the

**Dr. Karl Remeis-Sternwarte Bamberg  
Erlangen Center for Astroparticle Physics  
Friedrich-Alexander-Universität  
Erlangen-Nürnberg**

supervisor:

**Prof. Dr. Jörn Wilms**

in collaboration with

**Lawrence Livermore National Laboratory**

supervisor:

**Dr. Gregory V. Brown**

17.02.2012



## Zusammenfassung

Massereiche Röntgendoppelsterne (HXMB) sind sehr gut geeignet, die starken Sternwinde massereicher Sterne zu untersuchen. Auf Grund seiner langen Beobachtungsgeschichte stellt Cygnus X-1 mit seinem Begleitstern, dem Überriesen HDE 226868, wahrscheinlich das am gründlichsten studierte dieser Systeme dar. Daher birgt Cyg X-1 den Vorteil, dass seine Systemparameter sehr gut bekannt sind, und qualifiziert sich dementsprechend als perfekter Kandidat, um Windeigenschaften zu untersuchen.

Hanke (2011) und Miškovičová et al. (2011) weisen nach, dass im Falle eines Abfallens der Strahlungsintensität (Dips) in der Lichtkurve dieses Systems die  $K\alpha$ -Linien von wasserstoff- und heliumähnlichem Silizium und Schwefel beinahe vollständig aus den zugehörigen Spektren verschwinden. Stattdessen können Absorptionslinien von niedrigeren Ionisationsgraden dieser Elemente beobachtet werden. Dieses Verhalten suggeriert, dass die Dips durch Inhomogenitäten in der Dichte des Sternwinds, auch als "Klumpen" bezeichnet, verursacht werden, die unsere Sichtlinie zum Schwarzen Loch kreuzen. Die am häufigsten vertretene Theorie über die Struktur dieser Inhomogenitäten besagt, dass das Windmaterial sich selbst gegen die Röntgenstrahlung des Schwarzen Lochs abschirmt. Da die Röntgenstrahlung aber für das Aufheizen und Ionisieren des Windmaterials verantwortlich ist, führt die Selbstabschirmung gegen die Strahlung zu einer Schalenstruktur der Klumpen aus immer kälterem, weniger ionisiertem Material. In diesem Fall wird erwartet, dass die in den Klumpen enthaltene Materie sich unabhängig von seinem Ionisationsgrad mit der selben Geschwindigkeit fortbewegt. Folglich wäre das Herleiten und der Vergleich der Dopplerverschiebungen der Absorptionslinien unterschiedlichen Ladungszustandes eine Möglichkeit, diese Theorie zu testen.

Bisher wurden die Linienzentren für niedriger Ionisationsgrade für die meisten Elemente, Silizium und Schwefel eingeschlossen, noch nicht im Labor gemessen. Darüber hinaus sind die wenigen existierenden Berechnungen dieser Linien nicht genau genug, um mögliche Dopplerverschiebungen mit großer Genauigkeit bestimmen zu können. Ein früherer eher quantitativer Vergleich der  $K\alpha$ -Linien in den Cyg X-1 Spektren mit theoretischen Linienpositionen legen eine recht große Diskrepanz zwischen den beobachteten und theoretischen Linien nahe, mit unterschiedlich starken Verschiebungen für unterschiedliche Ionisationsgrade. Da die Qualität der verwendeten Referenzlinien eher fragwürdig ist, bleibt die Frage bestehen, ob die Verschiebungen real sind oder eher durch das Fehlen von brauchbaren Atomdaten verursacht werden. Aus diesem Grund werden in dieser Arbeit die  $K\alpha$ -Spektren von Silizium und Schwefel im Lawrence Livermore National Laboratory zunächst mit einer Elektronenstrahl-Ionen-Falle (EBIT) als Emissionslinien erzeugt und schließlich mit dem EBIT Kalorimeter Spektrometer (ECS) aufgenommen. Numerische Simulationen dieser Spektren werden mit dem Flexible Atomic Code (FAC) berechnet. Durch den Vergleich der gemessenen Spektren mit diesen theoretischen Linienzentren werden die Linien mit denjenigen Übergängen identifiziert, die laut der Simulation den stärksten Beitrag zu deren Entstehung leisten.

Die Dopplerverschiebungen der Absorptionslinien werden aus dem Vergleich der Labor-, berechneten und Cyg X-1 Spektren hergeleitet und sind mit einer Geschwindigkeit des Absorbermaterials von null konsistent. Da insbesondere die so erhaltenen Geschwindigkeiten für die verschiedenen Ionisationsgrade innerhalb der Fehlerbalken gleich sind, liefern diese Ergebnisse einen Beleg für das Bild der Zwiebelschalenstruktur der Klumpen, was gleichzeitig andere mögliche Erklärungsmodelle für die Ursache der Dips und die Struktur des Windes unwahrscheinlicher macht.



## Abstract

High mass X-ray binaries (HMXB) are very well suited to probe the strong stellar winds of massive stars. Due to its long observation history, Cygnus X-1 with its supergiant companion HDE 226868 is probably the best studied of these systems. Thus Cyg X-1 provides the advantage of quite well known system parameters, which qualifies the system as a perfect candidate for the investigation of wind properties.

Hanke (2011) and Miškovičová et al. (2011) find that during the event of dips in the intensity of the system's light curve the hydrogen and helium like  $K\alpha$  lines of silicon and sulfur almost vanish in the corresponding spectra. Instead the spectra show absorption lines originating from lower charge states of these elements. This behavior suggests that the dips are caused by density inhomogeneities, often referred to as "clumps", in the stellar wind passing through our line of sight to the black hole. The most favored theory about the structure of these inhomogeneities proposes self-shielding effects blocking the X-radiation of the black hole. Since the X-radiation is responsible for the heating and ionization of the stellar wind, this self-shielding leads to a shell structure of successively colder and less ionized material in the clumps. In this case the material contained in the clumps is expected to move with the same speed regardless of the ionization state. Hence, one way to test this scenario is to derive and compare the Doppler shifts of the absorption lines of each ionization state.

Laboratory measurements of the line centers have not been carried out so far for the lower charge states of most elements, including silicon and sulfur, and the few existing calculations do not provide information accurate enough to constrain a possible Doppler shift very well. Previous rather quantitative comparisons of the  $K\alpha$  forest in the Cyg X-1 spectra with theoretical line centers imply a large discrepancy between the observed and theoretical lines with different shifts for different ionization states. Since the quality of the employed reference line centers is arguable, the question remains whether these differences are real or whether they are rather caused by the lack of atomic data. Thus, in this thesis the  $K\alpha$  spectra of silicon and sulfur are produced with the electron beam ion trap (EBIT) and measured with the EBIT calorimeter spectrometer (ECS) at the Lawrence Livermore National Laboratory (LLNL). Numerical simulations of these spectra are computed with the Flexible Atomic Code (FAC). Through comparison of the measured spectra with these theoretical line centers the lines are identified with the transitions yielding the strongest contribution to the production of these lines.

By comparison of the laboratory, calculated and Cyg X-1 spectra Doppler shifts of the absorption lines are derived which are consistent with zero velocity of the absorbing material. Since especially the derived velocity is the same for all ionization states within the errorbars, the results provide evidence for the picture of the onion like structure of the clumps, making other possible explanations less likely.

# Contents

<b>1</b>	<b>Introduction</b>	<b>11</b>
<b>2</b>	<b>High Mass X-Ray Binaries</b>	<b>13</b>
2.1	Stellar Evolution . . . . .	13
2.2	Roche Lobes . . . . .	14
2.3	Stellar Winds . . . . .	17
2.4	Accretion . . . . .	19
2.5	Spectral States . . . . .	22
2.6	Cygnus X-1 . . . . .	23
2.6.1	The System . . . . .	23
2.6.2	Absorption Dips . . . . .	25
2.6.3	Low Charge States of Si and S . . . . .	27
<b>3</b>	<b>X-Ray Spectra</b>	<b>29</b>
3.1	The Hydrogen Atom . . . . .	29
3.2	Hydrogenic Ions . . . . .	32
3.3	Fine Structure Splitting . . . . .	33
3.4	Further Splitting . . . . .	34
3.5	Many-electron Systems . . . . .	36
3.6	LS-vs. jj-coupling . . . . .	38
3.6.1	LS-coupling . . . . .	38
3.6.2	jj-coupling . . . . .	39
3.6.3	Transition from LS- to jj-coupling . . . . .	39
3.6.4	Matching the Notation . . . . .	40
3.7	Selection Rules . . . . .	41
3.7.1	Parity . . . . .	42
3.7.2	Back to the Selection Rules . . . . .	42
3.8	$K\alpha$ Spectra . . . . .	44
3.9	Radiative Transitions . . . . .	47
3.9.1	Spontaneous Emission . . . . .	48
3.9.2	Induced/ Stimulated Emission and Absorption . . . . .	48
3.9.3	Relation between the Einstein Coefficients . . . . .	49
3.10	Collisional Excitation and Ionization . . . . .	50
3.10.1	Collisional Excitation . . . . .	50
3.10.2	Collisional Ionization . . . . .	51
3.10.3	Photoionization . . . . .	52
3.11	Line Intensities . . . . .	52

---

3.12	Atomic Codes . . . . .	55
3.12.1	Calculation of House (1969) . . . . .	56
3.12.2	Calculation of Palmeri et al. (2008) . . . . .	56
3.12.3	Calculations with FAC . . . . .	57
3.12.4	FAC vs. Palmeri et al. (2008) . . . . .	60
3.12.5	Spectra Simulated with FAC . . . . .	60
<b>4</b>	<b>Laboratory Measurements</b>	<b>64</b>
4.1	Electron Beam Ion Trap . . . . .	64
4.2	Measurement . . . . .	68
4.3	EBIT Calorimeter Spectrometer . . . . .	69
4.4	Calibration . . . . .	72
4.5	Quality of the Calibration . . . . .	75
4.5.1	The He-like Lines . . . . .	77
4.5.2	The Separation of the Lyman's . . . . .	79
4.6	Influence of the Fit Range . . . . .	80
4.7	Line Identification . . . . .	81
4.7.1	Silicon . . . . .	83
4.7.2	Sulfur . . . . .	88
4.8	The FAC Model . . . . .	91
<b>5</b>	<b>Chandra's View of Cyg X-1</b>	<b>94</b>
5.1	Chandra . . . . .	94
5.1.1	The Mirrors . . . . .	95
5.1.2	The Gratings . . . . .	96
5.1.3	HETGS . . . . .	97
5.1.4	The ACIS Detector . . . . .	98
5.1.5	Readout modes . . . . .	99
5.2	ObsID 3814 . . . . .	100
5.2.1	Lightcurves and Color-Color Diagrams . . . . .	102
5.2.2	Continuum . . . . .	102
5.2.3	Absorption Lines and Equivalent Widths . . . . .	105
5.2.4	Comparison to Laboratory Spectra . . . . .	105
5.3	ObsID 8525 . . . . .	112
<b>6</b>	<b>Conclusion and Outlook</b>	<b>116</b>
<b>A</b>	<b>Angular Momentum Notation</b>	<b>121</b>
<b>B</b>	<b>Rate Equations</b>	<b>122</b>
	<b>Bibliography</b>	<b>125</b>
	Acknowledgements . . . . .	132
	Declaration . . . . .	135





WE SEE how we may determine their forms, their distances, their bulk, their motions, but we can never know anything of their chemical or mineralogical structure.

Auguste Comte (1935) about stars  
in his book *Positive Philosophy*



It is reasonable to hope that in the not too distant future we shall be competent to understand so simple a thing as a star.

---

Arthur S. Eddington (1926)

# Chapter 1

## Introduction

Often texts about X-ray astronomy begin their introduction either reaching way back into the past when mankind started wondering about the stars in the skies or by resorting to the discovery of X-rays by Wilhelm Conrad Röntgen (1895). For a change, this introduction shall tell about the close relationship of astronomy and atomic physics.

Observational astrophysics – taking spectra in the optical or ultra-violet (UV) wavelength range with ground based observatories, examining the Sun’s X-ray spectrum with rocket flights, launching X-ray telescopes into orbit to observe distant celestial objects, etc. – has been going hand in hand with experimental and theoretical atomic physics for quite a long time. Indeed, it has been a very fruitful relationship for both parties. Everything began with Joseph von Fraunhofer (1814)’s discovery of dark lines (today known as Fraunhofer lines) in the continuous optical spectrum of the Sun. Kirchhoff (1860b) and Kirchhoff & Bunsen (1860) later showed that these lines are due to absorption of light by atoms after they had noticed that several of the lines mapped by Fraunhofer coincide with the wavelength of emission lines of heated elements (Kirchhoff, 1860a). The realization that each element has a characteristic set of lines not only led to the discovery of missing elements in the periodic table – e.g., cesium (Bunsen, 1860) and rubidium (Kirchhoff & Bunsen, 1861) – but also hinted at the chemical composition of the Sun’s atmosphere. The discipline of spectroscopy was born.

One of the most important elements that was first only detected in solar spectra and is therefore named after the Greek sun god is helium. It was discovered independently by the astronomers Janssen (1869) and Lockyer (1868) during the solar eclipse of 1868. It took another 27 years until helium was also isolated on Earth by Sir William Ramsay et al. (1895). Further studies of the origin of spectral lines showed that the complexity of the spectra increases with increasing atomic number  $Z$  of the elements. Balmer (1885) laid the foundation of a systematic description of spectral lines series when he empirically found a simple scaling law for the line series in hydrogen. This knowledge about the properties of spectral lines made it possible for Niels Bohr (1913a,b,c) to derive the Bohr model of the atom and to explain Balmer’s law theoretically (Bohr, 1920). Around the same time, Zeeman (1897) discovered the effect of a magnetic field on spectral lines. His suggestion of the possible astrophysical relevance led to Hale (1908a,b)’s detection of the Zeeman effect in the optical spectra of sunspots, providing a means to directly measure the strength of their magnetic field.

Another way atomic physics can help out with astrophysical measurements is by providing accurate rest wavelength of transitions in elements most commonly seen in stellar spectra.

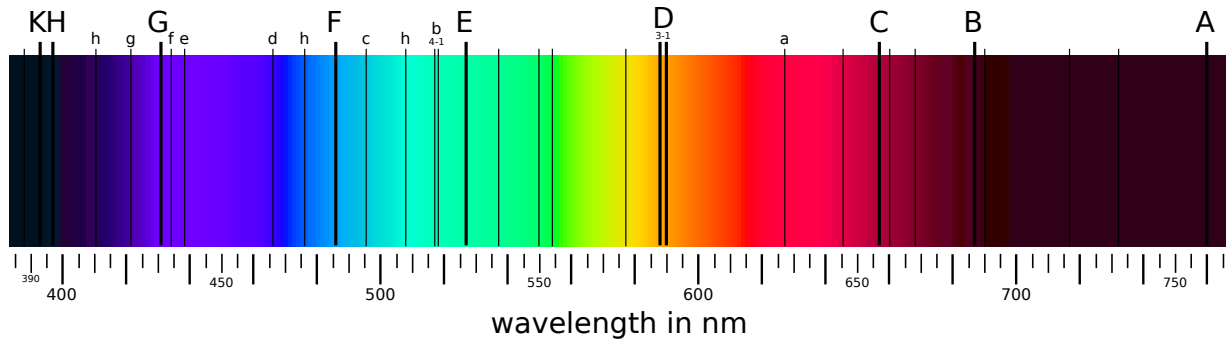


**Figure 1.1:** Sketch of the Fraunhofer lines in the optical solar spectrum (from [http://en.wikipedia.org/wiki/Fraunhofer\\_lines](http://en.wikipedia.org/wiki/Fraunhofer_lines)).

Doppler (1842) proposed the effect that the wavelengths of radiation emitted by a moving object are shifted to shorter or longer wavelengths depending on the direction of the motion relative to the observer. Knowing the exact position of these wavelengths at rest, the speed of the object can be easily derived via spectroscopy. For instance, the finding that most nebula have systematically redshifted spectra resulted in the discovery of Hubble's law in cosmology (Hubble, 1929).

A last of many available examples for the symbiosis of atomic physics and astronomy brings us back to the energy region in focus of this work: X-ray spectra. Fritz et al. (1967) found lines in the solar X-ray spectrum taken during a rocket flight which were of unusual type. They believed that these lines originated from  $K\alpha$  transitions in few times ionized material. The tables given by Fritz et al. (1967), ordered by increasing wavelength, suggest that spectral information about L-shell ions (3-10 electrons left) of elements like O, Si, Ar and Fe. Since the laboratory measurements and calculations so far had mainly been carried out for  $K\alpha$  transitions in singly ionized material and some for hydrogen and helium like ions, atomic physics was triggered to study these lines in all ionization states in order to be able to sufficiently identify the lines of the solar spectrum (House, 1969).

The scope of this work is a similar one. Hanke (2007) and Miškovičová et al. (2011) found absorption lines of lower ionization states of silicon and sulfur (as opposed to the more common He- and H-like ones) in the spectra of the high mass X-ray binary Cygnus X-1. This kind of transitions is not readily available in spectral databases. Therefore, we measured them in the laboratory and directly applied the results to the spectra of Cyg X-1.

To gain a little understanding of the origin of the lower ionization states of Si and S in Cyg X-1, chapter 2 gives an introduction to the physics in high mass X-ray binaries and stellar winds and tells the history of Cyg X-1, motivating the need for accurate atomic data. Chapter 3 explains the atomic physics behind our understanding of the structure of the atom, of ion production and radiative processes. It also provides a quick overview of how theoretical predictions of the atomic physics parameters are obtained. After a description of the production and gathering of X-ray spectra with an electron beam ion trap, the  $K\alpha$  lines of Si and S are identified and compared to theoretical predictions in chapter 4. Chapter 5 then combines the experimental results with the *Chandra* spectra of Cyg X-1 to try to confine the properties of the stellar wind in that system. Finally, in chapter 6 the applied methods and the quality of the results are shortly reviewed and prospects to improve the laboratory data and hence our knowledge of stellar wind properties are given.

## Chapter 2

# High Mass X-Ray Binaries

X-ray binaries are among the most luminous X-ray sources in the sky. They come in two flavors: low mass X-ray binaries (LMXB) and high mass X-ray binaries (HMXB). Both types of systems contain either a neutron star or a black hole<sup>1</sup> as a compact object accreting material from a companion star. Although the HMXBs and LMXBs differ in many respects including their optical properties (Lewin et al., 1995), the characteristic difference between them is the mass of the companion star. As their names already implicate, while LMXB comprise a low mass late type star, later than type A, or even a white dwarf, the companion in a HMXB is a very massive O or B type star with an optical/ultra-violet luminosity that may be even higher than that of the X-ray source. The X-ray source is powered by mass accretion onto the compact object through the released gravitational potential energy. The companion in an LMXB does not have a strong stellar wind sufficient to power the observed X-ray source and therefore in those systems the mass transfer is dominated by the companion filling its critical gravitational potential lobe, the Roche lobe (see section 2.2). In contrast, the OB companion in a HMXB has a strong stellar wind corresponding to a mass loss rate of about  $10^{-10}$  to  $10^{-6} M_{\odot} \text{ yr}^{-1}$  (Lewin et al., 1995), which will be captured by a close compact object.

## 2.1 Stellar Evolution

Before we learn the details of the stellar wind and the accretion and radiation mechanisms in a HMXB, we begin with a short reminder of stellar evolution. More or less detailed descriptions of stellar evolution can be found in most basic or overview astronomy textbooks, such as, e.g., Karttunen et al. (1987) and Carroll & Ostlie (2007).

A star spends the largest part of its life in a steady state, continuously radiating away energy produced through hydrogen burning in its core. As long as the radiation pressure counteracts the gravitational pressure, the star lives happily in hydrostatic equilibrium. Once it runs out of fuel in its core, the H-burning continues in a shell around the core. During this shell burning phase, the star becomes more luminous and blows up to a

---

<sup>1</sup>Black hole is a brief, more catchy expression for the phrase *gravitationally completely collapsed star* which is hard to say more than once in a row. The expression became popular when John A. Wheeler spread it after hearing it from someone in the audience during a discussion about these objects at a conference held at the Goddard Institute for Space Studies in New York in the fall of 1967. The discussion was actually about compact objects in the center of pulsars which later turned out to be neutron stars rather than black holes.

red giant. Heated by the energy production of the shell burning, the core can reach temperatures hot enough to ignite helium burning. For more massive stars this procedure can go on up to the production of iron, a natural limit since nuclear fusion then becomes endothermic, i.e., requiring energy for the reaction to take place. He burning, however can become unstable, causing the star to blow away its outer envelope. The ejected material can then be seen as a planetary nebula, illuminated from the inside by a white dwarf.

At some point all available fuel will be exhausted. Since the nuclear fusion rate grows stronger with the mass than the actual amount of burning material, massive stars undergo a faster evolution. With the increasing lack of fuel, the radiation pressure fades away. Hence, the gravitational pressure takes over and the star shrinks. If the remaining mass of the star is less than the Chandrasekhar limit of  $1.4 M_{\odot}$  (Chandrasekhar, 1931a,b), the star collapses to a white dwarf where gravity is counteracted by the degeneracy pressure of the Fermi-gas of electrons (Fermi, 1926).

Stars with an initial mass greater than about  $8 M_{\odot}$  may not lose enough energy during their life time and end up with a mass above the Chandrasekhar limit (Seeds & Backman, 2011). In this case, the gravitational pressure forces electrons and protons to combine to neutrons. Only the degenerate Fermi-gas of neutrons is able to withstand gravity. A neutron star is formed. A large number of escaping neutrinos produced during the neutronization of the core may contribute to the outer layers of the star being ejected in a supernova explosion.

The repulsive neutron-neutron interaction and the degeneracy pressure of the neutron gas, however, is not almighty. If the star has a yet higher remaining mass, this time above the Oppenheimer-Volkoff limit (Oppenheimer & Volkoff, 1939), gravity dominates all other forces and the compact object has to collapse further into a black hole. According to Postnov & Yungelson (2006) stars of a mass between 25 and  $60 M_{\odot}$  do not lose enough mass and are most likely to meet this fate. Due to the lack of a thorough understanding of the equation of state of this extremely dense nuclear matter, the Oppenheimer-Volkoff limit is not known as accurately as the Chandrasekhar limit but it is definitely below  $3 M_{\odot}$  (Shapiro & Teukolsky, 1983).

For a single star, this would probably be the end of the story. In a binary system, though, the contained stars can influence each other heavily in their evolution (Iben & Tutukov, 1985). Figure 2.1 gives an overview of how we end up with our HMXB: The more massive star (called the primary) in the system evolves faster than its companion. When it leaves the main-sequence, it expands and overfills its Roche lobe, i.e., the equi-potential surface that separates the region in space where material is gravitationally bound to one of the stars (see section 2.2), contaminating the atmosphere of the companion with possibly metallic<sup>2</sup> material. The additional mass loss due to the Roche lobe overflow can significantly change the outcome of the compact object. After the primary concluded its evolution to a compact object, the secondary is finally the companion with the higher mass. When the secondary is itself close to its Roche lobe, accretion of its stellar wind onto the compact object results in powerful X-ray emission.

## 2.2 Roche Lobes

Édouard Albert Roche (1849, 1850, 1851) is famous for his work in celestial mechanics, especially for his description of the gravitational potential in a binary system. The effective

---

<sup>2</sup>In astrophysics every element other than hydrogen and helium is called a *metal*.

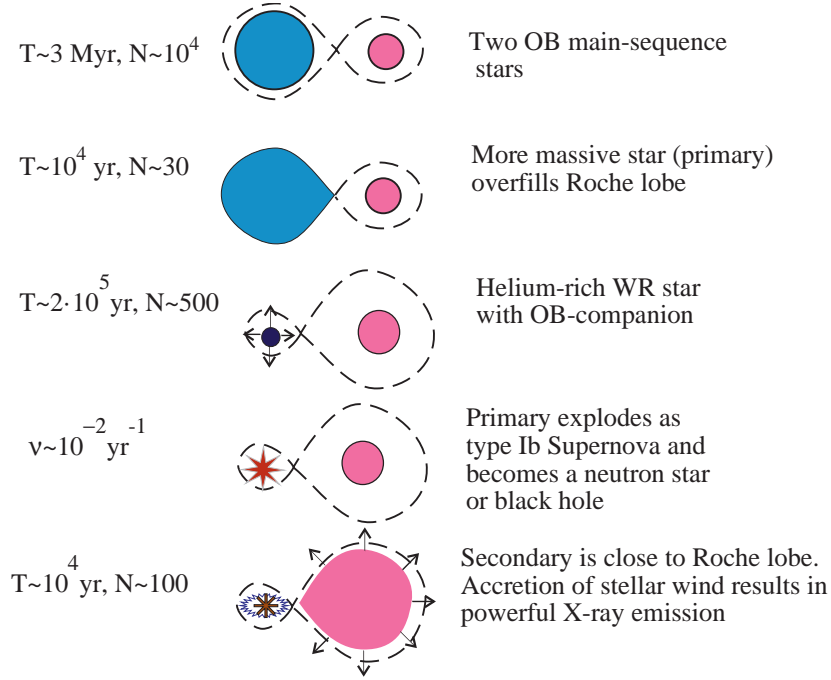


**Figure 2.1:** The evolution of a compact binary (from Postnov & Yungelson (2006), Fig. 4).

potential energy of test mass in the potential of a star whose rotation is synchronized with its orbit does not only depend on the gravity of the two bodies with masses  $M_1$  and  $M_2$  at positions  $\mathbf{r}_1$  and  $\mathbf{r}_2$  but also on the centrifugal potential of their angular motion with velocity  $\boldsymbol{\omega}$  around the barycenter  $\mathbf{r}_{\text{BC}} = (M_1\mathbf{r}_1 + M_2\mathbf{r}_2)/(M_1 + M_2)$ . Since all terms in the potential energy are proportional to the test mass  $m$ , we can cancel it for convenience and obtain the effective gravitational potential per unit mass

$$\Phi(\mathbf{r}) = -\frac{GM_1}{|\mathbf{r} - \mathbf{r}_1|} - \frac{GM_2}{|\mathbf{r} - \mathbf{r}_2|} - \frac{1}{2}[\boldsymbol{\omega} \times (\mathbf{r} - \mathbf{r}_{\text{BC}})]^2. \quad (2.1)$$

From Kepler's third law for the orbital period (Kepler, 1619)

$$\omega^2 = \left(\frac{2\pi}{P}\right)^2 = \frac{G(M_1 + M_2)}{a^3} \quad (2.2)$$

with  $a = |\mathbf{r}_2 - \mathbf{r}_1|$  being the binary separation, we know the norm  $\omega$  of the angular velocity  $\boldsymbol{\omega}$ . Therefore, the shape of the effective potential only depends on the mass ratio  $q := M_2/M_1$  of the two stars.

Without loss of generality, we are free to choose our coordinate system conveniently. The easiest choice is to put the primary star into the origin of the coordinate system, i.e.,  $\mathbf{r}_1 = \mathbf{0}$ , the secondary at a position  $\mathbf{r}_2 - \mathbf{r}_1$  on the positive  $x$ -axis and let the system rotate with  $\boldsymbol{\omega} = \omega\mathbf{e}_z$  pointing into the positive  $z$ -direction. To eliminate all parameters and constants but the mass ratio, dimensionless coordinates  $\mathbf{r}/a = (x, y, z)$  are used to obtain the scaled Roche potential

$$\frac{a}{GM_1}\Phi(\mathbf{r}) = \frac{-1}{\sqrt{x^2 + y^2 + z^2}} - \frac{q}{\sqrt{(x-1)^2 + y^2 + z^2}} - \frac{1+q}{2} \left[ \left(x - \frac{q}{1+q}\right)^2 + y^2 \right]. \quad (2.3)$$

There are five critical points in this potential where because of the vanishing gradient  $\nabla\Phi = 0$  there is no effective force on the test mass, i.e., the gravitational forces on  $m$  from

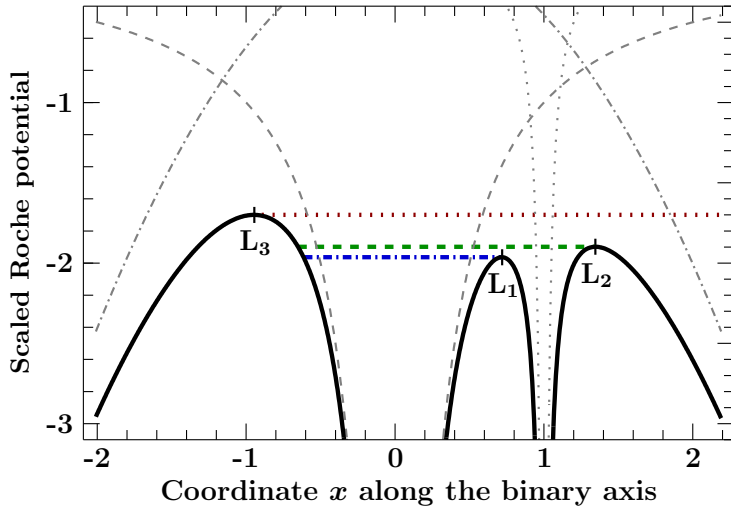


**Figure 2.2:** Roche potential of Eq. 2.1 for  $q = 1$  along the binary axis. Its components are shown in gray: potential of primary mass  $M_1$  (dashed), of secondary mass  $M_2$  (dotted) and centrifugal potential (dash-dotted). The horizontal lines indicate the limiting potentials of the  $L_1$  (blue),  $L_2$  (green) and  $L_3$  (red) saddle points (from Hanke (2011), Fig. 1.1).

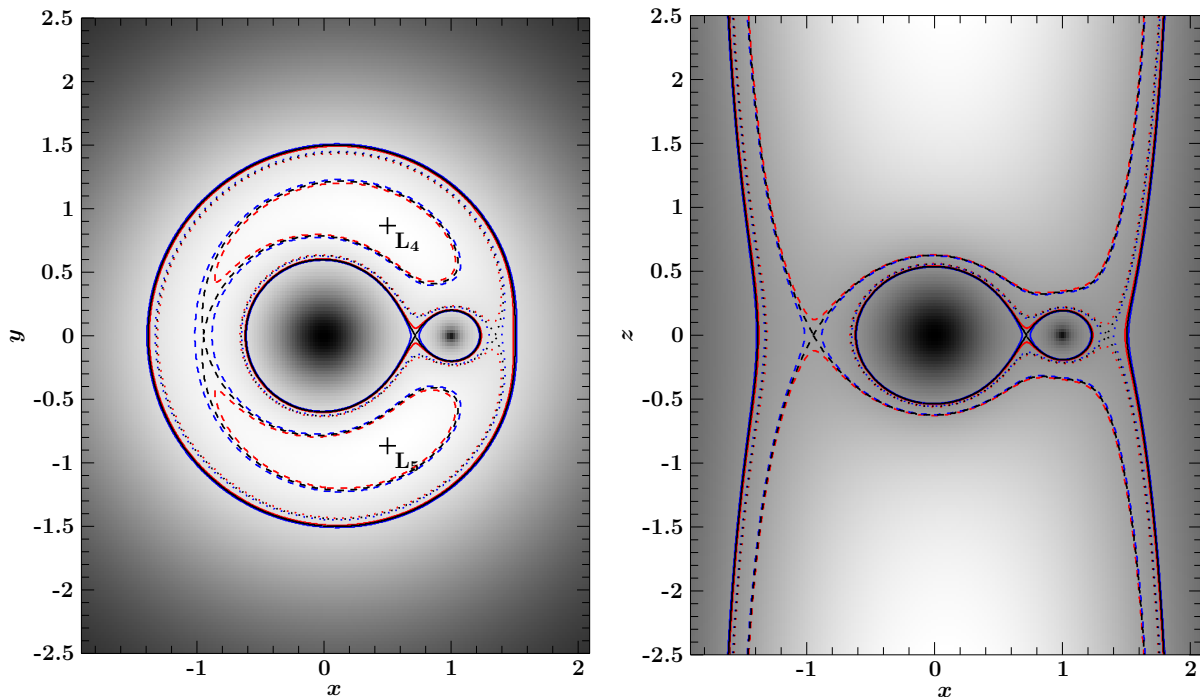


**Figure 2.3:** Roche potential for  $q = 0.1$  in the  $x$ - $y$ -plane at  $z = 0$  (left) and the  $x$ - $z$ -plane at  $y = 0$ . Brighter colors stand for higher potentials. The Roche lobes (through  $L_1$  are indicated by a black solid line, equi-potential surfaces through  $L_2$  and  $L_3$  by the black dotted and dashed lines, respectively. The red and blue lines trace the equi-potential surfaces of 0.5% higher and lower potentials. The local maxima of  $L_4$  and  $L_5$  are marked with labeled crosses (from Hanke (2011), Fig. 1.2).

the masses  $M_1$  and  $M_2$  exactly balance the centrifugal force. As these points constitute local maxima of  $\Phi$ , they are unstable equilibrium points (Lagrange, 1772). These points are called Lagrangian points  $L_1$ - $L_5$  in honor of Joseph Louis Lagrange who discovered them in his calculations of the three-body problem. Since  $\partial\Phi/\partial z = z \cdot f(x, y, z)$  with a positive function  $f(x, y, z) > 0$ , all of these saddle points are in the  $x$ - $y$ -plane, the plane of the rotation containing the centers of the stars and their barycenter.

Figure 2.2 (Hanke, 2011) shows the shape of the Roche potential (eq. 2.3) for  $q = 0.1$  along

the binary axis where the first three Lagrangian points can be found. A corresponding map of  $\Phi(\mathbf{r})$  in the  $x$ - $y$  plane at  $z = 0$  (viewing into the binary from the top) and from the side view in the  $x$ - $z$  plane at  $y = 0$  is displayed in figure 2.3 (Hanke, 2011). Here, brighter colors mean higher potential, revealing that the triangular Lagrange points  $L_4$  and  $L_5$  at  $(x, y) = (1, \pm\sqrt{3})/2$  to be the global maxima of the potential.

The equi-potential surface defined by the potential of the inner Lagrangian point  $L_1$  where matter feels the same drag into the directions of both stars is called Roche lobe. Co-rotating material inside the Roche lobe is gravitational bound to the corresponding star. Since the effective gravity is in each point perpendicular to the equi-potential surface, due to the hydrostatic equilibrium of the star the pressure is constant along constant potentials  $\Phi$ . Therefore, the shape of the star always coincides with an equi-potential surface of the Roche potential. This is also true if the star expands. Because of the shape of the potential a star in a binary system is only approximately spherical if it is small compared to its Roche volume. The more the star fills its Roche lobe, the more teardrop shaped it becomes.

## 2.3 Stellar Winds

The main-sequence with its H-burning is a relatively stable and quite phase in the life of a star. Nevertheless, its outer layers are very active like in an O or B type star where the outer layers of the atmosphere are pushed away by radiation pressure. This manifests itself in strong stellar winds. The main characteristics of stellar wind are the mass loss rate  $\dot{M}$  and the terminal velocity  $v_\infty$ . The terminal velocity is the velocity of a particle that is far enough away from the star that the star does no longer exert forces on it. Since they depend on the radiative transport in the star and possibly on magnetic fields, stellar winds are very complex phenomena. There is a variety of theories to describe the stellar wind of different kinds of stars as they are dominated by different physical processes and, hence, different approximations are possible to be applied to them. Here we focus on the line driven winds of early type stars. The textbook of Lamers & Cassinelli (1999) gives a nice overview of the subject. A somewhat shorter summary can be found in Fürst (2011). Ions of C, N, O, Si, P, S, and the Fe group elements have numerous resonance lines with a large optical depth in the UV energy range. Photons of the star's UV continuum with matching energies interact with the corresponding ions. During the absorption process the momentum of the photon is transferred to the absorbing ion. Since the photons are emitted radially away from the star and the transferred momentum is shared between neighboring particles (ions and electrons) through Coulomb coupling, there is a net increase of the atmospheric particles' momenta away from the star, which results in a steady outflow of matter, the stellar wind. The wind is especially optically thick for photons at resonance line energies, i.e., these photons are absorbed away in lower layers of the wind close to the surface of the star. Although the line opacity is strongly peaked, the Doppler effect (Doppler, 1842) arranges for a steady supply of absorbable photons. According to the Doppler effect a photon of frequency  $\nu > \nu_0$  higher than the frequency of a line at  $\nu_0$  can still be absorbed by this line if the stellar wind reaches a velocity of

$$v = \frac{\nu - \nu_0}{\nu_0} \cdot c, \quad (2.4)$$

where  $c$  is the speed of light, as the photon sees this line shifted to its own frequency  $\nu$ . Since the star appears to be receding from the ion's point of view, higher wind speed

corresponds to a stronger redshift of the radiation it sees, hence, higher photon energies can be absorbed. This way the stellar wind can become optically thick for the whole spectrum. In this case the entire momentum of the radiation,  $L/c$ , where  $L$  is the luminosity of the star, is transferred to the wind. Then the mass loss rate of the star is maximally  $\dot{M} \lesssim (L/c)/v_\infty$ . For a  $L = 10^6 L_\odot$  star with  $v_\infty = 3000 \text{ km s}^{-1}$  this estimate gives  $\dot{M}_{\text{max}} = 7 \cdot 10^{-6} M_\odot \text{ yr}^{-1}$  which is about the mass loss rate actually observed for OB supergiants (Cassinelli, 1979). With this mass loss rate the kinetic power of the wind  $\dot{M}v_\infty^2/2 = \frac{v_\infty}{2c} \cdot L \sim 0.05\% \cdot L$  is only a small fraction of the stellar luminosity, which hints at the photons being re-emitted isotropically rather than being destroyed. On average this emission is not Doppler shifted but adds some flux to the blueshifted absorption lines, resulting in P Cygni type line profiles (Castor & Lamers, 1979).

The forces acting on the wind at a given velocity depend on the interaction probability of the photons with plenty of line transitions. Sobolev (1960) calculated the radiative transfer of momentum in the limit of an infinitely narrow absorption region where the line width is so small that the absorption coefficient can be approximated by a  $\delta$ -function. Another approximation assumes that the wind density is with  $\rho \lesssim 10^{-12} \text{ g cm}^{-3}$  so low that collisional excitation is negligible such that only transitions from the ground level, low excitation and metastable levels contribute (Lamers & Cassinelli, 1999) to the radiative force. Based on these two assumptions early theories like the one of Lucy & Solomon (1970) only considered resonance lines, i.e., those involving the ground state. Castor et al. (1975), however, showed that the radiative force is actually dominated by subordinate absorption lines which connect different excited states. This Castor Abbott Klein (CAK) model predicts terminal wind velocities of  $v_\infty \approx 1500 \text{ km s}^{-1}$  and mass loss rates of  $\dot{M} \approx 10^{-6} M_\odot \text{ yr}^{-1}$ , in good agreement with measurements.

The velocity profile of the wind can be described by the velocity law (Puls et al., 2008)

$$v(r) \simeq v_0 + v_\infty \left(1 - \frac{R_*}{r}\right)^\beta \quad (2.5)$$

where  $v_0 = v(R_*)$  is the initial wind velocity at the photosphere of the star with radius  $R_*$ . The value of  $\beta$  depends on the details of the calculation, but with  $\beta = 1/2$  (Castor et al., 1975),  $\beta \approx 1$  (Friend & Castor, 1983) and  $\beta \approx 0.8$  (Pauldrach et al., 1986; Friend & Abbott, 1986) is in good agreement with the observation of  $\beta = 0.68 \pm 0.15$  by Groenewegen & Lamers (1989). According to Lucy & Solomon (1970)  $v_0$  can be estimated from mass conservation

$$\rho(r)v(r) = \frac{\dot{M}}{4\pi r} \quad (2.6)$$

where  $\rho(r)$  is the surface density under the assumption of a pure hydrogen envelope with an electron temperature  $T_e$  of 70 % of the surface temperature  $T_{\text{eff}}$  and an electron pressure of  $\log p_e = \log g - 0.5$ .

Line driven winds are intrinsically unstable (Lucy & Solomon, 1970) and therefore small perturbations grow quickly (Owocki & Rybicki, 1984). Random velocity fluctuations are self-enhancing: an ion that is a little faster than its environment sees a higher Doppler shift in the photons and can therefore access less absorbed regions of the UV continuum. The resulting higher momentum transfer then accelerates this ion even more whereby again new regions of the radiation continuum become available for absorption. The ion's velocity is increased above the local wind speed and clumps are forming. Non-stationary hydrodynamic simulations show that dense cool shells of gas build on all length scales and

move through the wind (Dessart, 2004; Dessart & Owocki, 2005) and can especially form already close to the photosphere (Feldmeier et al., 1997; Dessart & Owocki, 2003).

Simulations by Blondin et al. (1990, 1991) and Mauche et al. (2008) show that in a binary system even in a smooth wind clumps and density variations would be produced by the wind passing through the accretion wake of the compact object. The wind structure is not yet well understood and theorists as well as observers can not say much about the amount of clumping and the size of the structure – recent reviews are given by Puls et al. (2008) and Hamann et al. (2008) – but, e.g., for Cyg X-1 Mišková et al. (2011) and Hanke (2011) showed that there are probably cold clumps in highly ionized medium.

## 2.4 Accretion

Although theoretically black holes could evaporate on time scales of  $(M/M_\odot)^3 \cdot 10^{71}$  s through radiation due to quantum effects (Hawking, 1974), for black hole masses in the order of a few solar masses this process is negligible compared to the lifetime of  $< 5 \cdot 10^{71}$  s of the universe. Due to their immense gravitational potential, there is no other way for a black hole to emit radiation directly. Nevertheless, the high X-ray luminosity in the order of  $10^4 L_\odot$  has to be produced somehow. Here, the accretion of material donated by the companion star via stellar winds or Roche lobe overflow comes in handy. Accretion is indeed able to produce and release lots of energy, mainly in the X-ray regime. A typical X-ray binary has thus a luminosity of  $10^{36}$ – $10^{38}$  erg s<sup>-1</sup> in the energy range 2–20 keV (Lewin et al., 1995). For comparison, the bolometric luminosity of the Sun is  $L_\odot = 3.839 \cdot 10^{33}$  erg s<sup>-1</sup>.

In the process of accretion the gravitational potential energy of a particle with mass  $m$  falling from a large distance onto the accreting object of mass  $M$  with a radius  $R$  greater than the gravitational radius  $R_g$  is set free. The gravitational or Schwarzschild radius (Schwarzschild, 1916)

$$R_g = \frac{GM}{c^2} \quad (2.7)$$

is the radius of the sphere to which the whole mass of an object has to be compressed for the escape velocity of this object to become equal to the speed of light. With it the change in potential energy can be written as

$$\Delta E_{\text{grav}} = \frac{GMm}{R} = \frac{mc^2}{R/R_g}. \quad (2.8)$$

For very compact objects with small radius-to-mass ratios  $R/M$  and hence small  $R/R_g$ , i.e., with radii close to their Schwarzschild radius, the released gravitational energy is a large fraction of the accreted particle's rest mass  $mc^2$ . The total energy conversion efficiency  $\eta$  of this process is in the order of 10 percent. The luminosity coming from the released energy can then be calculated to (Carroll & Ostlie, 2007)

$$L = \eta \dot{m} c^2. \quad (2.9)$$

Therefore, a mass accretion rate of  $\dot{m} = 1.77 \cdot 10^{-10} M_\odot \eta^{-1} \text{ yr}^{-1}$  is required to produce the observed luminosity  $L = 10^{37}$  erg s<sup>-1</sup>.

A natural limit for the mass accretion rate is set by the Eddington (1916, 1917, 1925) luminosity which can be derived from the interaction between the accreted material and

the emitted radiation (Frank et al., 2002). Accretion is only possible as long as the gravitational force  $F_g$  dragging a particle at radius  $r$  towards the compact object is stronger than the radiative force  $F_{\text{rad}}$  pushing it away. Assuming a mass  $M$  spherically symmetrically accreting fully ionized pure hydrogen gas, the force imbalance

$$F_g = \frac{GMm_p}{r^2} > \frac{\sigma_T S}{c} = F_{\text{rad}}, \quad (2.10)$$

where  $\sigma_T$  is the cross section for Thomson (1903) scattering of photons with free electrons and  $S = L/(4\pi r^2)$  is the energy flux, leads to the Eddington limit

$$L < L_{\text{edd}} = \frac{4\pi GMm_p c}{\sigma_T} = 1.3 \cdot 10^{38} \frac{\text{erg}}{\text{s}} \cdot \frac{M}{M_\odot}. \quad (2.11)$$

Note that, although the Thomson cross section is negligible for protons, they are nevertheless affected by  $F_{\text{rad}}$  due to their interactions with the electrons through Coulomb (1785) coupling. The Eddington luminosity is a good estimate but not a hard limit because of its approximate nature.

For a compact object in a binary system it is easy to find accretable material. Only the details of the mass transfer mechanisms from the companion to the compact object depend on the type of the donor star. Therefore, mass transfer can be seen as another characteristic of the classification of binaries via their companion type.

Since LMXB do not have serious stellar winds, for a LMXB to transfer mass the late type companion has to fill its Roche lobe such that matter from its atmosphere can spill over the inner Lagrange point  $L_1$  to fall toward the compact object. Since the spilled material has orbital angular momentum, large accretion discs form. In contrast, the strong stellar wind of the (O/B) star takes care of the mass transfer in HMXB according to the model of Bondi & Hoyle (1944) and Bondi (1952). For a supergiant close to filling its Roche lobe, this wind can be particularly focused towards the compact object (Friend & Castor, 1982). The radial stellar wind, however, usually does not have much angular momentum. Therefore, HMXB develop only small accretion disks or none at all.

The properties of the accretion differ between black holes and neutron stars. Neutron stars can have very strong magnetic fields guiding the ionized matter to the magnetic poles of the star. There the kinetic energy of the accreted matter is deposited in an hot spot on the solid surface of the neutron star. Both is not the case for black holes.

Because of angular momentum conservation particles with angular momentum with respect to the accreting object can not just fall straight onto it. Unless the angular momentum can be deposited via interactions, the matter has to move on Kepler (1609) orbits. An accretion disk forms of matter slowly spiraling downward onto the compact object. Shakura & Sunyaev (1973), the standard theory of geometrically thin accretion disks, assumes some sort of viscosity of unspecified physical origin to transfer the directed kinetic motion due to the angular momentum into random thermal motion. For a constant accretion rate  $\dot{m}$  the energy of a steady accretion disk has to be dissipated at a rate

$$D(r) = \frac{dE}{dA dt} = \frac{3GM\dot{m}}{4\pi r^3} \left(1 - \sqrt{\frac{r_0}{r}}\right) \quad (2.12)$$

where  $r_0$  is the radius where the inner boundary condition of vanishing torque and dissipation is fulfilled. This radius is, for example, equal to the stellar radius  $R_*$  in case of an accretion disk around a star. The total disk luminosity

$$\int_{r_0}^{\infty} D(r) \cdot 2\pi r dr = \frac{GM\dot{m}}{2r_0} \quad (2.13)$$

constitutes only half of the accretion power. The other half comes from the kinetic energy of the accreted particles.

The temperature  $T(r)$  of the accretion disk can be estimated under the assumption of an optically thick disk which hence is in thermodynamic equilibrium. Then the Stefan (1879)-Boltzmann (1884) law

$$D(r) = 2\sigma_{\text{SB}}T(r)^4 \quad (2.14)$$

applies with an additional factor 2 as both sides of the disk radiate. Solving for  $T(r)$ , equation 2.12 becomes

$$T(r) = 2.7 \cdot 10^7 \text{ K} \cdot \left( \frac{\dot{m}[10^{-10} M_{\odot} \text{ yr}^{-1}]}{(M/M_{\odot})^2 \cdot (r/R_{\text{g}})^3} \right)^{1/4} \cdot \left( 1 - \sqrt{\frac{r_0}{r}} \right)^{1/4}. \quad (2.15)$$

For typical X-ray binaries the temperature at the inner boundary of the disk, corresponding to photon energies of  $E = k_{\text{B}}T = 0.086 \text{ keV} \cdot T/10^6 \text{ K}$  in the soft X-ray regime, thus exceeds  $10^6 \text{ K}$ . To calculate the spectrum  $S_{\text{E}}(E)$  of the full disk from all radii  $r_{\text{in}} < r < r_{\text{out}}$  due to thermal radiation the Planck (1901) function, the radiation curve of a black body,

$$B(E, T) \propto \frac{E^3}{\exp(E/kT) - 1} \quad (2.16)$$

has to be integrated over the whole area of the disk:

$$S_{\text{E}}(E) = \int_{r_{\text{in}}}^{r_{\text{out}}} B(E, T(r)) 2\pi r dr \approx \frac{8\pi}{3} r_{\text{in}}^2 \int_{T_{\text{out}}}^{T_{\text{in}}} \left( \frac{T_{\text{in}}}{T} \right)^{11/3} B(E, T) \frac{dT}{T_{\text{in}}}. \quad (2.17)$$

Here, the integral was simplified through the approximation

$$T \approx T_{\text{in}} \left( \frac{r_{\text{in}}}{r} \right)^{3/4}. \quad (2.18)$$

The resulting spectrum (Eq. 2.17) in parameters of the inner radius  $r_{\text{in}}$  and its temperature  $T_{\text{in}}$  is referred to as disk black body or multicolor disk spectrum (Mitsuda et al., 1984; Makishima et al., 1986). As in this approximation  $r_0$  was neglected,  $r_{\text{in}}$  lacks a ‘‘color correction’’ factor and hence does not represent the effective inner disk radius (Shimura & Takahara, 1995).

While an accretion disk can explain the soft thermal component observed in the spectra of many X-ray binaries, the hard powerlaw component originates from a completely different physical process: inverse Compton scattering. In inverse Compton scattering low energetic thermal photons gain energy by scattering off of high-energy electrons. The so called accretion disk corona of thin hot plasma is sufficient to provide these electrons (Balbus & Hawley, 1998). As the name already tells us, inverse Compton scattering is the inverse process of ‘‘normal’’ Compton (1923) scattering where electrons (assumed to be at rest) gain energy from photons via the process  $\gamma + e \rightarrow \gamma' + e'$ . After the scattering at an angle  $\theta$  the photon energy  $E$  reduces due to conservation of the 4-momentum to

$$E' = \frac{E}{1 + \frac{E}{m_e c^2} (1 - \cos \theta)}. \quad (2.19)$$

The energy loss averaged over all possible angles  $\theta$  is then

$$\langle E' - E \rangle = -\frac{E}{m_e c^2} \quad (2.20)$$

if the photon energy is much smaller than the rest energy of the electron ( $E \ll m_e c^2$ ). It can be shown (Rybicki & Lightman, 1979) that in the inverse process photons scattering with Maxwell (1867) distributed electrons with temperature  $T$  are up-scattered on average by

$$\frac{\langle E' - E \rangle}{E} = \frac{4k_B T - E}{m_e c^2}. \quad (2.21)$$

To produce a powerlaw spectrum

$$\frac{dN}{dE} \sim E^\Gamma \exp(E/E_0) \quad (2.22)$$

multiple scattering (Comptonization) is necessary. This spectrum has an exponential cutoff at  $E_0 \approx k_B T$ . The photon index  $\Gamma$  depends on the optical thickness of the electron plasma.

Markoff et al. (2005) suggest that such a powerlaw spectrum can alternatively be produced by synchrotron-radiation from jets, which are relativistic plasma outflows. In this case the base of the jet would provide the thin electron plasma needed for Comptonization.

## 2.5 Spectral States

We found two mechanisms likely to be responsible for different part of the X-ray spectrum: the soft thermal and the harder powerlaw component. But we have not come across a reference point that would indicate their relative contribution to the overall flux in the spectrum. Actually, repeated observations of the same source show that this relation can change over time. In black hole binaries there are mainly two spectral states which can be observed: the high/soft and low/hard state (Lewin et al., 1995). These states are classified via the relative strength of the soft and the hard spectral component, the total luminosity and the radio spectrum (Remillard & McClintock, 2006).

In the low/hard state, the X-ray luminosity is typically below 5 percent of the Eddington luminosity. The spectrum is dominated by the powerlaw component while the soft thermal component is either very weak or even absent. The powerlaw is rather flat with a photon index  $\Gamma$  in the range of 1.4 to 1.8. In this state some sources also show considerable radio emission corresponding to synchrotron radiation from a jet.

During the high/soft state, the luminosity is close to the Eddington limit. While the soft thermal component dominates the spectrum, a photon index of roughly 2.5 flattens the hard X-ray flux. There is no radio emission.

A transition between these two states takes place via an intermediate state. The differences between them can be physically explained with changes in the geometry of the binary system Brocksopp et al. (Fig. 2.4; 1999). In the soft state the accretion disk reaches very close to the innermost stable circular orbit (ISCO) resulting in a high accretion rate and therefore in high luminosity. Since the disk itself is very bright in this state, the soft X-ray flux is enhanced. The high X-ray flux additionally heats the stellar wind and the surface of the companion. In contrast, during the hard state the accretion disk is less luminous and recedes farther from the black hole. Instead a jet and a Comptonizing corona build. While the Comptonization is crucial for the production of hard X-rays, the weak disk is responsible for the low soft X-ray flux and does not provide enough food for the black hole, which leads to an overall decrease of luminosity.

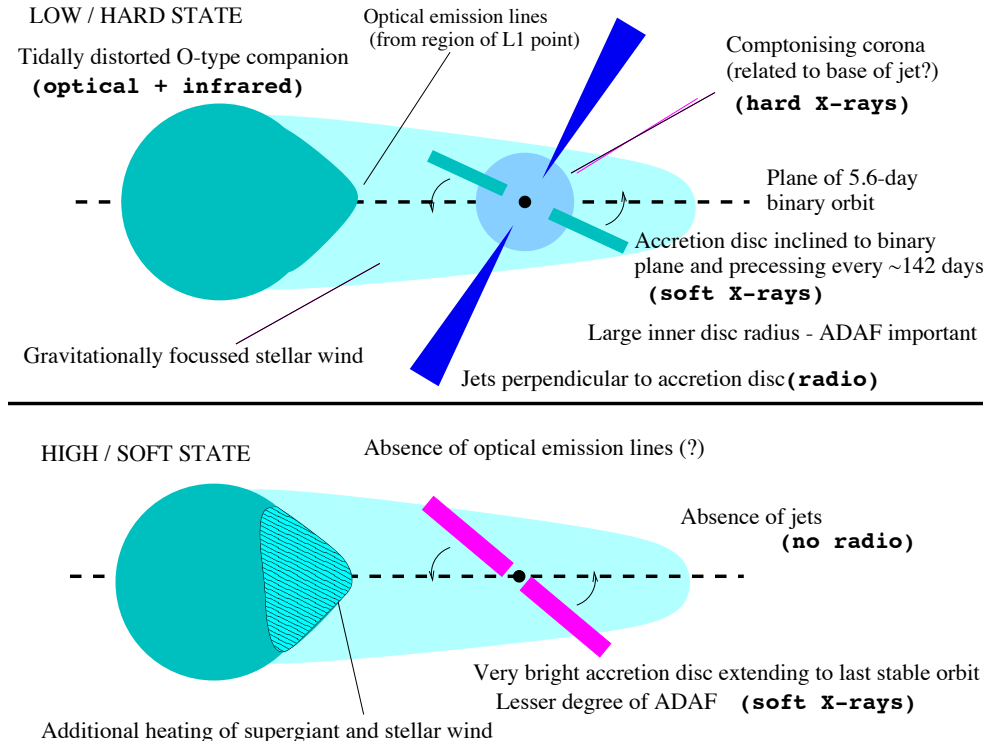


**Figure 2.4:** Sketched geometry of the hard (top) and soft (bottom) state of the HMXB Cyg X-1 (from Brocksopp et al., 1999, Fig. 7).

## 2.6 Cygnus X-1

### 2.6.1 The System

The HMXB in focus of this work is not only the first black hole candidate to be confirmed, it is also one of the best studied black hole systems with outstanding optical as well as X-ray data. Cyg X-1 was discovered as a bright X-ray source by Bowyer et al. (1965) during a rocket flight mission. Due to the simultaneous state transition of Cyg X-1 (Tananbaum et al., 1972) and the source of a radio flare around the same sky coordinates (Hjellming et al., 1971; Hjellming & Wade, 1971), it was possible to determine the position as accurate as  $5''$  and identify the X-ray source with its optical companion HDE 226868 (Murdin & Webster, 1971; Webster & Murdin, 1972; Bolton, 1972). This optical companion is a  $m_V = 8.84^{\text{mag}}$  bright O9.7Iab type supergiant (Walborn, 1973; Humphreys, 1978; Herrero et al., 1995). Radial velocity measurements of HDE 226868 confirm its binary nature and constrain its orbital period to about 5.6 days (Bolton, 1975; Guinan et al., 1979; Gies & Bolton, 1982; Sowers et al., 1998). The value of  $P_{\text{orb}} = 5.99829(16)$  d given by Brocksopp et al. (1999) is the one that is commonly used for recent calculations of the ephemerides, which define the epoch of phase  $\phi = 0$ , i.e., the superior conjunction of the black hole.

The system is located near  $\eta$  Cyg at right ascension  $\alpha = 19^{\text{h}}58^{\text{m}}21.67^{\text{s}}$  and declination  $\delta = 35^{\circ}12'5.23''$  (Reid et al., 2011) or galactic coordinates  $l_{\text{II}} = 71.3^{\circ}$ ,  $b_{\text{II}} = +3.1^{\circ}$ , i.e., close to the galactic plane (Liu et al., 2006). Earlier measurements, e.g., Bolton (1972) and Ninkov et al. (1987), put the system at a distance of about 2.5 kpc ( $1 \text{ kpc} = 3.085 \cdot 10^{19} \text{ m}$ ). The two most recent measurements, however, agree on a distance of roughly 1.8 kpc. One determines the distance from the dust scattering halo of the source to be  $1.81 \pm 0.09 \text{ kpc}$  (Xiang et al., 2011). The other one is using the VLBA to determine the trigonometric

parallax obtaining a distance of  $1.86_{-0.11}^{+0.12}$  kpc (Reid et al., 2011). This method is even so sensitive to the orbital period of the binary that Reid et al. (2011) could determine the orbit to be clockwise on the sky.

HDE 226868 has an effective surface temperature of  $T_{\text{eff}} = 32000$  K, a luminosity of  $L_* = 10^{5.4} L_{\odot} \approx 10^{39}$  erg s $^{-1}$  and a stellar radius of  $R_* = 17 R_{\odot}$  (Herrero et al., 1995). Its mass loss rate is quoted as  $\dot{M}_* = 3 \cdot 10^{-6} M_{\odot} \text{ yr}^{-1}$  due to a stellar wind with a terminal velocity of  $v_{\infty} = 2100$  km s $^{-1}$  (Herrero et al., 1995). The star has a long history of masses assigned to it. Hutchings (1978) deduced the orbital elements from the lightcurve and came up with a mass of 14 to 19 solar masses ( $M_{\odot}$ ). Gies & Bolton (1986) investigated the rotational broadening of absorption lines and inferred a due to the unconventional method probably too high mass of  $33 \pm 9 M_{\odot}$ . Herrero et al. (1995) employed unified models and derived a bunch of parameters, among them a companion mass of about  $15 M_{\odot}$  under the assumption of a synchronous rotation and an inclination of the system of  $35^{\circ}$ . Another non-standard method by Ziółkowski (2005) using the evolutionary status of the star also led to a somewhat too high mass prediction of  $40 \pm 5 M_{\odot}$ . The most recent estimate for the mass of the companion star, namely  $19.16 \pm 1.90 M_{\odot}$ , by Orosz et al. (2011) based on an eccentric orbit and non-synchronous rotation claims to be more direct and robust than the previous measurements, owing to their use of the new high precision distance measurement of Reid et al. (2011).

A similar odyssey is the search for the inclination  $i$  of the system, i.e., the angle between its orbital plane and our line of sight. Several approaches have been undertaken to find a value for this parameter but none of them is constrained very well. The change of the CIV UV line between the conjunction phases leads to  $i = 36^{\circ} - 67^{\circ}$  (Davis & Hartmann, 1983), the above mentioned investigation of the rotational line broadening yields  $i = 28^{\circ} - 38^{\circ}$  (Gies & Bolton, 1986). The polarization of the R, G, B flux hints at  $i = 25^{\circ} - 67^{\circ}$  Dolan & Tapia (1989) while the orbital modulation of the X-ray flux suggests  $i = 10^{\circ} - 40^{\circ}$  (Wen et al., 1999). Gies et al. (2003) derive  $i = 23^{\circ} - 37^{\circ}$  from the velocity components of the H $\alpha$  P Cygni line profile. The radial velocity curve of a Roche model covers  $i = 31^{\circ} - 44^{\circ}$  (Abubekkerov et al., 2004). Therefore, usually an inclination of  $i = 35^{\circ}$  is assumed for the Cyg X-1 system as this value is more or less the intersection of all these intervals. The recent radio measurements by Orosz et al. (2011), however, imply a more precise value of  $i = 27.1 \pm 0.8^{\circ}$  for the inclination.

Knowledge of the systems inclination is crucial for the determination of some of the systems parameters. Since the inclination is hard to measure and obviously not very well known, these parameters are often just cited in dependence of the inclination, i.e., their values measured in the projection of the orbit to the plane perpendicular to our line of sight. For example, the projected radius of HDE 226868's orbit

$$a_* \sin i = \frac{K_* P_{\text{orb}}}{2\pi} = 5.82(5) \cdot 10^9 \text{ m} = 8.36(8) R_{\odot} \quad (2.23)$$

can be inferred from the radial velocity semi-amplitude of HDE 226868 (Gies et al., 2003)

$$K_* = v_* \sin i = \frac{2\pi a_* \sin i}{P_{\text{orb}}} = 75.6(7) \text{ km s}^{-1}. \quad (2.24)$$

These values are also in good agreement with the results of LaSala et al. (1998) and Brocksopp et al. (1999) but larger than Gies et al. (2008) which again agree very well with Bolton (1975) and Sowers et al. (1998). According to Canalizo et al. (1995) this large systematic uncertainty – larger than the quoted error bars – could be explained by the fact that different photospheric absorption lines can differ in their radial velocity.

Applying Kepler (1619)'s third law

$$\frac{P_{\text{orb}}^2}{a^3} = \frac{4\pi^2}{G(M_* + M_X)}, \quad (2.25)$$

where  $a = a_* + a_X$  is the binary separation and  $M_X$  the mass of the black hole candidate, and using the center-of-mass definition  $a_* M_* = a_X M_X$  to rewrite the velocity semi-amplitude (Eq. 2.24 in terms of the binary separation

$$K_* = \frac{M_X}{M_* + M_X} \frac{2\pi a \sin i}{P_{\text{orb}}} \quad (2.26)$$

we obtain the spectroscopic mass-function (Karttunen et al., 1987)

$$f(M) := \frac{P_{\text{orb}} K_*^3}{2\pi G} = \frac{(M_X \sin i)^3}{(M_X + M_*)^2} = \frac{M_X \sin^3 i}{(1 + q^{-1})^2} \quad (2.27)$$

where  $q = M_X/M_*$  is again the mass ratio of the two components. If inclination and mass of the companion are known, the mass of the compact object can be calculated from this mass-function. For all derived values of the companion mass the mass of the compact object lies well above the Oppenheimer-Volkoff limit of  $3M_\odot$ . The most recent and possibly most accurate available value for the black hole mass is  $M_X = 14.8 \pm 1.0 M_\odot$  from Orosz et al. (2011). Cyg X-1 is therefore a very convincing black hole candidate.

The system spends most of its time in the hard state and only goes to the soft state in about 30 % of the time (Wilms et al., 2006b). In the hard state, which was first identified by Tananbaum et al. (1972), the powerlaw has a spectral index of  $\Gamma \approx 1.7$  above 2 keV and a cutoff at  $E_0 = 150$  keV (Wilms et al., 2006a). A spectrally flat radio emission of  $\sim 12$  mJy at 15 GHz indicates the presence of a jet (Wilms et al., 2006b). In the soft state the powerlaw is with  $\Gamma \approx 2.5$  (Zhang et al., 1997) much steeper than in the hard state and there is no cutoff up to 10 MeV (McConnell et al., 2002). There is evidence for a fluorescence iron  $K\alpha$  line at 6.4 keV which hardly contributes to the hard state (Ebisawa et al., 1996). The fluorescence iron line originates from the reflection of X-rays from the accretion disk where they ionize the accreted material.

## 2.6.2 Absorption Dips

Since HDE 226868 almost fills its Roche lobe, its stellar wind is highly focused toward the black hole, which influences the wind with its high gravitational potential. Friend & Castor (1982) have calculated the distribution of the mass loss of HDE 226868 depending on the angle of the wind with respect to the binary axis. They found that the mass loss rate in the direction of the black hole is about 4.5 times as high as the minimal value (Fig. 2.5). The accretion of that material results in an X-ray luminosity of  $L_X = 1.0 \cdot 10^4 L_\odot$ .

In the stellar wind section (sec. 2.3) we learned that the wind is highly structured due to density discontinuities which can form clumps. We expect light passing through this denser material to suffer from higher absorption. Consequently, if such a clump would pass our line of sight to the black hole – or, depending on the speed of the structure, if our line of sight would pass such a clump –, the observed intensity should decrease. Indeed, Li & Clark (1974) and Mason et al. (1974) encountered such a short time (usually a couple of minutes up to 8 hours in duration) decrease in X-ray intensity, so-called *X-ray dips*, already in early times of X-ray observation.

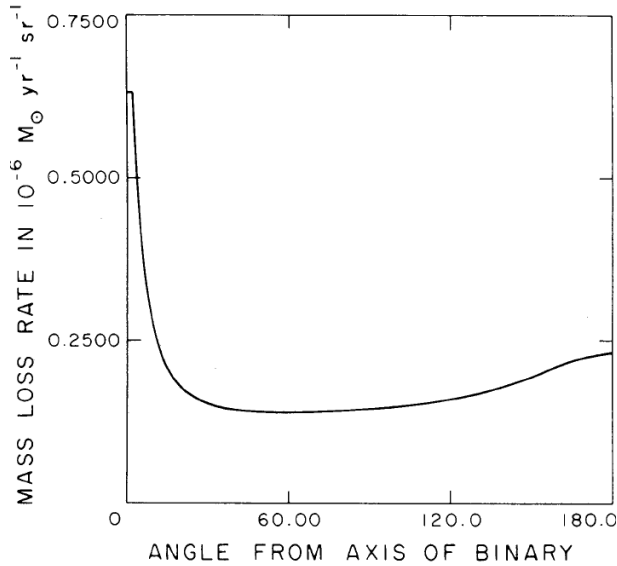


**Figure 2.5:** The mass loss rate of Cyg X-1 (from Friend & Castor, 1982, Fig. 4). The mass loss rate along the binary axis is about a factor 4.5 higher than the minimal value, leading to the picture of the focused wind.

Observations of the properties of these dips give evidence for our scenario and hence for the dips actually being caused by enhanced absorption through clumps. During the dips the spectrum hardens and becomes flatter, i.e., the flux of low energy photons is more strongly reduced than the flux of hard X-ray photons. If the reason for the flux reduction is photoabsorption, this behavior is plausible as the photoabsorption cross section is proportional to  $E^{-3}$ . The hardness of a spectrum can be determined quantitatively by the ratio of the flux of the hard to the soft energy band. A hardening of the spectrum would then be visible as a peak in the hardness curve, or as a valley in the softness curve (inverse ratio). Bałucińska-Church et al. (1997) found that a root mean square variability amplitude apparent in Cyg X-1 is proportional to the X-ray intensity and that this flickering is reduced during dips. Therefore, they conclude that the flickering has to be intrinsic to the emission region of the source and the dips have to be caused by absorption. Furthermore, Pravdo et al. (1980) has shown that the UV-spectrum, which is dominated by the emission of the O-star, remains unchanged during the dips. This stability of the UV-flux indicates that the absorption dips are likely caused by clumps in the accretion flow. This conclusion is supported by the fact that dips are mainly observed during superior conjunction of the black hole, i.e., when our line of sight passes at  $\phi = 0$  above the companion through the focused wind region to the emission region around the black hole. Bałucińska-Church et al. (2000) used *RXTE* observations to conduct a systematic study of the distribution of the dips over orbital phase. The result can be seen in Fig. 2.6. At  $\phi \approx 0.95$  there is a strong peak of dip occurrence with a FWHM of 0.25. Another much smaller peak at  $\phi \approx 0.6$  can probably be explained with the presence of a tidal stream trailing the black hole. This stream probably is produced by Roche lobe overflow of material of HDE 226868.

A characteristic property of the dense blobs in the focused wind is proposed by Bałucińska-Church et al. (2000): neutral material in the focused wind is highly ionized by the X-rays emitted by the accretion process. If due to the density variations discussed earlier clumps form, due to their high density (100 to 1000 times denser than the surrounding material) they shield themselves from the photoionization.

Hanke (2011) and Miškovičová et al. (2011) investigated several *Chandra* observations of Cyg X-1 in the hard state. Figure 2.7 shows the lightcurves of ObsIDs 3815 ( $\phi \approx 0.75$ ), 3814 ( $\phi \approx 0$ ), 8525 ( $\phi \approx 0.05$ ), 9847 ( $\phi \approx 0.2$ ) and 11044 ( $\phi \approx 0.5$ ), thus covering the different orbital phases very well. Since the hardening of a spectrum is defined via the flux

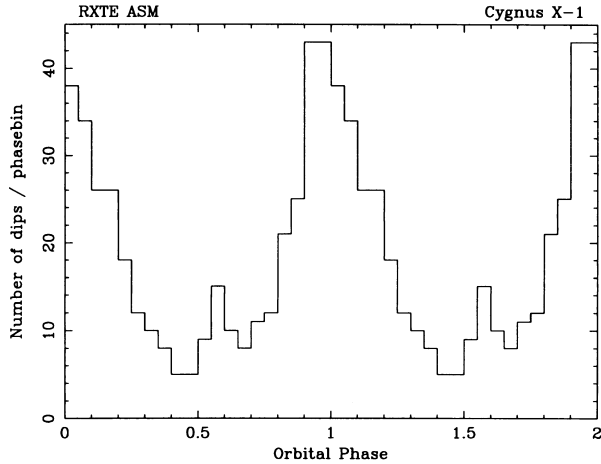


**Figure 2.6:** Distribution of the dips with orbital phase (from Bałucińska-Church et al., 2000, Fig. 5). Most of the dips are seen around  $\phi \approx 0$  where our line of sight crosses the focused wind. The smaller peak at  $\phi \approx 0.6$  probably comes from a tidal stream.

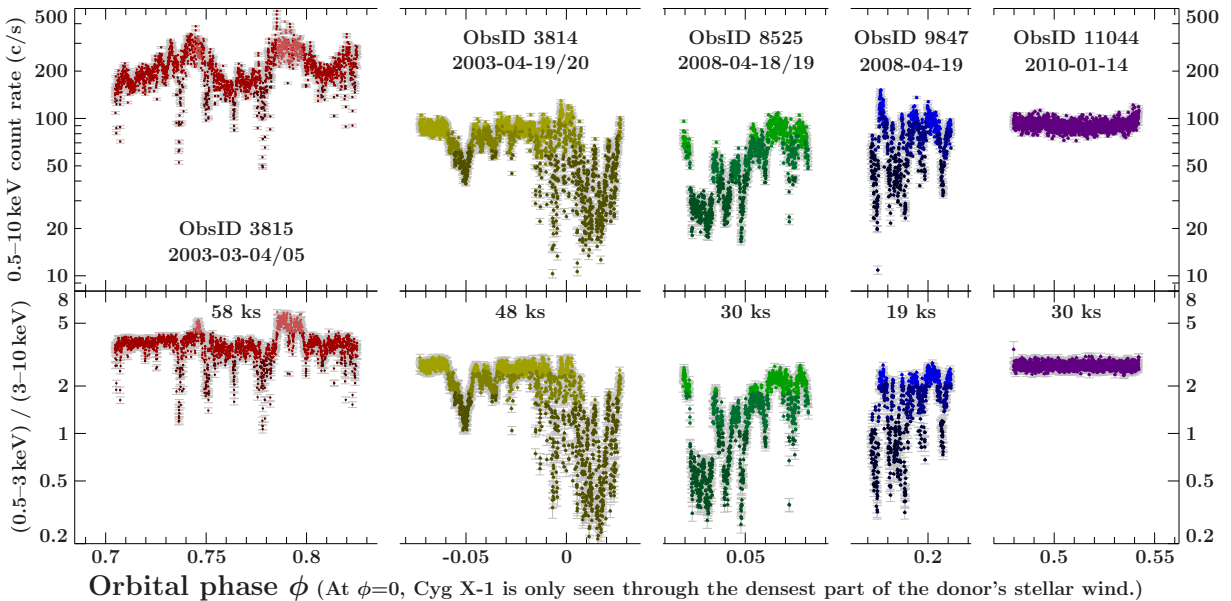


**Figure 2.7:** Lightcurves (top) and softness ratio (bottom) of *Chandra* observations of Cyg X-1 in the hard state. The strongest absorption dips occur around orbital phase  $\phi \approx 0^\circ$ . There is no dipping at all at  $\phi \approx 0.5^\circ$  (from Miškovičová et al., 2010).

ratio of the soft and the hard band, the lower panel also displays the softness ratio  $(0.5\text{--}3\text{ keV})/(3\text{--}10\text{ keV})$ . While each observation is displayed in different colors, the different shades of the same colors indicate the division of each lightcurve into different dipping states. In agreement with Bałucińska-Church et al. (2000) the strongest dipping is found around phase  $\phi \approx 0$  while the observation at  $\phi \approx 0.5$  shows no dipping at all.

### 2.6.3 Low Charge States of Si and S

Hanke (2011) and Miškovičová et al. (2011) extracted spectra of these *Chandra* observations according to the different dipping stages indicated in Figure 2.7. Their aim was to analyze how the spectra change with enhanced absorption in order to find some clues about the structure and composition of the stellar wind in this system. Indeed, they found some very interesting features: while the non-dip spectrum mainly exhibits absorption lines of hydrogen and helium like ions, with increasing stages of dipping those lines almost vanish for silicon and sulfur. Instead the charge balance of Si and S shifts towards mildly ionized

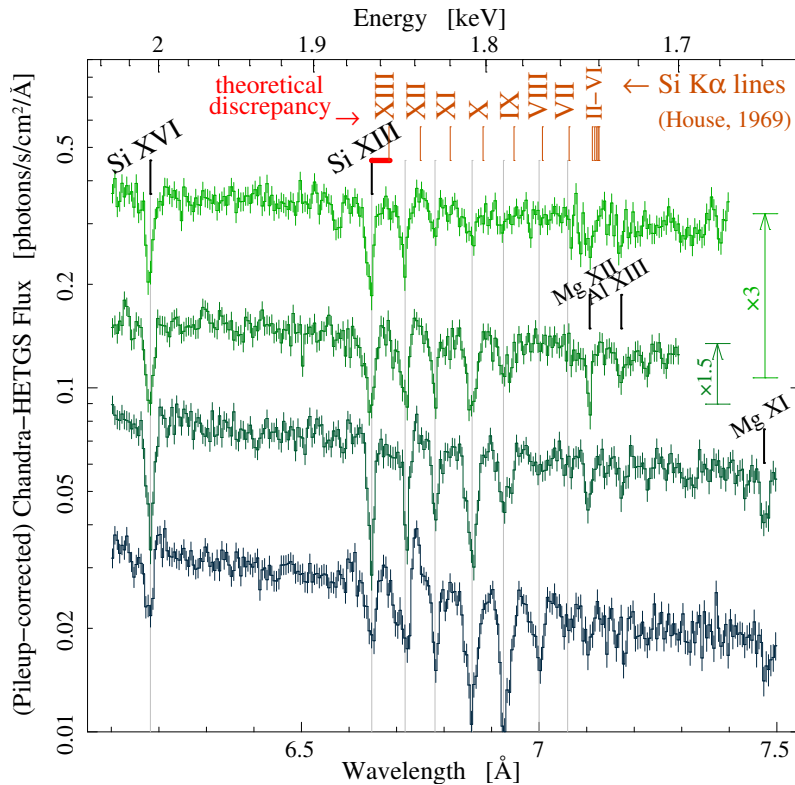


**Figure 2.8:** Spectra of the different dipping stages of Obs-ID 8525 in the silicon region, starting with no dipping at the top and ending with strong dipping at the bottom. The first two spectra are shifted in flux (cf. arrows) for visual clarity. At the very top the theoretical line centers of Si according to House (1969) are indicated in red. (from Miškovičová et al., 2010).

material and absorption lines of lower charge states start to show up (Fig.2.8).

The presence of transitions of low charge states in the wind material is per se already strong evidence for the presence of colder and hence probably denser material. Measuring the Doppler shift of the lines may beyond that even help to make a statement about the structure of the clumps. The only problem there is that to calculate the Doppler shift of a line the rest wavelength of this line has to be known. Unfortunately, experimental values and even theoretical calculations of the wavelength of the  $K\alpha$  spectrum of low charge states are only to be found very sparsely in atomic databases – if at all.

Above the spectra in Fig. 2.8 the wavelengths of the Si  $K\alpha$  lines calculated by House (1969) are indicated. It is not hard to see that these theoretical lines do not agree very well with the lines as observed in Cyg X-1 and have quite different shifts for different ionization states. In this case each ionization state would build small clumps of its own which would trail behind each other through our line of sight. Then an explanation for the presence of low charge states would be needed. An opposing theory is that the clumps are heated and hence highly ionized from the outside by the X-ray radiation of the accretion process while the material shields itself such that the inner regions of the clump consecutively see less radiation and consequently are cooler and less ionized. In this picture the clumps would have an onion-like structure and be rather stationary.

As discussed in section 3.12.1, the calculations of House (1969) are not very accurate. Therefore, the question remains whether the lines in Cyg X-1 are really strongly shifted or rather we are lacking good atomic physics data. The simplest way to answer this question is to go to the laboratory and measure these spectra under clean and controlled conditions. But first we will have a crash course in atomic physics.

# Chapter 3

## X-Ray Spectra

The simplest example to explain the physics and the composition of the atomic structure is usually the hydrogen atom. Although the photons emitted by transitions in the hydrogen atom do not belong to the X-ray spectrum but rather to the ultraviolet (UV) regime, hydrogen still makes for a good starting point. At the end of the derivation we will see that the transitions in focus of this work follow the same principles as the ones in the hydrogen atom and hence can easily be led back to it. Because of its fundamental role, basically every book about atomic physics and spectra treats the hydrogen problem. The following derivations mainly follow the books of Friedrich (1990) and Cowan (1981).

### 3.1 The Hydrogen Atom

The time-dependent Schrödinger equation

$$\hat{H}|\psi(t)\rangle = i\hbar \frac{d|\psi\rangle}{dt} \quad (3.1)$$

describes the evolution of a state  $|\psi\rangle$  with the time evolution of its corresponding physical system being determined by the Hamiltonian<sup>1</sup>  $\hat{H}$ , an Hermitian operator describing the energy of said system. The Hamiltonian usually can be expressed by the sum of the kinetic energy  $\sum_{i=1}^N \hat{\mathbf{p}}^2/2m_i$  of all components of the system and a potential energy  $\hat{V}(\hat{\mathbf{r}}_1, \dots, \hat{\mathbf{r}}_N)$ . In coordinate representation the (Schrödinger, 1926b,a) equation is a simple partial differential equation of the form

$$\hat{H}\psi(\mathbf{r}, t) = i\hbar \frac{\partial \psi}{\partial t}. \quad (3.2)$$

If  $|\psi_E\rangle$  is an eigenstate of  $\hat{H}$  with eigenvalue  $E$ , i.e.,

$$\hat{H}|\psi_E\rangle = E|\psi_E\rangle \quad (3.3)$$

which is known as the time-independent or stationary Schrödinger equation, and if the Hamiltonian has no explicit time dependency, then the wavefunction

$$|\psi(t)\rangle = \exp\left(-\frac{i}{\hbar}Et\right)|\psi_E\rangle \quad (3.4)$$

---

<sup>1</sup>named after its inventor William Rowan Hamilton (1833) for revolutionizing classical mechanics with his principle of varying action.

is a solution of the Schrödinger equation. The eigenvalue with the smallest energy corresponds to the ground state of the system. Any linear combination of solutions of the time-dependent Schrödinger equation is again a solution. Consequently, the eigenstates  $|\psi_E\rangle$  of  $\hat{H}$  can be used to set up a general solution:

$$|\psi(t)\rangle = \sum_n c_n \exp\left(-\frac{i}{\hbar}Et\right) |\psi_E\rangle. \quad (3.5)$$

In order to solve the time-dependent Schrödinger equation in case of a time-independent Hamiltonian, it is therefore sufficient to find all eigenvalues of  $\hat{H}$ . This information can be applied to the hydrogen atom.

The hydrogen atom in its most abundant form consist of a proton and an electron (Thomson, 1906). In non-relativistic quantum mechanics the Hamilton operator of their interaction can be expressed as

$$\hat{H} = \frac{\hat{\mathbf{p}}_p^2}{2m_p} + \frac{\hat{\mathbf{p}}_e^2}{2m_e} - \frac{e^2}{|\mathbf{r}_e - \mathbf{r}_p|} \quad (3.6)$$

where the first two terms represent the kinetic energy through the momentum  $\mathbf{p}_{p,e}$  of the proton and electron, respectively, and the last term stands for the Coulomb interaction between these two elementary charges at positions  $\mathbf{r}_e$  or  $\mathbf{r}_p$  (Friedrich, 1990). This two-body Hamiltonian can be re-written in terms of the center-of-mass coordinate  $\mathbf{R} = \frac{m_p\mathbf{r}_p + m_e\mathbf{r}_e}{m_p + m_e}$  and the relative distance  $\mathbf{r} = \mathbf{r}_e - \mathbf{r}_p$  between the proton and electron. In this coordinate system

$$\hat{\mathbf{P}} = \hat{\mathbf{p}}_p + \hat{\mathbf{p}}_e = \frac{\hbar}{i} \nabla_R \quad (3.7)$$

denotes the total momentum while

$$\frac{\hat{\mathbf{p}}}{\mu} = \frac{\hat{\mathbf{p}}_e}{m_e} - \frac{\hat{\mathbf{p}}_p}{m_p} = \frac{\hbar}{i} \nabla_r \quad (3.8)$$

stands for the momentum of the relative motion.  $\mu = \frac{m_e m_p}{m_e + m_p}$  is the reduced mass. Since the proton is about 1840 times heavier than the electron,  $\mu \approx m_e$ . The Hamiltonian then looks like

$$\hat{H} = \frac{\hat{\mathbf{P}}^2}{2(m_p + m_e)} + \frac{\hat{\mathbf{p}}^2}{2\mu} - \frac{e^2}{r}. \quad (3.9)$$

The first term describes the free motion of the center of mass. The solution for this part of the problem is known to be a plane wave (Friedrich, 1990) but is of lesser interest for the structure of the energy levels. The second part is the internal Hamiltonian of an electron moving in the central Coulomb potential of the proton. Therefore, the two-body problem is reduced to solving the Schrödinger equation of the one-body problem of the internal Hamiltonian.

Due to the radial symmetry of the problem, it makes sense to express the internal Hamiltonian in terms of the Laplace operator  $\hat{\Delta} = \nabla^2$  in spherical coordinates. With the help of the orbital angular momentum operator

$$\hat{\mathbf{L}} = \mathbf{r} \times \hat{\mathbf{p}} = -i\hbar \mathbf{r} \times \nabla \quad (3.10)$$

the Laplace operator can even be expressed in terms of a more physical variable than just the angles  $\theta$  and  $\phi$ . Making this change the new expression for the Hamiltonian is (Cowan, 1981)

$$\hat{H} = \frac{\hat{\mathbf{p}}^2}{2\mu} - \frac{e^2}{r} = -\frac{\hbar}{2\mu} \hat{\Delta} - \frac{e^2}{r} = -\frac{\hbar}{2\mu r} \partial_r^2 r + \frac{\hat{\mathbf{L}}^2}{2\mu r^2} - \frac{e^2}{r}. \quad (3.11)$$

Since the angular momentum commutes with the Hamiltonian, i.e.,  $[\hat{H}, \hat{\mathbf{L}}] = 0$ , the wavefunction can be separated into a radial and an angular component

$$\psi(r, \theta, \phi) = R(r)Y_{lm}(\theta, \phi) \quad (3.12)$$

where  $Y_{lm}$  are spherical harmonics<sup>2</sup>.  $l$  and  $m$  are integers and correspond to the eigenvalues of the quadratic orbital angular momentum operator  $\hat{\mathbf{L}}^2|\psi\rangle = \hbar^2 l(l+1)|\psi\rangle$  and its third vector component

$$l_z|\psi\rangle = \hbar m|\psi\rangle. \quad (3.13)$$

For this reason only the radial component of the wavefunction contributes to the derivatives in the Hamiltonian and the Schrödinger equation to be solved reads

$$\left( \frac{1}{r} \partial_r^2 r - \frac{l(l+1)}{r^2} + \frac{2}{a_0 r} - 2\tilde{E} \right) R(r) = 0. \quad (3.14)$$

Here,  $a_0 = \frac{\hbar^2}{\mu e^2} \approx a_0 = 0.53 \text{ \AA}$  denotes the Bohr radius, which is defined as the most probable distance between the proton and the electron in a hydrogen atom in its ground state, and  $\tilde{E} = \frac{\mu}{\hbar^2} E$  with  $E < 0$  is the rescaled energy eigenvalue. To get an idea of the solution of this equation we first take a look at the asymptotic solutions of the problem at the origin and infinitely large distances:

$$r \rightarrow \infty \quad \left( \partial_r^2 + 2\tilde{E} \right) R = 0 \quad \implies \quad R \propto e^{-\gamma r} \quad \gamma = \sqrt{2|\tilde{E}|} \quad (\& \quad e^{+\gamma r}) \quad (3.15)$$

$$r \rightarrow 0 \quad \left( \frac{1}{r} \partial_r^2 r - \frac{l(l+1)}{r^2} \right) R = 0 \quad \implies \quad R \propto r^l \quad (\& \quad r^{-(l+1)}). \quad (3.16)$$

In the limit  $r \rightarrow \infty$  the positive solution  $e^{+\gamma r}$  is discarded as otherwise the probability to find the electron at infinitely large distances would grow exponentially, which is not the case for a bound particle. For the  $r \rightarrow 0$  limit, the  $r^{-(l+1)}$  solution is neglected as it would lead to divergences. Now that the asymptotic behavior is known and secured to be convergent, we can assume that the remaining part of the radial wavefunction can be described by a polynomial. This assumption can be made as the polynomials form a complete base and hence every function can be expressed through them. Inserting the ansatz

$$R(r) = F(r)r^l e^{-\gamma r} \quad (3.17)$$

with the general form of a polynomial  $F(r) = \sum c_\nu r^\nu$  into the Schrödinger equation 3.14 leads to

$$rF''' + 2(l+1-\gamma r)F' + \left( \frac{2}{a_0} - 2\gamma(l+1) \right) F = 0. \quad (3.18)$$

Comparison of the coefficients for  $r^\nu$  provides us with a recursion relation for the coefficients of the polynomial

$$c_{\nu+1} = -2 \frac{\frac{1}{a_0} - \gamma(l+1+\nu)}{(\nu+1)(\nu+2l+2)} c_\nu \quad \text{with } c_0 \neq 0. \quad (3.19)$$

---

<sup>2</sup>Spherical harmonics are the product of the phase  $\exp(i m \phi)$  and the associated Legendre polynomials  $P_{l,m}(\cos \theta)$  with the normalization  $(-1)^m \sqrt{\frac{(2l+1)}{4\pi} \frac{(l-m)!}{(l+m)!}}$ . Associated Legendre polynomials are defined as  $P_{l,m}(x) = (1-x^2)^{m/2} \frac{d^m}{dx^m} P_l(x)$  where the Legendre (1785) polynomial  $P_l(x) = \frac{1}{2^l l!} \frac{d^l}{dx^l} (x^2-1)^l$  is the solution of Legendre's differential equation  $\frac{d}{dx} \left[ (1-x^2) \frac{d}{dx} P_n(x) \right] + n(n+1)P_n(x) = 0$ .

If the polynomial is allowed to grow for ever, at large  $\nu$  the recursion simplifies to  $c_{\nu+1} = \frac{2\gamma}{\nu+1} c_\nu \approx \frac{(2\gamma)^{\nu+1}}{(\nu+1)!}$ , which converts the polynomial into an exponential function

$$F \approx \sum \frac{(2\gamma r)^\nu}{\nu!} = e^{2\gamma r}. \quad (3.20)$$

Again, we cannot let the probability to find the electron at large distances grow exponentially to infinity. Therefore, the recursion has to break at a certain point  $\nu = N$ , i.e.  $c_{N+1} \stackrel{!}{=} 0$ , which translates to the condition

$$\sqrt{2|\tilde{E}|}(l+1+N) = \frac{1}{a_0} \implies \tilde{E} = -\frac{1}{2a_0^2(l+N+1)^2}. \quad (3.21)$$

Apparently the energy of the single levels of the hydrogen atom only depends on one parameter  $n = l + N + 1$ , the principal quantum number denoting the shell of the electron. Revoking the rescaling of the energy finally leads to the energy spectrum of the hydrogen atom:

$$E_n = -\frac{\hbar^2}{2\mu a_0^2} \frac{1}{n^2} = -\frac{\text{Ry}}{n^2}, \quad n = 1, 2, 3, \dots, \quad l = 0, 1, 2, \dots, n-1 \quad (3.22)$$

with the Rydberg constant  $\text{Ry} = \frac{\hbar^2}{2\mu a_0^2}$ , which was first found experimentally by the Swedish physicist Johannes Rydberg (1889, 1890) and later derived analytically from quantum mechanics by Niels Bohr (1920). Unknown to Rydberg, five years earlier Johann Balmer (1885) had derived a similar but less general formula to find the Rydberg constant.

## 3.2 Hydrogenic Ions

It is found that the same set of lines shows up in plasmas of elements with higher nuclear charge which are so highly ionized that only one electron is left in each ion, the so-called iso-electronic sequence of hydrogen. The above calculations can easily be adjusted for these hydrogenic ions with only two corrections: In the formula for the reduced mass  $\mu$  of the system, the proton mass  $m_p$  has to be substituted with the higher nuclear mass  $m_{\text{nuc}}$  of the heavier element. These nuclei are even more massive compared to the electron than the proton already was such that the reduced mass comes even closer to the electron mass. The second change is in the description of the Coulomb potential. The Coulomb potential depends on the product of the charges of the involved particles. The electron charge remains the same but the nuclear charge increases with the number of protons  $Z$ . Therefore, the the internal Hamiltonian has to be modified to

$$\hat{H} = \frac{\hat{\mathbf{p}}^2}{2\mu} - \frac{Ze^2}{r}. \quad (3.23)$$

Consulting the single steps of the above derivation, it can be seen that the result in eq. 3.22 still holds as long as a more general definition of the Rydberg constant and the Bohr radius are used:

$$\text{Ry} \rightarrow \text{Ry}_Z = \frac{\hbar^2}{2\mu a_Z^2}, \quad a_0 \rightarrow a_Z = \frac{\hbar^2}{\mu Z^2 e^2} = Z^{-2} \cdot 0.53 \text{ \AA}. \quad (3.24)$$

The hydrogenic ions are the simplest example of an iso-electronic sequence. Unfortunately, the other iso-electronic sequences do not follow such a simple scaling rule for the level energies. This is due to the fact that only the electron-nucleus interaction scales with the nuclear charge  $Z$  while the interactions between the electrons around the nucleus are unaffected by  $Z$  (Friedrich, 1990).

### 3.3 Fine Structure Splitting

Although for low- $Z$  elements the derived energy levels in eq. 3.22 are a quite good description of experimental findings, the ansatz with the time dependent Schrödinger equation has a major problem. The reason is that it violates the symmetry requirements of the theory of special relativity as it contains the second spatial derivative but only the first derivative with respect to time. Paul Dirac (1928) proposed an alternative equation which also only contains the first derivative with respect to spatial coordinates with the Hamiltonian  $\hat{H} = c\boldsymbol{\alpha}\hat{p} + \beta m_0 c^2$ . This Hamiltonian is constructed such that its square fulfills the relativistic energy momentum relation  $E^2 = p^2 c^2 + m_0^2 c^4$  and therefore goes along with special relativity. The only way  $\boldsymbol{\alpha}$  and  $\beta$  can meet this criterion is if they constitute at least  $4 \times 4$  matrices. In this case also the wavefunctions  $\psi(\mathbf{r}, t)$  have to be turned into four-component spinors, making the Dirac equation really a set of four partial differential equations. In the standard representation  $\beta$  and the three components of  $\boldsymbol{\alpha}$  are composed of combinations of Pauli (1927)'s two-dimensional spin matrices.

The stationary ansatz  $\psi(\mathbf{r}, t) = \psi(\mathbf{r}, t = 0) \exp(-\frac{i}{\hbar}Et)$  can also be applied to the Dirac equation. A potential  $V$  added to the Hamiltonian then leads us from the time-independent Dirac equation of a free particle to a comparable point as the time-independent Schrödinger equation: with the time-independent Dirac equation of a particle in a potential

$$(c\boldsymbol{\alpha}\hat{p} + \beta m_0 c^2 + V)\psi = E\psi \quad (3.25)$$

we “only” need to find the energy eigenvalues in order to solve the problem. One could argue that the addition of a central potential again violates the requirements of the theory of special relativity as it sets one frame of reference apart from all the others. A relativistic treatment, however, does not allow to differentiate the two-body problem into a center-of-mass motion and an internal Hamiltonian as was done above with the non-relativistic Schrödinger equation. Since also the nucleus of the atom can be considered at rest due to its comparatively high mass, a relativistic approach can nevertheless be justified as long as the energy of the electron is small compared to the rest mass  $m_{\text{nuc}}c^2$  of the nucleus (Friedrich, 1990).

In the discussion so far nothing changed in terms of the radial symmetry of the Coulomb potential of the nucleus. Therefore,  $\psi$  can still be separated into radial and angular components, the latter represented by spherical harmonics. With this separation, the Dirac equation can be simplified to a system of two coupled ordinary differential equations, called the radial Dirac equation, which in principle is not harder to solve than the radial Schrödinger equation.

Often the completely relativistic ansatz is omitted, especially if mainly the outer valence electrons are in the focus of interest. Instead first-order relativistic corrections, derived from the Dirac equation under the assumption that the velocity of the electron is small compared to the speed of light, are added to the non-relativistic Hamiltonian used in the Schrödinger equation (Cowan, 1981):

$$-\frac{1}{2\mu c^2}(E - V)^2 - \frac{\hbar^2}{4\mu^2 c^2} \left( \frac{dV}{dr} \right) \left( \frac{\partial}{\partial r} - \frac{2}{r} \hat{\mathbf{1}} \cdot \hat{\mathbf{s}} \right). \quad (3.26)$$

The first term represents the kinetic energy of the electron and is a correction to the kinetic energy term in eq. 3.9 due to the relativistic variation of mass with velocity. This term also introduces the energy eigenvalue  $E$  of the Schrödinger equation directly into the Hamilton operator itself.  $-\frac{\hbar^2}{4\mu^2 c^2} \left( \frac{dV}{dr} \right) \frac{\partial}{\partial r}$  is known as the Darwin term and accounts for the relativistic

non-localizability of the electron. The last term is the spin-orbit term  $\frac{\hbar^2}{4\mu^2 c^2} \left( \frac{dV}{dr} \right) \frac{2}{r} \hat{\mathbf{l}} \cdot \hat{\mathbf{s}}$  which for the calculation of the energy-level structures of complex atoms might be considered the most important one of these corrections. It stands for the interaction between the electron's spin angular momentum  $\hat{\mathbf{s}}$ , i.e., the rotation of the electron around its own axis, and the magnetic field seen by the electron due to its charge moving through the nuclear electric potential.

The spin-orbit term, which was introduced to the fully relativistic approach through the product of the Pauli spin matrices and the momentum vector, is in both, the partially and the fully relativistic treatment of the problem, responsible for the canceling of some of the degeneracies of the energy levels. As the orbital angular momentum  $\hat{\mathbf{l}}$  and the electron spin  $\hat{\mathbf{s}}$  act on different sets of coordinates<sup>3</sup>, they commute with each other (Cowan, 1981). Therefore, their product can be rewritten as

$$\hat{\mathbf{l}} \cdot \hat{\mathbf{s}} = \frac{1}{2} (\hat{\mathbf{j}}^2 - \hat{\mathbf{l}}^2 - \hat{\mathbf{s}}^2) \quad (3.27)$$

introducing the new parameter of the total angular momentum  $\hat{\mathbf{j}} = \hat{\mathbf{l}} + \hat{\mathbf{s}}$ . This substitution has the advantage that, in contrast to  $\hat{\mathbf{l}} \cdot \hat{\mathbf{s}}$ , the eigenvalues of  $\hat{\mathbf{j}}^2$ ,  $\hat{\mathbf{l}}^2$  and  $\hat{\mathbf{s}}^2$  can easily be derived:  $\hat{\mathbf{l}}^2 |\psi\rangle = \hbar^2 l(l+1) |\psi\rangle$ ,  $\hat{\mathbf{s}}^2 |\psi\rangle = \hbar^2 s(s+1) |\psi\rangle = 3/4 \hbar^2 |\psi\rangle$  and  $\hat{\mathbf{j}}^2 |\psi\rangle = \hbar^2 j(j+1) |\psi\rangle$ . Since the spin always equals  $\pm 1/2$ , in a one electron system for every total angular momentum there are only two possible values for the angular momentum quantum number  $l = j \pm 1/2$ .

After all operators are sufficiently substituted by their eigenvalues in the fully and partially relativistic ansatzes, the resulting differential equations can be solved. Up to a certain degree both approaches then lead to the same result (Friedrich, 1990; Cowan, 1981)

$$E_{nj} = m_0 c^2 \left[ 1 - \frac{(Z\alpha)^2}{2n^2} - \frac{(Z\alpha)^4}{2n^3} \left( \frac{1}{j+1/2} - \frac{3}{4n} \right) + (\dots) \right]. \quad (3.28)$$

The first and second term are already known as the rest energy of the particle and the non-relativistic spectrum with the binding energies  $E_n = \text{Ry}/n^2$ . Much more interesting is the third term. While it lowers the energy of all levels, the shift is largest for total angular momenta  $j = 1/2$  and smallest for  $j = n - 1/2$ . This difference in the energy shifts lifts the degeneracy of levels with the same principal quantum number  $n$  but different total angular momenta  $j$ . A scheme of this splitting is shown in Fig. 3.1 for levels  $n = 1$  to  $n = 3$  in hydrogen. This level splitting is commonly referred to as fine structure splitting. Accordingly,  $\alpha = e^2/(\hbar c) \approx 1/137$  is called the fine structure constant characterizing the strength of the electromagnetic interaction. We will keep in mind for later that the separation of the  $2p_{1/2}$  and  $2p_{3/2}$  energy levels increases with the fourth power of the nuclear charge.

### 3.4 Further Splitting

The more approximations are replaced by accurate calculations, the more degeneracies can be overcome, at least theoretically; unfortunately, experiments are usually restricted in their resolving power by the state of the technology. For instance, treating the electron-proton interaction far beyond the capabilities of Dirac with methods of quantum electrodynamics (QED) draws up a small splitting also between the  $ns_{1/2}$  and  $np_{1/2}$  levels, called

<sup>3</sup>The orbital angular momentum depends on the spatial coordinates,  $\mathbf{r}$ , while the rotation of the electron around its axis is independent of the orbital position of the electron and provides its own spin coordinate.

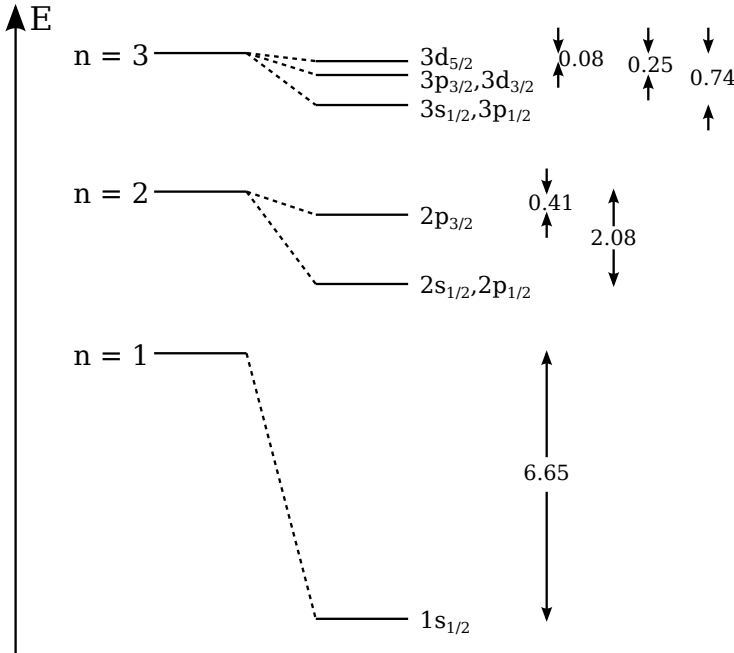


**Figure 3.1:** Fine structure splitting of the energy levels of the  $n=1$  to  $n=3$  shells of the hydrogen atom, according to the Dirac equation. The numbers are the energy shifts in units of  $10^{-6}$  atomic units. Sketch after Friedrich (1990).

the Lamb-shift (Lamb & Retherford, 1947). If the atomic nucleus is seen as an object with small finite size and intrinsic angular momentum (nuclear spin) instead of a structureless point particle, the more complex calculation leads to corrections even smaller than those of the fine structure, otherwise known as hyperfine structure. Both effects play no role for our measurements. The resolution is not good enough to distinguish lines separated by them.

The presence of external electric and magnetic fields can also lead to line shifts and splittings through the interaction of these external fields with the electric and magnetic momenta of the atom. The Zeeman effect (Zeeman, 1896a,b, 1897) describes the influence of a uniform external magnetic field of flux density  $\mathbf{B}$  with the intrinsic magnetic moment  $\boldsymbol{\mu}$  of the atom. The interaction between the two of them has to be accounted for with an additional term

$$\hat{H}_{\text{mag}} = -\mathbf{B} \cdot \boldsymbol{\mu} \quad (3.29)$$

in the Hamiltonian of the system. Because of the direct interaction of the magnetic field with the magnetic moment of the atom, the  $(2J + 1)$ -fold degeneracy in the magnetic quantum number of the energy levels is removed as the total angular momentum vector precesses around the direction of the magnetic field. With  $\boldsymbol{\mu} = -\mu_B[\mathbf{J} + (g_s - 1)\mathbf{S}]$ , where  $g_s \approx 2$  is the anomalous gyromagnetic ratio of the electron spin and the Bohr magneton, the intrinsic magnetic moment is proportional to the Bohr magneton (Procopiu, 1913)

$$\mu_B \approx 0.06 \text{ meV T}^{-1}. \quad (3.30)$$

For very strong magnetic fields, the interaction becomes so strong that  $\mathbf{L}$  and  $\mathbf{S}$  uncouple. The splitting of the energy levels due to the magnetic field is then stronger than the multiplet splitting (Herzberg, 1937). This effect is called Paschen-Back effect (Paschen & Back, 1912, 1913).

In 1913 Johannes Stark found a similar effect for external static magnetic fields (Stark, 1913, 1914; Stark & Wendt, 1914). The electric field  $\mathbf{E}$  does not act directly on the intrinsic magnetic moment of the atom associated with  $\mathbf{J}$  but rather with its electric dipole moment. In the presence of the electric field, the atom becomes electrically polarized, i.e.,

the positively charged nucleus is separated from the center of gravity of the negative charges. Because of the resulting electric dipole moment  $\mathbf{D}$ , the atom tries to set itself in the direction of the smallest energy. The corresponding precession of  $\mathbf{J}$  again leads to a separation of the energy levels in the magnetic moment,  $M$ . As for the Zeeman and Paschen-Back effects, a very strong field arranges for decoupling of  $\mathbf{L}$  and  $\mathbf{S}$  (Herzberg, 1937). The additional term to the system's Hamiltonian is

$$\hat{H}_{\text{elec}} = -\mathbf{E} \cdot \mathbf{D} = -\mathbf{E} \sum_i e \mathbf{r}_i \quad (3.31)$$

and results in an energy shift in the order of

$$\Delta E = 3e|\mathbf{E}| \frac{a_0}{Z} \approx 1.59 \cdot 10^{-10} \frac{e|\mathbf{E}[\text{kV m}^{-1}]|}{Z} [\text{keV}] \quad (3.32)$$

where  $a_0$  is the Bohr radius (Bransden & Joachain, 1937).

Although there are relatively strong magnetic and electric fields around in an electron beam ion trap, because of the very small values of the Bohr magneton (eq. 3.30) and the energy shift due to the electric dipole moment (eq. 3.32) both effects are negligibly weak compared to the energy of the X-ray photons produced with this device.

### 3.5 Many-electron Systems

The Hamiltonian describing the hydrogen atom can be rather simply extended to many-electron systems. In principle, it just has to contain the electron-nucleus interaction for every electron instead of only one and additionally include the interactions between the electrons themselves. Again the choice is between the non-relativistic approach and relativistic corrections.

$$\begin{aligned} H &= H_{\text{kin}} + H_{\text{el-nuc}} + H_{\text{el-el}} + H_{\text{s-o}} \quad (+H_{\text{mass-velocity}} + H_{\text{Darwin}}) \quad (3.33) \\ &= \frac{\hat{\mathbf{p}}_{\text{nuc}}^2}{2m_{\text{nuc}}} + \sum_{i=1}^N \left( \frac{\hat{\mathbf{p}}_{\text{e},i}^2}{2m_{\text{e}}} - \frac{Ze^2}{|\mathbf{r}_{\text{e},i} - \mathbf{r}_{\text{nuc}}|} \right) + \sum_{i < j} \frac{e^2}{|\mathbf{r}_{\text{e},i} - \mathbf{r}_{\text{e},j}|} + \sum_i \xi_i(\mathbf{r}_i)(\mathbf{l}_i \cdot \mathbf{s}_i) \quad (+ \dots) \end{aligned}$$

$H_{\text{s-o}}$  denotes the spin-orbit interaction of every electron and, as in eq. 3.26, is mostly described by

$$\xi = \frac{\alpha^2}{2} \frac{1}{r} \left( \frac{dV}{dr} \right). \quad (3.34)$$

The mass-velocity and the Darwin term only depend on the distances between the electrons and the nucleus  $|\mathbf{r}_{\text{e},i} - \mathbf{r}_{\text{nuc}}|$ . Therefore, they only shift the absolute energies of a group of related levels but not their relative positions to each other and are hence not specified here in greater detail.

If there was no two-body interaction, the Hamiltonian would just be the sum of  $N$  single particle Hamiltonians whose eigenfunction would be equal to the sum of those of the hydrogenic ion. Unfortunately, the two-body interaction is everything but small. The search for an analytical solution of the Schrödinger or Dirac equation for the many-electron Hamiltonian is therefore a much more complex issue. The values of  $4N$  variables (each electron has three spatial and one spin coordinate) have to be found. For  $N \geq 2$  there are no exact solutions and approximations have to be applied. Usually this is done by

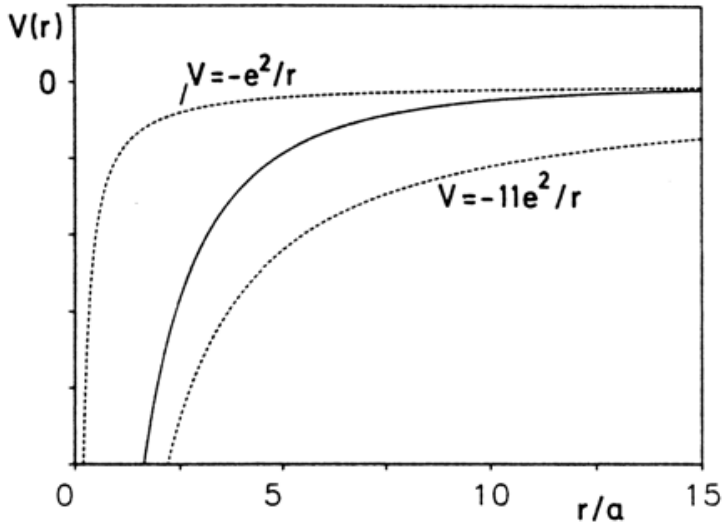


**Figure 3.2:** The single-particle mean potential between the limits of the full Coulomb potential and the completely screened one for Na (from Friedrich, 1990).

equipping the wavefunctions with several adjustable parameters. Through variation of these parameters a “best fit” according to some sensible criterion has to be found (Cowan, 1981).

If the correlation among the positions of various electrons caused by their Coulomb repulsion is accounted for through the explicit appearance of the distance  $\mathbf{r}_{ij}$  between two electrons in  $\psi$ , systems consisting of three to four electrons are already almost impossible to solve analytically. Even a much simpler treatment of the electron–electron interaction through perturbative calculations of just their energy correlations becomes extremely extensive for  $N > 6$ . This complexity is a real issue, since depending on the research interest the energy levels of systems with a number of electrons up to the order of 100 are desired.

Although the correlations between the electron positions need to be accounted for in the base functions, here it shall be enough to shortly introduce the mean field approximation which discards a large fraction of this interaction. In the mean field approximation, many of the electrons present are combined to an average single-particle potential, the mean field (Friedrich, 1990). That is, the electrostatic repulsion suffered by an electron from all other electrons is described by the average repulsive potential that modifies the attractive potential of the nucleus as it is felt by the electron. In other words, any given electron moves independently of the others in the (stationary) nuclear field and an additional spherically symmetric field due to the time-average over the motion of the remaining electrons. Then every electron not contained in the mean field only constitutes a residual two-body interaction, which is much less than the normal two-body interaction. In case there is only one electron left, it can be described sufficiently by an one-electron wavefunction.

In an ion with  $N$  electrons and nuclear charge  $Z$ , this electron then sees a screened Coulomb potential  $-(Z - N + 1)e^2/r$  at large distances to the nucleus as most of the attractive nuclear potential is shielded by the electron cloud of the other  $N - 1$  electrons. If the electron is positioned close to the nucleus, it will rather see the completely unscreened potential of the nucleus  $-Ze^2/r$ . In regions in between, the potential changes smoothly between these two limits (see Fig. 3.2). As this potential is no longer a pure Coulomb potential but still radially symmetric, the eigenstates with a given principal quantum number  $n$  are not degenerate in the angular momentum quantum number  $l$ .

## 3.6 LS-vs. jj-coupling

Since an  $N$ -electron ion has a plethora of eigenstates, degenerate or not, it is convenient to find a self-consistent scheme to label them unambiguously. The best way to do this is to describe them by a combination of their characteristic properties. Therefore, we look for constants of motion, i.e., operators that are commuting with the Hamiltonian. These are called *good quantum numbers*.

### 3.6.1 LS-coupling

In case of no spin-orbit coupling and for light atoms where the spin-orbit interactions are negligibly weak compared to the interactions between electrons, the total spin is a constant of motion as the remaining portions of the Hamiltonian are independent of the spin. Since the total angular momentum is a good quantum number, also the construct  $\hat{\mathbf{L}} = \hat{\mathbf{J}} - \hat{\mathbf{S}}$  has to be a constant. Coupled through electrostatic interaction, the orbital angular momenta and the spins of the single electrons combine to these total angular momentum

$$\hat{\mathbf{L}} = \sum_i l_i \quad (3.35)$$

and spin operators

$$\hat{\mathbf{S}} = \sum_i s_i. \quad (3.36)$$

Their eigenvalues are

$$\hat{\mathbf{L}}^2|\psi\rangle = L(L+1)\hbar^2|\psi\rangle \quad (3.37)$$

and

$$\hat{\mathbf{S}}^2|\psi\rangle = S(S+1)\hbar^2|\psi\rangle \quad (3.38)$$

respectively. There are  $(2L+1) \times (2S+1)$  degenerate eigenstates per  $(\hat{\mathbf{L}}, \hat{\mathbf{S}})$ -pair, corresponding to the third components  $L_z$  and  $S_z$  of the momentum operators with eigenvalues  $m_L$  and  $m_S$ , which range from  $-L$  to  $+L$  and  $-S$  to  $+S$ , respectively, in integer steps. The naming scheme following this convention is called Russell-Saunders coupling scheme after its “inventors” Russell & Saunders (1925). An overview over the angular momentum notation can be found in appendix A.

Historically certain series of observed spectral lines were named after their looks: sharp (s), principal (p), diffuse (d) and fundamental (f). Only later it was realized that these correspond to different values of the same physical parameter, the orbital angular momentum. Since it is often easier to reference a certain configuration with a set of letters instead of a bunch of numbers, these historically grown abbreviations were kept but associated with their new physical meaning, i.e., values of  $l = 0, 1, 2, 3, \dots$  are written as  $l = s, p, d, f, \dots$  (continuing alphabetically). For higher values of  $L$  the alphabet is just continued, omitting the letters already in use. To distinguish between the total orbital angular momentum and the momenta of the single electrons, capital letters indicate the former while the latter are denoted by small letters like throughout the previous derivations.

The spin quantum number can be used to determine the number  $2S+1$  of levels each term splits into or, in other words, how many different total angular momenta can be realized through the combination of  $L$  and  $S$ . This number, called *multiplicity*, is noted to the upper left corner of the orbital angular momentum. In practice, the number of levels in a term is only given by the multiplicity if  $S < L$  but by  $2L+1$  for  $L < S$ .

Already for small spin-orbit coupling when LS-coupling still approximately holds, the term  $V_{LS}(\mathbf{r}_i)\hat{\mathbf{L}}_i \cdot \hat{\mathbf{S}}_i$  in the one-body interaction is responsible for the Hamiltonian not commuting with  $\hat{\mathbf{L}}$  and  $\hat{\mathbf{S}}$  anymore but only with the total angular momentum  $\hat{\mathbf{J}} = \hat{\mathbf{L}} + \hat{\mathbf{S}}$ . Through this magnetic interaction each term splits into  $\min\{(2S+1), (2L+1)\}$  levels with total momenta  $J = |L-S|, |L-S|+1, \dots, L+S$ . These are noted at the lower right corner of the total orbital angular momentum. The general level description then looks like

$${}^{2S+1}L_J. \quad (3.39)$$

Each of these levels still is  $(2J+1)$ -fold degenerate in the quantum number  $M_J$ , the eigenvalue of the  $z$ -component  $J_z$  of the total angular momentum vector, adopting values between  $-J$  and  $J$  with integer step size. This hyperfine structure only shows up if the nuclear spin  $I$  does not vanish and interacts with the momenta of the electrons.

Levels in different shells, i.e. with different principal quantum number  $n$ , can have the same such label. To specify which one exactly is referred to, atomic states are additionally labeled with  $nl$  of occupied single particle states. For instance, an electron with principal quantum number  $n=2$  and orbital quantum number  $l=1$  would be in the  $2p$  subshell. A complete set of these single-particle states are called a *configuration*. Beyond that the naming convention speaks of a *term* if values of  $L$  and  $S$  are given. A *level* has the additional information about its total angular momentum  $J$ .

### 3.6.2 *jj-coupling*

The above classification in the LS-coupling scheme relies on  $L$  and  $S$  at least being approximate constants of motion. However, with increasing nuclear mass the spin-orbit coupling grows ever stronger up to a point where the LS-coupling really is not even approximately valid any more. In this limit rather the coupling between the single-electron orbital angular momentum and spin becomes a constant of motion. Then these single-particle total angular momenta  $j_i$  couple to the total angular momentum of the ion.

In this so-called *jj-coupling*, the level description is written as a list denoting how many electrons occupy a certain subshell. The total angular momentum  $J$  is then noted as a subscript to parentheses enclosing the label. For example,  $(1s_{1/2}2s^22p_{1/2}2p_{3/2}^2)_1$  describes a carbon-like system with one electron in the first shell and two in the  $2s$ , one in the  $2p_{1/2}$  and two in the  $2p_{3/2}$  subshells that has a total angular momentum of  $J=1$ . Closed shells and subshells are often omitted. As long as the total number of electrons for this system is known, the fragmentary notation is still legible. Unfortunately, this characterization of the levels is not completely unique. The same set of single-particle  $j_i$  can be combined in different ways to reach the same total angular momentum  $J$  of the whole system. These different paths of coupling lead to different level energies but can not be distinguished from the notation.

### 3.6.3 *Transition from LS- to jj-coupling*

For systems with pure LS coupling, the wavefunctions of states obeying the selection rules are strictly orthogonal. Therefore, for states not doing so, the overlap integral, line transition probabilities, and *gf*-values are equivalent to zero. The semi-forbidden or intercombination lines, where levels of different multiplicity are combined through electric quadrupole transitions, only occur in the regime where LS-coupling starts to mix with

jj-coupling. Once the spin-orbit interaction becomes much stronger than the Coulomb terms, the coupling conditions approach pure jj-coupling.

Usually, if the energy difference between two terms is larger than the fine structure splitting of these terms, LS coupling is applied, else jj-coupling is the method of choice (cf. Fig. 3.3). But this difference also depends on how the configurations are combined to the energy levels in the course of the calculation. In the transition region between LS- and jj-coupling there is no good ab initio rule of thumb whether to use one or the other for calculations. Consequently, for the same iso-nuclear sequence usually calculations in LS- as well as jj-coupling can be found. Due to their different physical bases they can not be converted into each other and thus are not easily comparable. The only way is to approximately match them up by hand so that their quantum numbers do not violate each other.

### 3.6.4 Matching the Notation

The best way to match the notation of LS- and jj-coupling is to determine all energy levels of an ion in either of the two schemes, sort them for energy and then assign them to each other in that order, keeping an eye on the total angular momentum.

There are various methods how to determine all possible configurations in the LS-coupling regime, especially the Journal of Chemical Education is rich of such cookbooks; see, e.g., Tuttle (1967), Vicente (1983), Pradhan & Nahar (2011), and, for writing down the ground state only, Gorman (1973). Here, only the underlying principle shall be outlined shortly. For a set of configurations, for example  $ns_{1/2}n's_{1/2}$  (with  $n \neq n'$ , non-equivalent electrons) or  $ns^q$  (equivalent electrons), write down all possible spin combinations resulting in the total spin magnetic moment  $M_S$ . Then for each of these  $M_S$  collect the possible combinations of orbital magnetic moments  $m_l$ , which can take on values from  $-l$  to  $+l$  in increments of 1, and sort them into groups with the same total orbital magnetic moments  $M_L = \sum m_l$ . For non-equivalent electrons, i.e., those differing in at least one of the quantum numbers  $n$  or  $l$ , all of these permutations also exist, while for equivalent electrons, i.e., with the same  $n$  and  $l$  the Pauli (1925) exclusion principle has to be obeyed. Pauli's principle states that no two electrons in a system can have the exact same set of quantum numbers  $(n, l, m_l, m_s)$ . Therefore, the equivalent electron combinations can be obtained by crossing out all of the non-equivalent electron combinations where any  $(m_l, m_s)$  pair shows up more than once. Since for a certain  $L$ , the  $M_L$  goes from  $-L$  to  $L$  in increments of 1, we now can look for the highest  $M_L$  in our table; a term with that  $L$ -value has to exist. This  $L$ -value is written down at the same time noting the occurring  $M_S$ . For this set of  $-L, -L + 1, \dots, L$  values one corresponding  $M_L$  configuration is crossed out of the table and again the highest  $M_L$  is selected. These steps are taken until no entries remain in the table. Afterwards, for each  $L$ -value the same procedure is applied to the  $M_S$  values to determine the corresponding spin multiplicities. The total orbital angular momentum  $J$  in each multiplet then runs from  $|L - S|$  to  $(L + S)$ .

To sort the terms obtained this way for their energy, Hund (1925)'s rules have to be applied. They state

- *S-rule*: the LS-term with the highest spin multiplicity  $(2S + 1)$  is lowest in energy,
- *L-rule*: for states of the same multiplicity those with highest total  $L$  are lowest in energy,
- *J-rule*: for less than half-filled subshells the lowest  $J$ -level has the lowest energy, but, since the distribution of holes and electrons in a subshell is equivalent, this rule turns

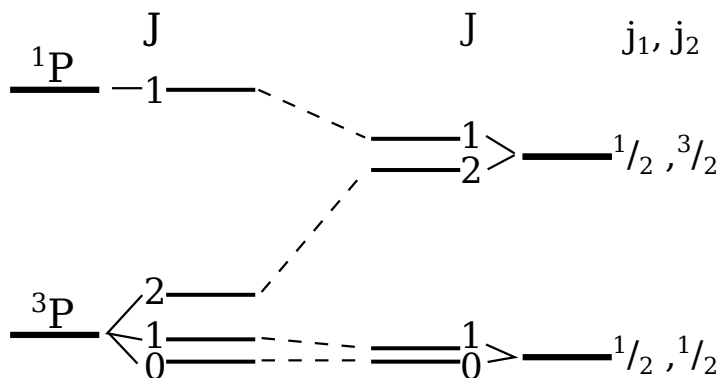


**Figure 3.3:** Relative positions of a  $ps$  configuration (after Herzberg, 1937). The left hand side shows the levels in LS-coupling where the splitting of the terms is larger than the fine structure splitting, the right hand side in jj-coupling.

around for more than half-filled subshells, where the highest  $J$ -level lies lowest in energy.

Similarly, to obtain the jj-coupling levels the easiest and most secure (in terms of completeness) approach is to set up tables; see, e.g., Rubio & Perez (1986), Gauerke & Campbell (1994), Orofino & Faria (2010) and Tuttle (1980) for various methods. This time, first the possible  $j$  values for an electron have to be found via  $j = l \pm s$ . Keeping the Pauli principle in mind in case equivalent electrons (for jj-coupling the unique sets of quantum numbers are  $(l, s, j, m)$ ), for all combinations of the  $j_i$  the corresponding  $m_j$  are permuted to calculate and tabulate the possible  $M_J$  which are, as for  $M_L$  in LS-coupling, used to derive the possible  $J$ -values for each of these configurations.

Since in jj-coupling,  $L$  and  $S$  are no good quantum numbers, Hund's first two rules are not applicable here. Nevertheless, we would expect configurations to have increasing energy with increasing  $\sum |j_i|$ , i.e., for the example of two equivalent  $l = p$  electrons,  $(1/2)^2$ ,  $(1/2)(3/2)$ ,  $(3/2)^2$  have subsequently higher energies. Within these configurations, the  $J$  follow Hund's third rule, the  $J$ -rule.

This approach, however, has a few flaws. Although very useful, Hund's rules are only empirical regularities but not strict laws. It is found that for the higher energy levels there are often exceptions to these rules. One of these exceptions is, for example, the  $1s^2 2s_{1/2} 3p^3$  configuration of carbon. Here, the observed term order is

$${}^5S < {}^3D < {}^3P < {}^1D < {}^3S < {}^1P \quad (3.40)$$

while according to Hund the  ${}^3S$  with its higher multiplicity should have lower energy than the  ${}^1D$  term (Levine, 1983). Therefore, they should only be used for the lower energy levels close to the ground state. Hund's rules may be used for excited states, but due to more than one subshell being open, they become increasingly inaccurate (Pradhan & Nahar, 2011). Moreover, the sorting within multiplets (different  $J$  values) may sometimes change its energy order between LS- and jj-coupling (see, e.g., Fig. 1 in Gauerke & Campbell (1994)).

### 3.7 Selection Rules

If an ion is in an excited state with energy  $E_2$ , it may decay spontaneously to another state of lower energy  $E_1$ . The released energy leaves the system in form of a photon with energy  $E_2 - E_1$ . The energy of a photon can be translated into its frequency  $\nu$ , wavelength  $\lambda = c/\nu$  or wavenumber  $\sigma = 1/\lambda$  via the relation  $E = h\nu = E_2 - E_1$ . In theory any two energy

levels could be combined in such a way to create a spectral line. This Ritz-combination principle was developed by Walther Ritz (1908) when he generalized the Rydberg-formula, which was found as a mathematical relationship between the lines in the Balmer-series<sup>4</sup> in hydrogen, to other atoms. Some of these combinations, however, have negligibly low transition probabilities and therefore only have very low intensities, while others dominate the spectrum. The difference is caused by various selection rules. These selection rules for the quantum numbers can be derived from quantum mechanical calculations, where the expectation value

$$\langle \psi | \hat{O} | \psi' \rangle \equiv \iiint_{-\infty}^{\infty} \psi^*(\mathbf{r}_i) \hat{O} \psi'(\mathbf{r}_i) dx_i dy_i dz_i \quad (3.41)$$

of the operator  $\hat{O}$  needs to be non-zero for the initial ( $\psi$ ) and final ( $\psi'$ ) wavefunctions.

### 3.7.1 Parity

Before we discuss some of the selection rules, we first have to learn about the parity of a state (Cowan, 1981). The total wavefunction  $\psi(\mathbf{r}_i, \mathbf{s}_i)$  is a function of the positional-coordinate vectors  $\mathbf{r}_i$  and the spin angular momenta  $\mathbf{s}_i$  of the  $N$  electrons in a system (atom or ion). At the same time the Hamiltonian  $\hat{H}$  is a function of the coordinates, the corresponding linear momenta  $\mathbf{p}_i$ , the angular momenta  $\mathbf{l}_i = \mathbf{r}_i \times \mathbf{p}_i$  and the spins  $\mathbf{s}_i$ . Together  $\psi$  and  $\hat{H}$  have to fulfill the Schrödinger equation with eigenvalue  $E$  for all possible values of the coordinates, even negative ones. The spin and orbital angular momenta are unaffected by flipping of the coordinate signs  $\mathbf{r} \rightarrow -\mathbf{r}$ ,  $\mathbf{p} \rightarrow -\mathbf{p} = i\hbar\nabla$ . For an isolated system with no external field, flipping of the system does not affect the internal energy structure, i.e.,  $H(-\mathbf{r}, -\mathbf{p}, \mathbf{l}, \mathbf{s}) = H(\mathbf{r}, \mathbf{p}, \mathbf{l}, \mathbf{s})$ . Thus  $\psi(\mathbf{r}, \mathbf{s})$  and  $\psi(-\mathbf{r}, \mathbf{s})$  are solutions to the same Schrödinger equation and can only differ by a constant factor:  $\psi(-\mathbf{r}, \mathbf{s}) = c \cdot \psi(\mathbf{r}, \mathbf{s})$ . Since this relation is true for all coordinates, also  $\psi(\mathbf{r}, \mathbf{s}) = c \cdot \psi(-\mathbf{r}, \mathbf{s})$  is true and consequently  $c = \pm 1$ . According to the value of  $c$ , a wavefunction is said to have even (+) or odd (-) parity. Applying the inversion of the coordinates ( $\mathbf{r} \rightarrow -\mathbf{r}$ ,  $\theta \rightarrow \pi - \theta$ ,  $\phi \rightarrow \pi + \phi$ ) to the wavefunction

$$\psi = R(\mathbf{r}) Y_{lm}(\theta, \phi) \sigma_{m_s}(s_z) \quad (3.42)$$

separated in radial, angular and spin functions, we find

$$\psi(\mathbf{r}, \mathbf{s}) = R(\mathbf{r}) Y_{lm}(\theta, \phi) \sigma_{m_s}(s_z) \rightarrow \psi(-\mathbf{r}, \mathbf{s}) = (-1)^l R(\mathbf{r}) Y_{lm}(\theta, \phi) \sigma_{m_s}(s_z). \quad (3.43)$$

The parity for coupled wavefunctions,  $\psi = \prod_i \psi_{l_i, m_i}$ , is therefore given by

$$p = (-1)^{\sum l_i}. \quad (3.44)$$

For odd parity the LS notation is extended by a superscript  $^{\circ}$ , e.g.,  $^2P_{1/2}^{\circ}$ .

### 3.7.2 Back to the Selection Rules

Now consider an operator  $\hat{O}$  to have parity  $p_o$ . If we change the signs of the integration variables  $\mathbf{r} \rightarrow -\mathbf{r}$ , the expectation value of  $\hat{O}$  changes for wavefunctions with parities  $p$

<sup>4</sup>transitions from  $n \geq 3$  to the  $n = 2$  shell

and  $p'$  like (Cowan, 1981)

$$\begin{aligned}
 \langle \psi | \hat{O} | \psi' \rangle &= \iiint_{-\infty}^{\infty} \psi^*(-\mathbf{r}_i) \hat{O}(-\mathbf{r}_i) \psi'(-\mathbf{r}_i) (-dx_i) (-dy_i) (-dz_i) \\
 &= (-1)^{p+p_o+p'} \iiint_{-\infty}^{\infty} \psi^*(\mathbf{r}_i) \hat{O}(\mathbf{r}_i) \psi'(\mathbf{r}_i) dx_i dy_i dz_i \\
 &= (-1)^{p+p_o+p'} \langle \psi | \hat{O} | \psi' \rangle.
 \end{aligned} \tag{3.45}$$

Obviously  $p+p_o+p'$  has to be even for the minus sign to vanish or else the expectation value would have to be zero. For zero expectation value, however, the transition between the two states does not take place. So if the operator  $\hat{O}$  has odd parity, the parity of the initial wavefunction  $\psi$  must have opposite parity of the final wavefunction  $\psi'$ . For operators with even parity, the parity of the wavefunctions has to be the same. The wavefunctions for an isolated field-free ion then must have the same parity since the corresponding Hamiltonian has even parity. For instance, an atom in an external magnetic field  $-\mathbf{B}\boldsymbol{\mu}$  ( $\boldsymbol{\mu}$  being the magnetic moment of the atom) has an energy with even parity, while the interaction between an external electric field  $\boldsymbol{\mathcal{E}}$  and the atom's electric dipole  $\sum_i(-e)\mathbf{r}_i$  has odd parity.

Similar but less general calculations can be done for other quantum numbers. The amplitude  $|\mathbf{M}_{if}|^2$  of the transition momentum integral

$$\mathbf{M}_{if} = \int \psi_i \hat{\boldsymbol{\mu}} \psi_f^* d\mathbf{r} \tag{3.46}$$

gives the transition probability of one eigenstate of the atom or ion to another one. From the dependency of the integral of the transition momentum operator  $\boldsymbol{\mu}$  follows that any selection rules derived from this equation are only valid for the considered transition moment. In other words, there is a separate set of selection rules for each of the electric dipole, magnetic dipole, electric quadrupole, etc., transitions. The integral does not have to be solved explicitly to determine the selection rules. Since only transitions between eigenstates are allowed for which the integral is non-zero, symmetry considerations are sufficient to derive the selection rules.

For demonstration purposes, let us have a look at electric dipole transitions in hydrogenic ions, following the calculations of Schpolski (1976). The electric dipole moment is given by  $\mathbf{d} = -e \sum_I \mathbf{r}_i = -e\mathbf{r}$ . We also remember that the wavefunctions separate into radial and angular contributions  $\psi_{nlm} = R_n(r)Y_{lm}(\theta, \phi)$ . Then

$$\mathbf{M}_{if} = - \int R_n(r) Y_{lm}^*(\theta, \phi) e\mathbf{r} R_{n'}(r) Y_{l'm'}(\theta, \phi) r^2 \sin \theta dr d\theta d\phi \tag{3.47}$$

where  $(nlm)$  and  $(n'l'm')$  denote the initial and final set of quantum numbers.

There is no restriction for the principal quantum number  $n$ , i.e., the electron can jump over as many shells as it wants to (with some care about ionization limits). Since a product is zero if only one of the factors is zero and because the angular part of the integral does not depend on the distance  $\mathbf{r}$  of the electron to the nucleus, it is enough to examine the integration over the angles. With  $Y_{lm} \propto e^{im\phi} P_{lm}(\cos \theta)$ ,  $Y_{lm}^* \propto e^{-im\phi} P_{lm}(\cos \theta)$ ,  $\mathbf{r}$  in spherical coordinates<sup>5</sup>, and cosine and sine expressed through the exponential function,

<sup>5</sup> $x = r \cos \phi \sin \theta$ ,  $y = r \sin \phi \sin \theta$ ,  $z = r \cos \theta$

we can write the three angular components of the integral as

$$\begin{aligned}
 M_{if,x} &\propto \frac{1}{2} \int_0^{2\pi} \left[ e^{i(m'-m+1)\phi} + e^{i(m'-m-1)\phi} \right] d\phi \int_0^\pi P_{lm} P_{l'm'} \sin^2 \theta dr d\theta \\
 M_{if,y} &\propto \frac{1}{2} \int_0^{2\pi} \left[ e^{i(m'-m+1)\phi} - e^{i(m'-m-1)\phi} \right] d\phi \int_0^\pi P_{lm} P_{l'm'} \sin^2 \theta dr d\theta \\
 M_{if,z} &\propto \int_0^{2\pi} e^{i(m'-m)\phi} d\phi \int_0^\pi P_{lm} P_{l'm'} \cos \theta \sin \theta dr d\theta.
 \end{aligned} \tag{3.48}$$

Although the magnetic quantum number  $m$  is only important in the case of hyperfine splitting of levels, we start with this parameter.  $\int_0^{2\pi} e^{ikx} dx$  is only non-zero for  $k = 0$ . Therefore, only if the selection rule

$$\Delta m = m' - m = 0, \pm 1 \tag{3.49}$$

is fulfilled, there is at least one component of  $\mathbf{M}_{if}$  with a finite value.

For the selection rules of the orbital angular momentum quantum number, we first have a look at  $M_{if,z}$ . We already know that  $m \equiv m'$  if this component is not supposed to vanish. With the additional substitution  $\cos \theta \rightarrow x$ , the proportionality of  $M_{if,z}$  simplifies to

$$M_{if,z} \propto \int_{-1}^{+1} P_{lm} P_{l'm} x dx. \tag{3.50}$$

A recurrence formula for the associated Legendre polynomials  $P_{lm}$  with constant  $m$  reads (Abramowitz & Stegun, 1964)

$$xP_{lm}(x) = \frac{l+m}{2l+1} P_{l-1,m} + \frac{l-m+1}{2l+1} P_{l+1,m}. \tag{3.51}$$

The  $P_{lm}$  are also orthonormal functions, i.e.,  $\int P_{lm} P_{l'm'} dx = \delta_{ll'} \delta_{mm'}$ . Substituting the recurrence formula eq. 3.51 into  $M_{if,z}$  (eq. 3.50) leads to the selection rule

$$\Delta l = l' - l = \pm 1. \tag{3.52}$$

Using a second recurrence formula for  $P_{lm}$  (Abramowitz & Stegun, 1964)

$$P_{l+1,m} = P_{l-1,m} + (2l+1)\sqrt{1-x^2}P_{l,m-1}, \tag{3.53}$$

which connects functions with  $m$  and  $m-1$ , and the integrals for  $M_{if,x}$  and  $M_{if,y}$  together with  $\Delta m = \pm 1$  results in the same selection rule as in equation 3.52.

Selection rules for even more quantum numbers like, e.g., the spin, the quantum numbers of many-electron systems and special conditions like LS-coupling can be found in a similar manner. One of the important selection rules is  $\Delta S = 0$  which forbids electrons to jump between terms of different multiplicity. Table 3.1 gives an overview over the selection rules for electric and magnetic dipole and electric quadrupole transitions.

## 3.8 $K\alpha$ Spectra

As indicated in section 3.1 the Rydberg series of spectral lines connects levels of different principle quantum numbers  $n$  but the same subshell with orbital angular momentum  $l$ .

**Table 3.1:** Selection rules in atomic spectra (from Garstang, 1962, Table I).

	Electric dipole	Magnetic dipole	Electric quadrupole
(1)	$\Delta J = 0, \pm 1$ ( $J = 0 \leftrightarrow 0$ )	$\Delta J = 0, \pm 1$ ( $J = 0 \leftrightarrow 0$ )	$\Delta J = 0, \pm 1, \pm 2$ ( $J = 0 \leftrightarrow 0, 1/2 \leftrightarrow 1/2, 0 \leftrightarrow 1$ )
(2)	$\Delta M = 0, \pm 1$	$\Delta M = 0, \pm 1$	$\Delta M = 0, \pm 1, \pm 2$
(3)	Parity change	No parity change	No parity change
(4)	One electron jump $\Delta l = \pm 1$	No electron jump $\Delta l = 0$ $\Delta n = 0$	One or no electron jump $\Delta l = 0, \pm 2$
(5)	$\Delta S = 0$	$\Delta S = 0$	$\Delta S = 0$
(6)	$\Delta L = 0, \pm 1$ ( $J = 0 \leftrightarrow 0$ )	$\Delta L = 0$	$\Delta L = 0, \pm 1, \pm 2$ ( $J = 0 \leftrightarrow 0, 0 \leftrightarrow 1$ )

## NOTES

Rules (1) to (3) are rigorous as long as nuclear perturbations and two-quantum processes are absent.

Rule (4) only holds for negligible configuration interaction.

Rules (5) and (6) are for LS-coupling only.

Forbidden lines can occur if (1) to (3) are only violated for the electric dipole transitions but not for one of the others, if the approximate rules (4)-(6) are violated, if the atom suffers from external or nuclear perturbations or if two-quantum processes take place.

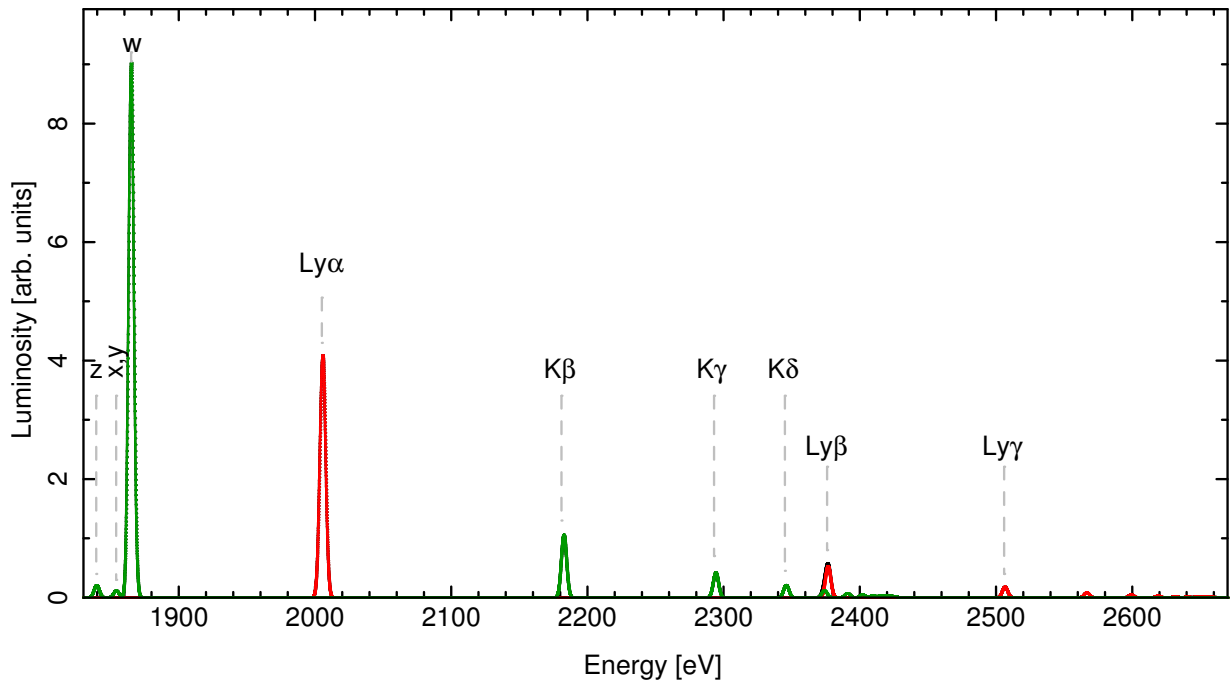


**Figure 3.4:** The Rydberg series for He-like (green) and H-like silicon, calculated with FAC (see section 3.12).

In a similar manner as the quantum number  $l$  is denoted with letters, the electron shells  $n = 1, 2, 3, \dots$  also have letter equivalents  $n = K, L, M, \dots$ . Since the allowed values of the orbital angular momentum are  $l = 0, 1, 2, \dots, n - 1$ , which due to the interaction with the spin again splits further into sublevels  $j = |l \pm \frac{1}{2}|$ , it is readily seen that the K-level is single, the L-level triple and the M-level quintuple, etc..

In X-ray spectra line series very similar to the Rydberg series in hydrogen were found (compare Fig. 3.4). But while in optical spectra the structure is quite different for elements belonging to different columns of the periodic table<sup>6</sup>, in X-ray spectra the structure of the line series is of the same type in all elements. Since the chemical behavior is determined by the electrons in the outer region of the atom, the likeness of X-ray spectra of different elements points to their origin in the interior of the atom (Born, 1969). An electron is ionized away from the innermost shell (K) by collisional or photoionization, leaving behind a vacancy in the tightly bound subshell. Through radiative transitions of one of the outer electrons, the excited state relaxes back into the ground state. This relaxation can either happen through a single transition or through a cascade of transitions where every transition leaves a vacancy in a less tightly bound shell to be filled by the next transition. In our case of highly ionized material, however, there are not many subshells available to create lengthy cascades.

In his book *Spektroskopie der Röntgenstrahlung* (Siegbahn, 1924), Karl Manne Siegbahn, one of the pioneers in X-ray spectroscopy, proposed a notation to characterize these transitions, today known as Siegbahn notation. According to his convention the levels of an electron shell are counted toward increasing energy and added as a numerical subscript to the shells letter. That is, the levels  $1s_{1/2}, 2s_{1/2}, 2p_{1/2}, 2p_{3/2}, 3s_{1/2}, \dots$  are referenced as  $K_I, L_I, L_{II}, L_{III}, M_I, \dots$ . The subscript roman numerals are also often just written as Arabic numbers. Transitions between those subshells are then either noted as a combination of the Siegbahn labels (IUPAC<sup>7</sup> notation), or similar to the notation of the Rydberg series (Siegbahn notation): the series is named after the letter of the principal quantum number of the destination level, e.g., for transitions to the K-shell, we have the K series. The series denomination is followed by a Greek letter indicating the origin of the transition, i.e., a transition from the next higher shell is labeled with  $\alpha$ , from the second to next shell with  $\beta$ , and so on. If fine structure splitting plays a role, the sublevels are denoted by a subscript numeral. For example, a spectral line corresponding to a transition from the 2p shell to the 1s shell can be identified as

$$\begin{aligned} K\alpha_1 &\hat{=} KL_3 \hat{=} 1s_{1/2} \rightarrow 2p_{3/2} \\ K\alpha_2 &\hat{=} KL_2 \hat{=} 1s_{1/2} \rightarrow 2p_{1/2} \\ K\alpha &\hat{=} KL \hat{=} \text{unresolved KL doublet.} \end{aligned}$$

An exception to this rule is the notation for hydrogenic ions. For historical reasons, the notation for H-like ions follows the description of the Lyman series (Lyman, 1906), i.e.,  $Ly \alpha, Ly \beta$ , etc..

Moseley (1913, 1914) was able to deduce an empirical law for the energies of  $K\alpha$  lines of different elements from his measurements:

$$E = \frac{1}{h} \frac{3}{4} \text{Ry} (Z - a)^2 = \frac{1}{h} \text{Ry} (Z - a)^2 \left( \frac{1}{1^2} - \frac{1}{2^2} \right). \quad (3.54)$$

<sup>6</sup>Elements belonging to different columns of the periodic table of elements have different chemical characters.

<sup>7</sup>International Union of Pure and Applied Chemistry, an international agency to standardize nomenclatures and symbols

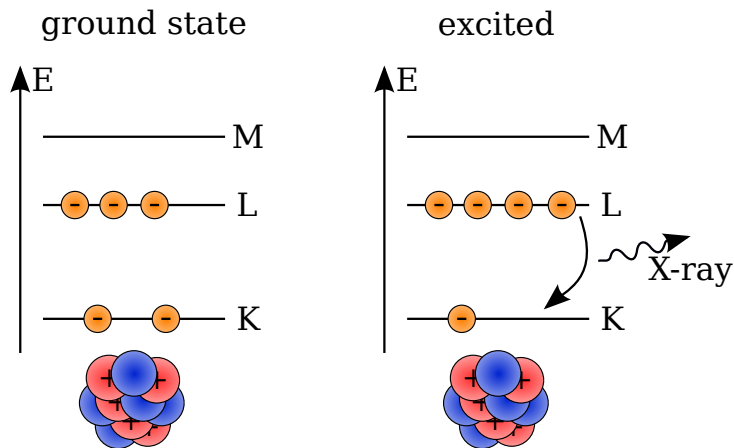


**Figure 3.5:**  $K\alpha$  transitions: an electron of the L-shell of an excited atom or ion with a vacancy in the innermost K-shell decays to the ground state. The released energy is emitted as an X-ray photon.

This law reminds of the equation for the energies of the Rydberg series. In this formula  $Ry$  is the Rydberg constant,  $a$  is called the screening constant and has about the same value for all elements; in case of neutral atoms  $a \approx 1$ . Thus the  $K\alpha$  line energies lie on a straight line as a function of nuclear charge  $Z$ .

But what causes the clear separation of the  $K\alpha$  lines emitted by different ions of the same iso-nuclear sequence? We have learned in section 3.2 that the level energies in a hydrogenic ion and hence the spectral line energy, i.e., the difference between those levels, scale with the square of the nuclear charge as the Coulomb potential deepens linearly with  $Z$ . Thus, the higher the atomic number of an element is, the higher the energy of its spectral lines will be. The mean field approximation has a similar effect. The more electrons shield the nuclear charge, the lower is the effective  $Z$  in the Coulomb potential. But with a shallower effective Coulomb potential due to a higher number of electrons and therewith lower  $Z_{\text{eff}}$ , also the transition energies decrease. The effect is large enough that in the  $K\alpha$  spectrum the transitions of different ionic states separate. At least for the H- to O-like ions it is possible to just count through the major peaks of the spectrum from higher to lower energies in order to determine the charge of the emitting ion. However, starting with F- and Ne-like ions, the separation of the lines according to their charge state becomes so small, that usually (except maybe for extremely good instrumental resolution) these lines blend so much into each other that they can not be distinguished anymore.

## 3.9 Radiative Transitions

Of the transitions between two energy levels  $E_1$  and  $E_2$  which are allowed according to the selection rules, we are interested the most in radiative decay and photoabsorption. Absorption lines in the continua of astrophysical sources, caused by photoabsorption, tell us the composition of the environment close to said source. In contrast, photons emitted by radiative decay are more easily produced in the laboratory. Because these emission lines are usually created and observed under clean general conditions (controllable or at least pretty well known), they can help to constrain the implications of and to interpret the results obtained from astrophysical sources. There are three types of radiative transitions: spontaneous and stimulated emission and stimulated absorption.

### 3.9.1 Spontaneous Emission

Since nature generally seeks to obtain states of minimal energy, an excited atom, i.e., an atom with higher energy than the ground state, has a certain probability to decay. An isolated field-free atom with total angular momentum  $J_i$  is  $(2J_i + 1)$ -fold degenerate in the magnetic quantum number  $M_i$ . The number  $g_i = 2J_i + 1$  of these states with the same energy  $E_i$  is called *statistical weight*. Often the index of  $g$  is omitted with the understanding that then  $g$  is always the statistical weight of the initial level. The probability per unit time to spontaneously decay from a specific of these  $g_i$  states to any of the  $g_j$  states with energy  $E_j < E_i$  is given by the Einstein coefficient  $A_{ij} = 1/\tau_{\text{spon}}$ , where  $\tau_{\text{spon}}$  is the decay time. If level  $i$  can make a transition to several lower levels, then the decay time follows the more general relation

$$\frac{1}{\tau_{\text{spon}}} = \sum_j A_{ij}. \quad (3.55)$$

with  $\tau_{\text{spon}}$  being the natural lifetime of state  $i$ . Consequently, the change of the number of atoms in state  $i$  into state  $j$  can be expressed as

$$\left(\frac{dN_i}{dt}\right)^{i \rightarrow j} = - \left(\frac{dN_j}{dt}\right)^{i \rightarrow j} = -N_i(t)A_{ij}. \quad (3.56)$$

So if no other processes of excitation or de-excitation are involved, the population of level  $i$  suffers from exponential decay  $N_i(t) = N_i(t = 0) \exp(-t/\tau_{\text{spon}})$  Cowan (1981). This exponential decay with a finite natural lifetime introduces an uncertainty  $\Delta t$  to the actual lifetime  $\tau_{\text{spon}}$  of an atom in state  $i$ . Due to the Heisenberg (1927) uncertainty principle

$$\Delta E \approx \frac{\hbar}{\Delta t} \quad (3.57)$$

the spectral line of a transition has a natural line width contradicting the assumption that each level of an atom has a perfectly definite energy value, i.e., is mono-chromatic. The intensity distribution of these energies can be described with a Lorentzian (Lorentz, 1906)

$$I(E) = \frac{1}{\pi} \frac{\Gamma}{\Delta E^2 + \Gamma^2} \quad (3.58)$$

where  $\Gamma$  is the half-width at half maximum (HWHM) of the line. This broadening of the spectral line, however, is usually very small and therefore negligible compared to other broadening mechanisms like, e.g., Doppler broadening through the Maxwellian velocity distribution (Maxwell, 1867) of the Brownian motion<sup>8</sup> of the particle in the plasma. Accordingly, the natural line width can only be resolved in very high resolution experiments.

### 3.9.2 Induced/ Stimulated Emission and Absorption

In the presence of a radiation field, the decay can be sped up through the interaction between the photons of the field and the atom. We assume an isotropic and unpolarized

<sup>8</sup>named after the Scottish botanist Robert Brown (1828) who discovered strange random motion of pollen grains in a solution under the microscope. The forgotten but true discoverer of this stochastic behavior, however, was the Dutch physician and botanist Jan Ingen-Housz (1785) who found irregular movement of coal dust on the surface of alcohol. The history of the description of this kind of motion can be traced even farther back to poems of Titus Lucretius Carus (60 BC) who wrote about the battle of dust particles in the air.

electromagnetic field with energy density (energy per unit volume) of  $\rho(E)dE$  in the energy range  $dE$ . If this energy density is approximately constant over a range of several natural line widths on either side of the line, the interaction of a photon with an atom in state  $i$  results in a transition to the lower level  $j$  at the rate

$$\left(\frac{dN_i}{dt}\right)^{i \rightarrow j} = -\left(\frac{dN_j}{dt}\right)^{i \rightarrow j} = -N_i(t)\rho(E_{ij})B_{ij}. \quad (3.59)$$

$B_{ij}$  is called the Einstein coefficient of stimulated emission.

It is as well possible that the interaction with the photon results in an induced or stimulated transition from state  $j$  to a higher energetic state  $i$  via the absorption of the photon

$$\left(\frac{dN_j}{dt}\right)^{j \rightarrow i} = -\left(\frac{dN_i}{dt}\right)^{j \rightarrow i} = -N_j(t)\rho(E_{ji})B_{ji}. \quad (3.60)$$

### 3.9.3 Relation between the Einstein Coefficients

Because of the principle of detailed balance, the rate of transitions between levels  $i$  and  $j$  due to absorption has to be equal to the rate of transitions between the same levels due to emission:

$$N_j B_{ji} \rho(E_{ij}) = N_i A_{ij} + N_i B_{ij} \rho(E_{ij}). \quad (3.61)$$

This equation shows a linear relationship between the Einstein coefficients, introduced by Einstein (1917), making them dependent of each other. In thermodynamic equilibrium at temperature  $T$ , the energy density of the radiation field is given by Planck's law (Planck, 1900)

$$\rho(E) = \frac{8\pi E^3}{h^2 c^3} \frac{1}{e^{E/kT} - 1} \quad (3.62)$$

while the relative population of the different quantum states is described by the Maxwell-Boltzmann law (Maxwell, 1867; Boltzmann, 1872)

$$\frac{N_j}{N_i} = \frac{g_j}{g_i} e^{-\frac{E_j - E_i}{kT}}. \quad (3.63)$$

Inserting equations 3.62 and 3.63 into equation 3.61 together with the argument that the law of detailed balance has to hold for any temperature, leads to the equations:

$$A_{ij} - \frac{g_j}{g_i} \frac{8\pi E^3}{h^2 c^3} B_{ji} = 0 \quad \text{and} \quad -A_{ij} + \frac{8\pi E^3}{h^2 c^3} B_{ij} = 0. \quad (3.64)$$

Thus, the relations between the Einstein coefficients are

$$A_{ij} = \frac{8\pi E^3}{h^2 c^3} B_{ij} \quad \text{and} \quad g_j B_{ji} = g_i B_{ij}. \quad (3.65)$$

The assumption that the atoms are in equilibrium with the radiation field is merely valid, which is indicated by the fact that spectroscopic sources usually show a line spectrum rather than a black-body continuum. If the radiation density is low, stimulated emission is negligible compared to spontaneous emission (Cowan, 1981). Independent of that, the population of the lower levels may be much greater than the population of the higher levels so that stimulated absorption becomes important. In laser experiments, however, these

parameters can be adjusted through the experimental setup in such a way, that stimulated emission becomes dominant, resulting in an effective line narrowing.

Since the Einstein coefficients are related to each other, it is sufficient to link only one of them to quantum mechanics. The Einstein coefficient for spontaneous emission can be written in term of the line strength  $S_{ji}$

$$A_{ij} = \frac{64\pi^4}{2h^4c^3} \frac{1}{g_i} E_{ij}^3 S_{ij}. \quad (3.66)$$

The line strength is defined via the transition dipole matrix element (compare eq. 3.46)

$$M_{ij}^2 = S_{ij} g_i = e^2 |\langle \psi_f | \mathbf{r} | \psi_i \rangle|^2 \propto e^2 n^4 \frac{a_0^2}{Z^2} \quad (3.67)$$

where  $n^2 a_0 / Z$  is the radius of the electron orbit. The line strength is symmetrical in the upper and lower state labels:  $S_{ij} = S_{ji}$ . With a proportionality of  $E^3$ , the transition probability  $A_{ij}$  for spontaneous emission is strongly dependent of the transition energy. So if there are two paths for the radiative decay, the one with the higher energy will always be favored by the branching ratio (Dopita & Sutherland, 2003).

Hilborn (2002) published a nice overview over Einstein coefficients,  $gf$ -values and line strengths. He discusses different conventions regarding their exact definitions, derive relations of these parameters and warn about common pitfalls.

## 3.10 Collisional Excitation and Ionization

In section 3.8 we learned that  $K\alpha$  transitions are due to inner shell transitions. These vacancies in the inner shell have to be produced somehow. Also we heard about the differences in the energies of different ions of the same iso-nuclear sequence. Therefore, we need a means to create various ionic stages of the same atom and that possibly provides excited states of these ions at the same time. An electron beam ion trap (see section 4.1) is capable of both. Through collisions with the highly energetic electrons of the beam the injected gas gets constantly ionized and excited. Once it is excited and not touched any more, it will decay radiatively at some point. Because of the collisions with electrons, these processes are also often referred to as electron impact excitation and ionization. But how does collisional ionization and excitation work? Dopita & Sutherland (2003) can help us with the answer to that question.

### 3.10.1 Collisional Excitation

A factor that is most certainly very important for these mechanisms is the cross section of collisions between the atoms and the electrons. To excite an electron from the inner shell, the atom needs to be supplied with energies around a few keV, depending on element and numbers of electrons. The cross section is thus a strong function of the impact energy and does not make for a good parameter to describe states of atoms. Therefore, the cross section  $\sigma_{ij}(E)$  is written in terms of the collision strength  $\Omega_{ij}$  to separate constant atomic characteristics, which can easily be collected in data tables, from energy dependencies:

$$\sigma_{ij}(E) = \frac{h^2}{8\pi m_e E} \frac{\Omega_{ij}}{g_i}. \quad (3.68)$$

Here,  $m_e$  and  $E$  are electron mass and energy and  $g_i$  is the statistical weight of the ground state. The collision strength can be derived from quantum mechanics and has the advantage of being symmetric between lower and upper states:  $\Omega_{ij} = \Omega_{ji}$ . Again we assume thermal equilibrium, which gives us the ratio of the population densities as stated by the Maxwell-Boltzmann equation (Eq. 3.63) at electron temperature  $T$ . If the energy of the electrons follows the Maxwell-Boltzmann energy distribution (Maxwell, 1867; Boltzmann, 1872)

$$f(E)dE = \sqrt{\frac{4}{\pi(kT)^3}} \sqrt{E} \exp\left(-\frac{E}{kT}\right) dE, \quad (3.69)$$

the collisional excitation rate of the upper level per unit volume can be computed to

$$\begin{aligned} R_{ij} &= n_e N_i \int_{E_{ij}}^{\infty} \sigma_{ij}(E) \cdot E \cdot f(E) dE \\ &= n_e N_i \left(\frac{2\pi\hbar^4}{km_e}\right)^{1/2} T^{-1/2} \left(\frac{\Omega_{ij}}{g_i}\right) \exp\left(-\frac{E_{ij}}{kT}\right) \\ &= n_e N_i \alpha_{ij} \end{aligned} \quad (3.70)$$

in units of  $\text{cm}^{-3} \text{s}^{-1}$  and the collisional de-excitation rate is

$$\begin{aligned} R_{ji} &= n_e N_j \int_0^{\infty} \sigma_{ji}(E) \cdot E \cdot f(E) dE \\ &= n_e N_j \left(\frac{2\pi\hbar^4}{km_e}\right)^{1/2} T^{-1/2} \left(\frac{\Omega_{ij}}{g_i}\right) \\ &= n_e N_j \alpha_{ji} \end{aligned} \quad (3.71)$$

where  $n_e$  is the density of the electron gas and  $\alpha_{ij}$  and  $\alpha_{ji}$  are the collisional excitation and de-excitation coefficients in units of  $\text{cm}^3 \text{s}^{-1}$ . Due to the Boltzmann factor  $\exp\left(-\frac{E_{ij}}{kT}\right)$  and the different statistical weights, the  $\alpha$ 's are not symmetric in the upper and lower levels. Applying the principle of detailed balance to these rates yields a simple relation between the collision coefficients

$$\frac{N_j}{N_i} = \frac{\alpha_{ij}}{\alpha_{ji}} = \left(\frac{\Omega_{ij}}{g_i}\right) \left(\frac{\Omega_{ji}}{g_j}\right) \exp\left(-\frac{E_{ij}}{kT}\right). \quad (3.72)$$

A comparison with equation 3.63 proves the symmetry of the  $\Omega$ 's.

### 3.10.2 Collisional Ionization

Collisional ionization can be considered sort of the limit of collisional excitation. An electron is excited to the  $n \rightarrow \infty$  shell, i.e., the continuum where it is unbound from the core potential of the atom, if the energy supplied through the collision is larger than the ionization energy  $\Delta E_{A,i}$  of the atom:



Since the required ionization energy is subtracted from the colliding electron, collisional ionization effectively cools the electron gas. For supplied energies greater than the ionization potential, the ionization can take place to an excited level of the next ionic state. So the only difference between collisional ionization and excitation is that the former occurs

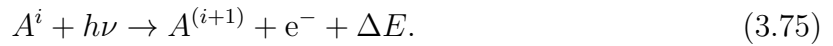
to a continuum of levels above the ionization limit while the latter occurs only to a single level. The collisional ionization rate is then

$$R_{\text{coll}}^{A,i} = n_e n_{A,i} \alpha_{\text{coll}}^{A,i} = n_e n_{A,i} \int_I^\infty \sigma_{\text{coll}}(E) \cdot E \cdot F(E) dE \quad (3.74)$$

where  $f(E)dE$  is the electron energy distribution and  $I$  the ionization limit but now  $n_{A,i}$  is the number density of the ions instead of just one level. Due to the higher complexity of the ionization process, this function is usually not solved analytically but rather fitted with a five-parameter function for each ionization channel.

### 3.10.3 Photoionization

There is nothing like an electron beam around the binary system Cyg X-1. Instead the gas contained in this system is ionized by the strong X-ray radiation emitted by the accretion onto black hole. The ionization of an atomic species through the absorption of the photon is called photoionization:



As for collisional ionization, the absorption of a photon can, depending on the photon energy, lead to the ground state or an excited state of the next ionic stage. For high photon energies, photoionization can lead to the removal of an inner-shell electron, which definitely results in an excited state of the next ion. Cascades back to the ground state then partially are seen as  $K\alpha$  emission. A photon of this cascade, however, can also be absorbed by an outer-shell electron before it can leave the ion. If it bears enough energy to overcome the ionization energy, the absorbing electron will be excited to the continuum. This process is known as radiationless autoionization.

## 3.11 Line Intensities

Generally, in equilibrium it can be assumed that all losses in the population of a certain energy level of an ion should be outweighed by the gain in population caused by transitions from other levels. This steady state model is commonly referred to as the principle of detailed balance<sup>9</sup>, where the rate equations can be written as  $n_i \sum_j P_{ij} = \sum_j n_j P_{ji}$ . Here,  $n_i$  is the relative abundance of particles occupying energy level  $i$ , while  $P_{ij}$  is the probability for this particle to make a transition from level  $i$  to level  $j$ . Using this assumption, the line intensity for every radiative transition can be estimated. The intensity of a line is defined as

$$I_\nu = \frac{1}{4\pi} n_u \nu_{ul} A_{ul}, \quad (3.76)$$

where  $u$  denotes upper and  $l$  lower levels. Obviously, besides the (known) properties of transition frequency  $\nu_{ul}$  and radiative transition rate  $A_{ul}$ , the relative occupation number  $n_u$  of the initial energy level has to be acquainted. The latter can be obtained by solving the rate equations. This set of linear equations is overdetermined since the single equations are not linearly independent of each other. Therefore, the additional constraint of particle number conservation

$$\sum_i^N n_i = 1 \quad (3.77)$$

<sup>9</sup>explicitly introduced for the first time by Boltzmann (1872) for collisions

has to be accounted for. To ease the process of solving the set of linear equations, it can be re-written to a matrix equation of the form

$$\vec{n}^T \mathbf{A} = \vec{e}_N^T \quad (3.78)$$

where  $\vec{n}$  is the vector of occupation numbers,  $\mathbf{A}$  is the matrix comprehending the transition probabilities and  $\vec{e}_N$  is the  $N^{\text{th}}$  unit vector. Solving this matrix equation is as easy as matrix inversion can be, analytically and numerically. The solution of the relative occupation numbers then is simply the last row of the inverted matrix.

The exact expression of the transition probabilities  $P_{ij}$  strongly depends on the processes taken into account. A very simple version of the transition probabilities, often used in plasma diagnostics of interstellar medium, planetary nebulae, etc., only considers spontaneous and (collisionally) stimulated emission (for  $i > j$ ) and collisional excitation ( $i < j$ ; Dopita & Sutherland, 2003). Using the collisional (de-)excitation rates deduced in section 3.10 and with spontaneous emission only being possible through transitions from upper to lower levels (for energetic reasons), the rates can in this case be written as (Drechsel & Przybilla, 2009):

$$i > j : \quad P_{ij} = A_{ij} + \left( \frac{2\pi\hbar^4}{k_B m_e^3} \right)^{1/2} \frac{N_e}{\sqrt{T_e}} \cdot \frac{\Omega_{i,j}}{g_i} \quad (3.79)$$

$$i < j : \quad P_{ij} = \left( \frac{2\pi\hbar^4}{k_B m_e^3} \right)^{1/2} \frac{N_e}{\sqrt{T_e}} \cdot \frac{\Omega_{j,i}}{g_i} \cdot \exp\left( -\frac{(E_j - E_i)}{k_B T_e} \right). \quad (3.80)$$

Here,  $A_{ij}$  denotes the Einstein A coefficients for spontaneous emission,  $\Omega_{ij}$  the collision strength,  $g_i$  the statistical weight and  $E_i$  the level energy. In astrophysics and in the above equations an energy distribution according to Maxwell-Boltzmann is assumed, while in the laboratory other distributions are possible. In EBIT, for example, the beam energy is better described by a Gaussian distribution (Gauß, 1809). The corresponding matrix equation<sup>10</sup> then looks like

$$(n_1, n_2, \dots, n_{N-1}, n_N) \begin{pmatrix} -\sum_{j \neq 1} P_{1j} & P_{12} & \dots & P_{1,N-1} & 1 \\ P_{21} & -\sum_{j \neq 2} P_{2j} & & \vdots & 1 \\ \vdots & & \ddots & \vdots & 1 \\ \vdots & & & -\sum_{j \neq N-1} P_{N-1,j} & 1 \\ P_{N1} & \dots & \dots & P_{N,N-1} & 1 \end{pmatrix} = \underbrace{(0, \dots, 0, 1)}_{N-1}. \quad (3.81)$$

In this simple case where only transitions inbetween levels of the same ion are considered, the diagonal matrix elements lists the loss terms of the energy levels, while the lower triangular matrix contains the gain from higher energy levels (de-excitation) and the upper triangular matrix resembles the gain from lower levels (excitation).

<sup>10</sup>In this matrix equation the rather unconventional row vectors are used for numerical reasons. To solve this equation analytically the inverse matrix has to be multiplied to both sides of the equation from the right hand side. Because only one entry of the vector on the right hand side is different from zero, the solution of the abundances are just the last row of the inverse matrix. In Fortran the most efficient way to read out the elements of an array is to read them row by row. Most other programming languages are built such that the most efficient read-out mode is column by column (priv. comm. with J.Wilms). For these languages the matrix equation can easily be re-written in terms of column vectors such that the solution is hidden in the last column of the inverse matrix. The conversion can be done easily by transposing the whole equation, i.e.,  $\mathbf{n}P = \mathbf{s} \rightarrow P^T \mathbf{n}^T = \mathbf{s}^T$  where  $\mathbf{n}^T$  is the column vector of the relative abundances and  $P^T$  is the transposed probability matrix.

This example only accounts for excitation in one sort of ions. The expression for the transition probabilities, however, can become way more complex; especially if in addition to the excitation processes ionization mechanisms are introduced, creating a link between energy levels of different ionization states of the same atom. A more general description of transition probabilities is given by Bautista & Kallman (2001), who include all possible types of transitions in their rate equations. In their notation, subindices also denote transitions between energy levels of the same ion. Superindices, in contrast, indicate transitions between ionic states.

$$\begin{aligned}
 n_i^0 \left( \underbrace{\sum_{j \neq i} R_{ij}}_{\text{losses to levels in same ion}} + \underbrace{\sum_{q>0} \Gamma_i^{0 \rightarrow q}}_{\text{losses through photo-ionization}} + \underbrace{N_e \alpha_i^{-1}}_{\text{losses through recombination}} + \underbrace{N_e Q_i^{0 \rightarrow 1}}_{\text{collsional ionization}} \right) = \\
 = \underbrace{\sum_{k \neq i} n_k^0 R_{ki}}_{\text{gain from levels in same ion}} + \underbrace{\sum_{q>0} \sum_l n_l^{-q} \Gamma_{li}^{-q \rightarrow 0}}_{\text{gain from photo-ionization}} + \underbrace{N_e \sum_l n_l^{-1} Q_{li}^{-1 \rightarrow 0}}_{\text{gain from collisional ionization}} + \underbrace{\sum_s n_s^1 N_e \alpha_{si}^0}_{\text{gain from recombination}} \quad (3.82)
 \end{aligned}$$

The left hand side of this equation describes all losses from level  $i$  in ionization state 0 to levels of the same ion as well as to other ionization states. The right hand side is the sum of all processes populating level  $i$  in ion 0. Transitions in the same ion,  $R_{ij} = n_e q_{ij}^e + n_p q_{ij}^p + A_{ij} + U_\nu B_{ij}$ , are covered by collisional (de-)excitation induced by collisions with electrons and protons (electron/proton collisional excitation rate coefficient  $q_{ij}^{e/p}$ ), spontaneous radiative decay ( $A_{ij}$ ) and transitions stimulated by a photon field with absorption radiation density  $U_\nu$  (stimulated transition coefficient  $B_{ij}$ ). Photoionization processes are indicated by  $\Gamma_{ij}^{k \rightarrow l}$ , which is the rate with which level  $i$  in ion  $k$  ionizes to level  $j$  in ion  $l$ . If there is only one subindex, ionization into any level of ion  $l$  is included implicitly, i. e.  $\Gamma_i^{k \rightarrow l} = \sum_j \Gamma_{ij}^{k \rightarrow l}$ . In the same manner,  $Q_{ij}^{k \rightarrow l}$  represents the collisional ionization coefficient. Recombination into ion  $k$  is given by  $\alpha^k$ . This coefficient can include radiative and dielectronic electron-ion recombination, three-body-recombination and stimulated recombination.

The translation of the above system of linear equations into a matrix equation can be found in appendix B. Again, to solve this equation, one column of the matrix has to be substituted by the condition of charge conservation

$$\sum_k \sum_i^{N_k} n_i^k = 1. \quad (3.83)$$

Fortunately, the rate equations can often be simplified by applying a few assumptions. For example, ionization usually only connects ionization states directly adjacent to each other, i.e., there is only one electron removed at a time. Transitions between non-neighboring ionic stages can be described by a sequence of processes, e.g., inner-shell ionization is likely followed by Auger-ionization, and accordingly have small transition rates. The same holds true for the inverse process of recombination: an ion only takes in one electron at a time. Also, most ionization and recombination processes happen to the ground state of the neighboring charge state. Therefore, rates to other levels are basically zero in large portions of the transition probability matrix. Some knowledge about the conditions in the observed plasma can reduce the number of the non-zero matrix elements and their components even further. Sources like Cyg X-1 are mainly driven by photo-ionization and

-excitation. In contrast, the photon field does not play a role in sources like an EBIT (see Sec. 4.1), where ions are created and excited through the collision of the injected gas with the electrons of the electron beam but where no powerful radiation source like a massive star or an X-ray laser is present. Consequently, photo-ionization can be neglected in this case. It is nevertheless a good idea to handle the huge amount of energy levels present in the ion mixture of the plasma by solving the system of rate equations numerically.

## 3.12 Atomic Codes

To be able to derive (at least the relative) intensities of radiative transitions, which can be used to simulate the spectrum, the atomic physics parameters describing the properties of the ions have to be known first. Since a lot of the resulting spectral lines vastly blend into each other and are therefore never to be resolved experimentally, these parameters are better to be calculated numerically. There are many codes available for this purpose. They can be divided into two categories: there are codes which really calculate the atomic physics data like the energy levels and all kinds of ionization, recombination and (de-)excitation cross sections and transition rates. And then there are codes that use these databases to calculate properties of plasmas under certain conditions and simulate the spectra emitted by them.

Only a small, rather incomplete overview over the variety of available codes can be given here. SUPERSTRUCTURE (Eissner et al., 1974) is one of the codes that is only capable of calculating atomic structure and bound state problems (term energies, intermediate coupling energy levels, term-coupling coefficients, permitted and forbidden radiative transition probabilities and cascade coefficients). It uses the ansatz of relativistic corrections. The MCHF code of Froese Fischer (2000) also applies relativistic corrections to derive energy levels, transitions between LS and LSJ coupling and hyperfine interactions. A fully relativistic approach but mainly for the calculation of energy levels is prepared by the MCDF code of Grant et al. (1980). In order to avoid inconsistencies between the treatment of continuum and bound states and to ease the handling of the programs also for people other than its author, also some integrated packages have been written. There is, for example, the SZ code of Sampson et al. (1989) and Zhang et al. (1989) based on a fully relativistic ansatz. AUTOSTRUCTURE<sup>11</sup> evolved from and uses SUPERSTRUCTURE, adding the possibility to compute autoionization rates, photo-ionization cross sections (Badnell, 1986, 1997) and electron impact excitation (Badnell, 2011). The Hebrew University Lawrence Livermore Atomic Code (HULLAC; Bar-Shalom et al., 2001) is a package that provides a coherent set of programs for relativistic quantum mechanical calculations of atomic structure and collisional and radiative atomic processes and cross sections. It even comes with a routine to derive line intensities in a plasma, but is unfortunately not publically available. This flaw is overcome by the Flexible Atomic Code (FAC Gu, 2004, see section 3.12.3 for details).

All of the codes mentioned above have in common that they usually produce very good results for H- and He-like systems. The high accuracy of these lines and their good agreement with experimental data is due to the simplicity of their systems. The atomic nucleus can be considered a single particle (with increasing mass for increasing  $Z$ ), every electron adding one more body to the equation. A two-body problem can be solved very well, a three-body-problem is still easy enough, but with every additional body the

---

<sup>11</sup>available online at <http://amdpp.phys.strath.ac.uk/autos/>

inaccuracy of the calculated lines increases more and more. Depending on the goal to be achieved with the code, the authors of the codes use different theoretical and numerical approaches to solve the many-body-problem. An additional factor to be considered is the regime the code is written for: does LS-coupling still hold or is jj-coupling already advisable?

### 3.12.1 Calculation of House (1969)

In this work, two sets of theoretical predictions for line energies are compared to the experimental data. One is the work of Palmeri et al. (2008), the other one is a calculation carried out with FAC. A third one by House (1969), although cited in Fig. 2.8, is omitted. At his time,  $K\alpha$ -type X-ray transitions other than the "normal"  $K\alpha$  transition (transitions to the K-shell in singly ionized material) had just recently been observed in solar X-ray spectra which had been taken during rocket observations carried out by the Naval Research Laboratory. It was theorized that inner-shell ionization of an already ionized state leads to similar transitions as the normal  $K\alpha$  line, but shifted to higher energies due to the reduced shielding of the X-ray transition. Following the lack of laboratory measurements of these transitions, House (1969) utilized the Hartree-Fock approach in the LS-coupling regime to provide the community with calculations of the  $K\alpha$  wavelength of singly ionized to He-like carbon through copper. Although he stated that the influence of angular momentum coupling becomes important in incomplete shells, term structure was only treated in elements with an open  $n = 2$  shell. For higher  $Z$  elements, i.e., Na-Co, the multiplet structure was completely neglected as a deviation from LS-coupling would be expected anyway. Additionally, for these elements, the calculations are arbitrarily forced into agreement with their corresponding observed normal  $K\alpha$  transitions by shifting the whole isonuclear sequence by this difference in wavelength. For some experimental data only measurements carried out with solid material were available, which slightly differ from wavelength in gases. As can be seen in Fig. 2.8 and Hanke (2011), the precision of these results and, in view of laboratory measurements, their resolution are not sufficient for our purposes.

### 3.12.2 Calculation of Palmeri et al. (2008)

Palmeri et al. (2008) compare different versions of their own calculations of the Ne, Mg, Si, S, Ar, and Ca isonuclear sequences with various other published data tables. First, they study the impact of the core relaxation effects in the radiative decay process by calculating radiative transitions with AUTOSTRUCTURE, once with all considered electron configurations having a common basis of orthogonal orbitals and another time optimizing the energy of each configuration separately, which leads to a basis of non-orthogonal orbitals. A comparison of the obtained  $f$ -values with the standard reference table of Drake (1988) for the He-like isonuclear sequence leads to the conclusion that accounting for core relaxation effects may not necessarily improve the radiative data. The atomic data tables to be found in the electronic version of the *Astrophysical Journal Supplement*<sup>12</sup>, however, are created using the HFR code which also relies on bases of non-orthogonal orbits and includes relativistic corrections. The tables given are split into two parts: one lists the computed energy levels compared to the spectroscopic energy available in the

<sup>12</sup><http://iopscience.iop.org/0067-0049/177/1/408/fulltext>

NIST Atomic Spectra Database<sup>13</sup>, the corresponding radiative width and the Auger width and fluorescence yield where applicable. The second table provides a list of transitions, identified with the indices of the upper and lower energy levels, its wavelength,  $A$ -value and  $gf$ -value. Usually, the difference in wavelength between experiment and theory increases with increasing number of electrons along an isoelectronic sequence. For first-row ions (ions with 3 to 9 electrons) this trend and a comparison between theory and experiment can be used to fine-tune computed data with empirical corrections. Since there are no measurements for second-row ions available, this approach is not feasible and, therefore, their results remain uncorrected. Palmeri et al. (2008)'s investigation of the accuracy of the published tables suggests an agreement of the line energies of better than 2 eV for ions with up to four electrons. The presented  $A$ -values and Auger width greater than  $10^{13} \text{ s}^{-1}$  are within 15% and 20%, respectively. Palmeri et al. (2008) also is used as a reference for radiative and Auger width for photoionization cross section calculations in the XSTAR code (Bautista & Kallman, 2001).

### 3.12.3 Calculations with FAC

One of the codes available for calculations of atomic physics data is the Flexible Atomic Code (FAC<sup>14</sup>) by Ming Feng Gu (2004). While most programmes are mainly concerned with the atomic structure and bound-bound processes, i.e., no ionization processes, FAC is a compound package that provides functions to calculate the atomic structure, bound-bound as well as bound-free processes, and has subroutines to estimate the line intensities for given electron beam properties or plasma temperatures and even calculates the polarization of lines. Compared to, for example, the HULLAC package (Bar-Shalom et al., 2001) FAC has the major advantage that it is freely accessible for everyone. FAC is distributed with a manual and several unpublished papers to describe the theoretical background and numerical techniques and compares a few example calculations with other codes.

FAC is based on the fully relativistic ansatz via the Dirac equation. The assumed Hamiltonian of the system in atomic units<sup>15</sup>,

$$\hat{H} = \sum_{i=1}^N \hat{H}_D(i) + \sum_{i<j}^N \frac{1}{r_{ij}}, \quad (3.84)$$

contains all single-electron Dirac Hamiltonians  $\hat{H}_D$  for the potential due to the nuclear charge plus the interactions between the electrons. The coupling of the angular momenta of successive shell is handled in the standard jj-coupling regime. The atomic state functions  $\psi$  are approximated by mixing the basis states  $\Phi_\nu$  with same symmetries

$$\psi = \sum_{\nu} b_{\nu} \Phi_{\nu}. \quad (3.85)$$

The  $b_{\nu}$  are the mixing coefficients obtained from diagonalizing the total Hamiltonian. The central potential due to the nuclear charge  $V_N(r)$  is assumed to be

$$V_N(r) = \begin{cases} \frac{Z}{2} \left( \frac{r}{R_N} \right) \left[ 3 - \left( \frac{r}{R_N} \right)^2 \right] & \text{for } r \leq R_N \\ Z & \text{for } r < R_N \end{cases} \quad (3.86)$$

<sup>13</sup><http://physics.nist.gov/asd>

<sup>14</sup><http://sprg.ssl.berkeley.edu/~mfgu/fac/>

<sup>15</sup>1 a.u. = 2 Ry

with the statistical model radius of the nucleus  $R_N$  which is proportional to the atomic mass as  $R_N \propto A^{1/3}$ . The contribution of electron-electron interaction to the central potential is a rather complicated expression which depends on the sought radial orbitals. Therefore, a self consistent iteration is needed to solve the Dirac equation of the system. To derive the potential, in each iteration the orbitals from the previous step are used such that the eigenvalue problem reduces to one with a known potential. The Dirac equation is converted into a Schrödinger-like equation and the radial distance  $r$  is substituted by a function  $t(r)$  which allows to use a uniform grid in the new variable  $t$  for better numerical handling during the calculations. There are different candidates for such a function. The MCHF code of Froese Fischer (2000) applies a logarithmic transformation  $t(r) \propto \ln(r)$ , which is not suitable for highly excited atoms and ionization processes. ATOM (Amusia et al., 1998) uses a hybrid form  $t(r) = c_1 r + c_2 \ln(r)$  that – for the right choice of  $c_1$  and  $c_2$  – is able to cope with the calculation of highly excited orbitals and continua below a certain limit. To be able to also take high energies into account, FAC follows the path of HULLAC (Bar-Shalom et al., 2001) which employs yet another method. The oscillation period of the wavefunction can be shown to be proportional to  $\sqrt{r}$  for large  $r$ . So in order for one oscillation period to contain approximately the same number of grid points at large distances, the transformation  $t(r) = c_1 \sqrt{r} + c_2 \ln(r)$  is applied, which allows a given number of grid points to cover a larger radial distance than the linear form.

To get as accurate results as possible for the atomic structure, the interaction between different configurations has to be taken into account (multiconfiguration approach). The number of these interacting configurations sometimes can become very large, resulting in huge dimensions of the Hamiltonian to be diagonalized. The larger the Hamiltonian, the more expensive in CPU time and memory the calculation becomes. Since often the focus of interest lies in a small subset of energy levels from a large configuration space, most of the configuration levels are only included to account for the mixing to the desired levels. Therefore, the configuration space is subdivided into the main group, which gives a good zeroth order approximation of the desired energy levels, and a perturbing group with only weak interaction with the main group. Then only interactions of the main group with itself and the perturbing group is considered, while all interactions within the perturbing group are neglected. For perturbing groups much larger than the main group, this approximation eases the computation a lot. The eigenvalues and eigenvectors of the simplified Hamiltonian are then determined iteratively.

Once the atomic structure is known, radiative transition rates can be calculated. While the user is free to choose according to which multipoles the transitions should be calculated, the code does not take into account interference between different multipoles. Starting from the atomic structure also all other kinds of excitation and ionization processes can be calculated. Testing of the code was done by its author Gu (2004) who carried out calculations with his code and other available packages each for the same set of configurations. Comparisons between the results of the different codes and some experimental results as well lead him to the conclusion that in ions other than H-like the computed energy levels are accurate up to a few eV or 10-30 Å at  $\sim 10$  Å. Radiative transition rates and cross sections are accurate to  $\sim 10 - 20\%$ . Near-neutral ions or atoms may have even larger errors (cf. FAC manual).

For the simulation of the silicon and sulfur  $K\alpha$  spectra, the atomic structure and radiative transitions are calculated with FAC. To get more accurate estimations for the single level populations not only interactions between the first and second shells are taken into account but also interactions with  $\Delta n = 0$ . Since in an EBIT the production of ions and excited

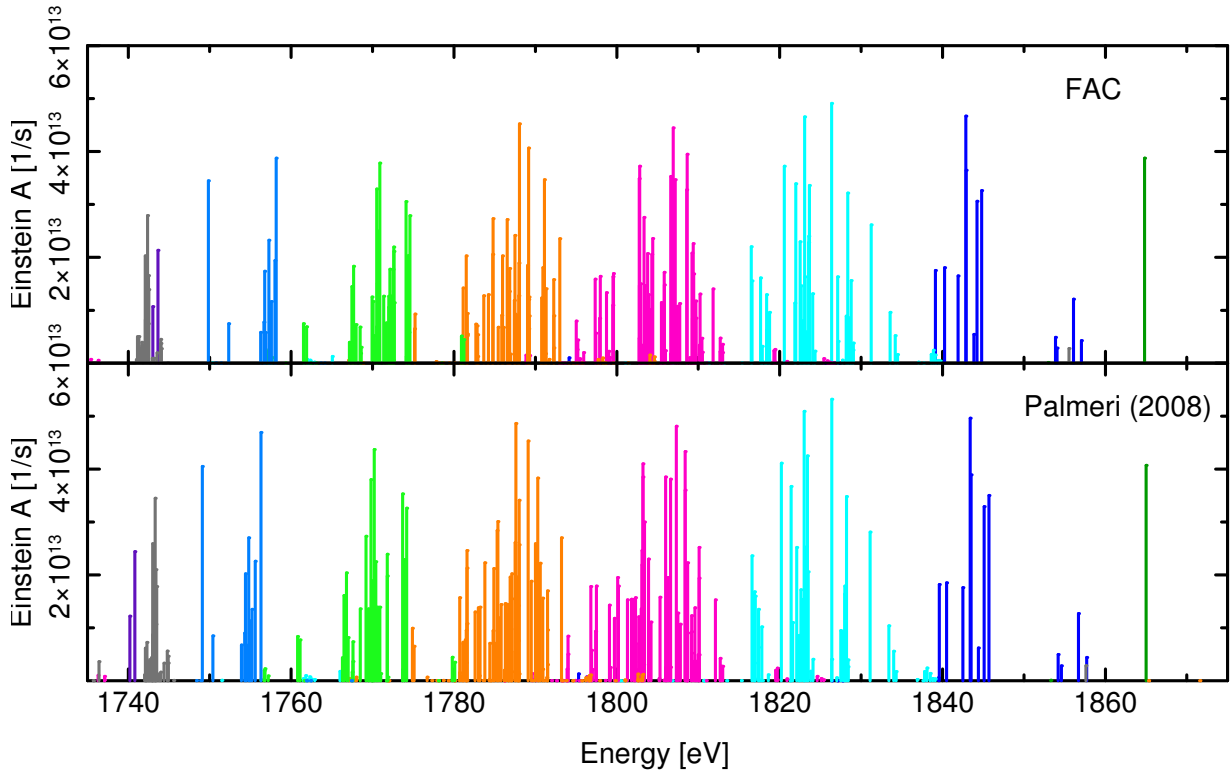


**Figure 3.6:** A crude comparison between the atomic data of Si presented by Palmeri et al. (2008) (lower panel) and the calculation with FAC (upper panel) for He- through Ne-like ions. Different colors represent different ionization states. The color code is consistent throughout this work (see table 3.2).

**Table 3.2:** Whenever different ionization states are color coded in this work, the color scheme listed in this table is used.

Ionic state	$N_e$	Color	Ionic state	$N_e$	Color
H-like	1	red	C-like	6	orange
He-like	2	dark green	N-like	7	green
Li-like	3	dark blue	O-like	8	blue
Be-like	4	light blue	F-like	9	dark purple
B-like	5	pink	Ne-like	10	light gray

states is dominated by electron-ion and ion-ion collisions, also collisional excitation and ionization rates are computed. In addition, subsequent ionization of excited levels via autoionization processes is tabulated for completeness reasons. Only photoionization and its inverse process, radiative recombination, are discarded because of the lack of a serious photon field in EBIT. FAC is also capable of calculating the effects of external electric and magnetic fields (Zeeman, Paschen-Back, Stark effects). Since there are strong electric and magnetic fields employed in an EBIT, one has to think about including these terms. Nevertheless, as shown in section 3.3, the level splitting due to these effects is in the order of less than 1 meV, i.e., much smaller than the resolution of our measurements around 2 keV. Therefore, external fields are omitted in this calculation.

### 3.12.4 FAC vs. Palmeri et al. (2008)

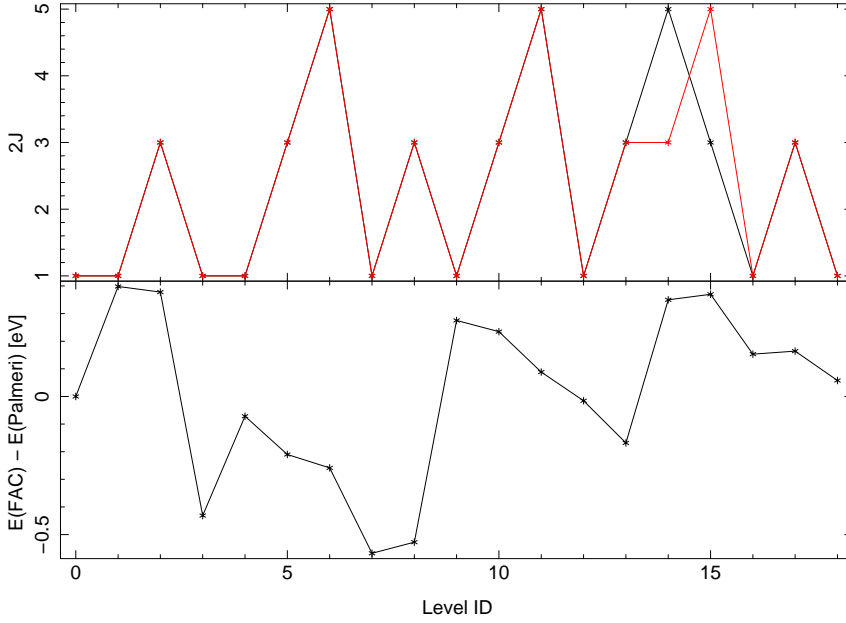
A qualitative comparison between the results obtained with FAC and the lines published by Palmeri et al. (2008) is displayed in Fig. 3.6. Different ionization stages are associated with different colors to be able to distinguish them by eye. The color code can be looked up in table 3.2 and is consistently applied throughout this work whenever these ions are plotted. As expected do the He-like lines (dark green) agree very well between the two calculations. For lower ionization states only the general distribution of the lines agrees anymore. Groups of lines can still be perceived to correspond to each other. But the separation of certain line features has obvious differences. For instance, there are two O-like lines (blue) around 1750 eV for which the ratio of the transition probabilities is approximately the same in both calculations. The separation of their line energies, however, is about twice as large in FAC as in Palmeri et al. (2008). There is also one outstanding aspect of the Palmeri et al. (2008) results that arises suspicion: the two (purple) F-like spectral lines have distinctly lower energies than the (gray) Ne-like lines although the Ne-like iso-electronic sequence has an electron more than the F-like ions. This inconsistency can probably be ascribed to the fact that the F-like lines are shifted by an empirical value according to measurements after the calculation was performed while for Ne-like lines no such shift was applied due to the lack of measurements.

Later when the laboratory measurements are compared to theoretical calculations (section 4.7), the identification is mainly done via the spectra simulated with FAC. Nevertheless, the results of Palmeri et al. (2008) shall be incorporated into the table as well. Therefore, the LS-coupling energy levels corresponding to the chosen jj-coupling energy levels have to be found. Because of the inadequateness of the analytical approach described in section 3.6.4, a rather numerical method is chosen to reach this goal. According to theory both calculations should result in the same number of levels. These levels are sorted after increasing energy for both calculations and then matched to each other via their level ID. After the energy sorting special attention is paid to the total angular momentum  $J$  since it is the only good quantum number and therefore should be the same in both notations. If the  $J$  value of supposedly corresponding energy levels differ from each other, a closer look is taken at the energies. Usually in these cases the energy difference between succeeding levels is in the order of or smaller than the energy difference between the FAC and Palmeri et al. (2008) results. Then these levels are switched with each other such that they have the same total angular momentum as their corresponding FAC levels.

This approach shall be demonstrated on the example of Li-like Si. Table 3.3 lists the sorted energy levels for both, FAC and Palmeri et al. (2008), Figure 3.7 visualizes their total angular momentum. The energy difference between the levels of different calculation methods are within their stated accuracy of at least 2 eV. Obviously, the levels with the IDs 14 and 15 are mismatched. They belong to the doublet  $^2D$  with a fine structure splitting of roughly 0.1 eV. This difference is small compared to the  $\sim 0.4$  eV between FAC and Palmeri. It is therefore perfectly valid to exchange those two levels; i.e., FAC level 14 corresponds to Palmeri level 15 and the other way round.

### 3.12.5 Spectra Simulated with FAC

The atomic data tables compiled with FAC are then finally used in a second step to create theoretical spectra of the desired  $K\alpha$  lines. Therefore, the FAC module `crm` is employed. It uses an iterative linear equation solver to invert the level population equations explained in section 3.11 to derive a collisional radiative spectral model for optically thin plasmas.

**Figure 3.7:**

Comparison between FAC and Palmeri et al. (2008) energy levels for Li-like Si. The top panel shows two times the total angular momentum (black: FAC, red: Palmeri) of the levels sorted by energy, where the level ID equal to zero corresponds to the ground state. The lower panel displays the difference between these energy of the two calculations.

**Table 3.3:** Comparison of the FAC and Palmeri et al. (2008) energy levels of Li-like Si. With the exception of levels 14 and 15 which have to be switched, this table can be used to match the LS- and jj-coupling notations. The level IDs are the same as in Fig. 3.7.

Level		FAC / jj-coupling		Palmeri / LS-coupling		
ID	label	2J	E (eV)	label	2J	E (eV)
0	$1s^2 2s_{1/2}$	1	0.0000	$1s^2 2s \ ^2S_{1/2}$	1	0.0000
1	$1s^2 2p_{1/2}$	1	24.2052	$1s^2 2p \ ^2P_{1/2}^o$	1	23.8072
2	$1s^2 2p_{3/2}$	3	25.1950	$1s^2 2p \ ^2P_{3/2}^o$	3	24.8172
3	$1s_{1/2} 2s^2$	1	1819.3324	$1s 2s^2 \ ^2S_{1/2}$	1	1819.7636
4	$((1s_{1/2} 2s_{1/2})_1 2p_{1/2})_{1/2}$	1	1825.5664	$1s(^2S) 2s 2p(^3P^o) \ ^4P_{1/2}^o$	1	1825.6379
5	$((1s_{1/2} 2s_{1/2})_1 2p_{1/2})_{3/2}$	3	1825.8421	$1s(^2S) 2s 2p(^3P^o) \ ^4P_{3/2}^o$	3	1826.0523
6	$((1s_{1/2} 2s_{1/2})_1 2p_{3/2})_{5/2}$	5	1826.5196	$1s(^2S) 2s 2p(^3P^o) \ ^4P_{5/2}^o$	5	1826.7783
7	$((1s_{1/2} 2s_{1/2})_0 2p_{1/2})_{1/2}$	1	1844.2234	$1s(^2S) 2s 2p(^3P^o) \ ^2P_{1/2}^o$	1	1844.7912
8	$((1s_{1/2} 2s_{1/2})_0 2p_{3/2})_{3/2}$	3	1844.7978	$1s(^2S) 2s 2p(^3P^o) \ ^2P_{3/2}^o$	3	1845.3252
9	$1s_{1/2} 2p^6$	1	1851.4494	$1s(^2S) 2p^2(^3P) \ ^4P_{1/2}$	1	1851.1741
10	$((1s_{1/2} 2p_{1/2})_0 2p_{3/2})_{3/2}$	3	1851.8449	$1s(^2S) 2p^2(^3P) \ ^4P_{3/2}$	3	1851.6101
11	$(1s_{1/2} (2p_{3/2}^2)_2)_{5/2}$	5	1852.3764	$1s(^2S) 2p^2(^3P) \ ^4P_{5/2}$	5	1852.2880
12	$((1s_{1/2} 2s_{1/2})_1 2p_{3/2})_{1/2}$	1	1853.8790	$1s(^2S) 2s 2p(^1P^o) \ ^2P_{1/2}^o$	1	1853.8947
13	$((1s_{1/2} 2s_{1/2})_0 2p_{3/2})_{3/2}$	3	1854.0537	$1s(^2S) 2s 2p(^1P^o) \ ^2P_{3/2}^o$	3	1854.2217
14	$((1s_{1/2} 2p_{1/2})_1 2p_{3/2})_{5/2}$	5	1864.3231	$1s(^2S) 2p^2(^1D) \ ^2D_{3/2}$	3	1863.9732
15	$((1s_{1/2} 2p_{1/2})_0 2p_{3/2})_{3/2}$	3	1864.4458	$1s(^2S) 2p^2(^1D) \ ^2D_{5/2}$	5	1864.0761
16	$((1s_{1/2} 2p_{1/2})_1 2p_{3/2})_{1/2}$	1	1867.0930	$1s(^2S) 2p^2(^3P) \ ^2P_{1/2}$	1	1866.9400
17	$(1s_{1/2} (2p_{3/2}^2)_4)_{3/2}$	3	1868.0490	$1s(^2S) 2p^2(^3P) \ ^2P_{3/2}$	3	1867.8849
18	$(1s_{1/2} (2p_{3/2}^2)_0)_{1/2}$	1	1881.2675	$1s(^2S) 2p^2(^1S) \ ^2S_{1/2}$	1	1881.2095

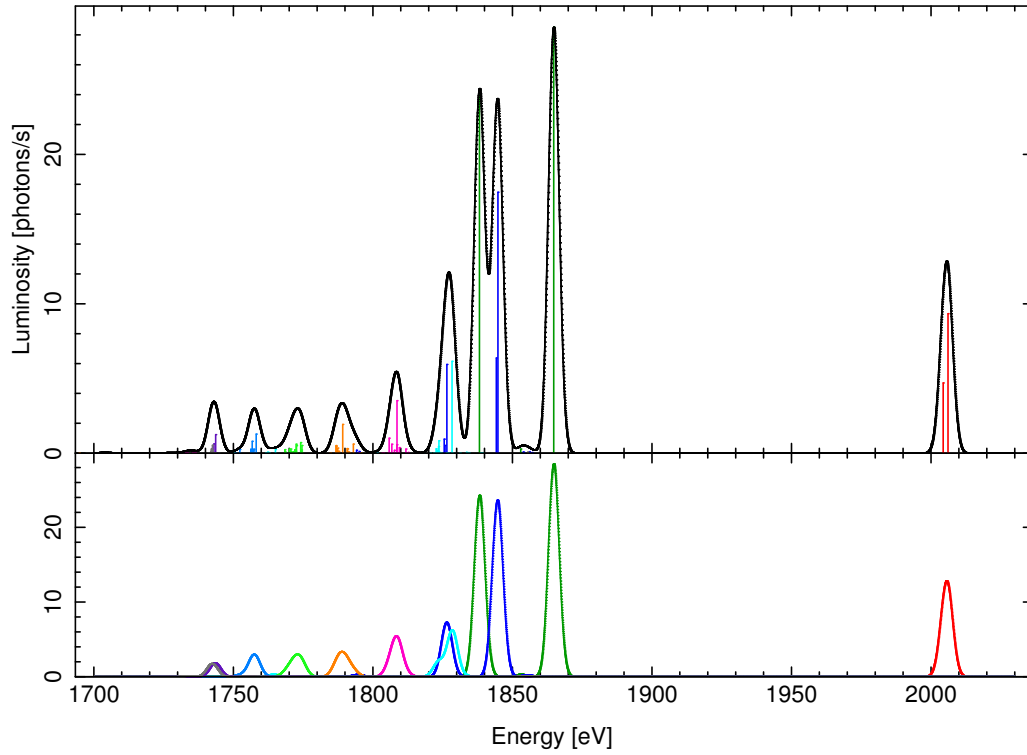


**Figure 3.8:** FAC simulation of Si  $K\alpha$  spectrum. Different colors represent different ionization stages. The top panel shows the transition energies with their predicted intensity and the total spectrum (black line). The lower panel shows the spectra for each ionization state, which in sum results in the black line of the top panel. Here, the impact of line blends can be seen quite clearly.

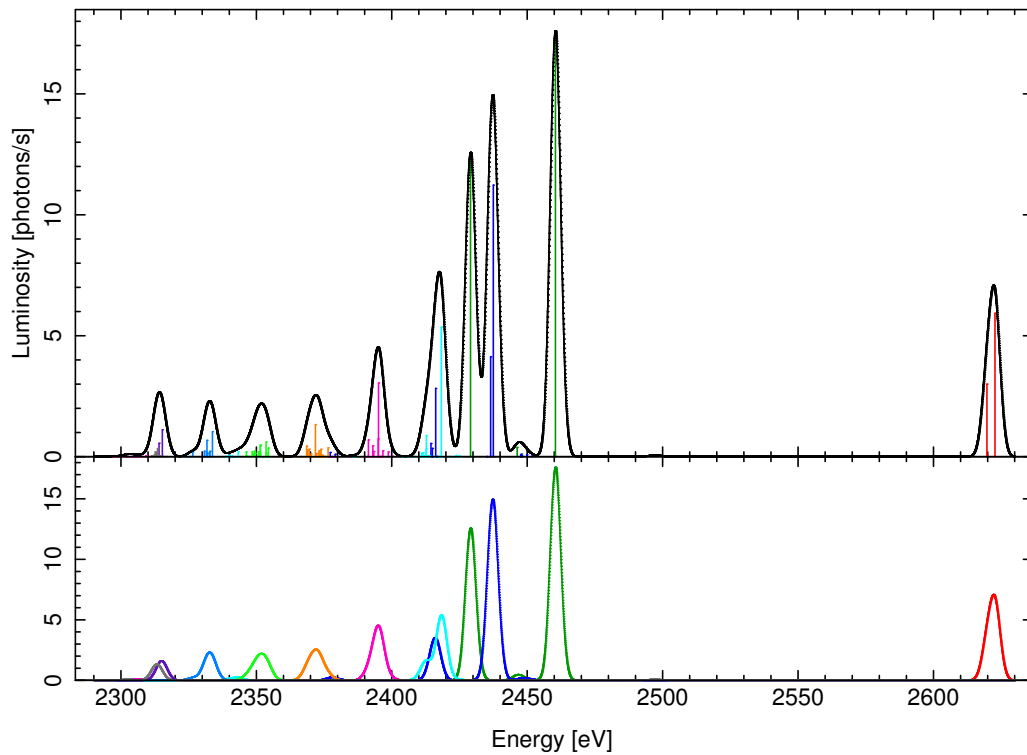


**Figure 3.9:** Same as Fig. 3.8 for S.

Since the populations of the various ions in EBIT are connected to each other via several ionization and recombination processes, the intensities of the levels in all ions are estimated at once.

To be able to fill the matrix given through the rate equations (eq. 3.82), FAC needs to know which processes to take into account. The most important process to be listed is radiative de-excitation as that is where our spectrum comes from. The inverse process of photoionization, in contrast, is discarded for the same reason as the photoionization parameters are not computed in the first step: there is no sufficient photon field around. Because of the constant collisions of the plasma with the electron beam, collisional excitation and de-excitation are both taken into account. To reproduce the high intensity of the usually forbidden line z (see section 4.5), which arises from inner-shell ionization of Li-like ions, collisional ionization is included. The inverse process of three-body recombination is not yet supported by the routine. For the sake of completeness then also autoionization and dielectronic recombination are included.

In order to fill the remaining parameters of the formulas, the plasma and beam properties have to be given. The calculations are performed with the same beam energy as was used during the measurements. The beam energy is assumed to follow a Gaussian distribution with an energy spread of around 40 eV and an electron density of  $10^{12} \text{ cm}^{-3}$ . To adjust the relative line intensities between different ionization states, an initial estimate for the charge balance in the plasma has to be provided. Unfortunately, the relative abundances of the ions in the trap can not be estimated very well. The simulation of the spectrum produced in the trap is therefore not self-consistent, which can lead to some unwelcome features in the spectrum.

Fig. 3.8 and 3.9 illustrate the resulting FAC simulation for silicon and sulfur, respectively, considering the presence of H- through Ne-like ions. The line centers of transitions calculated by FAC are convolved with a Gaussian line with a FWHM close to the resolution of the calorimeter used for the measurements (see sections 4.3 and 4.5.1). The correct normalization of these Gaussians is omitted for illustration reasons. The introduced error, however, has no influence on the depicted intensity ratios as the same FWHM is used for all lines, hence, the missing normalization factor would also be the same for all lines.

Scrooge McDuck: *What did you do??*

Gyro Gearloose: *Well, you did say to make it as real as it can be, so I did!*

---

Duck Tales

## Chapter 4

# Laboratory Measurements

### 4.1 Electron Beam Ion Trap

In the mid-80s Mort Levine (Lawrence Berkeley Laboratory [LBL]) and Ross Marrs (Lawrence Livermore National Laboratory [LLNL]) investigated ways to produce highly charged ions and maintain a certain charge balance as long as possible, as the electron beam ion source (EBIS) was not very successful with it. The first electron beam ion trap (EBIT; Levine et al., 1988; Marrs et al., 1988; Levine et al., 1989) was born and started operation in October 1986. First it was not clear whether it would work or not since there were theoretical predictions about a maximally reachable ionization state of  $q_{\max} \approx +50$  (Levine et al., 1988). But cooling mechanisms in EBIT lead to amazing results and so presently EBITs are the most efficient way of controlled ion production, even for very high states of ionization.

Basically, an EBIT consists of three main parts: the electron gun to produce the beam, the trapping region, and a collector assembly to dump the beam (see Section 4.1). The electron gun is a commercial Pierce-type gun (Pierce & Millburn, 1952). A Pierce-type electron gun has three cathodes coated with an electron emissive layer. The electron emissive coating is a material, in this case tungsten and bariumoxide, which has a low work function. The cathodes are heated radiatively thus the work function is overcome, electrons are boiled off and are emitted. This process is called thermionic emission and initially will leave positive charges behind in the emitting region. The ‘missing’ negative charge can be refilled by connecting the cathodes to a power supply and, therefore, neutralize the emitter and reset it to the state it was before the thermionic emission.

To focus the resulting electron beam, the cathodes are shaped conically. Further focusing is provided by a focus electrode. An anode with a hole in the middle to allow the beam to pass is used to accelerate the electrons. Afterwards the beam is guided through a set of three cylindrical electrodes, the drift tubes. The base potential of the drift tubes determines the energy of the electron beam. Around the drift tubes there is a pair of superconducting Helmholtz coils situated. The coils produce a strong magnetic field of 3 T, which is uniform to 0.02% and whose field lines are straight within 0.3 mrad in the trap region and is used to compress the electron beam (Levine et al., 1988). A liquid helium bath, which is shielded by liquid nitrogen from thermal radiation from the outside, cools the coils to  $\sim 4.2$  K. To enable the beam to originate in a field free environment, there is an additional bucking coil installed around the electron gun whose magnetic field compensates for the field coming

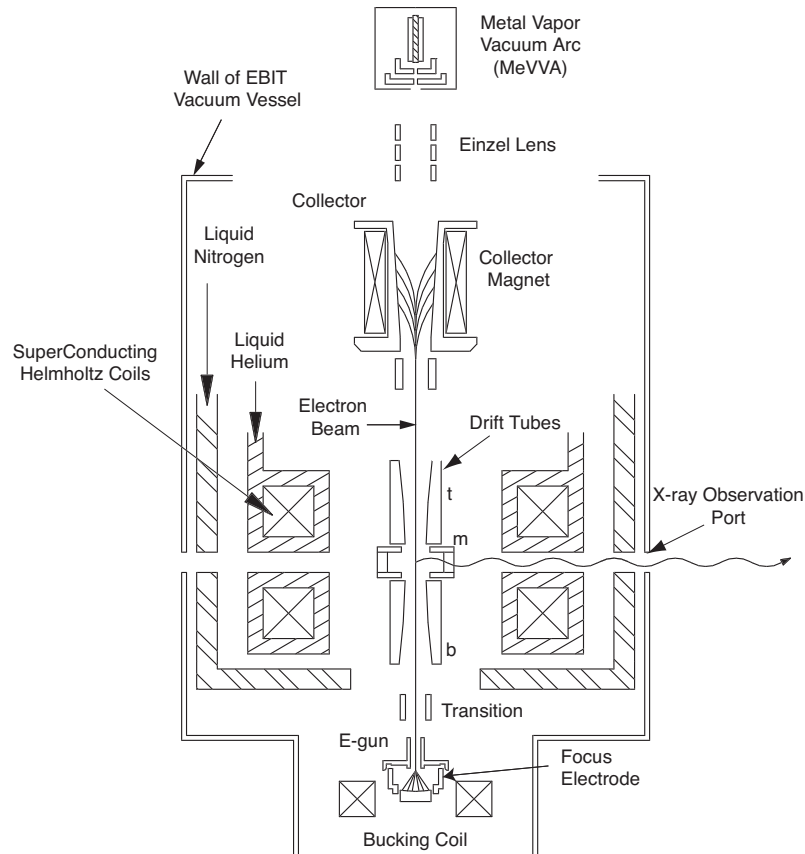


**Figure 4.1:** Sketch of an Electron Beam Ion Trap setup. Courtesy of G. V. Brown.

from the Helmholtz coils. Additionally, the gun chamber is under ultra high vacuum at room temperature to save the emitted electrons from scattering with neutral gas.

While the space charge potential of the electron beam confines the ions radially, the drift tube assembly can be used as an axial trap (Fig. 4.2). The space charge potential can be estimated as

$$V \approx 0.5(1 - f)I/\sqrt{E} \text{ (keV)} \quad (4.1)$$

with beam current,  $I$ , beam energy,  $E$ , and the fraction,  $f$ , of the space charge neutralized by the opposite charge of the ions (Beiersdorfer, 1997). The drift tube potentials are set separately for every drift tube, top, middle and bottom, in the way that the top and bottom electrodes are on a positive potential compared to the middle drift tube, creating a potential well for the ions (Fig. 4.2). The depth of this well as it is experienced by the ions, however, also depends on the charge state of the ions. Low-charge ions will see a shallower trap than highly charged ions and, therefore, will be able to escape the trap at a much lower temperature than higher ionization states. It can be shown that ion-ion collision is much more frequent than ion-electron collision (Spitzer, 1962). Consequently, elastic collisions between the ions heat the plasma. Because of conservation of momentum, heavier ions (higher nuclear charge) tend to kick lighter material out of the trap.

Once the electron beam has passed the trap, i.e., the drift tubes, it is no longer needed and can be disposed of. To avoid dumping a highly focused high energy electron beam directly onto the collector electrodes and, therefore, to extend the lifetime of the hardware, another set of magnets, the collector magnet, is installed. Its magnetic field defocuses the beam by increasing its cross section by a factor of 900. The collector electrodes are made of copper and are operated at a relatively low voltage to minimize the deposited energy.

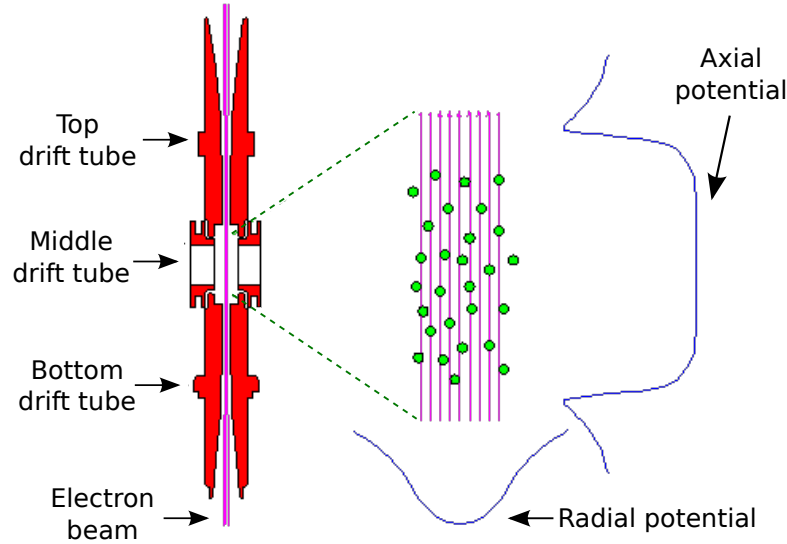


**Figure 4.2:** Drift tube setup and trapping potentials of EBIT (<https://ebit.llnl.gov/>).

They are cooled to 77 K with liquid nitrogen to suppress outgassing from ions burned out of the electrodes by the electron beam, which could pollute the plasma in the trap region. The distance between electron gun and collector is about 50 cm, the length of the ion trap about 2 cm. To avoid charge exchange reactions with neutral gas in the trap, the whole apparatus is contained in a vacuum vessel with ultra high vacuum ( $\sim 10^{-10}$  torr). To be able to directly observe the radiation coming from the ion cloud in the trap region, there are six ports in the middle drift tube. One of them is used for gas injection, the others have a set of various spectrometers installed, among them the EBIT calorimeter spectrometer (ECS). The ECS is a powerful tool as its real-time readout and display over a wide energy range provides instantaneous feedback about the charge balance and the processes in the trap.

The trap is filled by injecting neutral to mildly ionized gas directly into the trap region where it is ionized gradually by repeated collisions with the beam electrons. Gas can be injected directly through one of the ports with a gas injection system or a sublimator, depending on the properties of the source. In case of metals for which no donor molecules can be found that already build a gas or sublime, a Metal Vapor Vacuum Arc (MeVVA Brown et al., 1986) can be installed above the collector. In a MeVVA low charge metal ions are knocked out of an easily exchangeable metal wire cathode by an arc. The ions produced this way are led into the trap through the collector assembly and the top drift tube. This form of ion injection is not very efficient since not too many ions are produced that way and only a small fraction of them can be caught by the beam to make it all the way into the trap.

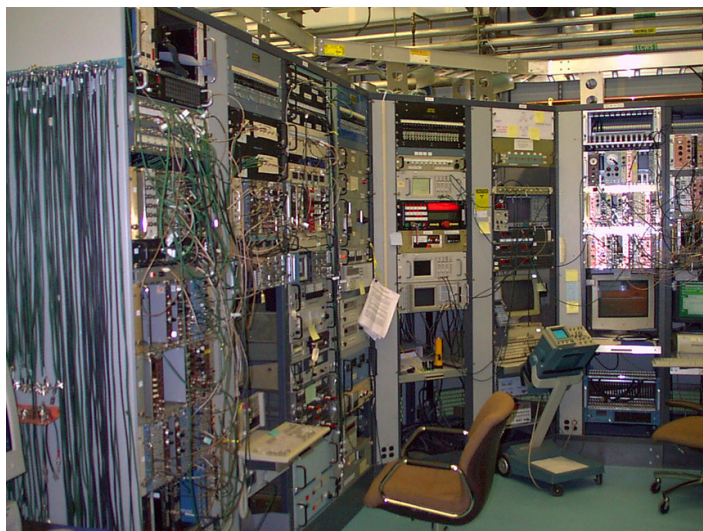
To overcome the ionization energy, beam currents of tens to hundreds mA are required. The beam energy is determined by the potential of the middle drift tube. It has a small energy spread of 20–50 eV and hence can be considered mono-energetic. Once the ions are created and excited, the emission of their spectra can begin. The emission rate in X-rays can be described by (Marrs, 2008)

$$Y_X = j_e \sigma N_i \quad (4.2)$$

where  $j_e$  is the current density of the beam,  $\sigma$  the X-ray production cross section, and  $N_i$  the abundance of the ions in the beam. The whole purpose behind all the focusing

**Figure 4.3:**

Artists conception of an EBIT  
(<https://ebit.llnl.gov/>)

**Figure 4.4:** The EBIT control room

(<https://ebit.llnl.gov/EBITPhotoGallery.html>)

and compressing of the beam described earlier is because of this proportionality of the X-ray emission rate to the beam current density. The e-beam current density of EBIT-I is usually around  $4000 \text{ A cm}^{-2}$ . Since the radius of the electron beam is only about  $30 \mu\text{m}$ , the ions in the trap are practically stationary, thus, no Doppler shifts occur and the rest wavelength of the transitions can easily be measured. With some effort in cooling of the plasma, thermal broadening of spectral lines can be brought to a minimum. Thus, so far, the resolution of the spectra is only limited by the resolution of the used spectrometers. This setup is a huge advantage over ion accelerators where usually high velocities of the ions have to be taken into account.

After the first EBIT (now called EBIT-I), more such devices were built. EBIT-II a copy of EBIT-I, which now resides at the Lawrence Berkeley National Laboratory, was installed, while in 1991/92 EBIT-I's gun and collector were exchanged for ones that could be biased negatively. Biasing the emitter of the electron gun negatively compared to its surroundings introduces an electric field at the emitter surface. This electric field reduces the potential barrier seen by the electron from the work function  $W$  to  $W - \Delta W$  (Schottky effect), i. e. the emission current is increased. With the new high energy assembly SuperEBIT, electron beam energies of over 200 keV could be reached. SuperEBIT provides enough power to produce bare uranium, that is 92 times ionized uranium.

Meanwhile, EBITs were built all around the world. The operating principle is the same for all of them, only the detailed specifications mentioned above are properties especially of EBIT-I. Two EBITs were assembled in Oxford, England, with only few changes to the design of EBIT-II. One of them made its way to the National Institute for Standards and Technologies (NIST) in Gaithersburg, Maryland. There are also EBITs in Berlin (Max-Planck-Institut für Plasmaphysik, Humboldt-University), at the Max-Planck-Institut für Kernphysik in Heidelberg (originally built at the Albert-Ludwig-University Freiburg), in Dresden (commercial mass production), Stockholm, Belfast, Vancouver, Shanghai, and Tokyo (Beiersdorfer, 2008). The Heidelberg group even built a portable version called the FLASH-EBIT whose purpose it is to be shipped to X-ray laser facilities to be able to do photo-ionization measurements directly in the ion trap (Epp, 2007).

## 4.2 Measurement

Usually, to get a good charge balance towards He- and H-like ionization states, it is recommended to operate with a well focused electron beam and a shallow trap. While for monitoring purposes the highly charged ions are still desired, the focus of interest lies in the intermediate charge states. Since the lower charge states are reached on the way of the production of the higher ones, to shift the charge balance towards lower charge states, the EBIT settings have to be adjusted to produce the highly charged ions less efficiently. This adjustment can be achieved by detuning the beam, deepening the trap potential and flooding the trap with larger amounts of neutral gas.

However, the day-to-day performance of an EBIT changes with parameters that do not lie in the experimentator's hands and some of them even stay unnoticed and unrecorded. Changes in the pollution of the vacuum with various materials, in vacuum pressure, in temperature, gun properties and so on affect the outcome of seemingly the same set of parameters. Once a parameter set is found that serves the investigator's purposes well, this set will in principle still give a good starting point for optimization later on. Therefore, keeping the above mentioned principles of EBIT operation in mind, trial and error will lead to the desired charge state and count rate.

Accordingly, for the Si measurement EBIT was operated with an electron beam energy of 8.16 keV at a beam current of 100.3 mA and a trap potential of 0.05 kV. The gas was continuously injected with a pressure of roughly  $1.4 \cdot 10^{-6}$  torr. Every 364 ms the trap was emptied to start the ionization process over. Figure 4.5 shows how the charge states in the trap slowly increase with the EBIT phase. A 0.5 mil thick beryllium window between the spectrometer and EBIT serves as a low energy cut-off for L-shell lines that originate mainly from background through atmospheric gases like nitrogen and oxygen. Through this filter the measured count rate is reduced in energy regions outside of our interest but is hardly affected in the Si and S  $K\alpha$  regions (compare Fig. 4.6). Since then it is less likely for two photons to hit the same pixel so shortly after each other that their pulses overlap, the resolution and hence the quality of the measured events increases.

In case of the sulfur, the EBIT conditions were at an electron beam energy of 7.1 keV and beam current of 70 mA with a trap potential of 0.1 kV. The  $SF_6$  was injected with a

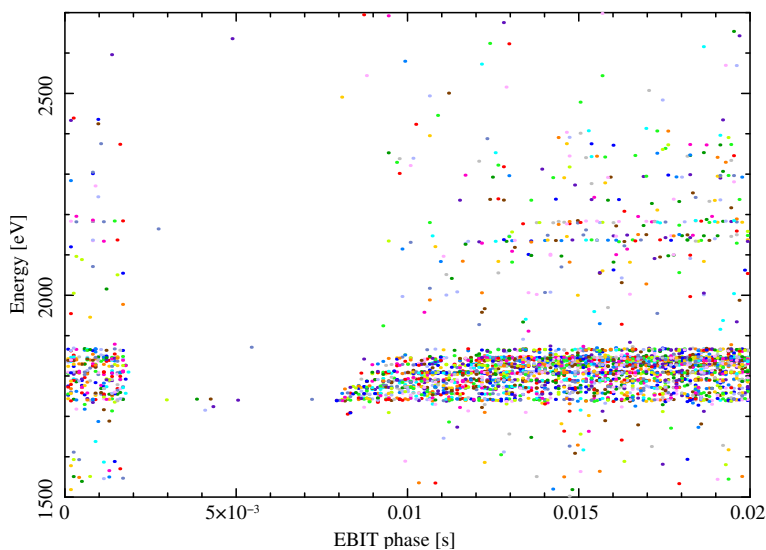


**Figure 4.5:** Evolution of the charge balance of the measured Si with EBIT phase. Different colors indicate different pixels. The measured events accumulate to horizontal lines where spectral lines are expected, i.e. projecting all events to the y-axis will result in the measured spectrum. The lower block is the  $K\alpha$  forest, weaker lines at higher energies come from K- and Ly-lines through decay from  $n \geq 3$  shells. The edge around phase  $2 \cdot 10^{-3}$  s indicates the dumping of the trap.

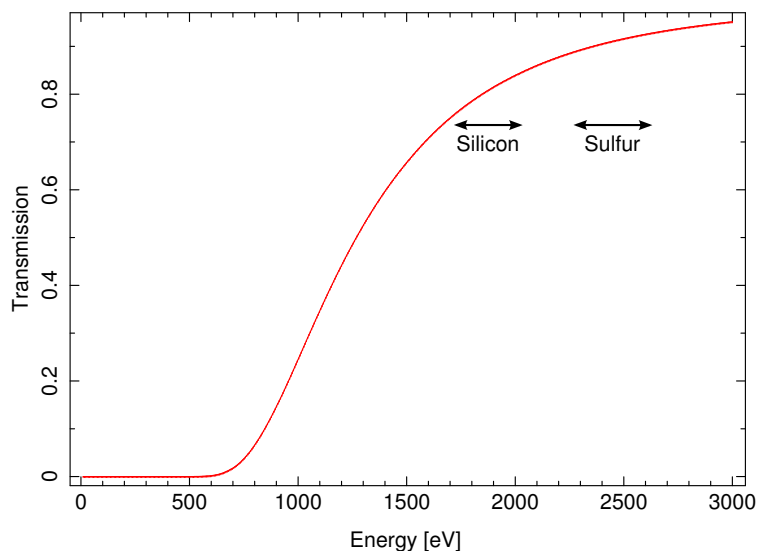


**Figure 4.6:** Transmission of a 0.5 mil Be window (table downloaded from the X-ray database of the Center for X-ray optics [CXRO, [http://henke.lbl.gov/optical\\_constants/](http://henke.lbl.gov/optical_constants/)]). The black arrows indicate the energy region of the Si and S  $K\alpha$  lines where the Be window is basically transparent.

pressure of roughly. An EBIT cycle lasted 245 ms. The  $K\alpha$  spectra produced with these EBIT parameters were then measured using the EBIT Calorimeter Spectrometer (ECS).

### 4.3 EBIT Calorimeter Spectrometer

The ECS is a microcalorimeter assembled by the X-ray calorimeter group around R. Kelley and C. Kilbourne at the Goddard Space Flight Center/NASA (Porter et al., 2008a,b, 2009a,b). It is the successor of the copy of the XRS on-board *Astro-E*<sup>1</sup>, which was built out of spare parts, then shipped to EBIT-I/LLNL and later on upgraded to the standards of the replacement mission *Suzaku*<sup>2</sup> (Porter et al., 2004). Had the *Suzaku* XRS not failed after only three weeks of operation in space, we now had the luxury of identical instruments in space and in the laboratory.

A calorimeter is a broad band photon detector capable of measuring the energy of the incident photon without any further dispersive elements in front of the detector. The main parts of the detector body are an absorber, a thermistor and a heat sink (see Fig. 4.7). When an X-ray photon hits the absorber, an electron of an atom in the absorber material is knocked loose and rattles around in the pixel body, disturbing more and more electrons. This increase in internal motion is equivalent to an increase in temperature of the absorber. The temperature change is measured with a sufficient sensor and then dissipated into the heat sink.

For this principle to work, absorber, sensor and the thermal link to the heat sink have to fulfill a few requirements. The absorber needs to be opaque to X-rays and sufficiently convert the incident energy to a temperature variation. Therefore, the absorber must thermalize very well, i.e., it has to distribute the complete incident energy across a thermal distribution of the absorber body efficiently in a reproducible way. Additionally, its heat

<sup>1</sup>Unfortunately, *Astro-E* was lost to the ocean due to the failure of its launch vehicle to reach orbit on 10 February 2000. Five years and five months later, *Astro-E2* a.k.a. *Suzaku* was launched, built on the basis of the *Astro-E* developments and upgraded to the new standards of technology. The bad luck of calorimeters in space continued when shortly after the launch the complete reservoir of liquid helium boiled off into space, making the XRS unusable. Much effort is put into the success of the calorimeter of the upcoming *NeXT/Astro-H* mission to be launched in 2014.

<sup>2</sup>almost doubled in spectral resolution

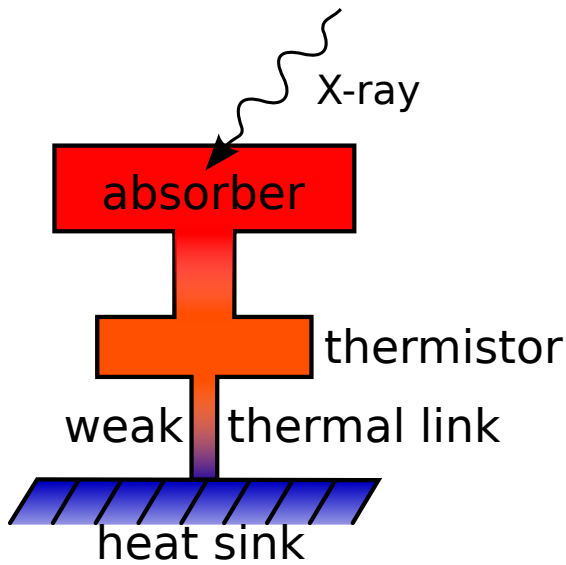


**Figure 4.7:** Sketch of the principle of a calorimeter.



**Figure 4.8:** EBIT Calorimeter Spectrometer (ECS) installed at EBIT-I in Livermore (from <https://ebit.llnl.gov/EBITPhotoGallery.html>).

capacity  $C$  should be low such that already small amounts of deposited energy result in a preferably large temperature change  $\Delta T$  (Stahle et al., 1999)<sup>3</sup>.

The sensor is attached to the absorber via a thermal link weak enough to allow the absorber material to come to equilibrium before the temperature change reaches the thermistor. The thermistor is a resistor whose resistance  $R$  strongly depends on the temperature  $T$  around the working point and hence is very sensitive to any temperature changes. The sensitivity of the thermistor is characterized by the dimensionless quantity

$$\alpha = \frac{T}{R} \frac{dR}{dT}, \quad (4.3)$$

describing the fractional resistance variation versus the temperature variation (Galeazzi et al., 2000). Higher sensitivity to temperature variations, and with it higher output signals, result in higher values of  $\alpha$ .

The change in resistance then can be measured by applying a bias current to the thermistor and monitoring the resulting voltages. In principle, the change in resistance could also be determined via a bias at constant voltage, i.e., monitoring the change in current, but this approach is rather unusual for commonly used solid state thermistors because of their large resistance (Galeazzi et al., 2000).

The temperature sensor is connected to a heat bath via an even weaker thermal link, which is weak enough to allow the energy deposited by the incident photon to thermalize completely before the temperature decreases again due to the lower temperature of the

<sup>3</sup>A more theoretical description of the functionality of calorimeters can be found in, e.g., Galeazzi & McCammon (2003) and McCammon (2005).

heat bath, but strong enough to cool the absorber to its base temperature as soon as the temperature change is recorded. This way the link makes sure that the energy of the incident photon is measured correctly and at the same time keeps the dead-time of the detector small. In other words, the time for the base temperature to be restored in the absorber material should be the slowest time constant in the system. If this time constant is too low, however, high count rates become a problem because of the overlap of the pulses of succeeding events.

The change of temperature in the absorber is proportional to the energy of the incident photon

$$\Delta T \propto \frac{E}{C} \quad (4.4)$$

and is usually in the order of a few milli-Kelvin. To maximize the relative increase in temperature  $\Delta T/T$  and to be able to distinguish the energy deposited by an incident photon from mere thermal noise, the heat bath is cooled down to a temperature in the order of 50 mK, i.e., close to absolute zero. A hypothetical instantaneous deposition of an energy  $E$  by an X-ray photon then produces a voltage pulse with exponential decay time constant  $\tau = C/G$  where  $G$  is the thermal conductivity of the thermal link. The voltage across the thermistor can be recorded continuously and analyzed for pulses instantaneously. Recognized pulses which meet certain criteria in shape are identified as events and flagged according to their quality. If telemetry is not an issue, it is possible to display the measured events in real-time, which allows to monitor the conditions in the trap easily.

Although calorimeters are far away from being able to compete with CCD cameras in terms of pixel size and number, they have the huge advantage that they cover a broad energy range with almost the same (high) resolving power over the whole region. Their quantum efficiency is limited below 1 keV due to the infra-red blocking filters that are supposed to shield the detector from thermal energy. Above 10 keV the absorption cross section of the absorbing material is a limiting factor (Porter et al., 2005). The latter can at least somewhat be overcome by employing a second set of thicker pixels, which cover a wider energy range although with generally less resolving power. For instance, the ECS consists of 18 midband pixels covering an energy range from 0.1 to 10 keV and 14 high-energy pixels for 0.5 to 100 keV. While a midband pixel comprises  $625 \times 625 \mu\text{m}^2$  of  $8 \mu\text{m}$  thick HgTe absorber material, a high-energy pixel is with  $625 \times 500 \mu\text{m}^2$  slightly smaller but with  $100 \mu\text{m}$  a lot thicker. The quantum efficiency of the midband array is thus 95 % at 6 keV corresponding to roughly 4.5 eV FWHM, of the high energy array it is 32 % at 60 keV, i.e., 32 eV FWHM.

The ECS operates at a temperature of 50 mK. To achieve and maintain this low temperature, a set of refrigerators and shields is installed. The detector housing contains infra-red absorbing materials. A liquid nitrogen ( $T = 77 \text{ K}$ ) shielded liquid helium ( $T = 4.2 \text{ K}$ ) dewar at atmospheric pressure separates the internal parts of the detector from the outside world at room temperature. Pumped helium can become even colder than its atmospheric 4.2 K. This cooling to 350 mK is done by a Chase Cryogenics<sup>4</sup> closed cycle  $^3\text{He}/^4\text{He}$  refrigerator. The rest of the way down to the operating temperature of 50 mK is undertaken by an Adiabatic Demagnetization Refrigerator (ADR). ADRs use certain types of salts composed of molecules that have high magnetic moments (Lounasmaa, 1974). These magnetic moments are usually de-aligned due to the random thermal motion of the molecules. If a strong external magnetic field is applied to the salt, the magnetic moments of its molecules align themselves with the magnetic field such that the magnetic energy of each molecule

<sup>4</sup>Chase Research Cryogenics Ltd., Uplands, 140 Manchester Road, Sheffield S10 5DL, UK.

is minimal. The surplus energy being released during this process can be dumped to the pre-cooler. With the slow reduction of the external magnetic field, the molecules slowly de-align themselves again. Because of the lack of any heat source (the thermal link to the pre-cooler is disconnected) the demagnetization happens adiabatically, effectively cooling the salt. Once the salt is at the desired temperature of the heat bath, it is thermally linked to the detector pixels. Now the demagnetization instead consumes the heat deposited by the incident photons. The reduction speed of the external magnetic field can be controlled in such a way that the salt, i.e., the heat bath, stays at a constant temperature. After a while the magnetic moments of the salt are de-aligned to such an extent that the cooling power of the ADR runs out. The whole cycle has to be restarted. In case of the ECS, this happens after about 65 hours.

The next generation of microcalorimeters will use superconducting transition edge sensors (TES), i.e., sensors that are very close to a phase transition and therefore extremely sensitive to temperature variations; even more than the so far commonly used thermistors. Such a next generation calorimeter built on the basis of significant improvements to the calorimeter technology developed for proposed X-ray satellite missions like *Constellation-X/IXO* will arrive at LLNL in the near future. It will constitute the fourth generation of microcalorimeters employed at this institute and more than double the spectral resolution to 2 eV at 6 keV (Porter et al., 2009b).

## 4.4 Calibration

With the XRS GSE extension written for IgorPro<sup>5</sup>, the incoming photons in the detector are read out simultaneously and event files are produced in which every single detected photon is stored together with the pixel it hit, a time stamp, the pulse height and the voltage measured at the thermistor. The change in temperature of the absorber caused by the incident photon, ideally is proportional to the energy carried by said photon. The underlying ground temperature of the absorber, and therefore the thermistor, however, strongly depends on external influences like the time in the duty cycle and energy deposited into the system by electronic and thermal noise. Consequently, as the detector is constructed to be sensitive to small changes in temperature, already small differences in the base temperature of the detector lead to some instability in the calibration of the measured voltage scale back to photon energy. The difference is not large enough to shift line positions over several volts. For instance, for the ECS the Si L-shell lines will always be found around 4 V (see Fig. 4.9). Still the drift is large enough to affect the resolution on short time scales like hours and shift the whole spectrum by a couple eV over longer time periods. Accordingly, for high precision, high resolution measurements of line energies, the calorimeter should be calibrated at least once per run, ideally even more to be able to account for drifts.

Additionally, the inconsistencies unavoidable in the geometry of the pixels cause differences in their response. Hence, each pixel has to be calibrated separately. In case of the ECS with only 16 pixels, this still could easily be done by hand. The next generation of microcalorimeters, however, will be equipped with a number of pixels in the order of a thousand. Luckily, the calibration can be automated to some extent by numerical means. To simplify the task of calibrating, Ming Feng Gu wrote a set of ISIS/S-Lang (Houck & Denicola, 2000) functions (the CXRS package) commonly used for the calibration of the

---

<sup>5</sup><http://wavemetrics.com/>

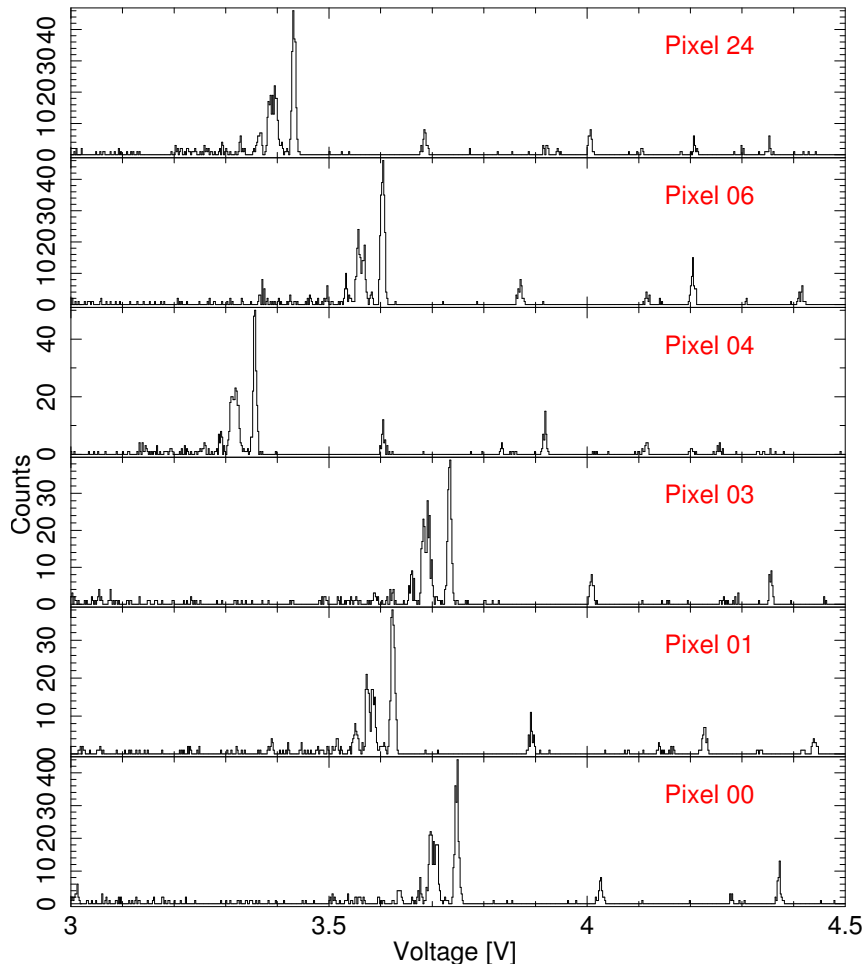


**Figure 4.9:** Example histograms of how the spectra of different pixels look in voltage space. The visible lines are the Si calibration spectrum.

two microcalorimeters, XRS and ECS, by the Livermore EBIT group. Assuming that the spectrum of X-rays coming from EBIT should look about the same in every pixel, Gu's algorithms use cross correlation to shift and stretch the scale of each pixel according to one reference pixel so that in the end they all look the same (see Fig. 4.10). The coefficients for the scaling functions are stored in text files for each pixel. The resulting spectra are plotted and can be checked for their accuracy by eye. Smaller features which do not match between different pixels can be noted and ignored when choosing calibration lines. After the re-scaling of the voltage space, all the pixels are added. In the added spectrum, several spectral lines can be chosen and are then fitted with a Gaussian line profile. The line centers of these calibration lines are then determined for each individual pixel via the inverted scaling function with the stored parameters. Finally, for each pixel the values of the line centers in voltage space are paired up with the value of their well-known rest energy and a 4<sup>th</sup> order polynomial is fitted to these pairs. This polynomial describes the relation between the voltage measured in the detector and the actual energy of an incident photon. Since ideally with no incident photon no extra heat load in the pixel bodies and, therefore, no change in resistance is expected, the constant parameter of the polynomial is frozen to zero during the fit. Consequently, a minimum of four calibration lines is required to determine the polynomial.

The only remaining question now is which lines to choose as calibration marks. In principle any set of spectral lines with well-known rest wavelength can be used. Due to the simplicity of their systems, there are very good theoretical predictions for the wavelength of the He-like K- and the H-like Lyman-series which also could be confirmed by experiments (see,

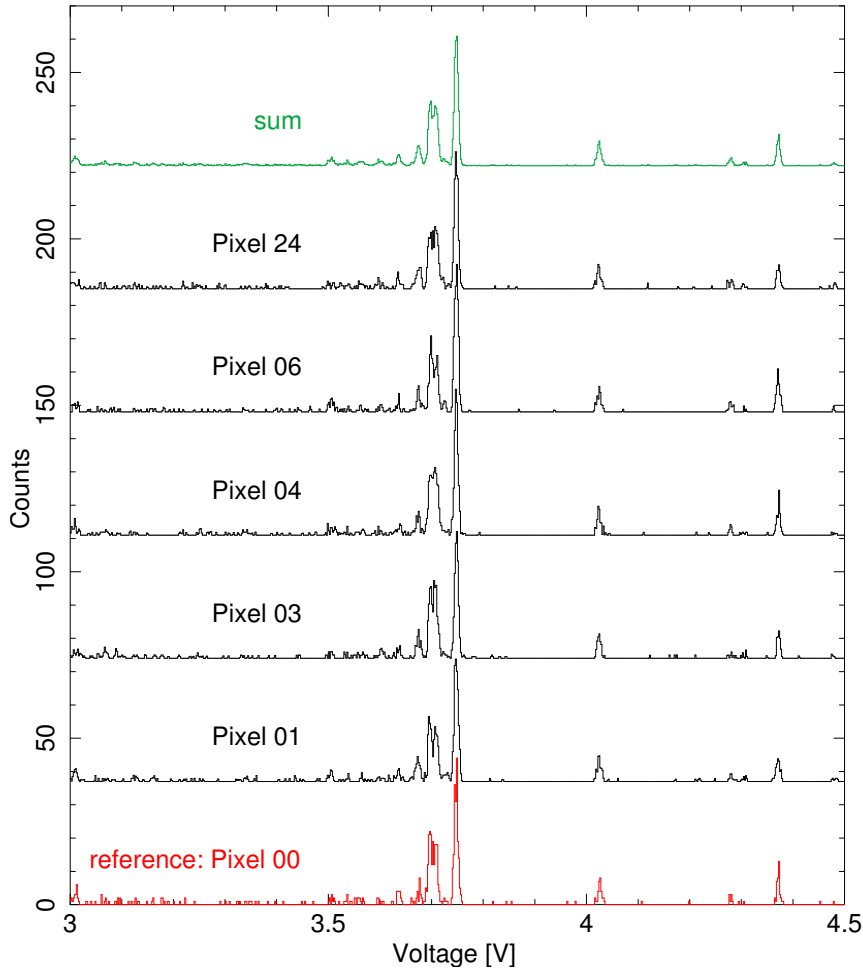


**Figure 4.10:** Spectra of the pixels shown in Fig. 4.9 aligned to a reference pixel (red) and added for energy calibration (green).

e.g., Garcia & Mack (1965) and Johnson & Soff (1985) for Ly and Drake (1988) and Vainshtein & Safronova (1985) with a review of Beiersdorfer et al. (1989) for K). With a device like EBIT, it is not hard to produce clean spectra with a good charge balance, showing He- and H-like lines. Therefore, these lines are perfect candidates for calibration. Ideally, one should fit the correct description of the relation between photon energy and measured voltage to the calibration lines. Unfortunately, this function is way too complex and not fully understood yet for this approach to be practical. At least we know that this function is quite well behaved. Over wide energy ranges it is close enough to being linear that a low order polynomial is a sufficient description, especially since most of the time the energy region in focus is limited to a few hundred eV. To get an energy scale as accurate as possible it is nevertheless recommended to find lines which frame the region of interest. Another aspect of this consideration, however, is the availability of material that can be injected into EBIT.

For the measurement of the transitions in the lower charge states of silicon, we therefore chose to calibrate with the Lyman series in He- and H-like neon at around 1 keV and silicon itself at around 2 keV. Si was injected with the gas injector as Decamethyltetrasiloxane<sup>6</sup>. In particular, the used Si lines were  $K\alpha$ – $K\gamma$  and  $Ly\alpha$ .  $Ly\beta$  blends with  $K\epsilon$  and was therefore neglected. In Ne these two lines are well separated, allowing for  $Ly\beta$  to also be included for calibration.

<sup>6</sup>which is an irritant for eyes, skin and the respiratory system but not as toxic and extremely flammable as silane. Since it is used in make-up production, it is only available in huge quantities, or as a small, free sample, which is still large enough to serve us for years.

To produce sulfur ions, sulfur hexafluoride ( $\text{SF}_6$ ) was injected. This gas has the advantage that it already comes with an additional element for calibration. Here, too, we chose the Lyman series of He- and H-like sulfur at 2.6 keV and fluorine at 800 eV, respectively. In order to still produce enough H- and He-like fluorine for calibration purposes, the EBIT parameters have to be chosen in a way that more or less ruins the charge balance in sulfur. This way a means is provided to monitor the energy scale while at the same time the desired lower charge states of sulfur are produced. The calibration was done with S  $\text{K}\alpha$ - $\text{K}\gamma$  and F  $\text{K}\alpha$ - $\text{K}\gamma$  and Ly  $\alpha$  and Ly  $\beta$ . S Ly  $\alpha$  was discarded since it was not fitted very well, S Ly  $\beta$  was not visible in the spectrum.

The reference wavelength used for calibration were taken from Drake (1988) in case of the  $\text{K}\alpha$  transitions (line w). Vainshtein & Safronova (1985) provide values for the K series up to  $\text{K}\delta$  but as discussed in Beiersdorfer et al. (1989) their results deviate noticeably from measurements with the deviation increasing strongly with increasing  $Z$ . However, while this issue mainly affects the  $\text{K}\alpha$  transitions, transitions from higher levels show much better agreement with experimental data. Therefore,  $\text{K}\beta$  and  $\text{K}\gamma$  are taken from Vainshtein & Safronova (1985) but are corrected for the ground state of Drake (1988). Values for the Lyman series originate from Garcia & Mack (1965). It is common practice to list line tables in units of Kayser =  $\text{cm}^{-1}$ . The conversion factor used in this work is  $1 \text{ eV} = 1.23984186 \cdot 10^{-4} \text{ cm}^{-1}$ .

Figures 4.11 and 4.12 show the Si and S spectra resulting from the combination of the used ECS pixels. After calibration the ECS events are binned to an energy grid with a bin width of 0.5 eV. Since the charge states can easily be distinguished in a  $\text{K}\alpha$  spectrum (section 3.8), the single peaks are already labeled with their corresponding ions.

## 4.5 Quality of the Calibration

The accuracy of the calibration strongly influences the quality of the results mainly in two ways. First of all, if the calibration is off differently for different pixels, there will be artificial broadening of the lines, unnecessarily reducing the resolution. If the shift is about the same for all pixels, they will align well enough but the energy of their line centers will be wrong. The impact depends on the purpose of the experiment. The energy calibration has to be as good as possible for determination of transition energies to get them with small uncertainties. For measurements of other properties like, e.g., the life time of a transition out of the shape of the natural line width, the exact line energy is of no concern as long as the resolution fits. Still, the better the calibration per pixel the better the overlap of the spectra of different pixels.

Since for each calibration the number of reference lines was higher than the number of free fit parameters, the resulting calibrated spectra are not expected to exactly match the reference wavelengths. However, the accuracy of the spectra can be quantized and any determined deviation stated as a systematic uncertainty. For this purpose, some of the calibration lines are fitted again in the calibrated spectra and the resulting line centers are directly compared to the input rest energy. As the relation between detector voltage and photon energy the shift of the spectrum is assumed to be energy dependent. For this reason, in the following only the He-like line w and the Ly  $\alpha$  lines of silicon and sulfur, but not of their additional calibration gases are compared to their reference values.

The resolution of the spectra is crucial for the number of spectral lines that can be distinguished. To estimate the resolution, it is assumed that the resolution of the calorimeter does not change over the small energy ranges examined. Therefore, a line which is known

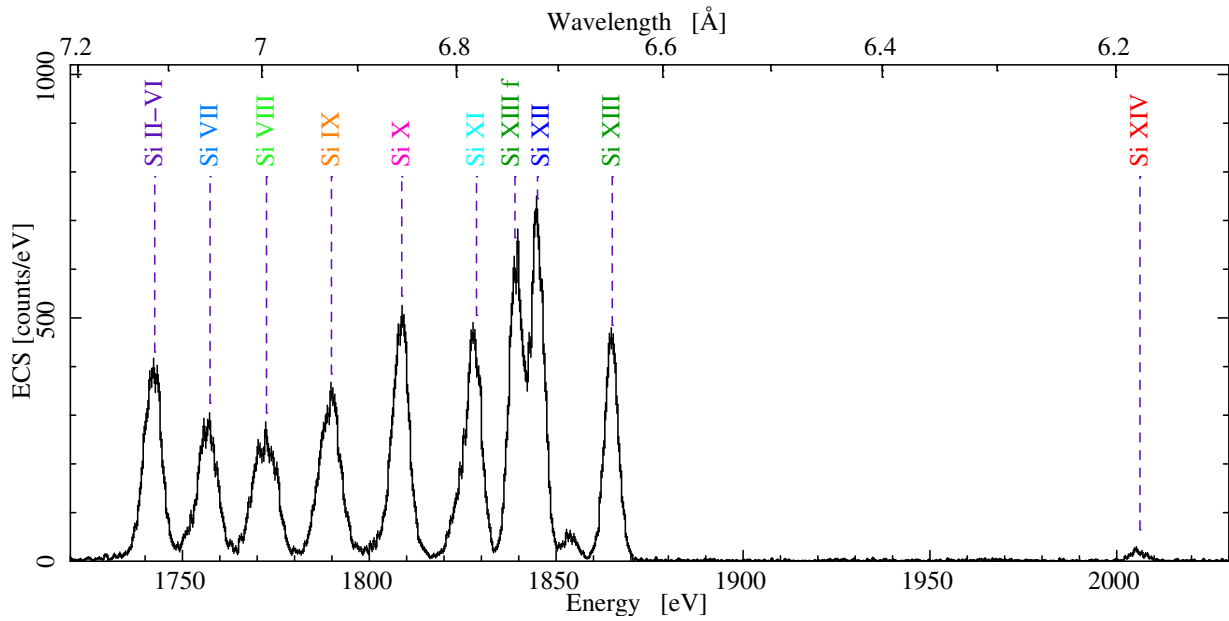


**Figure 4.11:** Final calibrated silicon spectrum added from all 16 used ECS pixels. Each peak can already roughly be assigned to a certain ionization state.

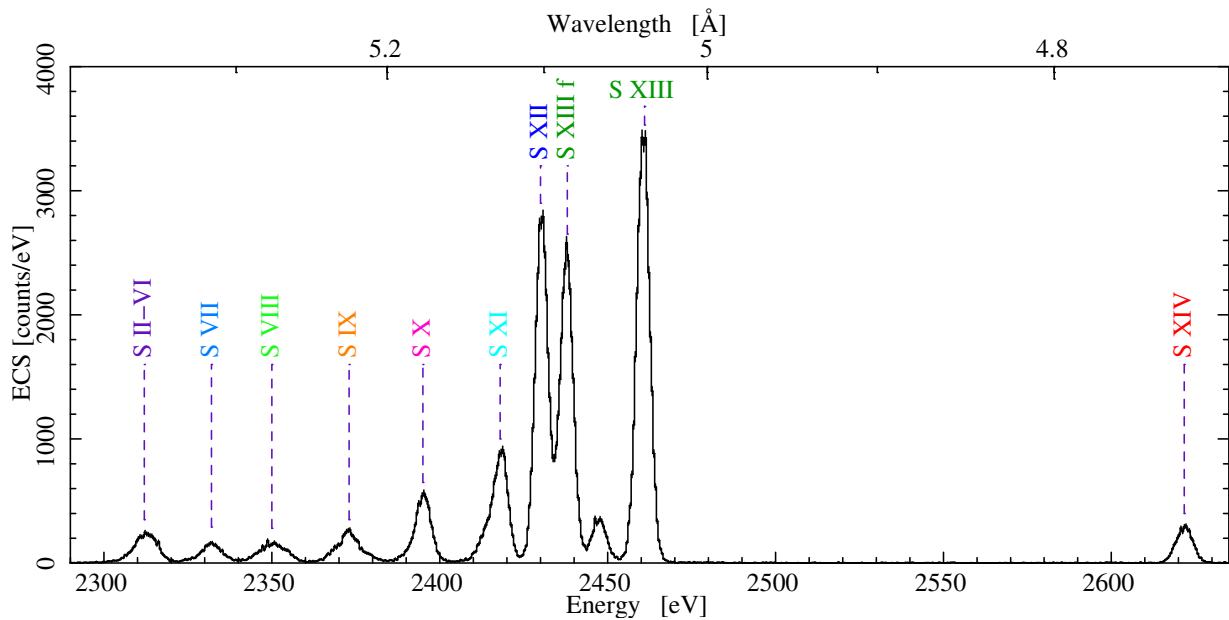


**Figure 4.12:** Final calibrated sulfur spectrum added from all 16 used ECS pixels. Each peak can already roughly be assigned to a certain ionization state.

not to be a blend with another line, i.e., He-like line w, is fitted separately with a Gaussian line. The width (FWHM) of such a line is then limited by the detector resolution as long as we are far away from the natural line width. Consequently, the whole spectrum is fitted with a set of Gaussian lines whose width is frozen to the determined resolution. This approach has the advantage that line blends can be determined more easily as due to the fixed line width it becomes necessary to increase the number of Gaussians instead of artificially broadening the line in order to find the best fit.

### 4.5.1 The He-like Lines

With only two electrons the He-like ions still build very simple systems with only few possibilities to distribute the two electrons over the first and second shell. Since we are interested in  $K\alpha$  transitions, at least one of the electrons has to be in the  $1s$  shell. Consequently, there are only six singly excited energy levels, namely  $(1s_{1/2}2s_{1/2})_{J=1}$ ,  $(1s_{1/2}2p_{1/2})_0$ ,  $(1s_{1/2}2p_{1/2})_1$ ,  $(1s_{1/2}2p_{3/2})_2$ ,  $(1s_{1/2}2s_{1/2})_0$  and  $(1s_{1/2}2p_{3/2})_1$  with increasing energy. Two of them are strictly forbidden because they would violate the selection rule  $\Delta J = 0$  only when  $J = 0 \leftrightarrow 0$  for any of the electric and magnetic multipole transitions. We are also only interested in  $K\alpha$  transitions, not transitions inside the  $n = 2$  shell. That leaves us with only four transitions, which hardly blend.

By far the strongest of these lines with the highest radiative transition probability is the electric dipole transition  $1s^2 \rightarrow (1s_{1/2}2p_{3/2})_1$ . In astrophysics, this line is usually referred to as the resonance line r (Dopita & Sutherland, 2003), while in atomic physics the labeling of Gabriel (1972) for Li- and He-like  $K\alpha$  transitions is more established. Thus the same line is often referred to as line w. The electric quadrupole transitions  $1s^2 \rightarrow (1s_{1/2}2p_{3/2})_2$  (line x) and  $1s^2 \rightarrow (1s_{1/2}2p_{1/2})_1$  (line y) are transitions between states of different multiplicities ( $^1S - ^3P$ ) and therefore called intercombination lines, in astrophysics denoted with an i. While they lie very close to each other, they are well distinguishable from line w. The

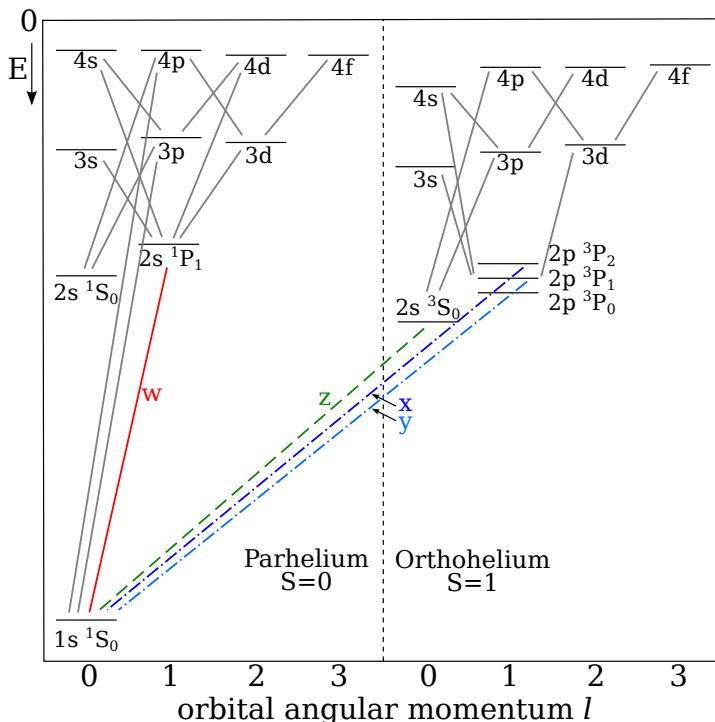


**Figure 4.13:** Grotrian (1928) diagram of helium, also indicating the notation of Gabriel (1972) for some  $K\alpha$  transitions.

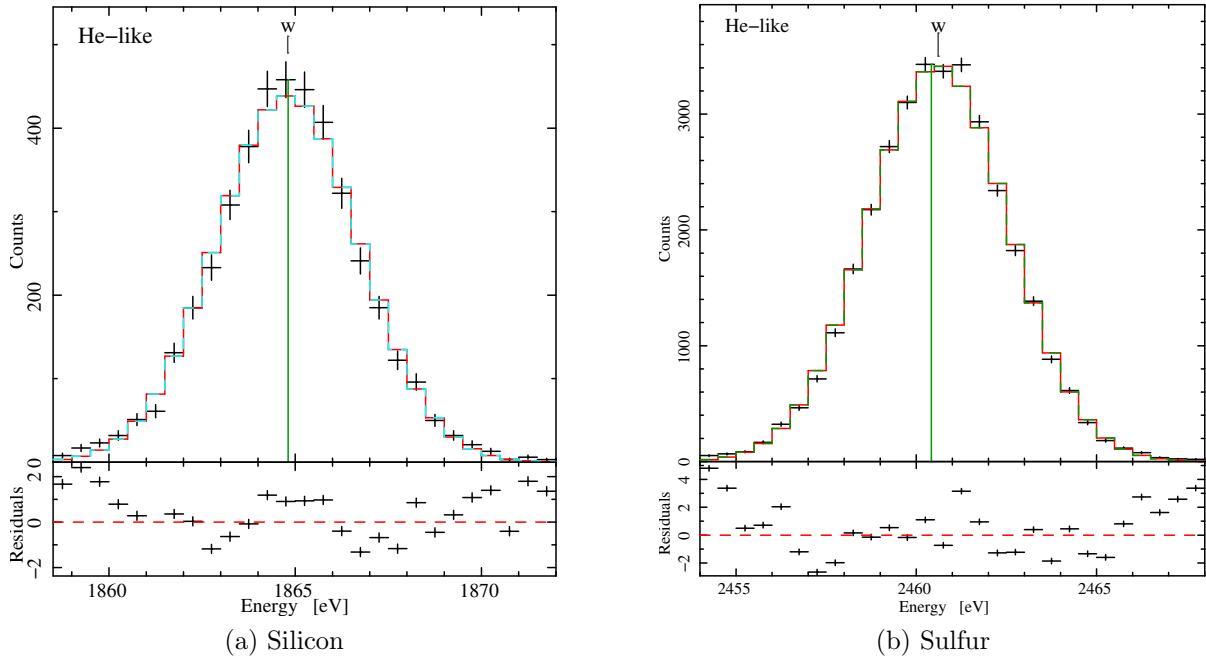


**Figure 4.14:** Gaussian fit of the He-like line w for (a) Si and (b) S. The vertical green line is the theoretical line center according to the FAC calculation.

**Table 4.1:** Comparison between the measured line center of the He-like line w with the theoretical value of Drake (1988), which was used for calibration, for Si and S. The width of the line (used as detector resolution throughout the fits) is listed as well.

$Z$	FWHM (eV)	line energy (eV)			$\Delta E_{\text{Drake}}$	$\Delta E_{\text{FAC}}$
		measured	Drake (1988)	FAC		
Silicon	$4.54 \pm 0.10$	$1864.79 \pm 0.05$	1864.9995	1864.811	-0.21	-0.02
Sulfur	$4.60 \pm 0.04$	$2460.605 \pm 0.018$	2460.6255	2460.417	-0.020	0.188

transition with the lowest energy in this set is  $1s^2 \rightarrow (1s_{1/2}2s_{1/2})_1$ . Because of its magnetic dipole nature, which leads to even lower radiative transition probabilities and can therefore mostly be seen in very thin plasmas where collisional de-excitation only happens on time scales longer than the spontaneous radiative decay of this state, it is called the forbidden line (f) or according to Gabriel (1972) line z. Due to the different sensitivity of these lines to the electron density and temperature, their intensity ratios can be used as a tool for plasma diagnostics (Porquet & Dubau, 2000; Smith et al., 2001).

As the spectral lines of lower ionization states are also found at distinctly lower energies, line w is truly an unblended line and accordingly the perfect candidate to estimate the resolution of the measured spectra. Fig. 4.14 shows a zoom into the fitted region of line w of silicon and sulfur respectively. As can be seen the center of the fitted Gaussian lines (red histogram) agrees quite well with the theoretical prediction of the FAC calculations (green vertical line). Since we do not want to rely on such a qualitative examination, Table 4.1 compares the fitted line centers with the calculations of Drake (1988), which were used for calibration, and FAC, which will be used as a guide for line identification. While FAC and Drake (1988) agree to within 0.2 eV with each other, there is a systematic

shift of 0.21 eV towards lower energies for the silicon spectrum and of 0.020 eV for sulfur between the measurement and the theory. The lower statistical uncertainty of the He-like sulfur line compared to the uncertainty of the silicon line can probably be ascribed to the much higher number of measured counts of sulfur. With a FWHM of 4.54 eV and 4.60 eV respectively, the resolution is well within the expectations for the ECS in this energy region.

### 4.5.2 The Separation of the Lymans

The advantage of fixing the width of the fitted Gaussian lines to the detector resolution can be seen very clearly on the example of Ly  $\alpha_1$  and Ly  $\alpha_2$ . As shown in section 3.3, the fine structure splitting of the subshells in hydrogen like ions is proportional to  $Z^4$ . In H-like silicon the energy difference between the  $2p_{1/2}$  and the  $2p_{3/2}$  subshells is only 1.76 eV. For sulfur with only two additional protons this separation is already 3.00 eV – just around the value where two Gaussian lines with FWHM of 4.6 eV begin to be distinguishable. If the width of the Gaussian line is allowed to vary freely, the fit will result in a line with much greater width of  $5.86 \pm 0.13$  eV at a line center of  $2621.74 \pm 0.07$  eV, which agrees very well with the mean energy of the levels, weighted with their statistical weights, of 2621.703 eV published by Garcia & Mack (1965). With the additional constraint of the known spectral resolution, the Lymans can not only be described perfectly well with two Gaussian components, they even become necessary to obtain a good fit (see table 4.2 and Fig. 4.15 for a comparison of fit and theory).

One could argue that in case of the silicon Ly  $\alpha$  lines the lower signal to noise ratio is to be blamed for the indistinguishability of the lines. Although already the small separation

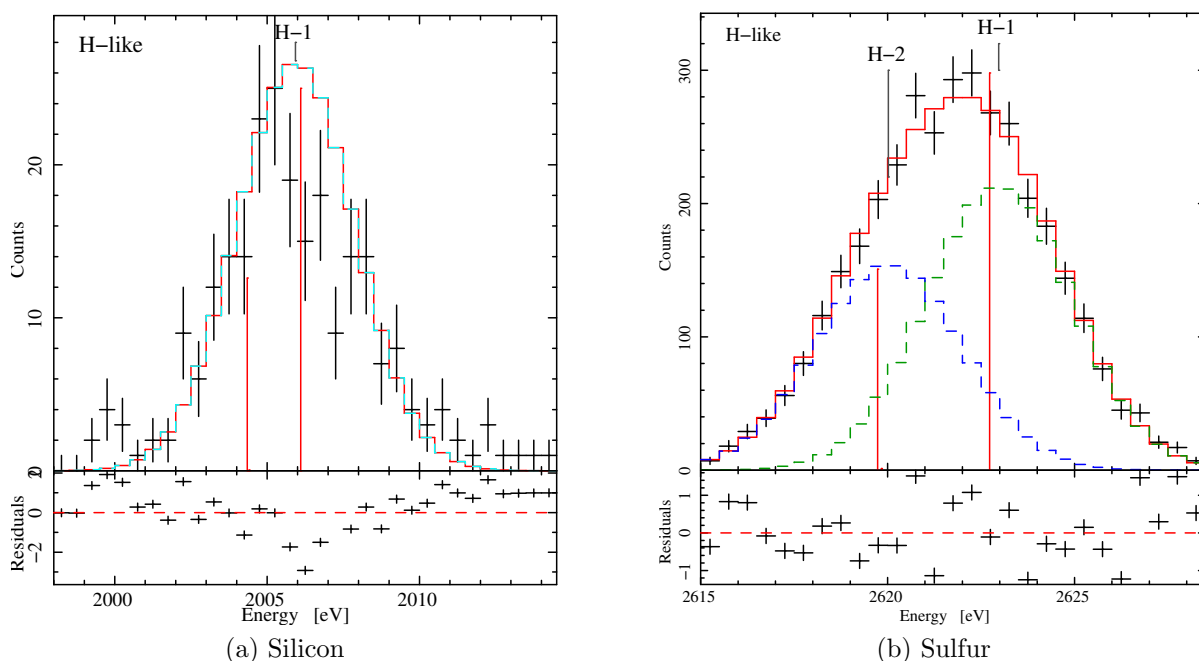


**Figure 4.15:** Fit of the Ly  $\alpha$  lines of (a) Si and (b) S. The histogram with red solid lines shows the model, the dashed histograms are the model components. The solid vertical red lines indicate the theoretical line centers of Ly  $\alpha_1$  and Ly  $\alpha_2$  according to the FAC calculations with line intensities in arbitrary units. As can be seen, in contrast to Si, in S the Lymans can be distinguished.

**Table 4.2:** Comparison between the measured line center (in eV) of the H-like Lyman lines with the theoretical value of Garcia & Mack (1965), which was used for calibration, and the FAC calculation for Si and S.

line	measured	Garcia & Mack (1965)	FAC	$\Delta E_{\text{Garcia}}$	$\Delta E_{\text{FAC}}$
Si Ly $\alpha$	$2005.93^{+0.17}_{-0.24}$	2005.494 <sup>†</sup>	2005.516 <sup>†</sup>	0.44	0.42
S Ly $\alpha_1$	$2622.97^{+0.20}_{-0.22}$	2622.700	2622.730	0.27	0.24
S Ly $\alpha_2$	$2620.02^{+0.25}_{-0.30}$	2619.701	2619.731	0.32	0.29

<sup>†</sup> Mean values calculated by weighing all contributing levels with their statistical weights.

of these lines can be held against this argument, a test of the calibration spectrum, where the statistics of the Ly  $\alpha$  line is much better, with the same approach confirms that with this resolution the usage of two Gaussian lines as a description of this peak can not be justified.

## 4.6 Influence of the Fit Range

While the Ly  $\alpha$  peak is separated by quite a large energy range from the other K $\alpha$  lines, the peaks of the remaining ions are pretty close to each other, covering an energy range of about 150 eV. Of course we could determine the energies of the single lines by rule of thumb but it would actually be nice to get some results with a little more precision.

There are several ways to approach the analysis of this part of the spectrum. One possibility would be to fit every peak separately like the hydrogen-like lines. For this approach the spectrum would be cut into pieces somewhere around the minimum between two peaks. Parts of the regions with extremely low count rates could even be left out since they would not lead to a statistically significant detection of a Gaussian line anyway. The advantage clearly would be to just dispose of these residual stray counts.

However, a small cricket sitting on the researcher's shoulder shouts out a warning that the fit of a Gaussian line is strongly determined by the tails of the line. The tails would be just the part that might get cut off depending on where exactly the cut is applied. Therefore, the influence of the fit region around a peak onto the resulting line centers is shortly examined.

The silicon line dominated by emission from transitions in Be-like Si XI shall serve as an example. It is nicely suited as it has a long, slowly draining out left tail that should emphasize the importance of tails. A model consisting of three Gaussian lines is fitted to this peak with various fit regions. The FWHM is frozen to the detector resolution as discussed before. Table 4.3 shows a comparison between these lines for a subset of the tried out energy ranges. The energy ranges in question are always a multiple of the bin size, i.e. the range is always changed in steps of 0.5 eV.

For an almost ridiculously large energy region of 1815 to 1835 eV, where already small portions of the adjacent peaks are included at the edges of the fit region, the best fit actually moves one of the Gaussian lines ( $1836.8^{+1.6}_{-1.7}$  eV) into the Li-like peak. Shrinking the range at the lower energy range even by as much as 2 eV leaves the resulting line centers basically unchanged; the 10 meV difference lies well within the uncertainties. Since the tail at the higher energy side is steeper, already a smaller change in the upper limit has a large impact. Decreasing the upper end of the fit region by only one or two bins, makes

**Table 4.3:** Comparison of line centers and their corresponding confidence limits for different fit regions around the Be-like Si peak.

fit range	gauss(1)	gauss(2)	gauss(3)
1815–1835 eV	$1836.8_{-1.7}^{+1.6}$	$1828.13_{-0.10}^{+0.07}$	$1823.27_{-0.26}^{+0.18}$
1817–1835 eV	$1836.8 \pm 1.7$	$1828.14_{-0.10}^{+0.07}$	$1823.28_{-0.26}^{+0.18}$
1817–1834 eV	$1828.25_{-0.09}^{+0.12}$	$1823.78_{-0.29}^{+0.54}$	$1818.7_{-1.8}^{+1.7}$
1816–1834 eV	$1828.26_{-0.10}^{+0.08}$	$1823.8_{-0.4}^{+0.3}$	$1818.5_{-1.1}^{+1.0}$
1818–1834 eV	$1831.0_{-1.9}^{+2.0}$	$1827.94_{-0.53}^{+0.16}$	$1823.12_{-0.32}^{+0.23}$
1820–1834 eV	$1831.6_{-1.8}^{+2.6}$	$1828.03_{-0.27}^{+0.14}$	$1823.35_{-0.26}^{+0.26}$
1818–1833 eV	$1828.25_{-0.11}^{+0.12}$	$1823.9_{-0.5}^{+1.1}$	$1820_{-4}^{+5}$

the 1837 eV line unnecessary. Instead a weak line near the lower boundary turns up with correspondingly large uncertainties. Going back towards the original lower limit then only has an effect on this new line as it is better constrained through the additional tail bins. However, if instead more of the lower limit is cut off up to 1818 eV, this third line moves back towards the upper end of the fit region, resulting in an so far unseen line at 1931 eV with high uncertainties. Removing two more electron volts shifts the two strong lines by as much as 0.1 and 0.2 eV but still within their errorbars. At last, the smallest fit region from 1818 to 1833 eV is not able to constrain the third Gaussian line at all.

There are two Gaussian lines which appear at around 1823 and 1828 eV independently of the chosen fit region. These are the two strongest lines in this part of the spectrum. The reason for their passable stability is that they do not directly reach into the tails of the peak but are somewhat shielded by the weaker lines around them. Their line centers still cover a pretty broad energy range, though, that is not even overlapping within the uncertainties of the fit. Apparently, the choice of the used fit range introduces a systematic uncertainty in the order of 1 eV to the measured line centers. And that is only for the strong lines. In case of the weak lines, the systematic uncertainty lies somewhere between non-detection and a couple of electron volts.

Another problem with this approach is that the number of small Gaussians needed to fit the continuum between the lines can be increased artificially. If there is a boarder or even a gap between the peaks, a model component could be needed to account for the continuum from each side of the border while a single component in the middle of the two peaks might be enough if they were fitted together. Therefore, it is advisable to fit the whole spectrum at once.

## 4.7 Line Identification

To avoid the error introduced by a certain choice of fit regions for every peak, the whole  $K\alpha$  forest is fitted at once. Nevertheless, we still want to take care of the minima between the main peaks. This continuum can be seen nicely in a logarithmic plot where the lower count rates are displayed more prominently (Fig. 4.17). A second order polynomial is included to the model to account for that. In order to better constrain the trend of this continuum model component, the fit range around the  $K\alpha$  forest is set amply to include some pure continuum regions. Accordingly, Si is fitted between 1720 and 1880 eV while S is between 2290 and 2480 eV. Gaussian lines are then distributed over the spectrum until

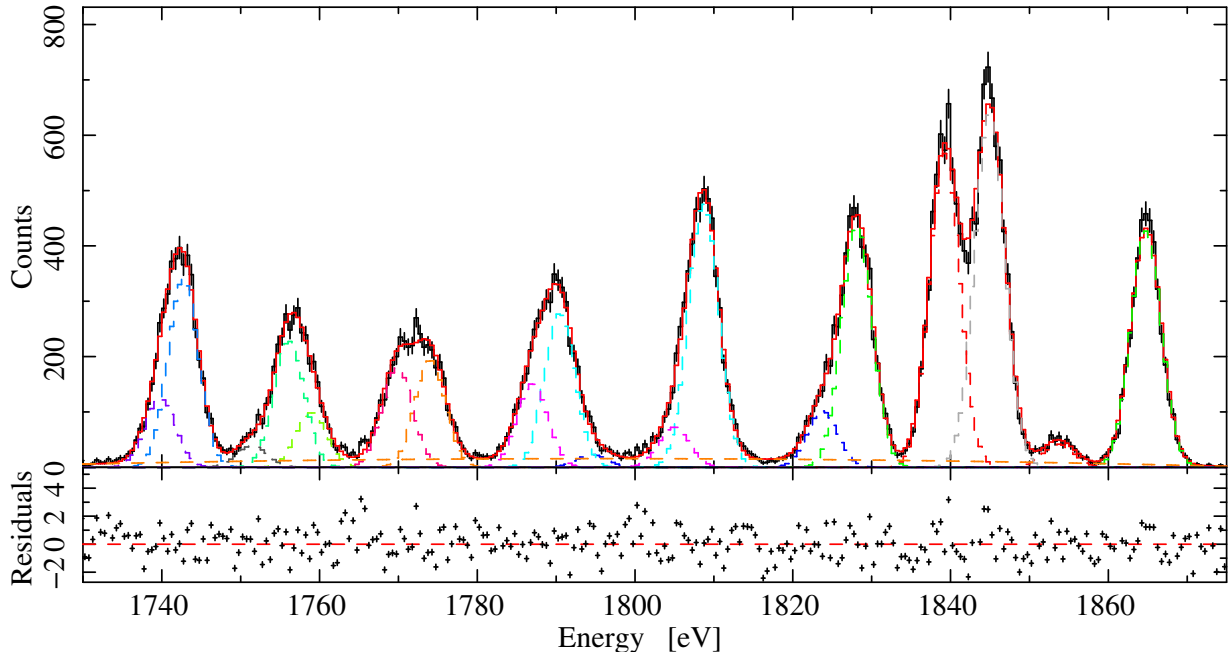


**Figure 4.16:** Overview over the components fitted to the Si spectrum. The data are shown in black, the red solid line shows the total model, model components are shown with dashed lines.

the residuals and the fit statistics look reasonably good. All fits are performed with the Interactive Spectral Interpretation System (ISIS; Houck & Denicola, 2000).

Whether or not the fit really improves with the inclusion of an additional Gaussian line is tested with a Monte Carlo simulation (Müller et al., 2012). The datasets are binned to a histogram for fitting. The fit function is evaluated on the energy grid of the data with its parameters set to the values of the best fit. A set of a thousand fake spectra is generated by filling each bin of the grid with a random number out of a Poisson distribution with mean equal to the value of the model in this bin. Then the fake spectra are fitted with the model out of which they were created (model A) and also with the model containing an additional feature, in this case an additional Gaussian line, (model B). In most cases, the  $\chi^2$  value for model B will at least be slightly better than the ones for model A. That is a normal effect caused by the increased number of available model parameters. Usually this improvement will not be very large. To determine whether the improvement of model B over A is significant, the distribution of the difference  $\Delta\chi_{\text{fake},i}^2 = \chi_{B,i}^2 - \chi_{A,i}^2$  has to be examined. If lots of these  $\Delta\chi_{\text{fake},i}^2$  are in the order of or larger than the  $\Delta\chi_{\text{real}}^2$  of the models fitted to the real data, then the additional model component is just a statistical fluctuation. In contrast, if none of the  $\Delta\chi_{\text{fake},i}^2$  reaches  $\Delta\chi_{\text{real}}^2$  even remotely, the line is probably real and will be included in the model.

The final distribution of the single Gaussian components are shown in Fig. 4.16 for silicon and in Fig. 4.17 for sulfur. The red line is the total model, data are black with randomly colored dashed lines overplotted to indicate the single model components. While the charge states can easily be attributed to the main peaks by counting, assigning which transitions provide the main contribution to the found Gaussian components is a bit trickier. Here, the theoretical predictions come in handy. For the line identification the FAC calculations are chosen over those of Palmeri et al. (2008). The reason is that the measured line strength strongly depends on the conditions in the plasma. A large Einstein A coefficient, i.e., a high probability to decay is not sufficient to produce a strong spectral line if the

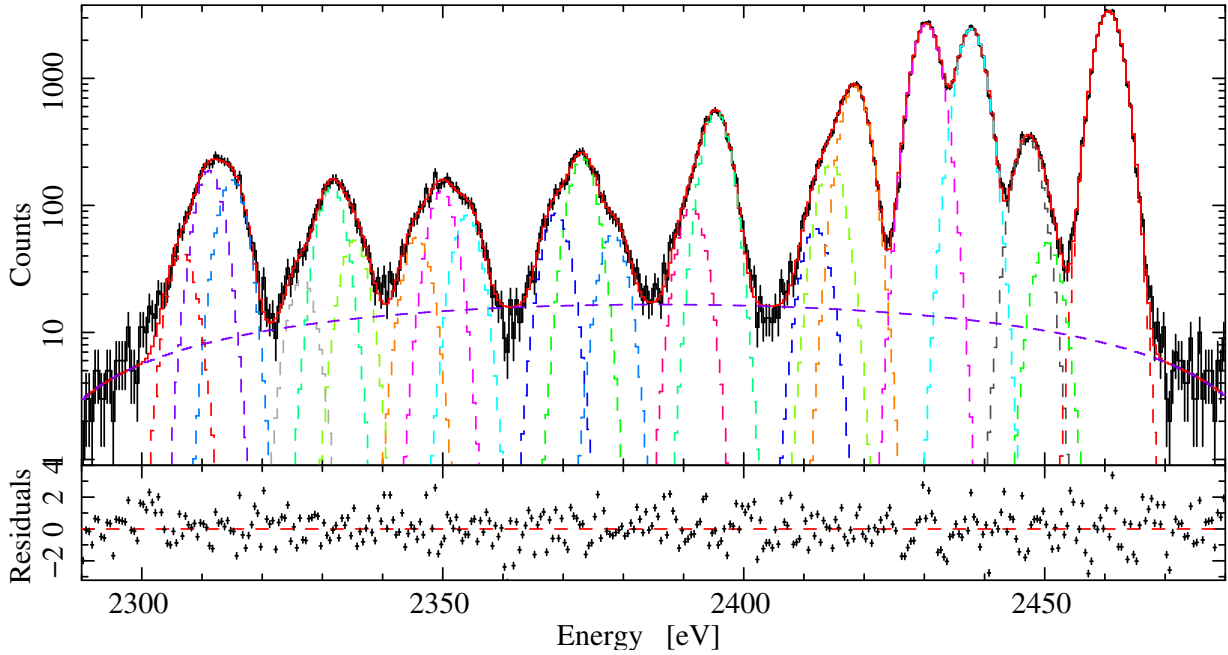


**Figure 4.17:** Overview over the components fitted to the S spectrum. The data are shown in black, the red solid line shows the total model, model components are shown with dashed lines.

corresponding configuration does not get populated, while a strongly populated level may even produce a strong line with a small transition probability. From Palmeri et al. (2008), we have, however, only information about the transition probabilities. The following two sections discuss the results obtained this way for silicon and sulfur.

### 4.7.1 Silicon

For better visualization, figure 4.18 shows magnifications of the fit components cut into regions according to the major peaks indicated in figure 4.11. The fit components are then labeled with the element symbol of the iso-electronic sequence dominating in that region, followed by a number (counting from higher to lower energies). In addition to the model components (dashed histograms, random colors) also the transitions calculated with FAC (sticks, color code as in table 3.2) are displayed. The FAC line strength is in arbitrary units. In each panel, however, the plotted strength of the FAC lines is renormalized such that the strongest FAC line has the same strength as the peak value of the strongest measured line in the same region; the relative line strength of the FAC lines are conserved in each panel but not between the different panels. The single Gaussian fit components are identified with the FAC transitions mainly contributing to their line strength. The results are listed in table 4.4. In each row the FAC lines are followed by the corresponding transitions as calculated by Palmeri et al. (2008).

For most Gaussian lines the distribution of the FAC lines agrees well enough with the measurements to allow a decent estimate of which transitions contribute strongest to the measured features. In case of the F-2 line at 1739.8 eV there are no lines of considerable strength apparent that could be used for identification. Most probably this line is a blend of very lowly charged ions ( $N_{e^-} > 10$ ) which follow shortly after each other beyond the Ne-like lines towards lower energies. These lines, however, are so weak and blend so strongly even between different charge states that a serious identification with only a few lines

would be impossible even if these ionization stages were included in the calculation.

In contrast to most of the lines hardly blending, for both, silicon and sulfur (see next section) the FAC line z (Si: 1838.20 eV, S: 2429.074 eV) has a huge offset compared to the measured line center (Si: 1839.25 eV, S: 2430.366 eV). This deviation of  $> 1$  eV appears in both, the Si and the S spectra. Experience (Beiersdorfer et al., 2009) and simulations with FAC, where line z appears as a strong line only if collisional ionization is taken into account, suggest that the identification of this line with line z is nevertheless correct. The same conclusion is supported by comparing the lines with the reference values of Drake (1988, Si: 1839.448 eV; S: 2430.347 eV). Consequently, the large difference of the FAC lines is due to FAC not being meant to be a high precision tool while Drake (1988) is a standard reference, and is a good example of how far off the FAC calculations can be.

In addition to the identification with the FAC lines, the calculations of Palmeri et al. (2008) are listed. The *LS*-coupling notation of Palmeri et al. (2008) is matched to the energy levels of FAC as described in section 3.12.4. Energies given in parentheses are not listed in the transition tables of Palmeri et al. (2008). These values are obtained by calculating the difference between the corresponding energy levels and shift the result by the average correction Palmeri et al. (2008) applied to the listed transition energies in the same ion.

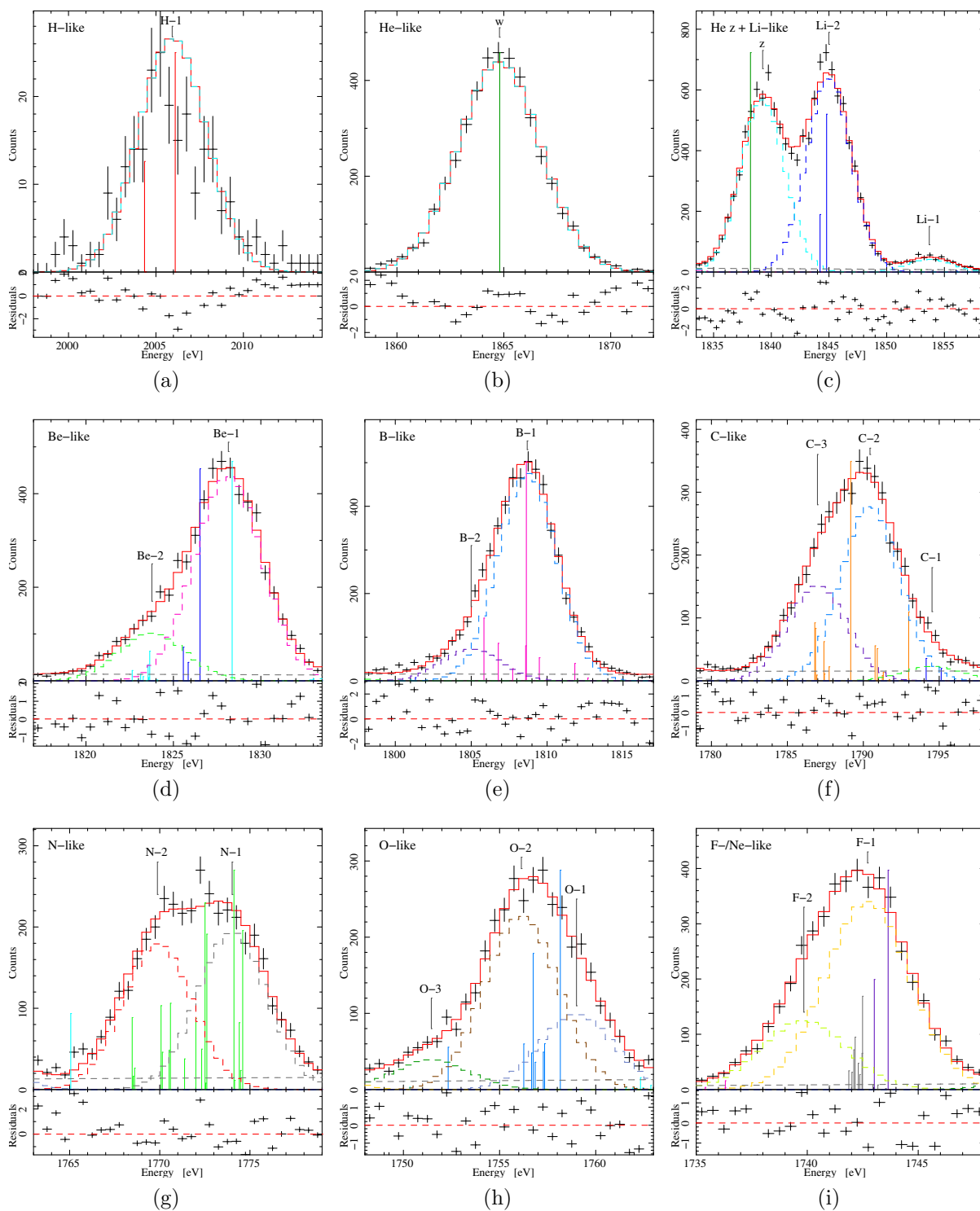


**Figure 4.18:** Fit of the measured Si  $K\alpha$  spectrum. The data are shown in black, the red line shows the model, model components are shown as dashed lines. Vertical lines resemble the theoretical predictions according to FAC.

**Table 4.4:** Identification of the fitted silicon line centers with lines of the FAC simulation. The first column is the key to the line labels in Figure 4.18, the third column indicates the ionization state. For the He-like lines the key of Gabriel (1972) is used. Columns 4–6 show the identification with FAC lines, columns 7–9 the corresponding transitions from Palmeri et al. (2008).

Key	Fit (eV)	Ion	jj-coupling			FAC (eV)	LS-coupling			Palmeri (eV)
			lower level	upper level			lower level	upper level		
H-1	2005.93 <sup>+0.17</sup> <sub>-0.24</sub>	H	1s <sub>1/2</sub>	2p <sub>3/2</sub>		2006.10	1s 2S <sub>1/2</sub>	1p 2P <sub>3/2</sub>	—	
w	1864.80 <sup>+0.06</sup> <sub>-0.05</sub>	H	1s <sub>1/2</sub>	2p <sub>1/2</sub>		2004.35	1s 2S <sub>1/2</sub>	1p 2P <sub>1/2</sub>	—	
Li-1	1853.69 <sup>+0.23</sup> <sub>-0.20</sub>	He	1s <sup>2</sup>	(1s <sub>1/2</sub> 2p <sub>3/2</sub> ) <sub>1</sub>		1864.81	1s <sup>2</sup> 1S <sub>0</sub>	1s2p 1P <sub>1</sub> <sup>o</sup>	1864.98	
		Li	1s <sup>2</sup> 2s <sub>1/2</sub>	((1s <sub>1/2</sub> 2s <sub>1/2</sub> ) <sub>1</sub> 2p <sub>3/2</sub> ) <sub>1/2</sub>		1853.88	1s <sup>2</sup> 2s 2S <sub>1/2</sub>	1s(2S) 2s2p(1P <sup>o</sup> ) 2P <sub>1/2</sub> <sup>o</sup>	1854.22	
		He	1s <sup>2</sup>	(1s <sub>1/2</sub> 2p <sub>3/2</sub> ) <sub>2</sub>		1853.87	1s <sup>2</sup> 1S <sub>0</sub>	1s2p 3P <sub>2</sub> <sup>o</sup>	(1854.24)	
		He	1s <sup>2</sup>	(1s <sub>1/2</sub> 2p <sub>1/2</sub> ) <sub>1</sub>		1852.98	1s <sup>2</sup> 1S <sub>0</sub>	1s2p 3P <sub>1</sub> <sup>o</sup>	1853.30	
Li-2	1844.99 <sup>+0.07</sup> <sub>-0.05</sub>	Li	1s <sup>2</sup> 2s <sub>1/2</sub>	((1s <sub>1/2</sub> 2s <sub>1/2</sub> ) <sub>0</sub> ) <sub>3/2</sub>		1844.80	1s <sup>2</sup> 2s 2S <sub>1/2</sub>	1s(2S) 2s2p(3P <sup>o</sup> ) 2P <sub>3/2</sub> <sup>o</sup>	1845.66	
		Li	1s <sup>2</sup> 2s <sub>1/2</sub>	((1s <sub>1/2</sub> 2s <sub>1/2</sub> ) <sub>0</sub> 2p <sub>1/2</sub> ) <sub>1/2</sub>		1844.22	1s <sup>2</sup> 2s 2S <sub>1/2</sub>	1s(2S) 2s2p(3P <sup>o</sup> ) 2P <sub>1/2</sub> <sup>o</sup>	1845.11	
z	1839.25 <sup>+0.07</sup> <sub>-0.05</sub>	He	1s <sup>2</sup>	(1s <sub>1/2</sub> 2s <sub>1/2</sub> ) <sub>1</sub>		1838.20	1s <sup>2</sup> 1S <sub>0</sub>	1s2s 3S <sub>1</sub>	(1838.97)	
Be-1	1828.14 ± 0.08	Be	1s <sup>2</sup> 2s <sup>2</sup>	(1s <sub>1/2</sub> 2s <sup>2</sup> 2p <sub>3/2</sub> ) <sub>1</sub>		1828.36	1s <sup>2</sup> 2s <sup>2</sup> 1S <sub>0</sub>	1s2s <sup>2</sup> 2p 1P <sub>1</sub> <sup>o</sup>	1828.19	
		Li	1s <sup>2</sup> 2s <sub>1/2</sub>	((1s <sub>1/2</sub> 2s <sub>1/2</sub> ) <sub>1</sub> 2p <sub>3/2</sub> ) <sub>5/2</sub>		1826.52	1s <sup>2</sup> 2s 2S <sub>1/2</sub>	1s(2S) 2s2p(3P <sup>o</sup> ) 4P <sub>5/2</sub> <sup>o</sup>	(1827.10)	
Be-2	1823.77 <sup>+0.25</sup> <sub>-0.23</sub>	Be	1s <sup>2</sup> (2s <sub>1/2</sub> 2p <sub>3/2</sub> ) <sub>2</sub>	((1s <sub>1/2</sub> 2s <sub>1/2</sub> ) <sub>1</sub> (2p <sub>3/2</sub> ) <sub>2</sub> ) <sub>2</sub>		1823.65	1s <sup>2</sup> 2s2p 3P <sub>2</sub> <sup>o</sup>	1s(2S) 2s2p(4P) 3P <sub>2</sub>	1823.43	
		Be	1s <sup>2</sup> (2s <sub>1/2</sub> 2p <sub>1/2</sub> ) <sub>0</sub>	((1s <sub>1/2</sub> 2s <sub>1/2</sub> ) <sub>0</sub> 2p <sub>1/2</sub> ) <sub>1/2</sub> 2p <sub>3/2</sub> ) <sub>1</sub>		1823.55	1s <sup>2</sup> 2s2p 3P <sub>0</sub> <sup>o</sup>	1s(2S) 2s <sup>2</sup> 2p(2D) 3D <sub>1</sub>	1823.32	
B-1	1808.69 <sup>+0.10</sup> <sub>-0.12</sub>	B	1s <sup>2</sup> 2s <sup>2</sup> 2p <sub>3/2</sub>	(1s <sub>1/2</sub> 2s <sup>2</sup> (2p <sub>3/2</sub> ) <sub>2</sub> ) <sub>3/2</sub>		1808.63	1s <sup>2</sup> 2s <sup>2</sup> 2p 2P <sub>3/2</sub> <sup>o</sup>	1s2s <sup>2</sup> sp <sup>2</sup> 2P <sub>3/2</sub>	1808.38	
		B	1s <sup>2</sup> 2s <sup>2</sup> 2p <sub>1/2</sub>	((1s <sub>1/2</sub> 2s <sup>2</sup> 2p <sub>1/2</sub> ) <sub>1</sub> 2p <sub>3/2</sub> ) <sub>1/2</sub>		1808.59	1s <sup>2</sup> 2s <sup>2</sup> 2p 2P <sub>1/2</sub> <sup>o</sup>	1s2s <sup>2</sup> sp <sup>2</sup> 2P <sub>1/2</sub>	1808.38	
		B	1s <sup>2</sup> 2s <sup>2</sup> 2p <sub>1/2</sub>	(1s <sub>1/2</sub> 2s <sup>2</sup> (2p <sub>3/2</sub> ) <sub>2</sub> ) <sub>3/2</sub>		1809.49	1s <sup>2</sup> 2s <sup>2</sup> 2p 2P <sub>1/2</sub> <sup>o</sup>	1s2s <sup>2</sup> sp <sup>2</sup> 2P <sub>3/2</sub>	1809.22	
B-2	1805.0 <sup>+0.5</sup> <sub>-0.7</sub>	B	1s <sup>2</sup> 2s <sup>2</sup> 2p <sub>3/2</sub>	((1s <sub>1/2</sub> 2s <sup>2</sup> 2p <sub>1/2</sub> ) <sub>1</sub> 2p <sub>3/2</sub> ) <sub>5/2</sub>		1805.8	1s <sup>2</sup> 2s <sup>2</sup> 2p 2P <sub>3/2</sub> <sup>o</sup>	1s2s <sup>2</sup> sp <sup>2</sup> 2D <sub>5/2</sub>	1805.3	
		B	1s <sup>2</sup> 2s <sup>2</sup> 2p <sub>1/2</sub>	((1s <sub>1/2</sub> 2s <sup>2</sup> 2p <sub>1/2</sub> ) <sub>0</sub> 2p <sub>1/2</sub> ) <sub>0</sub> 2p <sub>3/2</sub> ) <sub>3/2</sub>		1806.8	1s <sup>2</sup> 2s <sup>2</sup> 2p 2P <sub>1/2</sub> <sup>o</sup>	1s2s <sup>2</sup> sp <sup>2</sup> 2D <sub>3/2</sub>	1806.1	
C-1	1794.5 <sup>+1.6</sup> <sub>-1.7</sub>	Li	1s <sup>2</sup> 2p <sub>3/2</sub>	1s <sub>1/2</sub> 2s <sup>2</sup>		1794.1	1s <sup>2</sup> 2p 2P <sub>3/2</sub> <sup>o</sup>	1s2s <sup>2</sup> 2S <sub>1/2</sub>	1795.3	
		Li	1s <sup>2</sup> 2p <sub>1/2</sub>	1s <sub>1/2</sub> 2s <sup>2</sup>		1795.1	1s <sup>2</sup> 2p 2P <sub>1/2</sub> <sup>o</sup>	1s2s <sup>2</sup> 2S <sub>1/2</sub>	1796.3	
C-2	1790.44 <sup>+0.29</sup> <sub>-0.50</sub>	C	1s <sup>2</sup> (2s <sup>2</sup> 2p <sub>1/2</sub> 2p <sub>3/2</sub> ) <sub>2</sub>	((1s <sub>1/2</sub> 2s <sup>2</sup> 2p <sub>1/2</sub> ) <sub>1</sub> (2p <sub>3/2</sub> ) <sub>2</sub> ) <sub>2</sub>		1789.17	1s <sup>2</sup> 2s <sup>2</sup> 2p <sup>2</sup> 1D <sub>2</sub>	1s2s <sup>2</sup> 2p <sup>3</sup> 1D <sub>2</sub> <sup>o</sup>	1789.09	
		C	1s <sup>2</sup> 2s <sup>2</sup> (2p <sub>3/2</sub> ) <sub>2</sub>	(1s <sub>1/2</sub> 2s <sup>2</sup> (2p <sub>3/2</sub> ) <sub>3/2</sub> ) <sub>2</sub>		1790.78	1s <sup>2</sup> 2s <sup>2</sup> 2p <sup>2</sup> 3P <sub>2</sub>	1s2s <sup>2</sup> 2p <sup>3</sup> 2P <sub>2</sub> <sup>o</sup>	1790.41	
		C	1s <sup>2</sup> 2s <sup>2</sup> (2p <sub>3/2</sub> ) <sub>2</sub>	((1s <sub>1/2</sub> 2s <sup>2</sup> 2p <sub>1/2</sub> ) <sub>1</sub> (2p <sub>3/2</sub> ) <sub>0</sub> ) <sub>1</sub>		1790.92	1s <sup>2</sup> 2s <sup>2</sup> 2p <sup>2</sup> 3P <sub>2</sub>	1s2s <sup>2</sup> 2p <sup>3</sup> 3P <sub>1</sub> <sup>o</sup>	1790.59	
		C	1s <sup>2</sup> (2s <sup>2</sup> 2p <sub>1/2</sub> 2p <sub>3/2</sub> ) <sub>2</sub>	(1s <sub>1/2</sub> 2s <sup>2</sup> (2p <sub>3/2</sub> ) <sub>3/2</sub> ) <sub>1</sub>		1792.99	1s <sup>2</sup> 2s <sup>2</sup> 2p <sup>2</sup> 1D <sub>2</sub>	1s2s <sup>2</sup> 2p <sup>3</sup> 1P <sub>1</sub> <sup>o</sup>	1793.23	

Table 4.4 – continued

Key	Fit (eV)	Ion	jj-coupling		FAC (eV)	LS-coupling		Palmeri (eV)
			lower level	upper level		lower level	upper level	
C-3	1786.98 <sup>+0.29</sup> <sub>-0.40</sub>	C	1s <sup>2</sup> 2s <sup>2</sup> (2p <sub>3/2</sub> ) <sub>0</sub>	(1s <sub>1/2</sub> 2s <sup>2</sup> (2p <sub>3/2</sub> ) <sub>3/2</sub> ) <sub>1</sub>	1786.85	1s <sup>2</sup> 2s <sup>2</sup> 2p <sup>2</sup> <sup>1</sup> S <sub>0</sub>	1s 2s <sup>2</sup> 2p <sup>3</sup> <sup>1</sup> P <sub>0</sub>	1786.88
			1s <sup>2</sup> 2s <sup>2</sup> (2p <sub>3/2</sub> ) <sub>2</sub>	((1s <sub>1/2</sub> 2s <sup>2</sup> 2p <sub>1/2</sub> ) <sub>1</sub> (2p <sub>3/2</sub> ) <sub>2</sub> ) <sub>3</sub>	1786.81	1s <sup>2</sup> 2s <sup>2</sup> 2p <sup>2</sup> <sup>3</sup> P <sub>2</sub>	1s 2s <sup>2</sup> 2p <sup>3</sup> <sup>3</sup> D <sub>3</sub> <sup>o</sup>	1786.26
			1s <sup>2</sup> (2s <sup>2</sup> 2p <sub>1/2</sub> 2p <sub>3/2</sub> ) <sub>1</sub>	((1s <sub>1/2</sub> 2s <sup>2</sup> 2p <sub>1/2</sub> ) <sub>0</sub> (2p <sub>3/2</sub> ) <sub>2</sub> ) <sub>2</sub>	1787.41	1s <sup>2</sup> 2s <sup>2</sup> 2p <sup>2</sup> <sup>3</sup> P <sub>1</sub>	1s 2s <sup>2</sup> 2p <sup>3</sup> <sup>3</sup> D <sub>2</sub> <sup>o</sup>	1786.67
N-1	1774.02 <sup>+0.15</sup> <sub>-0.19</sub>	N	1s <sup>2</sup> 2s <sup>2</sup> (2p <sub>1/2</sub> 2p <sub>3/2</sub> ) <sub>5/2</sub>	((1s <sub>1/2</sub> 2s <sup>2</sup> 2p <sub>1/2</sub> ) <sub>1</sub> (2p <sub>3/2</sub> ) <sub>3/2</sub> ) <sub>3/2</sub>	1774.11	1s <sup>2</sup> 2s <sup>2</sup> 2p <sup>3</sup> <sup>2</sup> D <sub>5/2</sub> <sup>o</sup>	1s 2s <sup>2</sup> 2p <sup>4</sup> <sup>2</sup> P <sub>3/2</sub>	1773.66
			1s <sup>2</sup> 2s <sup>2</sup> (2p <sub>1/2</sub> 2p <sub>3/2</sub> ) <sub>3/2</sub>	((1s <sub>1/2</sub> 2s <sup>2</sup> 2p <sub>1/2</sub> ) <sub>1</sub> (2p <sub>3/2</sub> ) <sub>3/2</sub> ) <sub>1/2</sub>	1774.60	1s <sup>2</sup> 2s <sup>2</sup> 2p <sup>3</sup> <sup>2</sup> D <sub>3/2</sub> <sup>o</sup>	1s 2s <sup>2</sup> 2p <sup>4</sup> <sup>2</sup> P <sub>1/2</sub>	1774.19
			1s <sup>2</sup> 2s <sup>2</sup> (2p <sub>1/2</sub> 2p <sub>3/2</sub> ) <sub>5/2</sub>	((1s <sub>1/2</sub> 2s <sup>2</sup> 2p <sub>1/2</sub> ) <sub>1</sub> (2p <sub>3/2</sub> ) <sub>3/2</sub> ) <sub>5/2</sub>	1772.51	1s <sup>2</sup> 2s <sup>2</sup> 2p <sup>3</sup> <sup>2</sup> D <sub>5/2</sub> <sup>o</sup>	1s 2s <sup>2</sup> 2p <sup>4</sup> <sup>2</sup> D <sub>5/2</sub>	1771.78
N-2	1769.87 <sup>+0.16</sup> <sub>-0.21</sub>	N	1s <sup>2</sup> 2s <sup>2</sup> (2p <sub>1/2</sub> 2p <sub>3/2</sub> ) <sub>3/2</sub>	(1s <sub>1/2</sub> 2s <sup>2</sup> 2p <sub>1/2</sub> ) <sub>1</sub> (2p <sub>3/2</sub> ) <sub>2</sub> ) <sub>3/2</sub>	1772.61	1s <sup>2</sup> 2s <sup>2</sup> 2p <sup>3</sup> <sup>2</sup> D <sub>3/2</sub> <sup>o</sup>	1s 2s <sup>2</sup> 2p <sup>4</sup> <sup>2</sup> D <sub>3/2</sub>	1771.76
			1s <sup>2</sup> 2s <sup>2</sup> (2p <sub>1/2</sub> 2p <sub>3/2</sub> ) <sub>1/2</sub>	((1s <sub>1/2</sub> 2s <sup>2</sup> 2p <sub>1/2</sub> ) <sub>1</sub> (2p <sub>3/2</sub> ) <sub>3/2</sub> ) <sub>1/2</sub>	1770.59	1s <sup>2</sup> 2s <sup>2</sup> 2p <sup>3</sup> <sup>2</sup> P <sub>0</sub> <sup>o</sup>	1s 2s <sup>2</sup> 2p <sup>4</sup> <sup>2</sup> P <sub>1/2</sub>	1770.01
			1s <sup>2</sup> 2s <sup>2</sup> (2p <sub>3/2</sub> ) <sub>3/2</sub>	((1s <sub>1/2</sub> 2s <sup>2</sup> 2p <sub>1/2</sub> ) <sub>1</sub> (2p <sub>3/2</sub> ) <sub>3/2</sub> ) <sub>3/2</sub>	1770.07	1s <sup>2</sup> 2s <sup>2</sup> 2p <sup>3</sup> <sup>2</sup> P <sub>0</sub> <sup>o</sup>	1s 2s <sup>2</sup> 2p <sup>4</sup> <sup>2</sup> P <sub>3/2</sub>	1769.46
O-1	1759.0 ± 0.6	O	1s <sup>2</sup> 2s <sup>2</sup> (2p <sub>3/2</sub> ) <sub>3/2</sub>	((1s <sub>1/2</sub> 2s <sup>2</sup> 2p <sub>1/2</sub> ) <sub>1</sub> (2p <sub>3/2</sub> ) <sub>3/2</sub> ) <sub>5/2</sub>	1768.47	1s <sup>2</sup> 2s <sup>2</sup> 2p <sup>3</sup> <sup>2</sup> P <sub>3/2</sub> <sup>o</sup>	1s 2s <sup>2</sup> 2p <sup>4</sup> <sup>2</sup> D <sub>5/2</sub>	1767.59
			1s <sup>2</sup> 2s <sup>2</sup> (2p <sub>1/2</sub> 2p <sub>3/2</sub> ) <sub>3/2</sub>	(1s <sub>1/2</sub> 2s <sup>2</sup> 2p <sub>1/2</sub> ) <sub>1</sub> (2p <sub>3/2</sub> ) <sub>3/2</sub> ) <sub>1</sub>	1758.2	1s <sup>2</sup> 2s <sup>2</sup> 2p <sup>4</sup> <sup>1</sup> D <sub>2</sub>	1s 2s <sup>2</sup> 2p <sup>5</sup> <sup>1</sup> P <sub>0</sub> <sup>o</sup>	1756.3
			1s <sup>2</sup> 2s <sup>2</sup> (2p <sub>1/2</sub> 2p <sub>3/2</sub> ) <sub>3/2</sub>	(1s <sub>1/2</sub> 2s <sup>2</sup> 2p <sub>1/2</sub> ) <sub>1</sub> (2p <sub>3/2</sub> ) <sub>3/2</sub> ) <sub>3/2</sub>	1756.3	1s <sup>2</sup> 2s <sup>2</sup> 2p <sup>4</sup> <sup>3</sup> P <sub>1</sub>	1s 2s <sup>2</sup> 2p <sup>5</sup> <sup>3</sup> P <sub>2</sub> <sup>o</sup>	1753.9
O-2	1756.1 <sup>+0.4</sup> <sub>-0.5</sub>	O	1s <sup>2</sup> 2s <sup>2</sup> (2p <sub>1/2</sub> 2p <sub>3/2</sub> ) <sub>3/2</sub>	(1s <sub>1/2</sub> 2s <sup>2</sup> 2p <sub>1/2</sub> ) <sub>1</sub> (2p <sub>3/2</sub> ) <sub>3/2</sub> ) <sub>2</sub>	1756.7	1s <sup>2</sup> 2s <sup>2</sup> 2p <sup>4</sup> <sup>3</sup> P <sub>0</sub>	1s 2s <sup>2</sup> 2p <sup>5</sup> <sup>3</sup> P <sub>1</sub>	1754.3
			1s <sup>2</sup> 2s <sup>2</sup> 2p <sub>3/2</sub>	(1s <sub>1/2</sub> 2s <sup>2</sup> 2p <sub>1/2</sub> 2p <sub>3/2</sub> ) <sub>2</sub>	1756.7	1s <sup>2</sup> 2s <sup>2</sup> 2p <sup>4</sup> <sup>3</sup> P <sub>2</sub>	1s 2s <sup>2</sup> 2p <sup>5</sup> <sup>3</sup> P <sub>2</sub>	1754.4
			1s <sup>2</sup> 2s <sup>2</sup> 2p <sub>1/2</sub> (2p <sub>3/2</sub> ) <sub>2</sub>	(1s <sub>1/2</sub> 2s <sup>2</sup> 2p <sub>1/2</sub> 2p <sub>3/2</sub> ) <sub>1</sub>	1757.3	1s <sup>2</sup> 2s <sup>2</sup> 2p <sup>4</sup> <sup>3</sup> P <sub>0</sub>	1s 2s <sup>2</sup> 2p <sup>5</sup> <sup>3</sup> P <sub>0</sub>	1755.0
O-3	1751.5 <sup>+0.6</sup> <sub>-0.7</sub>	O	1s <sup>2</sup> 2s <sup>2</sup> (2p <sub>1/2</sub> 2p <sub>3/2</sub> ) <sub>3/2</sub>	(1s <sub>1/2</sub> 2s <sup>2</sup> 2p <sub>1/2</sub> 2p <sub>3/2</sub> ) <sub>0</sub>	1757.3	1s <sup>2</sup> 2s <sup>2</sup> 2p <sup>4</sup> <sup>3</sup> P <sub>1</sub>	1s 2s <sup>2</sup> 2p <sup>5</sup> <sup>3</sup> P <sub>0</sub>	1754.8
			1s <sup>2</sup> 2s <sup>2</sup> 2p <sub>1/2</sub> (2p <sub>3/2</sub> ) <sub>0</sub>	(1s <sub>1/2</sub> 2s <sup>2</sup> 2p <sub>1/2</sub> 2p <sub>3/2</sub> ) <sub>3/2</sub> ) <sub>1</sub>	1752.3	1s <sup>2</sup> 2s <sup>2</sup> 2p <sup>4</sup> <sup>1</sup> S <sub>0</sub>	1s 2s <sup>2</sup> 2p <sup>5</sup> <sup>1</sup> P <sub>0</sub>	1750.4
			1s <sup>2</sup> 2s <sup>2</sup> 2p <sub>1/2</sub> (2p <sub>3/2</sub> ) <sub>3/2</sub>	1s <sub>1/2</sub> 2s <sup>2</sup> 2p <sup>6</sup>	1743.64	1s <sup>2</sup> 2s <sup>2</sup> 2p <sup>5</sup> <sup>2</sup> P <sub>3/2</sub> <sup>o</sup>	1s 2s <sup>2</sup> 2p <sup>6</sup> <sup>2</sup> S <sub>1/2</sub>	1740.79
F-1	1742.72 <sup>+0.17</sup> <sub>-0.18</sub>	F	1s <sup>2</sup> 2s <sup>2</sup> 2p <sub>1/2</sub> 2p <sub>3/2</sub>	1s <sub>1/2</sub> 2s <sup>2</sup> 2p <sup>6</sup>	1743.02	1s <sup>2</sup> 2s <sup>2</sup> 2p <sup>5</sup> <sup>2</sup> P <sub>0</sub> <sup>o</sup>	1s 2s <sup>2</sup> 2p <sup>6</sup> <sup>2</sup> S <sub>1/2</sub>	1740.15
			1s <sup>2</sup> 2s <sup>2</sup> 2p <sub>1/2</sub> ((2p <sub>3/2</sub> ) <sub>3/2</sub> 3s <sub>1/2</sub> ) <sub>2</sub>	(1s <sub>1/2</sub> 2s <sup>2</sup> 2p <sup>6</sup> 3s <sub>1/2</sub> ) <sub>1</sub>	1742.49	1s <sup>2</sup> 2s <sup>2</sup> 2p <sup>5</sup> <sup>2</sup> P <sub>1/2</sub> <sup>o</sup>	1s 2s <sup>2</sup> 2p <sup>6</sup> <sup>2</sup> S <sub>1/2</sub>	1740.15
			1s <sup>2</sup> 2s <sup>2</sup> 2p <sub>1/2</sub> ((2p <sub>3/2</sub> ) <sub>3/2</sub> 3s <sub>1/2</sub> ) <sub>1</sub>	(1s <sub>1/2</sub> 2s <sup>2</sup> 2p <sup>6</sup> 3s <sub>1/2</sub> ) <sub>1</sub>	1742.16	1s <sup>2</sup> 2s <sup>2</sup> 2p <sup>5</sup> <sup>3</sup> P <sub>2</sub> <sup>o</sup>	1s 2s <sup>2</sup> 2p <sup>6</sup> <sup>3</sup> S <sub>0</sub>	1743.38
F-2	1739.8 <sup>+0.4</sup> <sub>-0.5</sub>	(?)			1742.16	1s <sup>2</sup> 2s <sup>2</sup> 2p <sup>5</sup> <sup>3</sup> P <sub>1</sub> <sup>o</sup>	1s 2s <sup>2</sup> 2p <sup>6</sup> <sup>3</sup> S <sub>0</sub>	1743.06

### 4.7.2 Sulfur

For the sulfur spectrum the same approach has been undertaken as for the silicon. The results are presented in figure 4.19 and table 4.5. Although the table lists weak lines of Ne- and B-like lines for the lines F-2 and F-3, as for silicon these lines are probably due to lowly charged ions not included in the calculation.

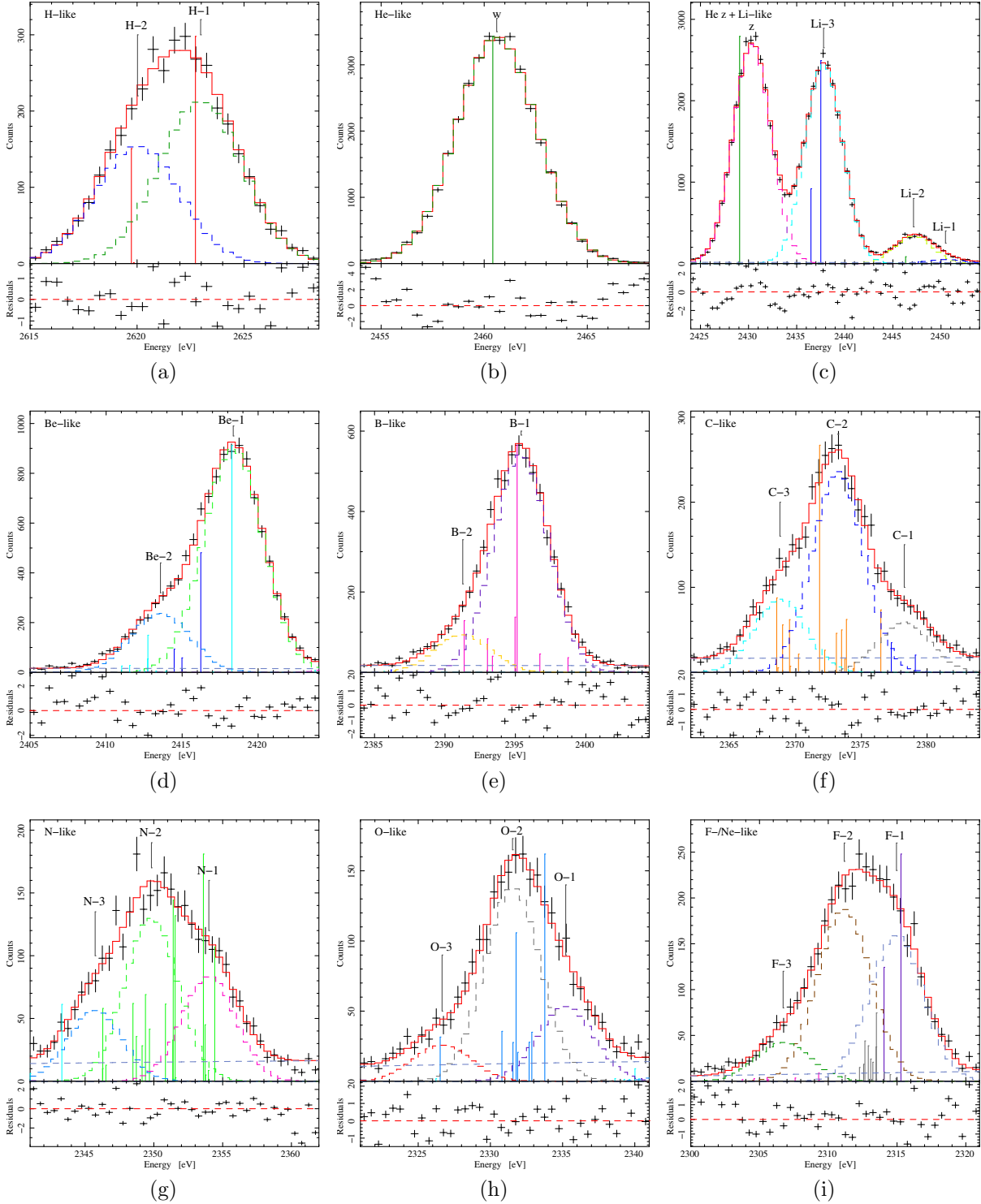


Figure 4.19: Same as Fig. 4.18 for the S spectrum.

Table 4.5: Same as table 4.4 for sulfur.

Key	Fit (eV)	Ion	ij-coupling		FAC (eV)	L-S-coupling		Palmeri (eV)
			lower level	upper level		lower level	upper level	
H-1	2622.97 <sup>+0.20</sup> <sub>-0.22</sub>	H	1s <sub>1/2</sub>	2p <sub>3/2</sub>	2622.73	1s <sup>2</sup> S <sub>1/2</sub>	1p <sup>2</sup> P <sub>3/2</sub>	—
H-2	2620.02 <sup>+0.25</sup> <sub>-0.30</sub>	H	2s <sub>1/2</sub>	2p <sub>1/2</sub>	2619.73	1s <sup>2</sup> S <sub>1/2</sub>	1p <sup>2</sup> P <sub>1/2</sub>	—
w	2460.605 <sup>+0.020</sup> <sub>-0.016</sub>	He	1s <sup>2</sup>	(1s <sub>1/2</sub> 2p <sub>3/2</sub> ) <sub>1</sub>	2460.417	1s <sup>2</sup> 1S <sub>0</sub>	1s2p <sup>1</sup> P <sub>1</sub> <sup>o</sup>	2460.638
Li-1	2450.5 <sup>+0.9</sup> <sub>-1.2</sub>	Li	1s <sup>2</sup> 2p <sub>3/2</sub>	(1s <sub>1/2</sub> 2p <sub>3/2</sub> ) <sub>0</sub> 1/2	2449.9	1s <sup>2</sup> 2p <sup>2</sup> P <sub>3/2</sub> <sup>o</sup>	1s(2S) 2p <sup>2</sup> (1S) 2S <sub>1/2</sub>	2450.7
Li-2	2447.14 <sup>+0.14</sup> <sub>-0.31</sub>	He	1s <sup>2</sup>	(1s <sub>1/2</sub> 2p <sub>1/2</sub> ) <sub>1</sub>	2446.32	1s <sup>2</sup> 1S <sub>0</sub>	1s2p <sup>3</sup> P <sub>1</sub> <sup>o</sup>	2446.65
		He	1s <sup>2</sup>	(1s <sub>1/2</sub> 2p <sub>3/2</sub> ) <sub>2</sub>	2447.92	1s <sup>2</sup> 1S <sub>0</sub>	1s2p <sup>3</sup> P <sub>2</sub> <sup>o</sup>	(2448.34)
		Li	1s <sup>2</sup> 2s <sub>1/2</sub>	((1s <sub>1/2</sub> 2s <sub>1/2</sub> ) <sub>1</sub> 2p <sub>3/2</sub> ) <sub>1/2</sub>	2447.62	1s <sup>2</sup> 2s <sup>2</sup> S <sub>1/2</sub>	1s(2S) 2s2p(1P <sup>o</sup> ) 2P <sub>1/2</sub> <sup>o</sup>	2448.01
Li-3	2437.797 <sup>+0.027</sup> <sub>-0.021</sub>	Li	1s <sup>2</sup> 2s <sub>1/2</sub>	((1s <sub>1/2</sub> 2s <sub>1/2</sub> ) <sub>0</sub> 2p <sub>3/2</sub> ) <sub>3/2</sub>	2437.509	1s <sup>2</sup> 2s <sup>2</sup> S <sub>1/2</sub>	1s(2S) 2s2p(3P <sup>o</sup> ) 2P <sub>3/2</sub> <sup>o</sup>	2438.474
		Li	1s <sup>2</sup> 2s <sub>1/2</sub>	((1s <sub>1/2</sub> 2s <sub>1/2</sub> ) <sub>0</sub> 2p <sub>1/2</sub> ) <sub>1/2</sub>	2436.481	1s <sup>2</sup> 2s <sup>2</sup> S <sub>1/2</sub>	1s(2S) 2s2p(3P <sup>o</sup> ) 2P <sub>1/2</sub> <sup>o</sup>	2437.515
z	2430.366 <sup>+0.028</sup> <sub>-0.017</sub>	He	1s <sup>2</sup>	(1s <sub>1/2</sub> 2s <sub>1/2</sub> ) <sub>1</sub>	2429.074	1s <sup>2</sup> 1S <sub>0</sub>	1s2s <sup>3</sup> S <sub>1</sub>	(2429.879)
Be-1	2418.36 <sup>+0.05</sup> <sub>-0.07</sub>	Be	1s <sup>2</sup> 2s <sup>2</sup>	(1s <sub>1/2</sub> 2s <sup>2</sup> 2p <sub>3/2</sub> ) <sub>1</sub>	2418.28	1s <sup>2</sup> 2s <sup>2</sup> 1S <sub>0</sub>	1s2s <sup>2</sup> 2p <sup>1</sup> P <sub>1</sub> <sup>o</sup>	2418.45
		Li	1s <sup>2</sup> 2s <sub>1/2</sub>	((1s <sub>1/2</sub> 2s <sub>1/2</sub> ) <sub>1</sub> 2p <sub>3/2</sub> ) <sub>5/2</sub>	2416.23	1s <sup>2</sup> 2s <sup>2</sup> 2S <sub>1/2</sub>	1s(2S) 2s2p(3P <sup>o</sup> ) 4P <sub>5/2</sub> <sup>o</sup>	(2416.98)
Be-2	2413.57 <sup>+0.13</sup> <sub>-0.19</sub>	Be	1s <sup>2</sup> (2s <sub>1/2</sub> 2p <sub>3/2</sub> ) <sub>2</sub>	((1s <sub>1/2</sub> 2s <sub>1/2</sub> ) <sub>1</sub> (2p <sub>3/2</sub> ) <sub>2</sub> ) <sub>2</sub>	2412.75	1s <sup>2</sup> 2s <sup>2</sup> 2p <sup>3</sup> P <sub>2</sub> <sup>o</sup>	1s(2S) 2s <sup>2</sup> 2p <sup>1</sup> P <sub>1</sub> <sup>o</sup>	2412.89
		Li	1s <sup>2</sup> 2s <sub>1/2</sub>	((1s <sub>1/2</sub> 2s <sub>1/2</sub> ) <sub>1</sub> 2p <sub>1/2</sub> ) <sub>1/2</sub>	2414.45	1s <sup>2</sup> 2s <sup>2</sup> 2S <sub>1/2</sub>	1s(2S) 2s2p(3P <sup>o</sup> ) 4P <sub>1/2</sub> <sup>o</sup>	2414.92
		Li	1s <sup>2</sup> 2s <sub>1/2</sub>	((1s <sub>1/2</sub> 2s <sub>1/2</sub> ) <sub>1</sub> 2p <sub>1/2</sub> ) <sub>3/2</sub>	2414.99	1s <sup>2</sup> 2s <sup>2</sup> 2S <sub>1/2</sub>	1s(2S) 2s2p(3P <sup>o</sup> ) 4P <sub>3/2</sub> <sup>o</sup>	2415.67
B-1	2395.40 <sup>+0.08</sup> <sub>-0.09</sub>	B	1s <sup>2</sup> 2s <sup>2</sup> 2p <sub>3/2</sub>	(1s <sub>1/2</sub> 2s <sup>2</sup> (2p <sub>3/2</sub> ) <sub>2</sub> ) <sub>3/2</sub>	2395.12	1s <sup>2</sup> 2s <sup>2</sup> 2p <sup>2</sup> P <sub>3/2</sub> <sup>o</sup>	1s2s <sup>2</sup> p <sup>2</sup> 2P <sub>3/2</sub>	2394.90
		B	1s <sup>2</sup> 2s <sup>2</sup> 2p <sub>1/2</sub>	((1s <sub>1/2</sub> 2s <sup>2</sup> 2p <sub>1/2</sub> ) <sub>1</sub> 2p <sub>3/2</sub> ) <sub>1/2</sub>	2394.98	1s <sup>2</sup> 2s <sup>2</sup> 2p <sup>2</sup> P <sub>1/2</sub> <sup>o</sup>	1s2s <sup>2</sup> p <sup>2</sup> 2P <sub>1/2</sub>	2394.86
B-2	2391.3 ± 0.4	B	1s <sup>2</sup> 2s <sup>2</sup> 2p <sub>3/2</sub>	((1s <sub>1/2</sub> 2s <sup>2</sup> 2p <sub>1/2</sub> ) <sub>1</sub> 2p <sub>3/2</sub> ) <sub>5/2</sub>	2391.4	1s <sup>2</sup> 2s <sup>2</sup> 2p <sup>2</sup> P <sub>3/2</sub> <sup>o</sup>	1s2s <sup>2</sup> p <sup>2</sup> 2D <sub>5/2</sub>	2390.9
		B	1s <sup>2</sup> 2s <sup>2</sup> 2p <sub>1/2</sub>	((1s <sub>1/2</sub> 2s <sup>2</sup> 2p <sub>1/2</sub> ) <sub>0</sub> 2p <sub>3/2</sub> ) <sub>3/2</sub>	2393.0	1s <sup>2</sup> 2s <sup>2</sup> 2p <sup>2</sup> P <sub>1/2</sub> <sup>o</sup>	1s2s <sup>2</sup> p <sup>2</sup> 2D <sub>3/2</sub>	2392.3
C-1	2378.3 ± 0.4	Li	1s <sup>2</sup> 2p <sub>3/2</sub>	1s <sub>1/2</sub> 2s <sup>2</sup>	2377.3	1s <sup>2</sup> 2p <sup>2</sup> P <sub>3/2</sub> <sup>o</sup>	1s2s <sup>2</sup> 2S <sub>1/2</sub>	2378.5
		Li	1s <sup>2</sup> 2p <sub>1/2</sub>	1s <sub>1/2</sub> 2s <sup>2</sup>	2379.1	1s <sup>2</sup> 2p <sup>2</sup> P <sub>1/2</sub> <sup>o</sup>	1s2s <sup>2</sup> 2S <sub>1/2</sub>	2380.4
C-2	2373.21 <sup>+0.17</sup> <sub>-0.19</sub>	C	1s <sup>2</sup> 2s <sup>2</sup> (2p <sub>3/2</sub> ) <sub>2</sub>	((1s <sub>1/2</sub> 2s <sup>2</sup> 2p <sub>1/2</sub> ) <sub>1</sub> (2p <sub>3/2</sub> ) <sub>0</sub> ) <sub>1</sub>	2373.86	1s <sup>2</sup> 2s <sup>2</sup> 2p <sup>2</sup> 3P <sub>2</sub>	1s2s <sup>2</sup> 2p <sup>3</sup> 3P <sub>1</sub> <sup>o</sup>	2373.36
		C	1s <sup>2</sup> 2s <sup>2</sup> (2p <sub>3/2</sub> ) <sub>2</sub>	(1s <sub>1/2</sub> 2s <sup>2</sup> (2p <sub>3/2</sub> ) <sub>3/2</sub> ) <sub>2</sub>	2373.49	1s <sup>2</sup> 2s <sup>2</sup> 2p <sup>2</sup> 3P <sub>2</sub>	1s2s <sup>2</sup> 2p <sup>3</sup> 3P <sub>2</sub> <sup>o</sup>	2372.95
		C	1s <sup>2</sup> 2s <sup>2</sup> (2p <sub>1/2</sub> 2p <sub>3/2</sub> ) <sub>1</sub>	((1s <sub>1/2</sub> 2s <sup>2</sup> 2p <sub>1/2</sub> ) <sub>1</sub> (2p <sub>3/2</sub> ) <sub>2</sub> ) <sub>1</sub>	2373.09	1s <sup>2</sup> 2s <sup>2</sup> 2p <sup>2</sup> 3P <sub>1</sub>	1s2s <sup>2</sup> 2p <sup>3</sup> 3S <sub>1</sub> <sup>o</sup>	2372.77
		C	1s <sup>2</sup> 2s <sup>2</sup> (2p <sub>1/2</sub> 2p <sub>3/2</sub> ) <sub>3</sub>	((1s <sub>1/2</sub> 2s <sup>2</sup> 2p <sub>1/2</sub> ) <sub>1</sub> (2p <sub>3/2</sub> ) <sub>2</sub> ) <sub>2</sub>	2371.81	1s <sup>2</sup> 2s <sup>2</sup> 2p <sup>2</sup> 1D <sub>2</sub>	1s2s <sup>2</sup> 2p <sup>3</sup> 1D <sub>2</sub> <sup>o</sup>	2371.59
C-3	2368.79 <sup>+0.28</sup> <sub>-0.29</sub>	C	1s <sup>2</sup> 2s <sup>2</sup> (2p <sub>1/2</sub> 2p <sub>3/2</sub> ) <sub>1</sub>	((1s <sub>1/2</sub> 2s <sup>2</sup> 2p <sub>1/2</sub> ) <sub>0</sub> (2p <sub>3/2</sub> ) <sub>2</sub> ) <sub>2</sub>	2369.52	1s <sup>2</sup> 2s <sup>2</sup> 2p <sup>2</sup> 3P <sub>1</sub>	1s2s <sup>2</sup> 2p <sup>3</sup> 3D <sub>2</sub> <sup>o</sup>	2368.55
		C	1s <sup>2</sup> 2s <sup>2</sup> (2p <sub>3/2</sub> ) <sub>0</sub>	(1s <sub>1/2</sub> 2s <sup>2</sup> (2p <sub>3/2</sub> ) <sub>3/2</sub> ) <sub>1</sub>	2369.00	1s <sup>2</sup> 2s <sup>2</sup> 2p <sup>2</sup> 1S <sub>0</sub>	1s2s <sup>2</sup> 2p <sup>3</sup> 1P <sub>1</sub> <sup>o</sup>	2368.87
		C	1s <sup>2</sup> 2s <sup>2</sup> (2p <sub>3/2</sub> ) <sub>2</sub>	((1s <sub>1/2</sub> 2s <sup>2</sup> 2p <sub>1/2</sub> ) <sub>1</sub> (2p <sub>3/2</sub> ) <sub>2</sub> ) <sub>3</sub>	2368.55	1s <sup>2</sup> 2s <sup>2</sup> 2p <sup>2</sup> 3P <sub>2</sub>	1s2s <sup>2</sup> 2p <sup>3</sup> 3D <sub>3</sub> <sup>o</sup>	2367.83

Table 4.5 – continued

Key	Fit (eV)	Ion	jj-coupling		FAC (eV)	Ls-coupling		Palmeri (eV)
			lower level	upper level		lower level	upper level	
N-1	2354.0 ± 0.4	N	1s <sup>2</sup> 2s <sup>2</sup> (2p <sub>1/2</sub> (2p <sub>3/2</sub> <sup>2</sup> ) <sub>2</sub> ) <sub>3/2</sub>	((1s <sub>1/2</sub> 2s <sup>2</sup> 2p <sub>1/2</sub> ) <sub>1</sub> (2p <sub>3/2</sub> <sup>3</sup> ) <sub>3/2</sub> ) <sub>1/2</sub>	2354.3	1s <sup>2</sup> 2s <sup>2</sup> 2p <sup>3</sup> 2D <sub>3/2</sub> <sup>0</sup>	1s2s <sup>2</sup> 2p <sup>4</sup> 2P <sub>1/2</sub>	2353.8
			1s <sup>2</sup> 2s <sup>2</sup> (2p <sub>3/2</sub> <sup>3</sup> ) <sub>3/2</sub>	1s <sub>1/2</sub> 2s <sup>2</sup> 2p <sub>3/2</sub> <sup>4</sup>	2353.7	1s <sup>2</sup> 2s <sup>2</sup> 2p <sup>3</sup> 2P <sub>3/2</sub> <sup>0</sup>	1s2s <sup>2</sup> 2p <sup>4</sup> 2S <sub>1/2</sub>	2352.9
			1s <sup>2</sup> 2s <sup>2</sup> (2p <sub>1/2</sub> (2p <sub>3/2</sub> <sup>2</sup> ) <sub>2</sub> ) <sub>5/2</sub>	((1s <sub>1/2</sub> 2s <sup>2</sup> 2p <sub>1/2</sub> ) <sub>1</sub> (2p <sub>3/2</sub> <sup>3</sup> ) <sub>3/2</sub> ) <sub>3/2</sub>	2353.6	1s <sup>2</sup> 2s <sup>2</sup> 2p <sup>3</sup> 2D <sub>5/2</sub> <sup>0</sup>	1s2s <sup>2</sup> 2p <sup>4</sup> 2P <sub>3/2</sub>	2352.9
N-2	2349.8 <sup>+0.4</sup> <sub>-0.5</sub>	N	1s <sup>2</sup> 2s <sup>2</sup> (2p <sub>1/2</sub> (2p <sub>3/2</sub> <sup>2</sup> ) <sub>2</sub> ) <sub>3/2</sub>	(1s <sub>1/2</sub> 2s <sup>2</sup> 2p <sub>1/2</sub> ) <sub>1</sub> (2p <sub>3/2</sub> <sup>2</sup> ) <sub>2</sub> ) <sub>3/2</sub>	2351.5	1s <sup>2</sup> 2s <sup>2</sup> 2p <sup>3</sup> 2D <sub>3/2</sub> <sup>0</sup>	1s2s <sup>2</sup> 2p <sup>4</sup> 2D <sub>3/2</sub>	2350.4
			1s <sup>2</sup> 2s <sup>2</sup> (2p <sub>1/2</sub> (2p <sub>3/2</sub> <sup>2</sup> ) <sub>2</sub> ) <sub>5/2</sub>	((1s <sub>1/2</sub> 2s <sup>2</sup> 2p <sub>1/2</sub> ) <sub>1</sub> (2p <sub>3/2</sub> <sup>3</sup> ) <sub>3/2</sub> ) <sub>5/2</sub>	2351.4	1s <sup>2</sup> 2s <sup>2</sup> 2p <sup>3</sup> 2D <sub>5/2</sub> <sup>0</sup>	1s2s <sup>2</sup> 2p <sup>4</sup> 2D <sub>5/2</sub>	2350.5
			1s <sup>2</sup> 2s <sup>2</sup> (2p <sub>1/2</sub> (2p <sub>3/2</sub> <sup>2</sup> ) <sub>2</sub> ) <sub>3/2</sub>	((1s <sub>1/2</sub> 2s <sup>2</sup> 2p <sub>1/2</sub> ) <sub>1</sub> (2p <sub>3/2</sub> <sup>3</sup> ) <sub>3/2</sub> ) <sub>3/2</sub>	2350.8	1s <sup>2</sup> 2s <sup>2</sup> 2p <sup>3</sup> 4S <sub>0</sub> <sup>0</sup>	1s2s <sup>2</sup> 2p <sup>4</sup> 4P <sub>3/2</sub>	2349.1
N-3	2345.7 <sup>+0.5</sup> <sub>-0.6</sub>	N	1s <sup>2</sup> 2s <sup>2</sup> (2p <sub>1/2</sub> (2p <sub>3/2</sub> <sup>2</sup> ) <sub>2</sub> ) <sub>3/2</sub>	((1s <sub>1/2</sub> 2s <sup>2</sup> 2p <sub>1/2</sub> ) <sub>1</sub> (2p <sub>3/2</sub> <sup>3</sup> ) <sub>3/2</sub> ) <sub>3/2</sub>	2349.4	1s <sup>2</sup> 2s <sup>2</sup> 2p <sup>3</sup> 2P <sub>1/2</sub> <sup>0</sup>	1s2s <sup>2</sup> 2p <sup>4</sup> 2P <sub>1/2</sub>	2348.6
			1s <sup>2</sup> 2s <sup>2</sup> (2p <sub>1/2</sub> (2p <sub>3/2</sub> <sup>2</sup> ) <sub>2</sub> ) <sub>5/2</sub>	((1s <sub>1/2</sub> 2s <sup>2</sup> 2p <sub>1/2</sub> ) <sub>1</sub> (2p <sub>3/2</sub> <sup>3</sup> ) <sub>3/2</sub> ) <sub>5/2</sub>	2348.5	1s <sup>2</sup> 2s <sup>2</sup> 2p <sup>3</sup> 2P <sub>3/2</sub> <sup>0</sup>	1s2s <sup>2</sup> 2p <sup>4</sup> 2P <sub>3/2</sub>	2347.6
			1s <sup>2</sup> 2s <sup>2</sup> (2p <sub>1/2</sub> (2p <sub>3/2</sub> <sup>2</sup> ) <sub>2</sub> ) <sub>3/2</sub>	((1s <sub>1/2</sub> 2s <sup>2</sup> 2p <sub>1/2</sub> ) <sub>1</sub> (2p <sub>3/2</sub> <sup>3</sup> ) <sub>3/2</sub> ) <sub>3/2</sub>	2346.3	1s <sup>2</sup> 2s <sup>2</sup> 2p <sup>3</sup> 2P <sub>3/2</sub> <sup>0</sup>	1s2s <sup>2</sup> 2p <sup>4</sup> 2D <sub>5/2</sub>	2345.2
O-1	2335.2 <sup>+0.6</sup> <sub>-0.7</sub>	O	1s <sup>2</sup> 2s <sup>2</sup> 2p <sub>3/2</sub> <sup>4</sup>	(1s <sub>1/2</sub> 2s <sup>2</sup> 2p <sub>1/2</sub> (2p <sub>3/2</sub> <sup>3</sup> ) <sub>3/2</sub> ) <sub>1</sub>	2333.8	1s <sup>2</sup> 2s <sup>2</sup> 2p <sup>4</sup> 1D <sub>2</sub>	2331.8	
O-2	2331.5 <sup>+0.4</sup> <sub>-0.5</sub>	O	1s <sup>2</sup> 2s <sup>2</sup> 2p <sub>1/2</sub> <sup>2</sup> (2p <sub>3/2</sub> <sup>2</sup> ) <sub>2</sub>	(1s <sub>1/2</sub> 2s <sup>2</sup> 2p <sub>1/2</sub> 2p <sub>3/2</sub> <sup>4</sup> ) <sub>1</sub>	2332.9	1s <sup>2</sup> 2s <sup>2</sup> 2p <sup>4</sup> 3P <sub>2</sub>	2330.2	
			1s <sup>2</sup> 2s <sup>2</sup> (2p <sub>1/2</sub> (2p <sub>3/2</sub> <sup>2</sup> ) <sub>2</sub> ) <sub>3/2</sub>	(1s <sub>1/2</sub> 2s <sup>2</sup> 2p <sub>1/2</sub> 2p <sub>3/2</sub> <sup>4</sup> ) <sub>0</sub>	2332.7	1s <sup>2</sup> 2s <sup>2</sup> 2p <sup>4</sup> 3P <sub>1</sub>	2329.8	
O-3	2326.7 <sup>+0.7</sup> <sub>-0.9</sub>	O	1s <sup>2</sup> 2s <sup>2</sup> 2p <sub>1/2</sub> <sup>2</sup> (2p <sub>3/2</sub> <sup>2</sup> ) <sub>2</sub>	(1s <sub>1/2</sub> 2s <sup>2</sup> 2p <sub>1/2</sub> (2p <sub>3/2</sub> <sup>3</sup> ) <sub>3/2</sub> ) <sub>2</sub>	2331.8	1s <sup>2</sup> 2s <sup>2</sup> 2p <sup>4</sup> 3P <sub>0</sub>	2329.1	
			1s <sup>2</sup> 2s <sup>2</sup> (2p <sub>1/2</sub> (2p <sub>3/2</sub> <sup>2</sup> ) <sub>2</sub> ) <sub>3/2</sub>	(1s <sub>1/2</sub> 2s <sup>2</sup> 2p <sub>1/2</sub> 2p <sub>3/2</sub> <sup>4</sup> ) <sub>1</sub>	2331.6	1s <sup>2</sup> 2s <sup>2</sup> 2p <sup>4</sup> 3P <sub>0</sub>	2328.9	
F-1	2314.96 <sup>+0.21</sup> <sub>-0.28</sub>	F	1s <sup>2</sup> 2s <sup>2</sup> 2p <sub>1/2</sub> <sup>2</sup> (2p <sub>3/2</sub> <sup>2</sup> ) <sub>2</sub>	(1s <sub>1/2</sub> 2s <sup>2</sup> 2p <sub>1/2</sub> (2p <sub>3/2</sub> <sup>3</sup> ) <sub>3/2</sub> ) <sub>1</sub>	2330.8	1s <sup>2</sup> 2s <sup>2</sup> 2p <sup>4</sup> 3P <sub>1</sub>	2328.2	
			1s <sup>2</sup> 2s <sup>2</sup> (2p <sub>1/2</sub> (2p <sub>3/2</sub> <sup>2</sup> ) <sub>2</sub> ) <sub>3/2</sub>	(1s <sub>1/2</sub> 2s <sup>2</sup> 2p <sub>1/2</sub> (2p <sub>3/2</sub> <sup>3</sup> ) <sub>3/2</sub> ) <sub>1</sub>	2326.5	1s <sup>2</sup> 2s <sup>2</sup> 2p <sup>4</sup> 1S <sub>0</sub>	2324.3	
F-2	2311.16 <sup>+0.29</sup> <sub>-0.43</sub>	Ne	1s <sup>2</sup> 2s <sup>2</sup> 2p <sub>1/2</sub> <sup>2</sup> (2p <sub>3/2</sub> <sup>2</sup> ) <sub>2</sub>	(1s <sub>1/2</sub> 2s <sup>2</sup> 2p <sub>1/2</sub> 2p <sub>3/2</sub> <sup>6</sup> ) <sub>2</sub>	2315.29	1s <sup>2</sup> 2s <sup>2</sup> 2p <sup>5</sup> 2P <sub>3/2</sub> <sup>0</sup>	2312.40	
			1s <sup>2</sup> 2s <sup>2</sup> (2p <sub>1/2</sub> (2p <sub>3/2</sub> <sup>2</sup> ) <sub>2</sub> ) <sub>3/2</sub>	(1s <sub>1/2</sub> 2s <sup>2</sup> 2p <sub>1/2</sub> 2p <sub>3/2</sub> <sup>6</sup> ) <sub>1</sub>	2314.05	1s <sup>2</sup> 2s <sup>2</sup> 2p <sup>5</sup> 2P <sub>1/2</sub> <sup>0</sup>	2311.15	
F-3	2306.7 <sup>+0.5</sup> <sub>-0.9</sub>	B	1s <sup>2</sup> (2p <sub>1/2</sub> (2p <sub>3/2</sub> <sup>2</sup> ) <sub>2</sub> ) <sub>5/2</sub>	((1s <sub>1/2</sub> 2s <sup>2</sup> 2p <sub>1/2</sub> ) <sub>1</sub> 2p <sub>3/2</sub> <sup>6</sup> ) <sub>5/2</sub>	2313.50	1s <sup>2</sup> 2s <sup>2</sup> 2p <sup>5</sup> 3P <sub>2</sub> <sup>0</sup>	2314.74	
			1s <sup>2</sup> (2p <sub>1/2</sub> (2p <sub>3/2</sub> <sup>2</sup> ) <sub>2</sub> ) <sub>3/2</sub>	((1s <sub>1/2</sub> 2s <sup>2</sup> 2p <sub>1/2</sub> ) <sub>1</sub> 2p <sub>3/2</sub> <sup>6</sup> ) <sub>3/2</sub>	2307.6	1s <sup>2</sup> 2p <sup>3</sup> 2D <sub>5/2</sub> <sup>0</sup>	2306.1	
						1s <sup>2</sup> 2p <sup>3</sup> 2D <sub>3/2</sub> <sup>0</sup>	2308.6	

## 4.8 The FAC Model

It has been indicated at various occasions throughout this work that especially for many-electron systems the numerical calculations of the energy levels in these ions can differ from reality by a few electron volts. To quantify this uncertainty for the FAC calculations in hand, the FAC output was combined to a model and fitted to the measured data. To limit the number of parameters in this model a few assumptions have to be made. First, it is assumed that the whole ion can be shifted in energy but that the relative distances between all lines of the same ion are correct. Remembering the terms going into the Hamiltonian for the relativistic hydrogen problem in section 3.3, there are some that can cause different shifts depending on any of the quantum numbers. The next assumption is that the relative line intensities within an ion are derived from the theory of detailed balance properly. There are two caveats to this assumption. The more severe one is the estimate that the radiative decay rates are only computed to within 20% of their true value. This uncertainty carries directly on to the intensities. The other issue is that, as discussed in section 3.12, the calculation of the line intensities is not yet self-consistent. The unknown charge balance in the ion trap is less crucial in case of no considered interaction between different ionization states as the normalization between the ions is neglected in this model anyway. But as soon as ion-ion interactions such as ionization and recombination mechanisms are taken into account, the abundance of one ion can seriously influence the line ratios in another ion. Then, last but not least, to stay consistent with the single-line fits of the previous sections and because the detector resolution has still not changed, all lines are frozen to the FWHM determined from the He-like lines.

With all these assumptions the model becomes relatively simple, though still computational expensive. All lines given by FAC for the same ion are convolved with a Gaussian of FWHM with mean equal to the FAC line minus some shift  $\Delta E$ . The simulated line intensity  $I_i$  is used as the norm of the single Gaussian lines while the norm of the compound is left as a fit parameter. Then the fit function for each ion is the sum over all of these Gaussians:

$$F(E_i, I_i, \Delta E, \text{FWHM}, N) = N \cdot \sum_i I_i \cdot 2 \sqrt{\left( \frac{\log(2)}{\pi \cdot \text{FWHM}} \right)} \int dE \exp \left( -4 \cdot \log(2) \cdot \frac{[E - (E_i - \Delta E)]^2}{\text{FWHM}^2} \right). \quad (4.5)$$

For the helium-like lines, the  $2p \rightarrow 1s$  and  $2s \rightarrow 1s$  transitions are computed in separate models as the abundant appearance of the forbidden line  $z$  is a special case. For all other ionization states, no  $2s \rightarrow 1s$  transitions are contained in the FAC output anyway because they are so weak that they fall under a certain threshold for lines to be listed. Since unfortunately all ionic states below F-like blend indistinguishably into each other, for this part of the spectrum also the relative line intensities and energies between the ions has to be considered to be correctly modeled such that the fit parameters for these ions are tied to each other.

The fits of the FAC model to the silicon and sulfur data are shown in Fig. 4.20 and 4.21. As expected this model does not lead to a perfectly well description of the data. Nevertheless, some of the line shapes agree remarkably well with the measurements; for instance, the (orange) C-like and the (pink) Be-like lines. How much the FAC data needs to be shifted to come to this agreement can be seen in table 4.6. The large discrepancy in the He-like  $z$  lines has already been discussed in the previous sections and is due to the

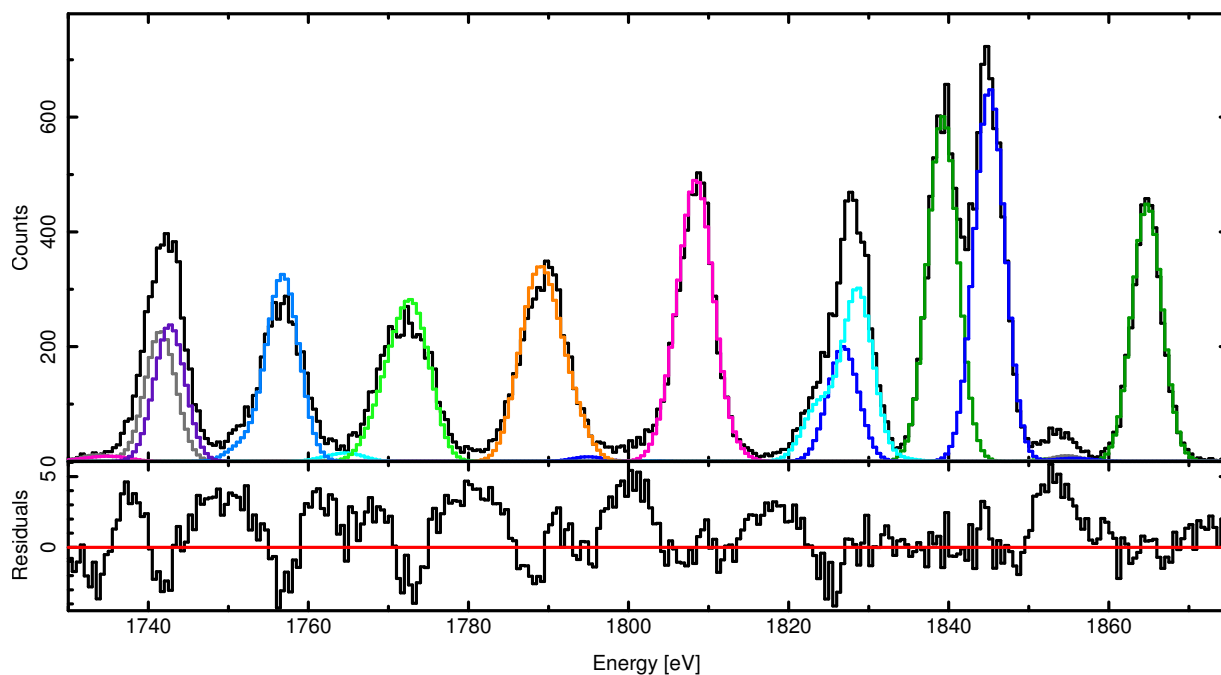


**Figure 4.20:** Fit of the silicon spectrum simulated with FAC to the laboratory measurement. The single components of the fit model are displayed in different colors. The color code indicates the iso-electronic sequences in the same convention as throughout the rest of this work.

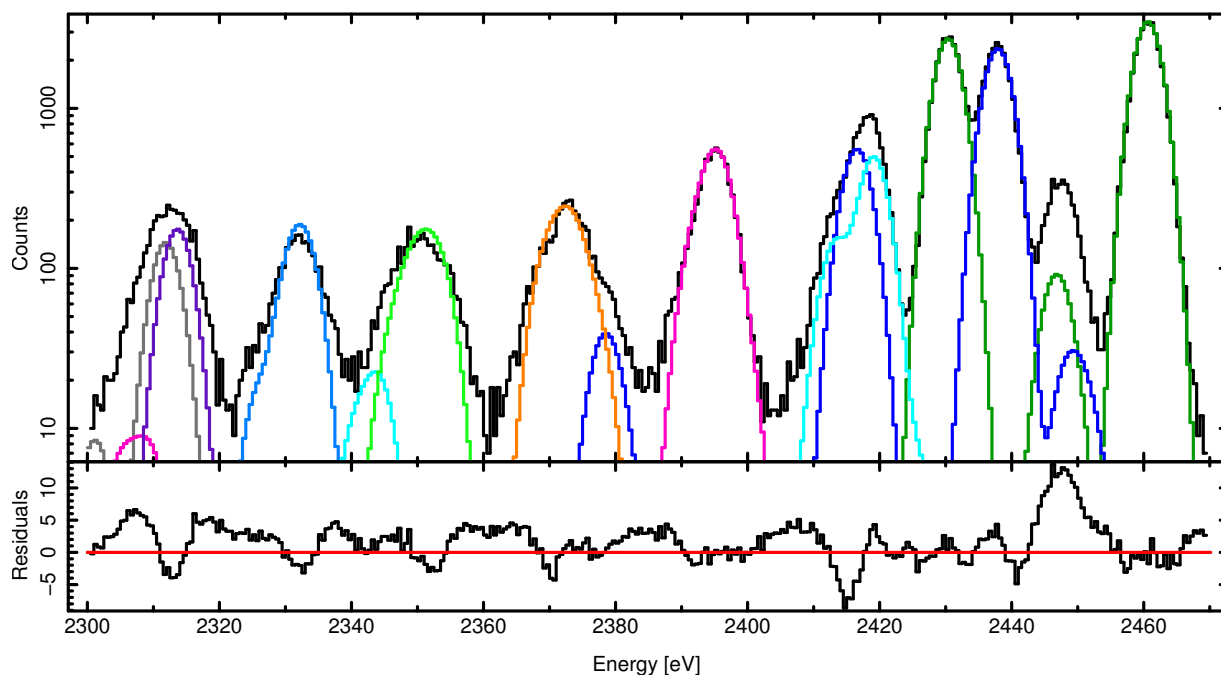


**Figure 4.21:** Fit of the sulfur spectrum simulated with FAC to the laboratory measurement. The single components of the fit model are displayed in different colors. The color code indicates the iso-electronic sequences in the same convention as throughout the rest of this work.

**Table 4.6:** Shifts of the FAC lines compared to the measured data. Due to the definition in equation 4.5 negative shifts  $\Delta E$  correspond to the FAC energy being higher than the measured one. The shifts are given in electron volts.

Ion	$\Delta E(\text{Silicon})$	$\Delta E(\text{Sulfur})$
H-like	$-0.24^{+0.28}_{-0.29}$	$-0.01 \pm 0.07$
He-like	$0.02 \pm 0.05$	$-0.192 \pm 0.017$
He z	$-1.06 \pm 0.06$	$-1.299 \pm 0.022$
Li-like	$-0.46 \pm 0.05$	$-0.647 \pm 0.023$
Be-like	$-0.28 \pm 0.09$	$-0.85 \pm 0.07$
B-like	$-0.12 \pm 0.06$	$-0.29 \pm 0.06$
C-like	$-0.21 \pm 0.08$	$-0.56 \pm 0.11$
N-like	$0.22 \pm 0.10$	$0.052 \pm 0.16$
O-like	$0.56 \pm 0.09$	$0.44 \pm 0.13$
F-/Ne-like	$0.76 \pm 0.07$	$1.24 \pm 0.13$

fact that numerical codes are not almighty. The apparently large shift of the F-/Ne-like lines can be explained from the calculation. Since no ions less ionized than the Ne-like iso-electronic sequence are considered when solving the rate equations, these lines are also missing in the FAC model with the effect that the F-/Ne-like complex has to be shifted to lower energies during the fit in order to account for the missing lines. Therefore, this last line of table 4.6 should only be taken with much care as it is dominated by systematics rather than the numerical problems of many-electron systems.

I don't care if anybody gets it. I'm going as the Doppler effect. If I have to, I can demonstrate:  
NYEEEROOOOM

Sheldon Cooper at a Halloween party  
in: *The Big Bang Theory*

## Chapter 5

# Chandra's View of Cyg X-1

### 5.1 Chandra

The *Chandra* X-ray observatory was launched on 1999, July 23 by the space shuttle *Columbia*. After it successfully reached its orbit, it was renamed from its working name *Advanced X-ray Astrophysics Facility (AXAF)* to honor the Indian-American astrophysicist Subrahmanyan Chandrasekhar (1910–1995). The energetic charged particles trapped in the van Allen belts by the Earth's magnetic field are extremely dangerous for the sensitive X-ray detectors on-board the satellite. Therefore, *Chandra* has a highly elliptical orbit with an eccentricity of  $\approx 0.88$  that leads it from as close as 3900 km perigee to around a third of the distance to the moon at roughly 145000 km apogee (December 2011 CXC, 2011). With these orbital parameters, *Chandra* spends around 80% of the 63.5 hour long orbital period outside of the radiation belts. The length of the orbit makes extremely long continuous observations of up to 160 ks possible.

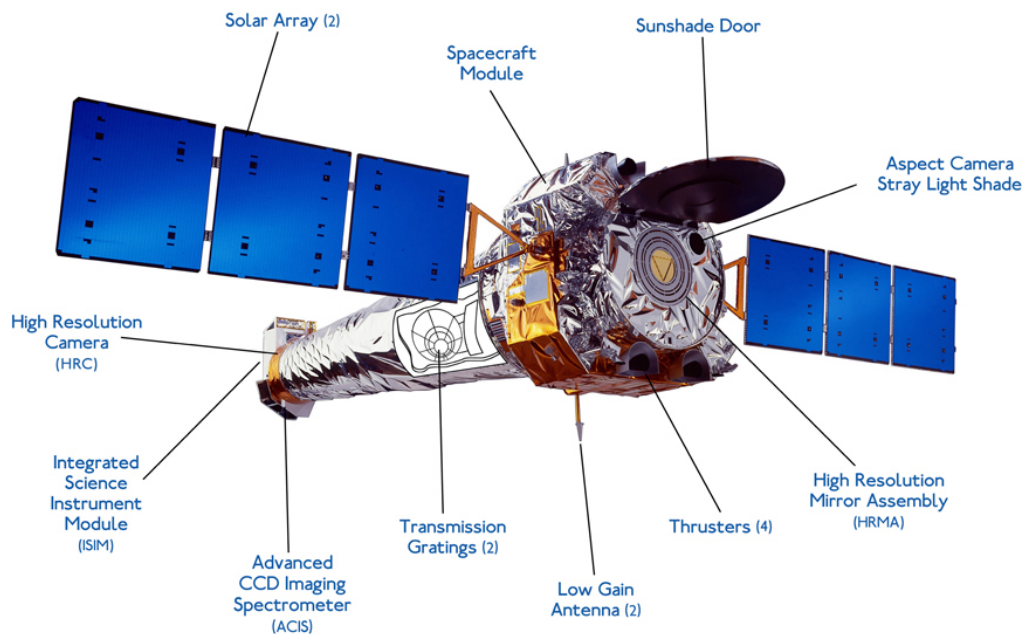


Figure 5.1: *Chandra* spacecraft (from <http://chandra.harvard.edu/about/spacecraft.html>).

*Chandra* is together with the *Hubble Space Telescope*, the late *Compton Gamma-Ray Observatory* and the *Spitzer Space Telescope* one of NASA's four Great Observatories. It comprises a number of high precision instruments (see Fig. 5.1). A complete description of them can be found in the Proposer's Observatory Guide (CXC, 2011). Here only an overview over the ones relevant for this work is given.

### 5.1.1 The Mirrors

An essential part of a telescope are the mirrors to collect and focus the light onto the detectors. Unfortunately, the index of refraction  $n$  is a function of the energy of the light. According to Snell's law of refraction

$$\frac{\sin \alpha_1}{\sin \alpha_2} = \frac{n_2}{n_1} = n, \quad (5.1)$$

where  $\alpha_i$  are the angles of incidence and refraction measured to the normal of the surface and  $n_i$  are the indices of refraction of the two materials, total internal reflection, i.e.,  $\alpha_2 \geq 90^\circ$ , only occurs below a critical angle  $\theta_c = 90^\circ - \alpha_1$  with

$$\cos \theta_c = n = \sqrt{\epsilon_r \mu_r}. \quad (5.2)$$

The index of refraction is defined as the ratio of the speed of light in vacuum and the speed of light in the medium and can be determined via the Maxwell relation  $n = \sqrt{\epsilon_r \mu_r}$  (Maxwell, 1865). The permeability  $\mu_r$  of the material is approximately unity and the dielectric constant  $\epsilon_r$  can be expressed in terms of the electron density  $ZN$  for free electrons (e.g. in a metal) if the frequency  $\omega$  is much larger than any resonance in the material:

$$\epsilon_r = 1 - \frac{\omega_p^2}{\omega^2} \quad \text{with the plasma frequency} \quad \omega_p = \sqrt{\frac{4\pi Z N e^2}{m_e}} \quad (5.3)$$

(Jackson, 2006). Since  $\epsilon_r$  is rather small and we hence expect small angles  $\theta_c$ , we can approximate  $\sqrt{\epsilon_r \mu_r} \approx 1 - (\epsilon_r - 1)/2$  and  $\cos \theta_c \approx 1 - \alpha^2/2$ . With  $N$  written in terms of the mass density  $\rho = A m_u N$  where  $A$  is the atomic mass number and unit  $m_u$ , the critical angle can be expressed as

$$\theta_c = \sqrt{\frac{1}{\pi} \frac{Z}{A} \frac{\rho}{m_u} \frac{e^2}{m_e c^2}} \cdot \lambda \quad (5.4)$$

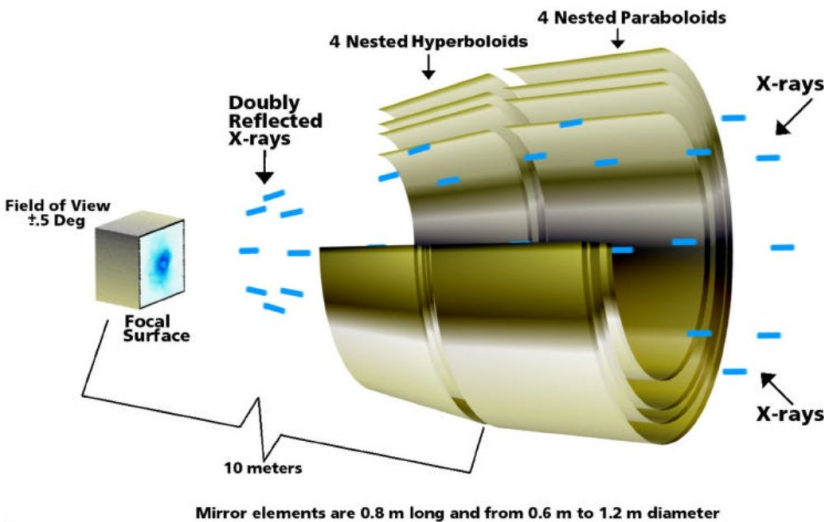


**Figure 5.2:**  
Chandra's mirror assembly  
(from [http://chandra.harvard.edu/about/telescope\\_system.html](http://chandra.harvard.edu/about/telescope_system.html)).

with the wavelength  $\lambda = c \cdot 2\pi/\omega$ . For realistic numbers for X-rays ( $\lambda \approx 1 \text{ \AA}$ ) and gold ( $Z = 79$ ,  $A = 197$ ,  $\rho = 19.3 \text{ g cm}^{-3}$ ) we then obtain a critical angle  $\theta_c \approx 1$ . Because of the small angle with respect to the surface of the material, the reflection is referred to as *grazing incident reflection* (Aschenbach, 1985).

This shallow angle means that the mirrors have to be aligned almost parallel to the incident X-rays and hence have a very long focal length and small effective reflecting area compared to the geometry of the mirror shells. Unfortunately, this condition also leads to severe problems with astigmatism. Wolter (1952) found that using paraboloid/hyperboloid or a hyperboloid/ellipsoid combinations of mirrors mounted coaxial and confocal instead of a single spherical mirror leads to major improvements of these problems. To increase the effective area, a set of nested mirror shells is used. Wolter (1952) was originally interested in X-ray microscopes to increase their resolving power. Only Giacconi & Rossi (1960) adopted the idea for X-ray telescopes where it is widely used nowadays. In the case of *Chandra* Wolter's ideas are implemented with a set of four nested paraboloids followed by the same number of hyperboloids (see Fig. 5.2). The mirrors are coated with a 33 nm thick iridium layer. Iridium has only two protons less than gold but is the element with the second highest density, thus maximizing the critical angle (eq. 5.4).

### 5.1.2 The Gratings

In order to be able to do spectroscopy with the focused light, *Chandra* is equipped with a set of gratings, which can either stay tilted to leave room for other instruments or be flipped into the optical path. The gratings disperse the transmitted light according to the grating equation

$$m \cdot \lambda = p \cdot \sin \beta \quad (5.5)$$

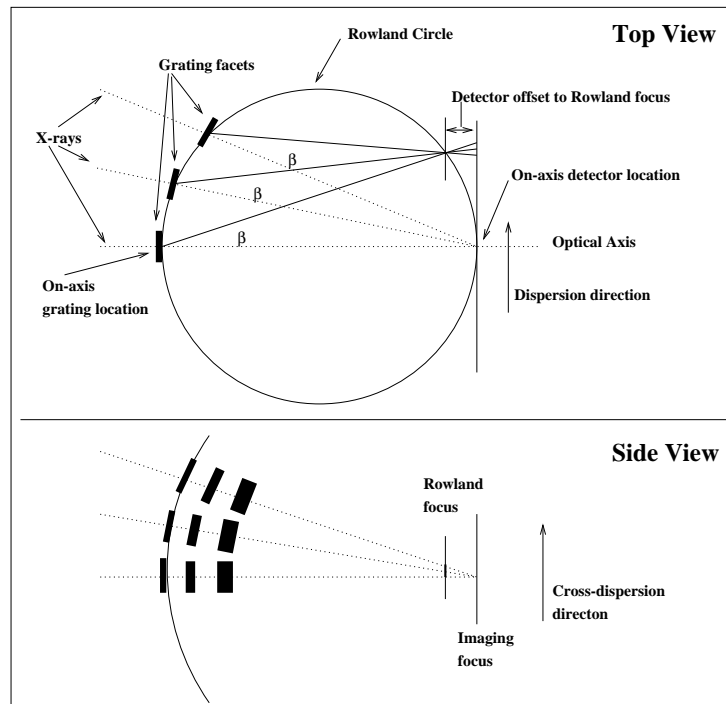


Figure 5.3: The Rowland geometry (from CXC, 2011).

where  $m$  is the order,  $\lambda$  the wavelength in Ångström,  $p$  the period of the grating and  $\beta$  the deflection angle. The angles of the different orders of the same wavelength only depend on the period of the grating's grooves, but not on their shape (Palmer & Loewen, 2005). By choosing the spacing of the grooves carefully, it can be controlled in which diffraction order most of the diffracted energy will end up. Also, diffracted beams might overlap depending on the incident wavelength range and grating density, i.e., the higher  $m$ , the stronger the overlap between succeeding diffraction orders. This overlap can be separated with energy dispersive X-ray detection in the focal plane.

There are two sets of gratings: the Low and the High Energy Transmission Gratings (LETG and HETG). The LETG operates in the energy range 0.08...0.2 keV. Therefore, only the HETG with an energy range of 0.4...10 keV is of interest for our purpose. The gratings on-board *Chandra* both follow the Rowland geometry (Rowland, 1882). The Rowland geometry reduces any additional optical aberrations coming from the gratings and ensures that light that has already been focused by the mirrors and goes through different grating facets are again focused at the same point. Figure 5.3 shows a sketch of the Rowland geometry as it is realized in the HETG. Grating facets are mounted with their centers being on the surface of the Rowland torus, which is formed by rotating the Rowland circle about the line through the on-axis focus parallel to the dispersion direction. So in the figure of the top view, the axis of the torus would be in the plane perpendicular to the optical axis while in the side view it would stick out perpendicular to the page. The Rowland circle is a circle with diameter equal to the distance between a grating facet on the optical axis and the position of the zeroth order image in the focal plane. This diameter is about 8.63 m for HETG.

As indicated in the top view of the sketch, the focal point for each diffraction angle belongs to a certain position on the edge of the Rowland circle. To maintain the focal properties of the telescope in dispersion direction for a large range of diffraction angles  $\beta$ , the shape of the image plane of an ideal detector would thus follow the counterpart of the Rowland circle. The deflection of photons by the grating becomes larger with decreasing photon energy, making the curvature of the Rowland circle more important. Thus, the HRC-S detector which is mostly used in combination with the LETG follows this curvature while ACIS-S for HETG is mounted tangentially to the Rowland circle.

### 5.1.3 HETGS

The HETG (Canizares et al., 2005) consists of two sets of gratings, the High Energy Grating (HEG) for the energy region of 0.8 to 10.0 keV and the Medium Energy Grating covering 0.4 to 5.0 keV. Their resolving power ( $E/\Delta E$ ) ranges from 65 (80) at high energies to 1070 (970) at the lower energy limit for HEG (MEG). This resolving power translates to an energy resolution of 0.4 to 77 eV FWHM.

The grating facets of HEG and MEG are both built out of gold bars attached to a polyimide plating base. They are mounted in two rings each on a support structure (1.1 m diameter) on the surface of the Rowland torus; compare Figure 5.4 where the inner two rings resemble the 144 grating facets of HEG and the outer two rings the 192 facets of MEG. The gold bars of HEG have a width of 1200 Å with a period of 2001 Å, while the MEG facets have a period of 4002 Å with 2080 Å wide bars. The one-half ratio of the bar width to the period suppresses even orders of dispersion such that the determination of photons in the first order is as unambiguous as possible. Since the dispersion directions of HEG and MEG differ by almost 10°, the image of a point source dispersed by HETG is a crossed pair of



**Figure 5.4:** HETG facets mounted on the Rowland torus (from [http://space.mit.edu/HETG/hetg\\_info.html](http://space.mit.edu/HETG/hetg_info.html)).

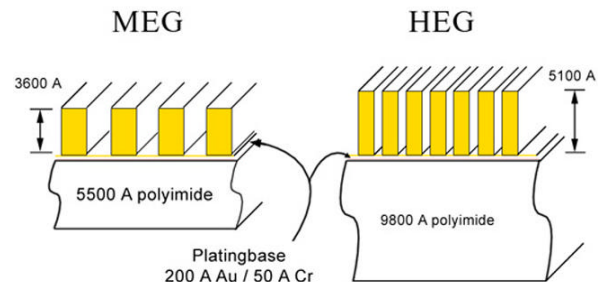


**Figure 5.5:** The High Energy Transmission Grating (from CXC, 2011).

arms (see Fig. 5.6).

The HETG is usually used in combination with the High Resolution Mirror Assembly (HRMA) and the Advanced CCD Imaging Spectrometer (ACIS), their combination being called High Energy Transmission Grating Spectrometer. Due to the smaller period of the HEG, it has a higher spectral resolution of  $5.5 \text{ m}\text{\AA}$  per ACIS detector pixel, while the MEG with its lower resolution of ‘only’  $11 \text{ m}\text{\AA}$  per ACIS pixel has the advantage of covering a larger energy range.

### 5.1.4 The ACIS Detector

The Advanced CCD Imaging Spectrometer (ACIS, Garmire et al., 2003) is one of two detectors in the Science Instrument Module (SIM). The interested reader can look up the details of the second detector, the High Resolution Camera (HRC), in CXC (2011). Both detectors can be used in two modes: one with a longish detector setup for grating spectroscopy (-S) or a square shaped setup for imaging (-I).

ACIS-I consists of 4 planar CCD chips in a  $2 \times 2$  array and is not employed for our Cyg X-1 observations. ACIS-S is an  $1 \times 6$  array of CCD chips numbered S0 to S5 successively. The CCD chips are silicon solid-state detectors with  $1024 \times 1024$  pixels. To prevent electrons in the valence band to be excited to the conduction band thermally rather than through the inner photon effect, the chips are operated at  $-90$  to  $-120^\circ \text{C}$ . The electron-hole pairs produced by incident X-ray photons result in a measurable charge that is proportional to the X-ray energy: every such pair corresponds to an X-ray energy of  $3.7 \text{ eV}$ . This energy dependence of the detector is in contrast to optical CCDs where each photon makes exactly one electron-hole pair such that the read-out charge is proportional to the intensity of the incoming light rather than the energy of its photons. Optical blocking filters (OBF) of  $3.5 \mu\text{m}$  thick layers of aluminum and polyimide are supposed to shield the CCD chips from contamination by optical light.

Four of the six chips are front-side-illuminated (FI) chips. This means that the charges are produced, stored and read-out at the front side of the chip, the side that is illuminated by the X-rays. Low-energetic cosmic protons, which are also focused by the mirror assembly,

damaged these chips already very early during the mission (Weisskopf et al., 2002). Since this hazard was discovered and its cause isolated, ACIS is removed from the focal plane of the mirrors during every pass of the satellite through the Earth's radiation belts. The other two chips (S1 and S3) are back-side-illuminated (BI) and therefore suffered from less damage through the radiation belts. Since X-rays are able to penetrate the silicon crystal, this approach is well possible. Over time the detection efficiency of ACIS has decreased slowly because of molecular contamination of the OBFs.

It is unavoidable to have small gaps between the single detector chips (corresponding to 18 pixels in the case of ACIS). To recover the information lost with the part of the spectrum hitting exactly those gaps, *Chandra* dithers in a Lissajous-pattern. Thus the image is spread over several pixels so that during an observation not always the same range of the dispersed spectra is affected. Since every photon event is recorded with a time stamp, the resulting differences in exposure time and effective area can be accounted for during the post-processing of the raw data. An additional advantage of *Chandra*'s dithering is that the impact of bad pixels has less influence on the data analysis.

### 5.1.5 Readout modes

A CCD is read out by applying voltages to each row in such a way that all electrons move one row towards the frame store register at the end of each column. The transfer from one row to another takes  $40 \mu\text{s}$  so that it is possible to read out the whole column in 41 ms. The readout of a full frame store, however, takes 3.2 s.

If the brightness of the source is low enough, it is suitable to choose the Timed Exposure (TE) read-out mode of ACIS. Here, the frame store is read out while the CCD is exposed to the incoming X-rays for some time  $t_{\text{exp}}$ . The minimum sensible exposure time is, of course, 3.2 s. The only way to increase this time resolution is to use only parts of the CCD chips.

In case of very bright sources, the probability increases for the CCD chip to be hit during the read-out process and for more than one photon to hit the same detector pixel. The former leads to a misidentification of the event position since the pixels have already been shifted. The latter is called pile-up and has the problem that two photons in the same pixel during one frame-time can not be distinguished. They are misinterpreted as a single event with an energy nearly as high as the sum of the two single events' energies. These events are either rejected by the software or are identified as higher order events, both causing a reduced flux in the main first order spectra. For nice reviews of pile-up in CCD chips see Ballet (1999, 2001) and Davis (2001).

To avoid these effects in very bright sources, another readout mode can be chosen for the observation. In Continuous Clocking (CC) mode the columns are read out continuously. Since then the information about the row that was hit by the photon is invalid, effectively decreasing the detector since to  $1024 \times 1$  pixels. In return for this sacrifice, the frame time is reduced to 3 ms. To obtain a valid flux calibration in this mode, the HEG and MEG spectra still have to be separated. However, due to their different dispersion, the internal energy resolution of the CCD chips is sufficient to distinguish these events. The afore mentioned suppression of the even order spectra ensures that the first order HEG spectrum can not be confused with the overlapping second order MEG spectrum.

**Table 5.1:** Start and end time of obs. ID 3814 (after Hanke (2007), p.53).

	date	Chandra-time <sup>a</sup>	MJD <sup>b</sup>	phase
start	2003-04-19, T16:47:31	167 158 051	52 748.69967	0.93
end	2003-04-20, T06:41:43	167 208 103	52 749.27897	0.03

<sup>a</sup>The Chandra-time is measured in seconds since 1998-01-01, T00:00:00 (MJD 50814).

<sup>b</sup>Modified Julian Date:  $MJD = JD - 2400000.5$  where JD is the Julian Date counted in days since noon of Jan 1<sup>st</sup>, 4713 BC.

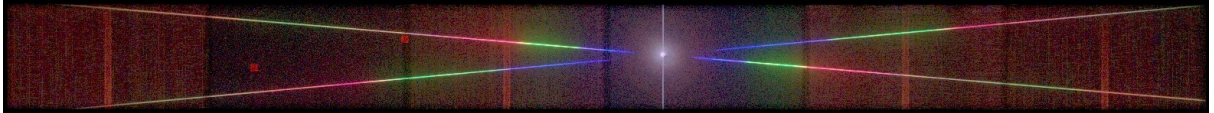


**Figure 5.6:** Sky-image of ObsID 3814, color-coding the photon energies (from Hanke (2007), Fig. 4.2).

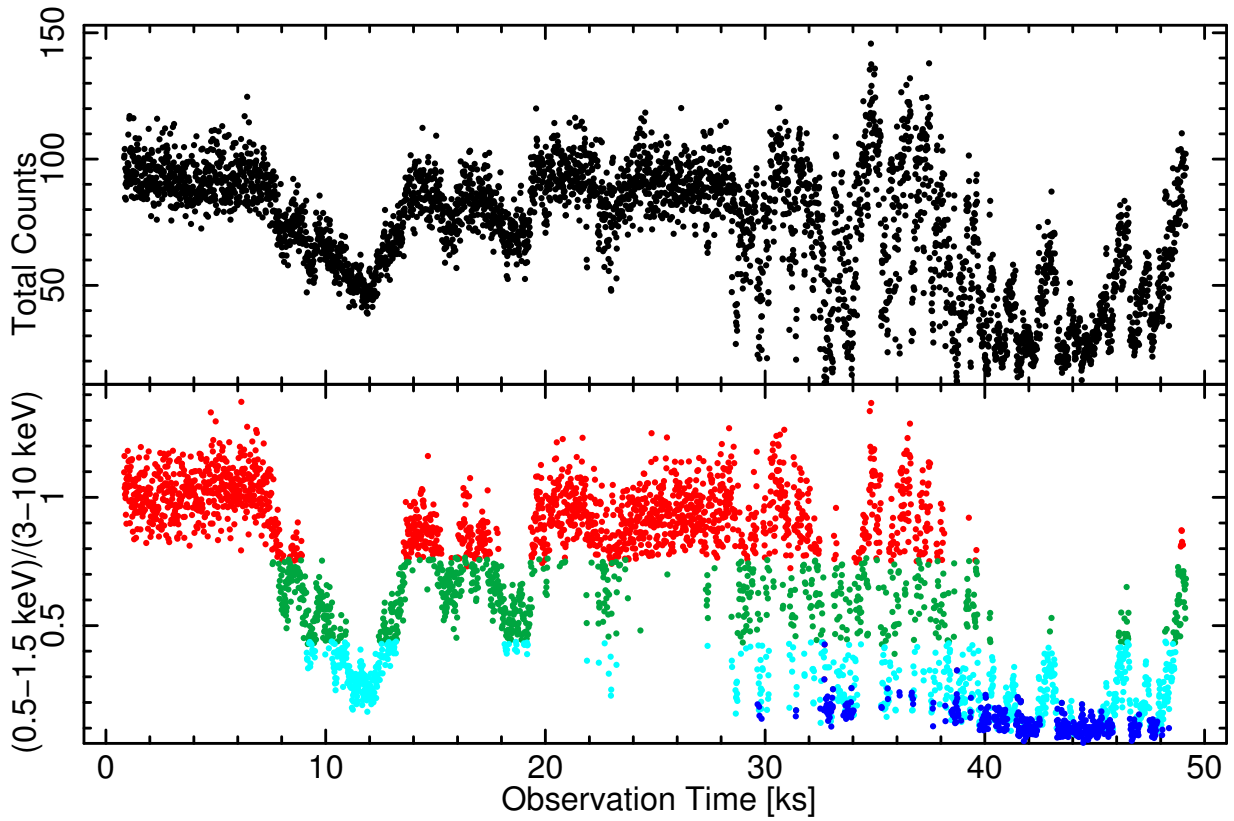
## 5.2 ObsID 3814

There are several *Chandra* observations available which were found to have absorption lines of low charge states of silicon and at least some also of sulfur (Hanke, 2011). The experimental results for the line centers of these two elements shall now be exemplarily applied to one of these observations to better constrain the origin of the lower charge states in the Cyg X-1 system. In the following sections, the focus is on the 48 ks *Chandra* observation # 3814. The observation was originally proposed by Katja Pottschmidt et al. to examine the soft X-ray absorption disk and probe the widely unknown properties of the stellar wind. The observation was carried out in 19/20 April 2003 when the black hole was in superior conjunction, i.e., around phase  $0^\circ$  where the absorptions dips preferentially occur. For a detailed description of the observation time see table 5.1.

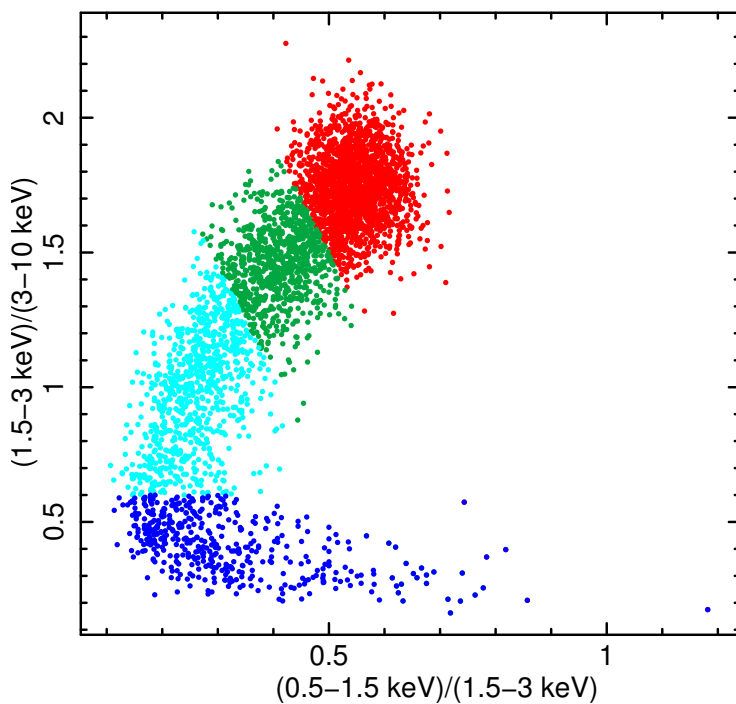
The observation was performed with HETGS and ACIS-S in timed exposure (TE) mode with a frame time of 1.741 s. This short frame time is possible by only reading out a 512 pixel sub-array. To avoid telemetry saturation, an attempt was made to cover the zeroth-order image with a  $40 \times 40$  pixel window but the source was not completely covered.

Figure 5.6 shows the image of the dispersion on the CCD chips. The shortest wavelength close to the zeroth-order image, corresponding to the energy band 2.5–8 keV is colored in blue, the mid energy band in green and the low energy band of 0.2–1.5 keV in red. Due to their lower dispersion the MEG arms, going from the upper left to the lower right corner, can be clearly distinguished from the HEG arms which run from the lower left corner to the upper right one. There are also two afterglow events and four hot columns visible. They are at fixed detector position and therefore at different sky positions.

The non-dip as well as the dip spectrum of this (Hanke, 2007; Hanke et al., 2009) and other *Chandra* observations (Hanke, 2011; Miškovičová, 2012) have already been analyzed extensively. Therefore, we can build up on these results and focus on the low charge states for which the atomic data tables have been missing so far. Nevertheless, for one observation we will quickly go through the steps needed to prepare the spectrum for fitting the Si and S regions.



**Figure 5.7:** Top: *Chandra* lightcurve from ObsID 3814. Bottom: Hardness ratio of the energy bands A (0.5–1.5 keV) and B (3–10 keV) to emphasize the periods of dipping. The color code indicates the cuts applied to extract spectra of different dipping strength, no (red), weak (green), intermediate (light blue) and strong (blue) dips.



**Figure 5.8:** Color-color diagram for ObsID 3814. The colors are defined as softness ratios of consecutive energy bands A (0.5–1.5 keV), B (1.5–3 keV) and C (3–10 keV).

### 5.2.1 Lightcurves and Color-Color Diagrams

We start with the lightcurve which is displayed in the top panel of figure 5.7. Two major dips occurred during this observation. The first one is rather compact and lasts around 1 h 43 min with the deepest core still having a duration of 40 min. The second dip is more extended with a duration of over 2 h and also somewhat deeper. Hanke (2007) followed the work of Pottschmidt et al. (2006) and defined the non-dip spectrum for times with a total count rate of at least  $82.7 \text{ counts s}^{-1}$ . Since the total count rate can be affected by various processes while the spectrum hardens during dipping (cf. Sec. 2.6.2), it is more sensible to set the cuts for the different dipping stages via the hardness ratio, or, to resemble the dip structure of the lightcurves, via the softness ratio rather than the lightcurve itself. Therefore, Hanke (2011) changed the previous approach and defined the different stages of dipping via the softness ratios in the color-color diagram (Fig. 5.8). Colors are defined as the intensity ratio of different energy bands. The soft X-ray color is the ratio of the 0.5–1.5 keV ( $A$ ) and the 1.5–3 keV ( $B$ ) *Chandra* count rate, the hard X-ray color the ratio of the 1.5–3 keV ( $B$ ) and the 3–10 keV ( $C$ ) rate.

Since this analysis is mainly based on the findings of Hanke (2011), the cuts applied there are adopted in this work. They are

$$\begin{aligned}
 B/C &\geq 3.5 - 4A/B \\
 3.5 - 4A/B > B/C &\geq 2.65 - 4A/B \\
 2.65 - 4A/B > B/C &\geq 0.6 \\
 0.6 > B/C. &
 \end{aligned} \tag{5.6}$$

for the ‘non-dip’ (red), ‘weak dip’ (green), ‘dip’ (light blue) and ‘strong-dip’ (dark blue) spectra. How these cuts in the CC-diagram translate to the softness ratio  $A/C$  can be seen in the lower panel of figure 5.7.

### 5.2.2 Continuum

Before we can take a closer look at the evolution of the Si and S absorption lines, we need to describe the continuum of the X-radiation that is absorbed by these elements. For each of the four spectra the continuum model is evaluated over the whole energy range of 2 to 15 Å. Since the detector can be affected by pile-up, the continuum model is wrapped in the ISIS function `simple_gpiled3` to reduce the effects of pile-up. During pile-up two or more photons arrive in the same pixel during the same frame time and are hence counted as only one photon of higher energy or different order. Pixels with high count rates are usually more affected by pile-up with the effect scaling exponentially. Assume  $C$  to be the number of counts in a pixel and  $p$  the pile-up fraction. Then the count rate of the pixel with the highest count rate  $\max_j \{C(j)\}$  is reduced by a factor  $1 - p$  by

$$C'(i) = C(i) \cdot (1 - p)^{\frac{C(i)}{\max_j \{C(j)\}}}. \tag{5.7}$$

Nowak et al. (2008)’s function `simple_gpiled` modifies an arbitrary model spectrum  $M(E)$  according to the pile-up formula (Eq. 5.7) by estimating the number of counts  $C_M$ : The total number of counts in a pixel  $B(i)$  in a single readout cycle is roughly given by the flux  $M$ , the ancillary response functions (ARFs)<sup>1</sup>  $A_m$  for each order  $m$  and the ratio of

<sup>1</sup>The ARF is a matrix containing the energy dependent effective area of the telescope. The effective area is smaller than the actual geometric collecting area of the telescope due to effects of reflectivity, vignetting and detector quantum efficiency.

frame time  $t_{\text{frame}}$  and exposure time  $t_{\text{exp}}(m, i)$ . The latter has to be used instead of the frame time as especially pixels close to the gaps between the CCD chips are not exposed to radiation for the full frame time due to the dithering of the satellite, resulting in an effective count rate  $c_m$  rather than  $C_m$  with

$$c_M^{\text{sim}}(i) = \sum_{m=1}^3 \frac{t_{\text{frame}}}{t_{\text{exp}}(m, i)} \cdot A_m(m, \langle E \rangle_{[E-i, E_{i+1}]}) \cdot \int_{E_i}^{E_{i+1}} dE M(m, E) \\ \rightarrow M'(i) = M(i) \cdot (1 - p)^{\frac{c_M^{\text{sim}}(i)}{\max_j \{c_M^{\text{sim}}(j)\}}}. \quad (5.8)$$

Obviously this model is non-local and should therefore only be fitted over the whole spectral range. Hanke (2007) introduced another parameter  $\beta$  to re-parametrize the pile-up model in a way that makes it possible to use it locally. A local pile-up modeling is desirable especially for local features like emission or absorption lines so that the value of one bin is not affected by modifications in a distant bin. The exponential scale  $\beta$  is defined via

$$(1 - p)^{\frac{c_M^{\text{sim}}(i)}{\max_j \{c_M^{\text{sim}}(j)\}}} \equiv \exp(-\beta \cdot c_M^{\text{sim}}(i)) \quad \text{with} \quad -\beta = \frac{\log(1 - p)}{\max_j \{c_M^{\text{sim}}(j)\}}. \quad (5.9)$$

With  $\log(1 - p) \approx -p$  for small pile-up fractions  $\beta$  is roughly proportional to  $p$ .

For a number of counts per pixel in one frame time of  $C = c \cdot t_{\text{frame}} \cdot \Delta\lambda$  a pile-up reduction of  $e^{-C}$  is expected from Poisson (1837) statistics. In a first approximation the exponential scale can therefore be estimated as

$$\beta_0 \approx t_{\text{frame}} \Delta\lambda, \quad \text{where} \quad \Delta\lambda_{\text{MEG}} = 3 \cdot 11 \text{ m\AA} = 2 \cdot \Delta\lambda_{\text{HEG}} \quad (5.10)$$

with the  $\Delta\lambda_{\text{HEG/MEG}}$  being the wavelength range covered by one ACIS pixel. The factor of 3 is introduced because the data processing uses  $3 \times 3$  pixel arrays to determine the order  $m$  of an event.  $\beta_0$  is then used as a starting point for determining the real  $\beta$ . Since the fractional exposure and the wavelength range per pixel can easily be read out from the data header files, it is convenient to define the fit parameter such that it is just a scaling factor to the automatically determined  $\beta_0$ . This simplification for the user is implemented in the ISIS function `simple_gpile3`.

The continuum itself in the simplest case, i.e., the non-dip spectrum, can be described by an absorbed powerlaw (Hanke, 2007). The nose-like shape of the data in the CC-diagram (Fig. 5.8), however, cannot be explained by neutral absorption alone (Hanke et al., 2008). Pure absorption with increasing column density of the interstellar medium (ISM) would lead to a track from the (soft) upper right to the (hard) lower left corner of the CC-diagram (Hanke, 2011). The bend observed during the deepest dip (dark blue) can be explained by a partial covering model for photoelectric absorption (e.g.; Stelzer et al., 1999; Bałucińska-Church et al., 2000)

$$f_c \cdot \exp(-N_{\text{H}} \cdot \sigma_{\text{eff}}(E)) + (1 - f_c) \exp(-N_{\text{H}}^{\text{ISM}} \cdot \sigma_{\text{eff}}(E)) \quad (5.11)$$

where a fraction  $f_c$  is absorbed by a column density  $N_{\text{H}}$  intrinsic to the source while the remaining  $1 - f_c$  is only absorbed by a constant  $N_{\text{H}}^{\text{ISM}}$  of the interstellar medium. In case of pure absorption ( $f_c = 100\%$ ) the track in the CC-diagram is strictly monotonic. Any track with a smaller covering fraction bends twice with increasing  $N_{\text{H}}$ , once for each of the two colors becoming dominated by the uncovered fraction  $1 - f_c$  instead of the more

**Table 5.2:** Parameters of the continuum model for ObsID 3814.

Joint parameters		Value	Individual parameters			
			Data set $i$	$f_c^{(i)}$ (%)	$N_H^{(i)}$ ( $10^{22} \text{ cm}^{-2}$ )	$c^{(i)}$ (%)
.....	<b>powerlaw</b>	.....				
	$N$ [ $\text{s}^{-1} \text{ cm}^{-2} \text{ keV}^{-1}$ ]	$1.59 \pm 0.10$				
	$\Gamma_1$	$1.66 \pm 0.04$	‘nondip’	$14 \pm 4$	$6.8_{-0.9}^{+1.0}$	$\equiv 100$
.....	<b>TBnew<sup>(0)</sup></b>	.....	‘weak dip’	$54.0 \pm 0.7$	$2.22_{-0.8}^{+0.9}$	$95.4 \pm 0.8$
	$N_H^{(0)}$ [ $10^{21} \text{ cm}^{-2}$ ]	$6.50_{-0.14}^{+0.15}$	‘dip’	$85.22 \pm 0.26$	$3.23 \pm 0.05$	$92.9 \pm 1.0$
			‘strong dip’	$96.59 \pm 0.08$	$8.65 \pm 0.10$	$85.5 \pm 0.9$

Notes: The joint parameters are determined via the non-dip spectrum which should not be affected by any additional absorption altering the apparent photo-index. These joint parameters are then fixed to the listed values while calculating the individual parameters. For each of the four data sets the four spectra ( $\pm$  first order of HEG/MEG) are fitted simultaneously).

	.....	<b>simple_gpile3(<math>i</math>).beta</b> [ $\beta_0$ ]	.....	
HETG arm	‘nondip’	‘weak dip’	‘dip’	‘strong dip’
HEG-1	$1.46 \pm 0.07$	$1.27 \pm 0.10$	$0.87 \pm 0.15$	$\leq 0.08$
HEG+1	$1.56 \pm 0.07$	$1.37 \pm 0.10$	$0.99_{-0.15}^{+0.14}$	$\leq 0.11$
MEG-1	$1.029 \pm 0.016$	$0.99 \pm 0.04$	$0.88_{-0.07}^{+0.06}$	$0.45 \pm 0.13$
MEG+1	$1.129 \pm 0.013$	$1.110 \pm 0.027$	$1.02 \pm 0.06$	$0.34 \pm 0.12$

strongly absorbed part  $f_c$  (see Hanke et al., 2008, Fig. 5b, for a plot of the tracks for varying  $N_H$  and  $f_c$ ).

Table 5.2 lists the fit results for the continuum model

$$\text{simple\_gpil3} \otimes \text{powerlaw} \times \text{TBnew}^{(0)} \times (f_c^{(i)} \cdot \text{TBnew}^{(i)} \cdot \text{cabs}^{(i)} + (1 - f_c^{(i)})) \cdot c^{(i)}. \quad (5.12)$$

While the **powerlaw** and **TBnew<sup>(0)</sup>** parameters are determined solely from the non-dip spectrum, which should be largely unaffected by absorption dips, the partial covering models are derived individually for the different spectra (index  $i$ ). **TBnew<sup>2</sup>** models the neutral absorption (Wilms et al., 2012). **cabs** models optically-thin Compton scattering which becomes important for the covering fraction  $f_c$  due to an additional absorber. As the Compton scattering depends on the same column density as the neutral absorption, the column densities of **cabs<sup>(i)</sup>** and **TBnew<sup>(i)</sup>** are tied to each other during the fit.  $c^{(i)}$  is a flux normalization constant to account for energy independent differences in the flux of the different dipping states. The fit results are in good agreement with the results of the partial coverer model in Hanke (2007).

Since the pile up rate strongly depends on the count rate and the count rate is severely decreased during dipping, keeping the **simple\_gpile3** parameters fixed to the non-dip values for all dipping stages would overestimate the effect of pile-up especially during the strong dip with very low flux. Therefore, these parameters are also fitted separately for each dipping stage. They are shown in table 5.2 together with the other continuum parameters. The fact that the pile-up rate is close to zero for the strong-dip spectra justifies this approach.

<sup>2</sup><http://pulsar.sternwarte.uni-erlangen.de/wilms/research/tbabs/>

### 5.2.3 Absorption Lines and Equivalent Widths

With the continuum fixed to the above values, the Si and S regions of each spectrum can now be examined more closely. The absorption lines of the various charge states are modeled with Gaussian line profiles. In contrast to Hanke (2011) not only the equivalent widths but also the line centers are allowed to vary between the different dipping stages. The equivalent width (EW) of a line is a measure for its line strength that is independent of the exact line profile. It is defined as the width of a rectangle with the same area (normalization) as the line profile and the height of the continuum flux, i.e, the equivalent width is the width of a rectangular area around the line center that emits no light at all (Karttunen et al., 1987).

Table 5.4 illustrates how the lower ionized lines grow stronger while the absorption from highly charged ions almost vanishes with increasing dipping, consistent with the theory of increased absorption due to clumps of denser and colder material crossing our line of sight. For a visual illustration of this line evolution with dipping see figures 5.9 and 5.10. For a qualitative comparison of these line centers with the reference lines measured in EBIT see figures 5.11 and 5.12.

A closer look at the line centers in table 5.3 already reveals that the absorption lines are pretty close to their rest wavelength. Moreover, the line centers are consistent with each other (within their uncertainties) during different stages of dipping, implying that the increased absorption is actually caused by a single compact object. Considering the good agreement between weak-dip and dip, the somewhat larger deviation of the line centers in the strong-dip spectrum are probably due to its extremely low number of counts and therefore rather low signal to noise ratio. This theory is supported by the much better agreement of the strong-dip lines with the lines observed during weaker dipping in the spectra of ObsID 8525 (see section 5.3).

Long dashes in the tables indicate lines that could either not be detected and/or not be constrained during the fit. This issue seems to occur predominantly with the Li-like sulfur line. The Li-like absorption lines in Cyg X-1 also have the problem that they are very close to the forbidden He-like line which usually appears as an emission line. Due to the degeneracy of these lines, the Li-like lines are more likely to be mis-described by the fit since the He z emission eats away one of its tails, causing the line fit to result in a narrower line with its line center slightly shifted to higher energies. That the sulfur region generally has worse statistics and weaker absorption lines can be explained with a hint at table 2.11 in Hanke (2011). This table shows the continuum for three *Chandra* observations of Cyg X-1 covering different phases of the binary and indicates that the absorption due to S is by a factor of 4 to 8 weaker than the absorption due to Si. With silicon being so much more abundant, line centers, equivalent widths and especially shifts of the C-like S line have to be taken with much care since it strongly blends with Si Ly  $\beta$ .

### 5.2.4 Comparison to Laboratory Spectra

Already a qualitative comparison of the EBIT and the Cyg X-1 spectra shows that now the assumed rest wavelengths of the Si and S K $\alpha$  spectra agree quite well with the astrophysical spectra (Fig. 5.11 and 5.12). In the preceding section we found the energies of the Si and S absorption lines in this observation. What we would really like to know, though, is the velocity of the material causing the lines. With the definition of the Doppler (1842) shift

$$\frac{v}{c} = \frac{E_{\text{theo}} - E_{\text{obs}}}{E_{\text{obs}}} = \frac{\Delta E}{E_{\text{obs}}}, \quad (5.13)$$

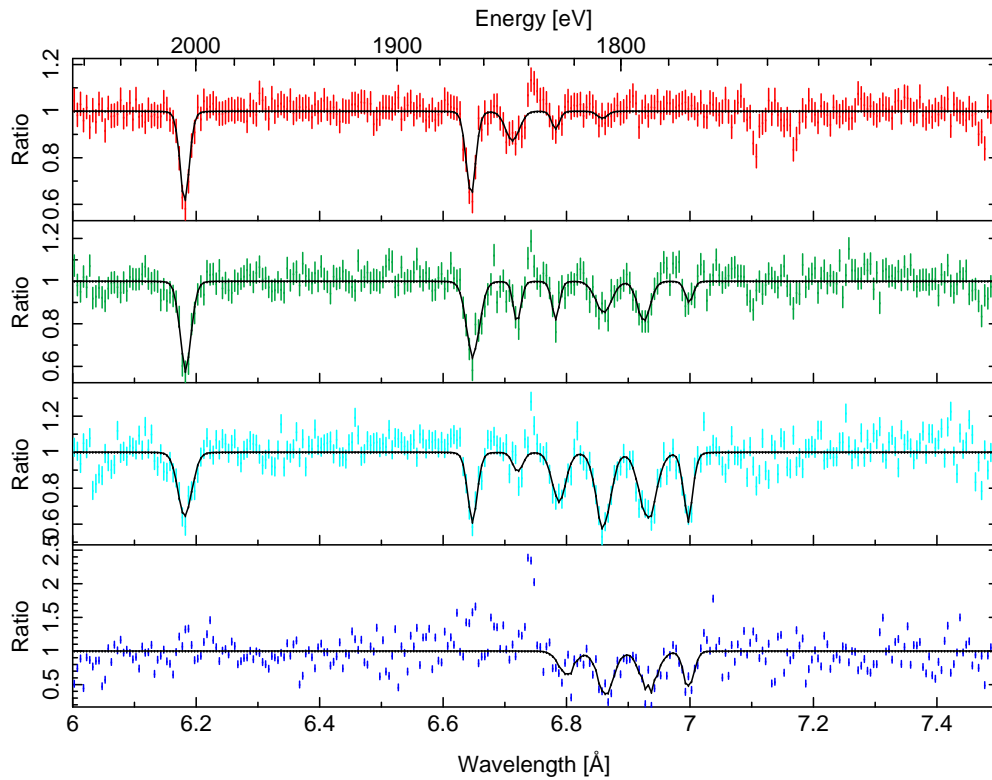


**Figure 5.9:** Evolution of the silicon lines with dipping stages (non-dip, weak dip, dip and strong dip from top to bottom). The four panels show the averaged HEG and MEG  $\pm$  first order spectra of ObsID 3814 normalized to their continua. The solid black line shows the line fits.

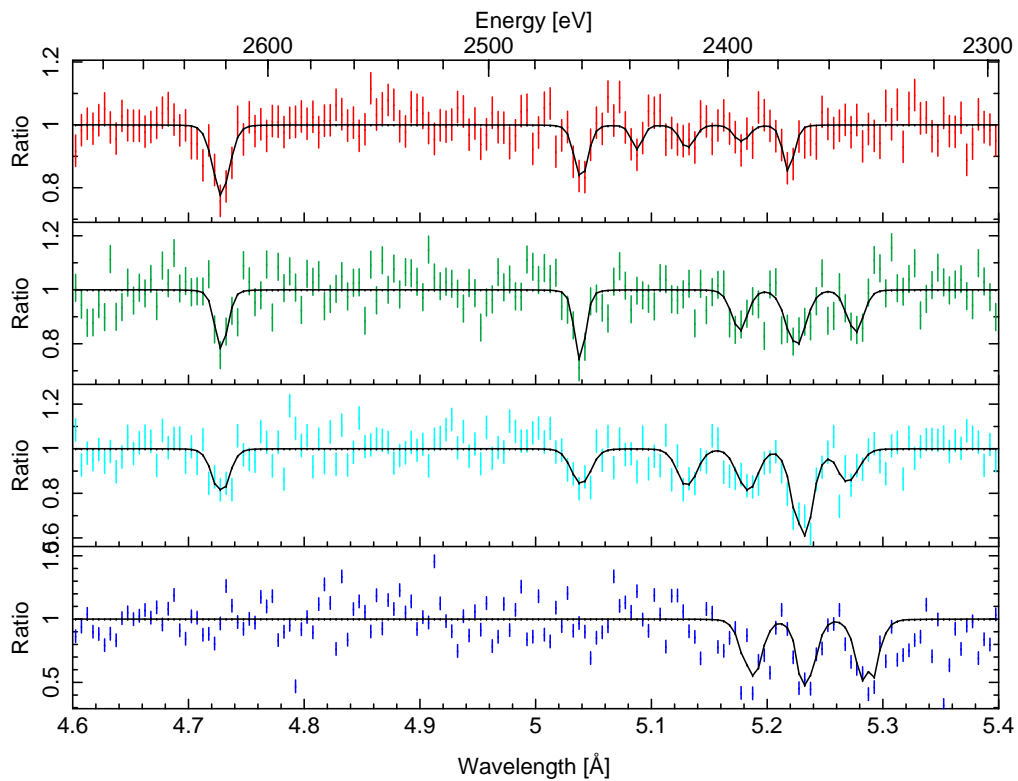


**Figure 5.10:** Same as figure 5.9 for the sulfur region.

**Table 5.3:** Silicon and sulfur line centers for ObsID 3814.

Ion	$E_{\text{obs}}$ [eV]				
	non-dip	weak-dip	dip	strong-dip	
H-like Si XIV	$2005.76 \pm 0.24$	$2005.3 \pm 0.4$	$2005.6^{+0.6}_{-0.7}$	—	
He-like Si XIII	$1865.84^{+0.25}_{-0.26}$	$1864.9 \pm 0.5$	$1865.1^{+0.5}_{-0.6}$	—	
Li-like Si XII	$1847.1 \pm 0.9$	$1845.0^{+0.8}_{-0.7}$	$1844.7^{+1.7}_{-1.3}$	—	
Be-like Si XI	$1828.1 \pm 0.8$	$1828.1^{+0.6}_{-0.5}$	$1826.6 \pm 0.7$	$1823.4^{+1.6}_{-1.7}$	
B-like Si X	$1807.9^{+2.2}_{-2.5}$	$1807.4 \pm 1.0$	$1807.4 \pm 0.5$	$1806.5 \pm 0.9$	
C-like Si IX	—	$1790.3 \pm 0.7$	$1788.7 \pm 0.6$	$1788.2 \pm 0.9$	
N-like Si VIII	—	$1771.6 \pm 1.0$	$1772.0 \pm 0.5$	$1771.7^{+1.0}_{-0.9}$	
H-like S XVI	$2622.2 \pm 1.0$	$2622.1^{+1.4}_{-1.8}$	$2622.4 \pm 1.9$	—	
He-like S XV	$2460.4^{+1.2}_{-1.0}$	$2460.8^{+0.9}_{-1.0}$	$2460.4 \pm 2.3$	—	
Li-like S XIV	$2437.0^{+2.0}_{-1.7}$	—	—	—	
Be-like S XIII	$2416.4^{+3.8}_{-2.8}$	—	$2416.5^{+2.4}_{-2.3}$	—	
B-like S XII	$2394^{+4}_{-5}$	$2395.3^{+2.0}_{-2.3}$	$2392.2^{+3.0}_{-2.9}$	$2390.5^{+2.9}_{-3.2}$	
C-like S XI	$2375.9^{+1.3}_{-2.4}$	$2373.0 \pm 1.8$	$2370.4 \pm 1.0$	$2368.9^{+1.6}_{-1.7}$	
N-like S X	—	$2350.0^{+2.8}_{-2.0}$	$2353 \pm 4$	$2345.3^{+1.9}_{-2.0}$	

**Table 5.4:** Evolution of the equivalent widths of the Si and S lines during the dipping stages for ObsID 3814.

Ion	Equivalent Width [eV]			
	non-dip	weak-dip	dip	strong-dip
H-like Si XIV	$-11.5^{+1.0}_{-1.1}$	$-13.9^{+1.6}_{-1.7}$	$-14.4 \pm 1.5$	—
He-like Si XIII	$-10.9 \pm 1.1$	$-13.9^{+1.8}_{-1.9}$	$-10.8^{+1.9}_{-2.0}$	—
Li-like Si XII	$-5.9^{+1.3}_{-1.4}$	$-4.5^{+1.2}_{-1.4}$	$-3.2^{+1.7}_{-1.8}$	—
Be-like Si XI	$-2.1 \pm 0.8$	$-4.4 \pm 1.0$	$-11.0^{+1.8}_{-1.9}$	$-15^{+6}_{-5}$
B-like Si X	$-1.2 \pm 1.0$	$-7.7^{+1.9}_{-1.7}$	$-18.0^{+2.1}_{-2.3}$	$-28^{+6}_{-4}$
C-like Si IX	—	$-7.8^{+1.6}_{-1.7}$	$-18.2^{+1.7}_{-1.6}$	$-27^{+6}_{-5}$
N-like Si VIII	—	$-2.6 \pm 1.3$	$-10.2^{+1.9}_{-2.1}$	$-15 \pm 5$
H-like S XVI	$-6.2^{+1.3}_{-0.9}$	$-4.7^{+1.5}_{-1.8}$	$-5.4^{+1.6}_{-1.5}$	—
He-like S XV	$-3.9^{+1.1}_{-1.4}$	$-4.9^{+1.2}_{-2.1}$	$-4.8^{+1.9}_{-1.8}$	—
Li-like S XIV	$-1.5 \pm 0.9$	$-1.1 \pm 1.3$	—	—
Be-like S XIII	$-1.8^{+1.2}_{-1.4}$	—	$-5.0^{+2.1}_{-1.9}$	—
B-like S XII	$-1.3^{+1.2}_{-1.3}$	$-3.9 \pm 1.6$	$5.8 \pm 1.9$	$-13 \pm 4$
C-like S XI	$-2.8^{+1.0}_{-2.0}$	$-6.3 \pm 1.8$	$-11.6^{+1.9}_{-1.8}$	$-14 \pm 5$
N-like S X	—	$-4.0^{+1.9}_{-2.2}$	$-4.7^{+2.7}_{-2.2}$	$-15 \pm 5$

where positive velocities correspond to a reddening of the spectrum from the emitted  $E_{\text{theo}}$  to the smaller  $E_{\text{obs}}$ , we only need to determine the difference between the lines seen in the Cyg X-1 spectra and the lines in the spectra taken from the plasma considered “at rest” in the laboratory. The observed energy is already known from the analysis in the previous section (cf. Table 5.3). Re-writing the Doppler shift in terms of the wavelengths

$$\frac{v}{c} = \frac{\lambda_{\text{obs}} - \lambda_{\text{theo}}}{\lambda_{\text{theo}}}, \quad (5.14)$$

would require us to know the theoretical centers of the blended lines. For this reason, the fits are done in the energy space although in astrophysics spectra at the considered energy range around 2 keV are more commonly examined in wavelength space.

To obtain the shift between the laboratory and the astrophysical spectra, the FAC model defined in section 4.8 is applied. With it the shift of the Cyg X-1 spectrum with respect to the theoretical spectrum is determined. As discussed in section 3.12, the uncertainty in those calculated line energies can be rather high – higher than the expected Doppler shift. Consequently the FAC model, due to some advantages of handling it as discussed below, is only used as a link to the laboratory spectra which shall provide the true reference energies. In table 4.6 the displacement,  $\Delta E_{\text{ebit}}$ , of the FAC calculations with respect to the measurement is listed for every distinguishable ionization state. A similar table (Tab. 5.6) shows the same information,  $\Delta E_{\text{cyg}}$ , for Cyg X-1.  $\Delta E$  between EBIT and Cyg X-1 is then just a simple combination of these and can be derived by thinking through a few possible constellations of their order in energy.

The FAC model is defined such that the resulting energy shift  $\Delta E_{\text{fac}}$ , where the subscript *fac* stands for any of the two fitted spectra *ebit* and *cyg*, is positive ( $\Delta E_{\text{fac}} > 0$ ) if the lines in the fitted spectrum are situated at higher energies than the FAC calculation. If now, for instance, the Cyg X-1 spectrum is at higher energies than the FAC spectrum which again is at higher energies than the EBIT spectrum, we know that the Cyg X-1 spectrum is blue shifted, i.e.,  $\Delta E < 0$ . According to the model definition we also have  $\Delta E_{\text{cyg}} > 0$  and  $\Delta E_{\text{ebit}} < 0$ . Since the FAC spectrum lies between the EBIT and the Cyg X-1 spectrum, in this case the absolute values of the shifts have to be added to get the distance  $|\Delta E| = |\Delta E_{\text{ebit}}| + |\Delta E_{\text{cyg}}|$ . The only way to realize this while preserving the signs of the displacements is by subtracting them from each other such that both virtually have the same sign. Therefore, keeping the blue shift in mind,

$$\Delta E = \Delta E_{\text{ebit}} - \Delta E_{\text{cyg}}. \quad (5.15)$$

Similar reasoning leads to the same result for all possible configurations. Thus, we find that in all cases the Doppler shift can be expressed as

$$\frac{v}{c} = \frac{\Delta E_{\text{ebit}} - \Delta E_{\text{cyg}}}{E_{\text{obs}}} \quad (5.16)$$

where  $\Delta E_{\{\text{ebit}/\text{cyg}\}} > 0$  if the FAC line energy is higher than the observed EBIT/Cyg X-1 energy.

During the fit of the FAC model to the astrophysical spectra, contrary to the approach for the laboratory spectrum it is not assumed that the resolution of the detector stays constant over the small fit region, i.e., also the FWHM is left free to vary. For satellite spectra this assumption is not valid because of the variations introduced by, e.g., the effective area of the mirrors which are not present in the laboratory. The (fixed) parameters listed in Table

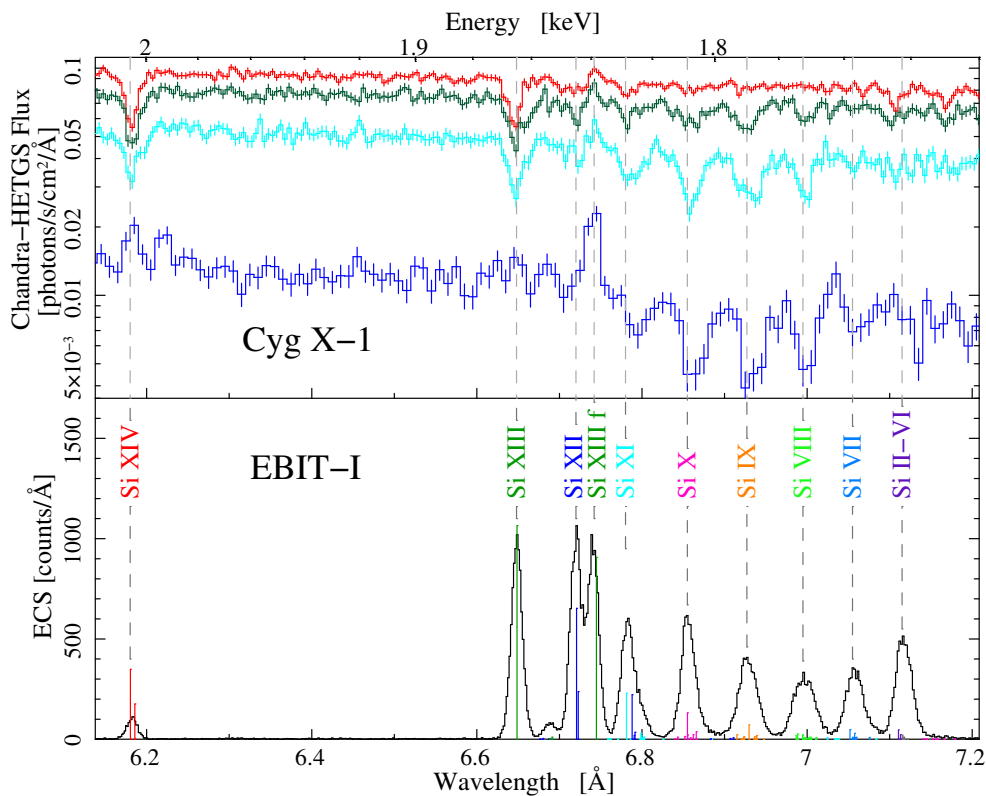


**Figure 5.11:** Comparison of the Cyg X-1 non-dip (red), weak dip (green), dip (light blue) and strong dip (blue) spectra (top) with the silicon K $\alpha$  spectrum produced with EBIT-I (bottom). The lines are in much better agreement than with House (1969, ; cf. Fig. 2.8).

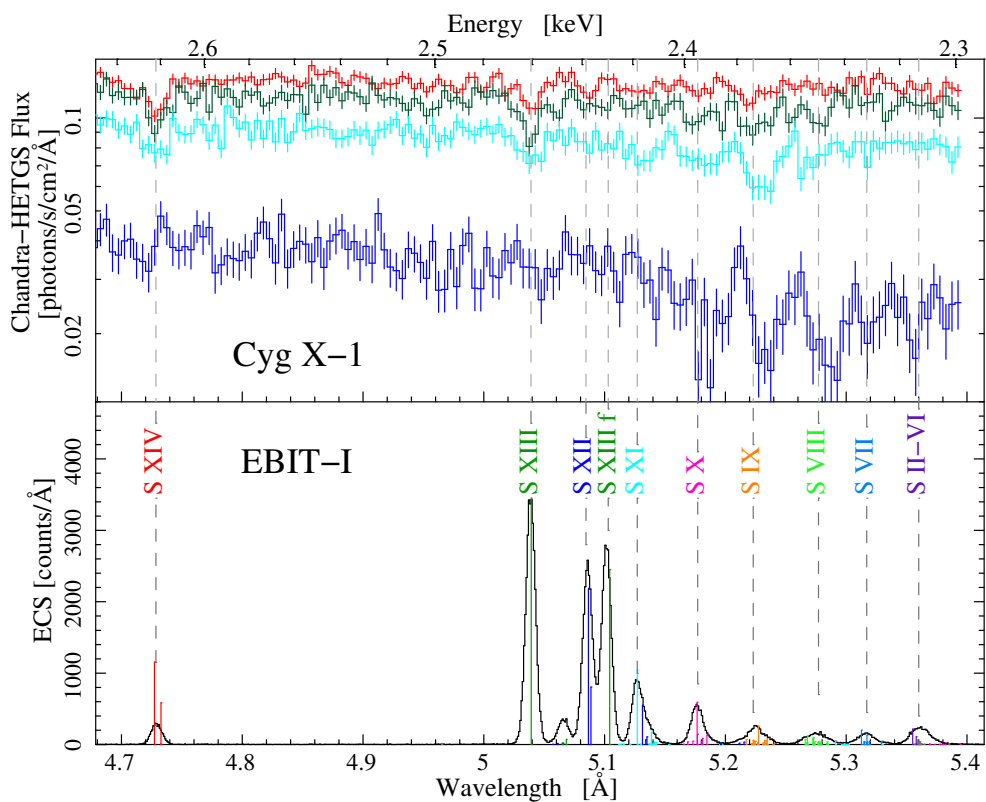


**Figure 5.12:** Comparison of the Cyg X-1 (top) and EBIT sulfur spectra.

**Table 5.5:** Difference  $\Delta E_{\text{cyg}}$  (eV) between line centers measured in Cyg X-1 and calculated with FAC for ObsID 3814.

Ion		$\Delta E_{\text{cyg}}$ [eV]			
		non-dip	weak-dip	dip	strong-dip
H-like	Si XIV	$-0.23 \pm 0.24$	$0.2 \pm 0.4$	$-0.2^{+0.7}_{-0.8}$	—
He-like	Si XIII	$-1.02 \pm 0.25$	$-0.1 \pm 0.5$	$-0.3^{+0.6}_{-0.5}$	—
Li-like	Si XII	$-2.0 \pm 0.8$	$-0.4^{+0.7}_{-0.8}$	$0.0^{+1.3}_{-1.7}$	—
Be-like	Si XI	$-0.0 \pm 2.0$	$0.0 \pm 0.5$	$0.9 \pm 0.8$	$4.3 \pm 1.6$
B-like	Si X	$-0.3^{+2.4}_{-1.6}$	$0.8 \pm 1.0$	$0.8 \pm 0.5$	$1.7 \pm 0.9$
C-like	Si IX	—	$-1.2 \pm 0.7$	$0.5 \pm 0.6$	$0.9 \pm 1.0$
N-like	Si VIII	—	$1.1^{+1.3}_{-1.2}$	$0.8^{+0.5}_{-0.6}$	$0.7 \pm 1.0$
H-like	S XVI	$-0.6 \pm 1.0$	$-0.3^{+1.6}_{-1.0}$	$-0.7 \pm 2.0$	—
He-like	S XV	$0.0^{+1.0}_{-1.3}$	$-0.5^{+1.0}_{-0.9}$	$0.0 \pm 2.3$	—
Li-like	S XIV	$0.1^{+1.6}_{-1.7}$	—	—	—
Be-like	S XIII	$0^{+4}_{-5}$	—	$0.7^{+2.3}_{-2.8}$	—
B-like	S XII	$0^{+5}_{-4}$	$-0.1^{+2.9}_{-2.6}$	$2.3^{+2.7}_{-2.9}$	$4.2^{+2.9}_{-3.0}$
C-like	S XI	$-4.1^{3.1}_{-1.4}$	$-1.1 \pm 1.9$	$1.4 \pm 1.0$	$3.0^{+1.7}_{-1.6}$
N-like	S X	—	$1.2^{+2.0}_{-3.2}$	$-1.6^{+3.7}_{-2.1}$	$6.3^{+2.2}_{-2.0}$

**Table 5.6:** Doppler shifts  $v$  ( $\text{km s}^{-1}$ ) derived from table 5.5 after equation 5.16 for ObsID 3814.

Ion		$v$ [ $\text{km s}^{-1}$ ]			
		non-dip	weak-dip	dip	strong-dip
H-like	Si XIV	$-3 \pm 60$	$-70 \pm 70$	$-13 \pm 120$	—
He-like	Si XIII	$170 \pm 50$	$10 \pm 80$	$50 \pm 80$	—
Li-like	Si XII	$250 \pm 130$	$-10 \pm 120$	$-80 \pm 240$	—
Be-like	Si XI	$-30 \pm 130$	$-50 \pm 90$	$-190 \pm 130$	$-750 \pm 260$
B-like	Si X	$30 \pm 420$	$-160 \pm 170$	$-150 \pm 70$	$-300 \pm 140$
C-like	Si IX	—	$170 \pm 110$	$-110 \pm 100$	$-190 \pm 160$
N-like	Si VIII	—	$-160 \pm 210$	$-100 \pm 90$	$-90 \pm 170$
H-like	S XVI	$60 \pm 130$	$40 \pm 150$	$80 \pm 220$	—
He-like	S XV	$-30 \pm 140$	$30 \pm 120$	$-30 \pm 280$	—
Li-like	S XIV	$-100 \pm 200$	—	—	—
Be-like	S XIII	$-200 \pm 500$	—	$-200 \pm 300$	—
B-like	S XII	$0 \pm 500$	$-20 \pm 340$	$-330 \pm 350$	$-560 \pm 370$
C-like	S XI	$440 \pm 280$	$70 \pm 240$	$-250 \pm 140$	$-450 \pm 210$
N-like	S X	—	$-90 \pm 330$	$270 \pm 370$	$-730 \pm 270$

5.2 again build the continuum for the absorption lines. Table 5.5 lists the fitted energy differences and table 5.6 the resulting Doppler shifts.

The spectrum simulated with FAC can, due to its numerical character, very easily be separated into the contributions of single ionization states, even if lines of two or more ions blend into each other. It is unlikely that the charge balance in the plasma around Cyg X-1 is the same as in EBIT during the measurements. With every ion having its own normalization parameter this difference can conveniently be taken care of. Another approach to determine the shift between the spectra would be to cut the laboratory spectra into pieces and convolve the single peaks, which constitute lines already convolved with the detector resolution of the ECS, with yet another Gaussian in order to smear them out to fit the HETGs resolution. Especially for the two close lines He-like line z and the Li-like peak, it is hard to justify where exactly to apply the cut and in some cases like the just mentioned these lines would also lose their tails. If the tail is missing, the line does not make for a good model as the fit is strongly determined by the tails of a fit function. Also lines whose shape is attributed to blends of lines coming from level transitions in different ions could not be corrected for the different charge balances in the different sources and might therefore introduce an error to the measured shift.

This reasoning is only to justify the choice between the available tools. Of course, there are also disadvantages in using the FAC calculations as a reference. But compared to the problems arising from the alternative approach, they seem to be acceptable for now. The deficiencies of the numerical calculations with atomic codes in general and with FAC in particular have been discussed before (Sections 3.12 and 4.8) but are of minor importance here as they introduce the same error to both fits. A more severe issue is that the FAC model has been calculated on the basis of collisional ionization and excitation. This assumption is perfectly valid for a plasma produced in an EBIT. The environment of Cyg X-1, however, is dominated by photoionization and -absorption of the radiation produced by the accretion process. Photoabsorption and collisional ionization can favor the population of completely different energy levels in the same ion, changing the shape of the spectrum. Hence, as “bad” as the description of the measurement through the FAC model is (cf. section 4.8), its validity with respect to the *Chandra* spectrum is worse. Strictly speaking, as it was produced itself through collisional processes, the fitting of the ECS spectrum to the *Chandra* spectrum would face the same problem such that this issue is not a disadvantage of the FAC approach over the spectrum cutting.

Table 5.5 lists the shift of the FAC spectra with respect to the Cyg X-1 spectra fitted on top of the same continuum as the line centers. Using the above method then the Doppler shifts are derived for all detected lines (table 5.6). Even with the new atomic data, the uncertainties in the measured velocities still seem rather high. Comparison with the error bars of the Doppler shifts of lines with already previously well known rest wavelengths (e.g., Hanke, 2011, Tab. 2.12), however, imply that the accuracy of the results is at least as high if not higher than the quoted values in other works. The derived uncertainties can indeed be ascribed to the error bars already emerging from the simple line fit (Tab. 5.3) rather than the applied method.

With the exception of only a few fluctuations, most of which appear in those lines causing problems as described in section 5.2.3, the derived Doppler shifts are consistent with zero and, even more important, with the Doppler shifts of the same line in different dipping stages. The latter provides evidence for the theory of inhomogeneities in the stellar winds building clumps of denser, due to self-shielding successively colder and therefore less ionized material moving as single compact chunks through the surroundings of the black hole.

Overall the observed absorption lines are basically at their rest wavelengths. With the free fall velocity

$$v(r) = \sqrt{\frac{GM}{r}} < v(R_S) = \frac{c}{\sqrt{2}}, \quad (5.17)$$

where  $R_S$  is the Schwarzschild radius, zero Doppler shift either means that the material causing the absorption is far away from the black hole or is moving perpendicular to our line of sight. Another characteristic velocity of the system is the projected orbital velocity of Cyg X-1. In analogy to Eq. 2.24 it can be calculated by substituting the center of mass ( $a_* M_* = a_X * M_X$ ) and the mass ratio  $q$  of the two components, and inserting the system parameters ( $a_* \sin i = 8.36 R_\odot$  (Gies et al., 2003),  $P_{\text{orb}} = 5.99829$  d Brocksopp et al. (1999),  $M_* = 19.16 M_\odot$  and  $M_X = 14.8 M_\odot$  Orosz et al. (2011)):

$$K_X = \frac{2\pi a_X \sin i}{P_{\text{orb}}} = \frac{2\pi a_* \sin i}{P_{\text{orb}}} \cdot q = 91.26 \text{ km s}^{-1}. \quad (5.18)$$

This Keplerian velocity of the black hole is not much higher than the found Doppler shifts. For some of the lines this velocity is even within the derived uncertainties. So since this observation was done around phase zero, i.e., in superior conjunction of the black hole where the black hole moves perpendicular to our line of sight, the observed clumps could actually be rather close to the black hole. A comparison of the analysis of absorption dips in observations of other orbital phases could help to get a better hint at these movements of the clumps.

### 5.3 ObsID 8525

To cross-check the above findings, the same analysis is also applied to the spectra of ObsID 8525, which is with  $\phi_{0.02-0.08}$  also around superior conjunction and should therefore lead to the same results as ObsID 3814. The observation was performed on 2008-04-18/19 with an exposure time of 30 ks. The detector setup chosen was similar (with a few improvements) to the one of 3814 (for details see Hanke, 2011). The hard state of the system was similar during both observations, as is the morphology of the resulting light curves.

For this observation only the silicon and sulfur lines are analyzed. The cutting into dipping stages and the description of the continuum is adopted from Hanke (2011, Tab. 2.11). Only the silicon and sulfur column densities of the warm absorber model are set to zero. This approach is necessary in order to be able to analyze the absorption lines since the purpose of the warm absorber model is to describe absorption of ionized material and therefore at least partially accounts for the lines of our interest. The results are listed in tables 5.7 through 5.10. They are consistent with and confirm the previous findings and also suggest that the rather large shifts of the strong-dip lines in ObsID 3814 are really due to the low count rate.

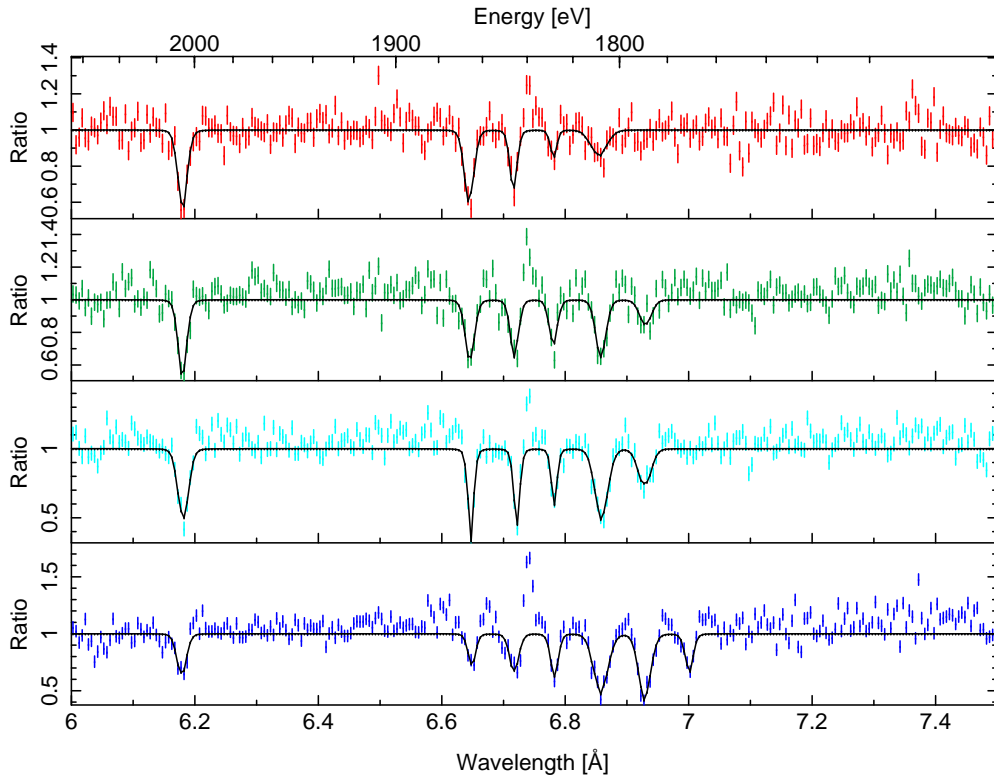


**Figure 5.13:** Evolution of the silicon lines with dipping stages (non-dip, weak dip, dip and strong dip from top to bottom). The four panels show the averaged HEG and MEG  $\pm$  first order spectra of ObsID 8525 normalized to their continua. The solid black line shows the line fits.

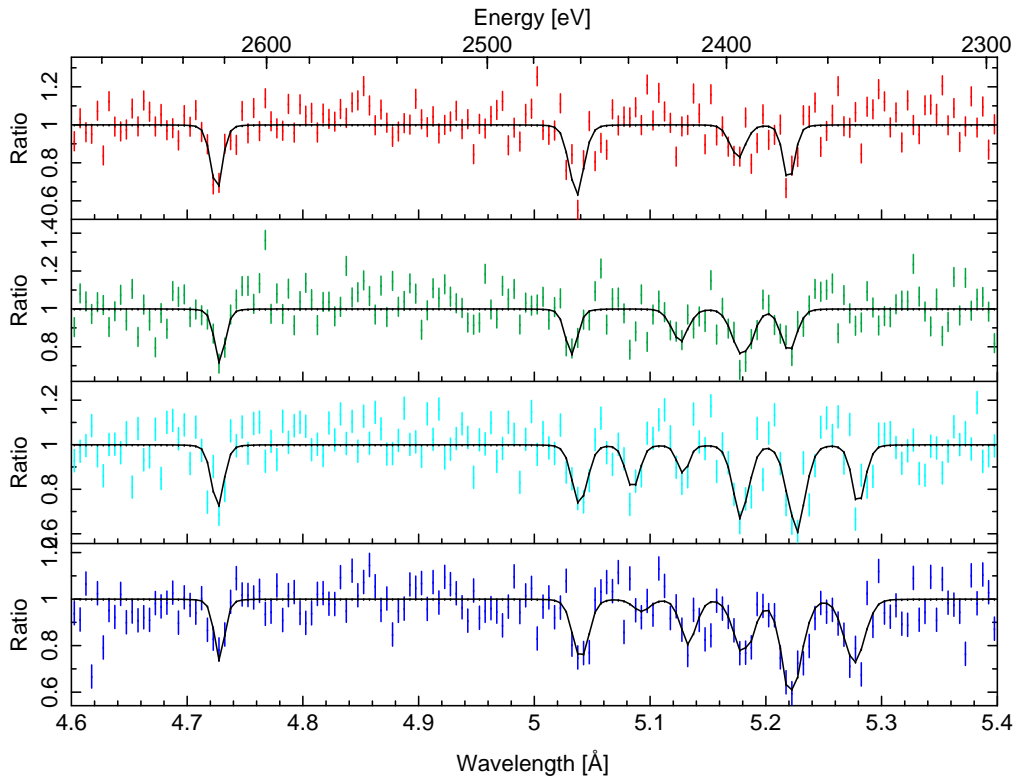


**Figure 5.14:** Same as figure 5.13 for the sulfur region.

**Table 5.7:** Silicon and sulfur line centers for ObsID 8525.

Ion		$E_{\text{obs}}$ [eV]			
		non-dip	weak-dip	dip	strong-dip
H-like	Si XIV	$2006.2 \pm 0.5$	$2006.2 \pm 0.5$	$2005.8 \pm 0.4$	$2006.7^{+0.7}_{-0.6}$
He-like	Si XIII	$1866.0 \pm 0.5$	$1865.8^{+0.7}_{-0.6}$	$1865.23^{+0.28}_{-0.27}$	$1864.8^{+0.8}_{-0.7}$
Li-like	Si XII	$1846.1 \pm 0.7$	$1845.7 \pm 0.7$	$1844.60^{+0.31}_{-0.28}$	$1845.8 \pm 1.0$
Be-like	Si XI	$1828.4^{+1.2}_{-0.9}$	$1828.5 \pm 0.5$	$1828.1 \pm 0.4$	$1828.0 \pm 0.4$
B-like	Si X	$1808.8 \pm 1.6$	$1807.9 \pm 0.5$	$1807.7 \pm 0.4$	$1808.0 \pm 0.4$
C-like	Si IX	—	$1789.1 \pm 1.2$	$1789.5 \pm 0.7$	$1789.5 \pm 0.4$
N-like	Si VIII	—	—	—	$1771.1 \pm 0.6$
H-like	S XVI	$2623.8^{+1.2}_{-1.8}$	$2622.2^{+1.4}_{-1.3}$	$2623.2 \pm 1.7$	$2622.4^{+2.6}_{-1.0}$
He-like	S XV	$2461.7^{+1.0}_{-1.5}$	$2463.9^{+1.6}_{-1.7}$	$2460.4^{+1.6}_{-1.5}$	$2460.0^{+1.4}_{-1.3}$
Li-like	S XIV	—	—	$2438.3^{+2.3}_{-1.7}$	—
Be-like	S XIII	—	$2418.9^{+2.8}_{-3.1}$	$2417.6^{+2.0}_{-2.2}$	$2415.4^{+2.3}_{-3.7}$
B-like	S XII	$2395.5^{+2.6}_{-3.5}$	$2393.6^{+2.0}_{-1.7}$	$2394.2^{+1.2}_{-1.3}$	$2393.2^{+1.8}_{-1.7}$
C-like	S XI	$2375.1^{+1.3}_{-1.2}$	$2375.2^{+1.9}_{-2.2}$	$2372.4 \pm 1.0$	$2374.0 \pm 1.0$
N-like	S X	—	—	$2348.0 \pm 1.4$	$2349.8 \pm 1.5$

**Table 5.8:** Evolution of the equivalent widths of the Si and S lines during the different dipping stages for ObsID 8525.

Ion		Equivalent Width [eV]			
		non-dip	weak-dip	dip	strong-dip
H-like	Si XIV	$-12.2^{+2.2}_{-2.5}$	$-11.9^{+1.8}_{-1.9}$	$-15.5^{+1.8}_{-1.9}$	$-9.8^{+1.7}_{-1.9}$
He-like	Si XIII	$-11.6^{+2.1}_{-2.3}$	$-10.2^{+2.2}_{-2.5}$	$-10.3^{+1.0}_{-2.1}$	$-5.9 \pm 1.6$
Li-like	Si XII	$-7.4 \pm 2.2$	$-8.5^{+2.0}_{-2.3}$	$-8.8^{+1.1}_{-1.2}$	$-8.4^{+2.6}_{-2.3}$
Be-like	Si XI	$-3.2^{+1.3}_{-1.8}$	$-7.1 \pm 1.3$	$-6.7^{+1.0}_{-2.5}$	$-8.1^{+1.3}_{-1.2}$
B-like	Si X	$-7.5^{+3.2}_{-2.2}$	$-11.0^{+1.8}_{-1.9}$	$-19.0^{+1.9}_{-2.0}$	$-20.3^{+2.0}_{-2.1}$
C-like	Si IX	—	$-5.7^{+2.0}_{-2.1}$	$-10.3^{2.0}_{-2.1}$	$-18.8^{+1.9}_{-2.0}$
N-like	Si VIII	—	—	—	$-7.6^{+1.6}_{-1.9}$
H-like	S XVI	$-6.4 \pm 1.9$	$-4.9 \pm 1.6$	$-5.6^{+1.7}_{-1.6}$	$-4.3^{+1.3}_{-2.1}$
He-like	S XV	$-8.3 \pm 2.6$	$-4.7 \pm 1.8$	$-6.4^{+2.2}_{-2.4}$	$-6.4^{+1.9}_{-2.1}$
Li-like	S XIV	—	—	$-4.5^{+1.9}_{-2.5}$	—
Be-like	S XIII	—	$-4.4 \pm 2.5$	$-2.5 \pm 1.8$	$-4.5^{+1.8}_{-1.7}$
B-like	S XII	$-4.2 \pm 2.2$	$-7.7^{+2.8}_{-2.7}$	$-8.1^{+2.4}_{-2.7}$	$-6.9^{+2.3}_{-1.9}$
C-like	S XI	$-5.4 \pm 1.8$	$-5.3^{+2.4}_{-2.7}$	$-10.2^{+2.3}_{-2.2}$	$-111.9 \pm 1.8$
N-like	S X	—	—	$-5.4 \pm 1.8$	$-8.4^{+2.2}_{-2.0}$

**Table 5.9:** Difference  $\Delta E_{\text{cyg}}$  (eV) between line centers measured in Cyg X-1 and calculated with FAC for ObsID 8525.

Ion		$\Delta E_{\text{cyg}}$ [eV]			
		non-dip	weak-dip	dip	strong-dip
H-like	Si XIV	$-0.7 \pm 0.5$	$-0.7 \pm 0.5$	$-0.3 \pm 0.4$	$-1.2^{+0.6}_{-0.7}$
He-like	Si XIII	$-1.2 \pm 0.5$	$-0.9^{+0.6}_{-0.7}$	$-0.42^{+0.27}_{-0.28}$	$0.0^{+0.7}_{-0.8}$
Li-like	Si XII	$-1.6 \pm 0.6$	$-1.3 \pm 0.6$	$-0.07 \pm 0.30$	$-1.2 \pm 0.8$
Be-like	Si XI	$-0.5^{+1.4}_{-1.5}$	$-0.4 \pm 0.8$	$-0.3 \pm 0.5$	$0.2 \pm 0.5$
B-like	Si X	$-0.2^{+1.2}_{-1.3}$	$0.3 \pm 0.5$	$0.5 \pm 0.4$	$0.2 \pm 0.4$
C-like	Si IX	—	$0.1 \pm 1.3$	$-0.3 \pm 0.7$	$-0.4 \pm 0.4$
N-like	Si VIII	—	—	—	$1.3^{+0.7}_{-0.8}$
H-like	S XVI	$-1.8^{+1.5}_{-1.4}$	$0.0^{+1.0}_{-1.9}$	$-1.7 \pm 1.8$	$-1.2^{+2.0}_{-2.2}$
He-like	S XV	$-1.3^{+1.4}_{-1.0}$	$-3.4^{+1.9}_{-1.6}$	$0.1^{+1.5}_{-1.6}$	$0.5 \pm 1.4$
Li-like	S XIV	—	—	$-1.8^{+2.2}_{-0.8}$	—
Be-like	S XIII	—	$-1.3^{2.9}_{-3.0}$	$0 \pm 4$	$3.0^{+2.7}_{-2.3}$
B-like	S XII	$0.5^{+2.6}_{-3.5}$	$1.1^{+1.7}_{-2.0}$	$0.4^{+1.2}_{-1.0}$	$1.4^{+1.7}_{-1.9}$
C-like	S XI	$-3.5^{+1.4}_{-1.5}$	$-3.3^{+2.2}_{-2.0}$	$-0.5 \pm 1.0$	$-1.9 \pm 1.2$
N-like	S X	—	—	$3.7^{+0.5}_{-0.4}$	$1.6^{+1.6}_{-1.7}$

**Table 5.10:** Doppler shifts  $v$  ( $\text{km s}^{-1}$ ) derived from table 5.9 after equation 5.16 for ObsID 8525.

Ion		$v$ [ $\text{km s}^{-1}$ ]			
		non-dip	weak-dip	dip	strong-dip
H-like	Si XIV	$70 \pm 90$	$70 \pm 80$	$10 \pm 80$	$140 \pm 100$
He-like	Si XIII	$200 \pm 80$	$150 \pm 100$	$70 \pm 50$	$-3 \pm 111$
Li-like	Si XII	$180 \pm 100$	$140 \pm 90$	$-60 \pm 50$	$120 \pm 130$
Be-like	Si XI	$170 \pm 240$	$20 \pm 130$	$1 \pm 70$	$-90 \pm 80$
B-like	Si X	$20 \pm 200$	$-70 \pm 80$	$-100 \pm 60$	$-60 \pm 70$
C-like	Si IX	—	$-50 \pm 210$	$20 \pm 120$	$40 \pm 60$
N-like	Si VIII	—	—	—	$-180 \pm 120$
H-like	S XVI	$200 \pm 170$	$-3 \pm 165$	$200 \pm 200$	$140 \pm 240$
He-like	S XV	$140 \pm 150$	$400 \pm 210$	$-30 \pm 190$	$-80 \pm 170$
Li-like	S XIV	—	—	$140 \pm 180$	—
Be-like	S XIII	—	$60 \pm 360$	$-100 \pm 500$	$-480 \pm 310$
B-like	S XII	$-100 \pm 400$	$-170 \pm 240$	$-90 \pm 140$	$-210 \pm 220$
C-like	S XI	$370 \pm 180$	$350 \pm 260$	$-2 \pm 137$	$170 \pm 250$
N-like	S X	—	—	$-400 \pm 60$	$-130 \pm 210$

There is a theory which states that if ever anyone discovers exactly what the universe is for and why it is here, it will instantly disappear and be replaced by something even more bizarre and inexplicable. There is another theory that this has already happened.

---

Douglas Adams, Restaurant at the End of the Universe

## Chapter 6

# Conclusion and Outlook

In this work the  $K\alpha$  spectra of silicon and sulfur have been measured with the LLNL EBIT-I and the ECS. The resulting lines have been identified via calculations using FAC and compared with the theoretical predictions of Palmeri et al. (2008). The largest uncertainty in the identification process is that the simulated spectra are not completely self-consistent because of the unknown charge balance in the trap and therefore (and because of numerical issues) do not have to resemble an accurate description of the ‘real’ world. To quantify the difference between theory and experiment, the calculated line centers have been converted into a model that can easily be fitted to the measured spectra. The shift between theory and experiment derived that way is on average 0.35 eV (Si) and 0.48 eV (S), respectively. One of the major problems with the FAC fitting ansatz is that, as can be seen in Fig. 3.6 by comparison of the Palmeri et al. (2008) and the FAC energy levels, the assumption that the relative energy differences in an ion are correctly modeled by the codes is probably invalid.

The same model has also been used to estimate the Doppler shift of silicon and sulfur lines whose charge balance decreases during the event of an absorption dip in two *Chandra* observations at orbital phase  $\phi \approx 0$  of the HMXB Cyg X-1. We find that the Cyg X-1 lines are basically not shifted with respect to their rest wavelengths. Neither does the shift change between different dipping stages nor between different ionization states. These results are consistent with the theory of the onion-like structure of the clumps in the wind preserving lower charge states due to self-shielding effects against the ionizing X-radiation from the accretion process.

From the purely atomic physics point of view there is much that can be done and would be interesting for the future: So far a general lack of experimental K vacancy level energies, except for the He-, Li- and sometimes Be-like isonuclear sequences, severely restricts the possibilities of fine-tuning the numerical codes (Palmeri et al., 2008). With the new results and even higher resolution measurements in planning, the next step in this direction can be taken. To obtain better resolution, measurements using a crystal spectrometer can be carried out. Another possibility would be to go to an X-ray laser facility like the Linac Coherent Light Source (LCLS) at the Stanford Linear Accelerator Center (SLAC). With a high intensity, high resolution photon beam ions trapped, e.g., in an EBIT can be excited and resonant lines measured with very high precision. The next step would then be to measure cross sections and life times to provide a handle to directly utilize the measured line centers without workarounds as the FAC model.

Also, improvements of the FAC model have to be made. Applying the collisionally ionized

plasma to both, the laboratory/EBIT spectra and the photoionized absorption/emission lines of astrophysical spectra like the ones from Cyg X-1 cannot yet be the best solution. Especially the strong blend of the Be-like lines with some of the Li-like lines (compare figures 3.8 and 3.9), which only become intense lines due to the collisionally dominated ionization and excitation, causes trouble in trying to constrain the shift of the Be-like peak in the astrophysical spectra.

To improve the uncertainties on line centers and Doppler shifts in the astrophysical spectra, a better treatment of P Cygni line profiles can contribute its fair bit. A phase dependency study of the Doppler shifts, i.e., applying the analysis method of the previous chapter to other observations, might help to constrain the properties, the origin and the habitat of the clumps in the stellar wind even more.

So far the analysis of the *Chandra* observations average over the structure of different clumps. Therefore, all conclusions we derive from this analysis have to bear in mind that we're only averaging over the structure. For example, the derived Doppler shifts have contributions of several clumps which could move with different speeds independently of each other. It would, however, be interesting to see how a single clump behaves. Unfortunately, the count rates in the observations are too low to analyze every single absorption dip in the lightcurves separately. At least it would be worth a try to isolate the pronounced deep absorption dips with a long duration.

The application of the method to derive Doppler shifts used in this thesis is not restricted

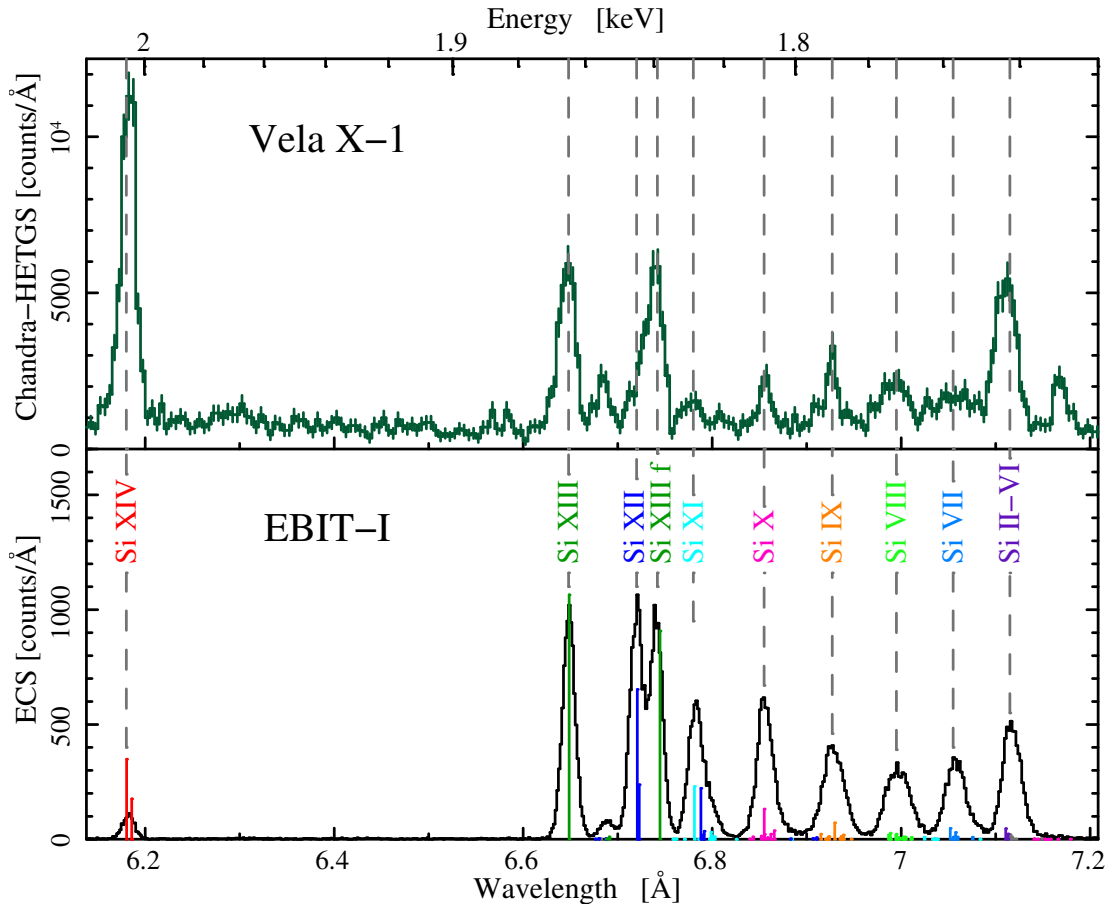


**Figure 6.1:** Comparison of the silicon region in the neutron star HMXB Vela X-1 (*Chandra*, ObsID 1927) spectra with the laboratory measurements.

to the case of Cyg X-1. In fact, Liedahl & Brown (2008) proposed measurements of the silicon X-ray spectra in order to apply them to the neutron star HMXB Vela X-1 and build a velocimeter to probe the properties of the stellar wind. A phase dependent study of the stellar wind in this system using *Chandra* observations has already been done by Watanabe et al. (2006). Due to the lack of atomic physics data, their examination is based on Monte Carlo simulations, though. Figure 6.1 shows a comparison between the Vela X-1 silicon region at phase  $\phi \approx 0.5$  (*Chandra* ObsID 1927) and the EBIT spectra.



IF WE were to go to the sun and to bring some portions of it and analyze them in our laboratories, we could not examine them more accurately than we can by this new mode of spectrum analysis.

Warren de la Rue (1861) about  
the invention of spectroscopy



# Appendix A

## Angular Momentum Notation

**Table A.1:** Angular momentum notation (from Cowan (1981)).

	Angular Momentum of One Electron			Angular Momentum of N-Electron Atom		
	Orbital	Spin	Total	Orbital	Spin	Total
General						
Vector	$\mathbf{J}$	$\mathbf{s}$	$\mathbf{j} \equiv \mathbf{l} + \mathbf{s}$	$\mathbf{L} \equiv \sum_{i=1}^N \mathbf{l}_i$	$\mathbf{S} \equiv \sum_{i=1}^N \mathbf{s}_i$	$\mathbf{J} \equiv \sum_{i=1}^N (\mathbf{l}_i + \mathbf{s}_i)$
Eigenfunction	$\psi_{jm_j}$	$\psi_{lm_l}(\theta, \phi)$	$\psi_{ljm}(\theta, \phi, s_z)$	$\psi_{LM_L}$	$\psi_{SM_S}$	$\psi_{LSJM}$ (for LS coupling $\psi_{LSJM}$ )
Operator	$\mathbf{j}^2$	$\mathbf{l}^2$	$\mathbf{j}^2$	$\mathbf{L}^2$	$\mathbf{S}^2$	$\mathbf{j}^2$
Eigenvalue	$j(j+1)\hbar^2$	$l(l+1)\hbar^2$	$j(j+1)\hbar^2$	$L(L+1)\hbar^2$	$S(S+1)\hbar^2$	$J(J+1)\hbar^2$
possible values of quantum numbers	$j=0,1,2,3,\dots$ or $j=\frac{1}{2}, \frac{3}{2}, \frac{5}{2}, \dots$	$l=0,1,2,3,\dots$	$j=l-\frac{1}{2} (l>0)$ and $j=l+\frac{1}{2}$	L integral ( $L_{\max} = \sum l_i$ )	S integral (N even), or S half-integral (N odd) ( $S_{\max} = \sum s_i = N/2$ )	J integral (N even), or J half-integral (N odd) ( $J_{\max} = \sum l_i + \sum s_i$ ) (for LS, $J =  L-S , \dots, L+S$ )
Operator	$\hat{J}_z$	$\hat{l}_z$	$\hat{j}_z$	$\hat{L}_z$	$\hat{S}_z$	$\hat{j}_z$
Eigenvalue	$m_j \hbar$	$m_l \hbar$	$m \hbar$	$M_L \hbar$	$M_S \hbar$	$M \hbar$
possible values of quantum numbers	$m_j = -j, -j+1, \dots, j-1, j$	$m_l = -l, -l+1, \dots, l-1, l$	$m_j = -j, -j+1, \dots, j-1, j$ $m_s = \pm \frac{1}{2}$	$M_L = -L, -L+1, \dots, L-1, L$	$M_S = -S, -S+1, \dots, S-1, S$	$M = -J, -J+1, \dots, J-1, J$

# Appendix B

## Rate Equations

In section 3.11 it was outlined how to solve the rate equations using matrix notation. Some more details of the set of rate equations, including the matrix for the matrix equation, shall now be shown in this appendix. We start with repeating the general rate equations of Bautista & Kallman (2001)

$$\begin{aligned}
 n_i^0 \left( \underbrace{\sum_{j \neq i} R_{ij}}_{\text{losses to levels in same ion}} + \underbrace{\sum_{q > 0} \Gamma_i^{0 \rightarrow q}}_{\text{losses through photo-ionization}} + \underbrace{N_e \alpha_i^{-1}}_{\text{losses through recombination}} + \underbrace{N_e Q_i^{0 \rightarrow 1}}_{\text{collsional ionization}} \right) = \\
 = \underbrace{\sum_{k \neq i} n_k^0 R_{ki}}_{\text{gain from levels in same ion}} + \underbrace{\sum_{q > 0} \sum_l n_l^{-q} \Gamma_{li}^{-q \rightarrow 0}}_{\text{gain from photo-ionization}} + \underbrace{N_e \sum_l n_l^{-1} Q_{li}^{-1 \rightarrow 0}}_{\text{gain from collisional ionization}} + \underbrace{\sum_s n_s^1 N_e \alpha_{si}^0}_{\text{gain from recombination}}. \quad (3.82)
 \end{aligned}$$

Here, subindices denote transitions between energy levels of the same ion while superindices indicate transitions between ionic states. A superindex of 0 indicates the currently considered ionic stage,  $-1$  and  $+1$  ( $\pm q$ ) denote an ion one ( $q$ ) times less or respectively higher ionized. The left hand side of the equation collects all processes causing a specific level to loose some of its population to other levels or ions. The right hand side in contrast sums over all gains to this same level.

To keep the matrix legible and emphasize its patterns, the processes described in the rate equations are hidden in a shorthand notation of their transition probabilities:

- inner-ion transitions:  $P_{ij}^k = R_{ij} = n_e q_{ij}^e + n_p q_{ij}^p + A_{ij} + U_\nu B_{ij}$   
covering collisional (de-)excitation through electrons (e) and protons (p), spontaneous ( $A_{ij}$ ) and by a photon field  $U_\nu$  stimulated ( $B_{ij}$ ) emission and absorption
- transitions between neighboring ions:

$$\begin{aligned}
 P_{ji}^{k-1 \rightarrow k} &= \Gamma_{ji}^{k-1 \rightarrow k} + n_e Q_{ji}^{k-1 \rightarrow k} && \text{(photo- and collisional ionization)} \\
 P_{ji}^{k+1 \rightarrow k} &= n_e \alpha_{ji}^k && \text{(two-body recombination)}
 \end{aligned}$$

- transitions to higher ionization states:  $P_{ji}^{l \rightarrow k} = \Gamma_{ji}^{l \rightarrow k}$  (for  $l < k$ )  
via photoionization followed by a cascade of autoionization
- losses through all of the above processes:  $L_i^k = \sum_{j \neq i} P_{ij}^k + \sum_{q > k} \Gamma_i^{k \rightarrow q} + n_e \alpha_i^{k-1} + n_e Q_i^{k \rightarrow k+1}$ .





Books serve to show a man that those original thoughts of his aren't very new after all.

Abraham Lincoln

# Bibliography

- Abramowitz M., Stegun I.A., 1964, Handbook of Mathematical Functions with Formulas, Graphs, and Mathematical Tables, Dover Publications, Inc., New York
- Abubekero M.K., Antokhina E.A., Cherepashchuk A.M., 2004, Astron. Rep. 48, 550
- Amusia M.Y., Chernysheva L.V., Natarajan L., 1998, Comput. Phys. 12, 148
- Aschenbach B., 1985, Reports on Progress in Physics 48, 579
- Badnell N.R., 1986, J. Phys. B 19, 3827
- Badnell N.R., 1997, J. Phys. B 30, 1
- Badnell N.R., 2011, Comput. Phys. Commun. 182, 1528
- Balbus S.A., Hawley J.F., 1998, Reviews of Modern Physics 70, 1
- Ballet J., 1999, A&AS 135, 371
- Ballet J., 2001, In: F. R. Harnden Jr., F. A. Primini, & H. E. Payne (ed.) Astronomical Data Analysis Software and Systems X, Vol. 238. Astronomical Society of the Pacific Conference Series, p. 381
- Balmer J.J., 1885, Pogg. Ann. 25, 80
- Balucińska-Church M., Church M.J., Charles P.A., et al., 2000, MNRAS 311, 861
- Balucińska-Church M., Takahashi T., Ueda Y., et al., 1997, Astrophys. J., Lett. 480, L115
- Bar-Shalom A., Klapisch M., Oreg J., 2001, J. Quant. Spectrosc. Radiat. Transfer 71, 169
- Bautista M.A., Kallman T.R., 2001, ApJS 134, 139
- Beiersdorfer P., 1997, In: American Institute of Physics Conference Series, Vol. 389. American Institute of Physics Conference Series, p.121
- Beiersdorfer P., 2008, Can. J. Phys. 86, 1
- Beiersdorfer P., Bitter M., von Goeler S., Hill K.W., 1989, Phys. Rev. A 40, 150
- Beiersdorfer P., Brown G.V., Clementson J.H.T., et al., 2009, In: 14th International Conference on the Physics of Highly Charged Ions (HCI 2008), Vol. 163. Journal of Physics Conference Series
- Blondin J.M., Kallman T.R., Fryxell B.A., Taam R.E., 1990, ApJ 356, 591
- Blondin J.M., Stevens I.R., Kallman T.R., 1991, ApJ 371, 684
- Bohr N., 1913a, Phil. Mag. 26, 1
- Bohr N., 1913b, Phil. Mag. 26, 476
- Bohr N., 1913c, Phil. Mag. 26, 857
- Bohr N., 1920, Z. Physik 2, 423
- Bolton C.T., 1972, Nat 235, 271
- Bolton C.T., 1975, ApJ 200, 269
- Boltzmann L., 1872, Wien. Ber. 66, 275

- Boltzmann L., 1884, *Ann. Phys.* 22, 291
- Bondi H., 1952, *MNRAS* 112, 195
- Bondi H., Hoyle F., 1944, *MNRAS* 104, 273
- Born M., 1969, *Atomic Physics*, Blackie and Son Ltd., Glasgow
- Bowyer S., Byram E.T., Chubb T.A., Friedman H., 1965, *Annales d'Astrophysique* 28, 791
- Bransden B.H., Joachain C.J., 1937, *Physics of Atoms and Molecules*, Prentice Hall, Inc.
- Brocksopp C., Tarasov A.E., Lyuty V.M., Roche P., 1999, *A&A* 343, 861
- Brown I.G., Galvin J.E., Gavin B.F., MacGill R.A., 1986, *Rev. Sci. Instrum.* 57, 1069
- Brown R., 1828, *Phil. Mag.* 4, 161
- Bunsen R., 1860, *Monatsberichte der Kgl. Akademie der Wissenschaften* 221–223
- Canalizo G., Koenigsberger G., Peña D., Ruiz E., 1995, *Rev. Mex. Astron. Astrophys.* 31, 63
- Canizares C.R., Davis J.E., Dewey D., et al., 2005, *PASP* 117, 1144
- Carroll B.W., Ostlie D.A., 2007, *An Introduction to Modern Astrophysics*, Pearson Education, Inc., 2<sup>nd</sup> edition
- Cassinelli J.P., 1979, *ARA&A* 17, 275
- Castor J.I., Abbott D.C., Klein R.I., 1975, *ApJ* 195, 157
- Castor J.I., Lamers H.J.G.L.M., 1979, *ApJS* 39, 481
- Chandrasekhar S., 1931a, *MNRAS* 91, 456
- Chandrasekhar S., 1931b, *ApJ* 74, 81
- Compton A.H., 1923, *Phys. Rev.* 21
- Coulomb C.A.d., 1785, *Histoire de l'Académie Royale des Sciences* 578–611
- Cowan R.D., 1981, *The Theory of Atomic Structure and Spectra*, University of California Press Berkeley Los Angeles London
- CXC 2011, *The Chandra Proposer's Observatory Guide*, <http://cxc.harvard.edu/proposer/POG/>
- Davis J.E., 2001, *ApJ* 562, 575
- Davis R., Hartmann L., 1983, *ApJ* 270, 671
- Dessart L., 2004, *A&A* 423, 693
- Dessart L., Owocki S.P., 2003, *A&A* 406, L1
- Dessart L., Owocki S.P., 2005, *A&A* 437, 657
- Dirac P.A.M., 1928, *Proc. R. Soc. Lond. A* 117, 610
- Dolan J.F., Tapia S., 1989, *ApJ* 344, 830
- Dopita M.A., Sutherland R.S., 2003, *Astrophysics of the Diffuse Universe*, Springer-Verlag Berlin Heidelberg New York
- Doppler C., 1842, *Abh. d. königl. böhm. Ges. d. Wiss.* 5, 465
- Drake G.W., 1988, *Can. J. Phys.* 66, 586
- Drechsel H., Przybilla N., 2009, *Astrophysik auf dem Computer (mit Einföhrung in Fortran)*
- Ebisawa K., Ueda Y., Inoue H., et al., 1996, *ApJ* 467, 419
- Eddington A.S., 1916, *MNRAS* 77, 16
- Eddington A.S., 1917, *MNRAS* 77, 596
- Eddington A.S., 1925, *MNRAS* 85, 408
- Einstein A., 1917, *Physikalische Zeitschrift* 18, 121
- Eissner W., Jones M., Nussbaumer H., 1974, *Comput. Phys. Commun.* 8, 270

- Epp S., 2007, Ph.D. thesis, Ruprecht-Karls-Universität Heidelberg
- Feldmeier A., Puls J., Pauldrach A.W.A., 1997, *A&A* 322, 878
- Fermi E., 1926, *Z. f. Phys.* 36, 902
- Frank J., King A., Raine D., 2002, *Accretion Power in Astrophysics*, Cambridge University Press, 3<sup>rd</sup> edition
- Fraunhofer J.v., 1814, *Denkschriften der Königlich Akademie der Wissenschaften zu München* 5, 193
- Friedrich H., 1990, *Theoretical Atomic Physics*, Springer-Verlag Berlin Heidelberg New York, 1<sup>st</sup> edition
- Friend D.B., Abbott D.C., 1986, *ApJ* 311, 701
- Friend D.B., Castor J.I., 1982, *ApJ* 261, 293
- Friend D.B., Castor J.I., 1983, *ApJ* 272, 259
- Fritz G., Kreplin R.W., Meekins J.F., et al., 1967, *Astrophys. J., Lett.* 148, L133
- Froese Fischer C., 2000, *Comput. Phys. Commun.* 128, 635
- Fürst F., 2011, Ph.D. thesis, Dr. Karl Remeis-Sternwarte, Astronomisches Institut der Universität Erlangen-Nürnberg, Sternwartstr. 7, 96049 Bamberg, Germany
- Gabriel A.H., 1972, *MNRAS* 160, 99
- Galeazzi M., McCammon D., 2003, *J. Appl. Phys.* 93, 4856
- Galeazzi M., McCammon D., Sanders W.T., 2000, In: *X-ray and inner shell processes: 18th International Conference*, Vol. 506. American Institute of Physics Conference Ser., p.638
- Garcia J.D., Mack J.E., 1965, *Journal of the Optical Society of America* 55, 654
- Garmire G.P., Bautz M.W., Ford P.G., et al., 2003, In: J. E. Truemper & H. D. Tananbaum (ed.) *X-Ray and Gamma-Ray Telescopes and Instruments for Astronomy*. Proc. SPIE 4851, p.28
- Garstang R.H., 1962, In: D. R. Bates (ed.) *Atomic and Molecular Processes.*, p. 1
- Gauerke E.S.J., Campbell M.L., 1994, *J. Chem. Edu.* 71, 457
- Gauß C.F., 1809, *Theoria motus corporum coelestium in sectionibus conicis solem ambientium*, Perthes et Besser, Hamburg
- Giacconi R., Rossi B., 1960, *J. Geophys. Res.* 65, 773
- Gies D.R., Bolton C.T., 1982, *ApJ* 260, 240
- Gies D.R., Bolton C.T., 1986, *ApJ* 304, 371
- Gies D.R., Bolton C.T., Blake R.M., et al., 2008, *ApJ* 678, 1237
- Gies D.R., Bolton C.T., Thomson J.R., et al., 2003, *ApJ* 583, 424
- Gorman M., 1973, *J. Chem. Edu.* 50, 189
- Grant I.P., McKenzie B.J., Norrington P.H., et al., 1980, *Comput. Phys. Commun.* 21, 207
- Groenewegen M.A.T., Lamers H.J.G.L.M., 1989, *A&AS* 79, 359
- Grottrian W., 1928, *Graphische Darstellung der Spektren von Atomen und Ionen mit ein, zwei und drei Valenzelektronen*, 2 Teile
- Gu M.F., 2004, *ApJS* 153, 389
- Guinan E.F., Dorren J.D., Siah M.J., Koch R.H., 1979, *ApJ* 229, 296
- Hale G.E., 1908a, *PASP* 20, 203
- Hale G.E., 1908b, *PASP* 20, 220
- Hamann W.R., Feldmeier A., Oskinova L.M., (eds.) 2008, *Clumping in Hot Star Winds*

- Hamilton W.R., 1933, Dublin University Review and Quarterly Magazine 1, 795
- Hanke M., 2007, *Diplomarbeit*, Dr. Karl Remeis-Sternwarte, Astronomisches Institut der Universität Erlangen-Nürnberg, Sternwartstr. 7, 96049 Bamberg, Germany
- Hanke M., 2011, Ph.D. thesis, Dr. Karl Remeis-Sternwarte, Astronomisches Institut der Universität Erlangen-Nürnberg, Sternwartstr. 7, 96049 Bamberg, Germany
- Hanke M., Wilms J., Nowak M.A., et al., 2009, ApJ 690, 330
- Hanke M., Wilms J., Nowak M.A., et al., 2008, In: *Microquasars and Beyond*.
- Hawking S.W., 1974, Nat 248, 30
- Heisenberg W., 1927, Zeitschrift für Physik 43, 172
- Herrero A., Kudritzki R.P., Gabler R., et al., 1995, A&A 297, 556
- Herzberg G., 1937, Atomic spectra and atomic structure, Prentice Hall, Inc.
- Hilborn R.C., 2002, arXiv:physics/0202029v1
- Hjellming R.M., Wade C.M., 1971, Astrophys. J., Lett. 168, L21
- Hjellming R.M., Wade C.M., Hughes V.A., Woodworth A., 1971, Nat 234, 138
- Houck J.C., Denicola L.A., 2000, In: N. Manset, C. Veillet, & D. Crabtree (ed.) *Astronomical Data Analysis Software and Systems IX*, Vol. 216. Astronomical Society of the Pacific Conference Series, p. 591
- House L.L., 1969, ApJS 18, 21
- Hubble E., 1929, Proceedings of the National Academy of Science 15, 168
- Humphreys R.M., 1978, ApJS 38, 309
- Hund F., 1925, Z. Physik
- Hutchings J.B., 1978, ApJ 226, 264
- Iben, Jr. I., Tutukov A.V., 1985, ApJS 58, 661
- Ingen-Housz J., 1785, *New Experiments and Observations on Diverse Physical Objects*, T. Barrois le jeune, Paris
- Jackson J.D., 2006, *Klassische Elektrodynamik*, Walter de Gruyter GmbH & Co. KG, Berlin, 4th edition
- Janssen J., 1869, Comptes rendus 67, 367
- Johnson W.R., Soff G., 1985, Atomic Data Nucl. Data Tables 33, 405
- Karttunen H., Kröger P., Oja H., et al., 1987, *Fundamental Astronomy*, Springer Berlin Heidelberg New York
- Kepler J., 1609, *Astronomia Nova*
- Kepler J., 1619, *Harmonices Mundi*, Linz
- Kirchhoff G., 1860a, *Annalen der Physik* 185, 275
- Kirchhoff G., Bunsen R., 1860, *Poggendorffs Annalen* 110
- Kirchhoff G., Bunsen R., 1861, *Poggendorffs Annalen* 113
- Kirchhoff G.R., 1860b, *Annalen der Physik* 185, 148
- Lagrange J.L., 1772, *Prix de l'Académie Royale des Sciences de Paris tome IX*
- Lamb W.E., Retherford R.C., 1947, Phys. Rev. 72, 241
- Lamers H.J., Cassinelli J.P., 1999, *Introduction to stellar winds*, Cambridge University Press
- LaSala J., Charles P.A., Smith R.A.D., et al., 1998, MNRAS 301, 285
- Legendre A.M., 1785, *Mémoires de Mathématiques et de Physique*, Tome X 411–435

- Levine I.N., 1983, *Quantum Chemistry*, Prentice Hall, New York, 5<sup>th</sup> edition
- Levine M.A., Marrs R.E., Bardsley J.N., et al., 1989, *Nucl. Instrum. Methods Phys. Res., Sect. B* 43, 431
- Levine M.A., Marrs R.E., Henderson J.R., et al., 1988, *Physica Scripta Volume T* 22, 157
- Lewin W.H.G., Paradijs J.v., van den Heuvel E.P.J., 1995, *X-Ray Binaries*, Cambridge Astrophysics Series, Cambridge University Press
- Li F.K., Clark G.W., 1974, *Astrophys. J., Lett.* 191, L27
- Liedahl D.A., Brown G.V., 2008, *Can. J. Phys.* 86, 183
- Liu Q.Z., van Paradijs J., van den Heuvel E.P.J., 2006, *A&A* 455, 1165
- Lockyer N., 1868, *Proc. R. Soc. Lond.* 17
- Lorentz H.A., 1906, *KNAW Proceedings Amsterdam* 8, 591
- Lounasmaa O.V., 1974, *Experimental Principles and Methods Below 1 K*, Academic Press Inc. London
- Lucretius Carus T., 60 BC, *De rerum natura*, Rome
- Lucy L.B., Solomon P.M., 1970, *ApJ* 159, 879
- Lyman T., 1906, *ApJ* 23, 181
- Makishima K., Maejima Y., Mitsuda K., et al., 1986, *ApJ* 308, 635
- Markoff S., Nowak M.A., Wilms J., 2005, *ApJ* 635, 1203
- Marrs R.E., 2008, *Can. J. Phys.* 86, 11
- Marrs R.E., Levine M.A., Knapp D.A., Henderson J.R., 1988, *Phys. Rev. Lett.* 60, 1715
- Mason K.O., Hawkins F.J., Sanford P.W., et al., 1974, *Astrophys. J., Lett.* 192, L65
- Mauche C.W., Liedahl D.A., Akiyama S., Plewa T., 2008, In: M. Axelsson (ed.) *Cool Discs, Hot Flows: The Varying Faces of Accreting Compact Objects*. American Institute of Physics Conference Ser. 1054, p.3
- Maxwell J.C., 1865, *Phil. Trans. Soc. Lond.* 155, 459
- Maxwell J.C., 1867, *Phil. Trans. Soc. Lond.* 157, 49
- McCammon D., 2005, *Thermal Equilibrium Calorimeters - An Introduction*. In: Enss C. (ed.) *Cryogenic Particle Detection*. Topics Appl. Phys., Vol. 99 Springer-Verlag Berlin Heidelberg, p.1
- McConnell M.L., Zdziarski A.A., Bennett K., et al., 2002, *ApJ* 572, 984
- Mitsuda K., Inoue H., Koyama K., et al., 1984, *PASJ* 36, 741
- Miškovičová I., Hanke M., Wilms J., et al., 2010, In: poster at the 7th Integral/BART Workshop, IBWS2010, 14-18 Apr 2010.
- Miškovičová I., Hanke M., Wilms J., et al., 2011, *Acta Polytechnica*, Vol. 51, No. 2., p. 85 51, 85
- Miškovičová I.e., 2012, in prep.
- Moseley H.G.J., 1913, *Phil. Mag.* 26, 1024
- Moseley H.G.J., 1914, *Phil. Mag.* 27, 703
- Müller S., Kühnel M., Caballero I., et al., 2012, in prep.
- Murdin P., Webster B.L., 1971, *Nat* 233, 110
- Ninkov Z., Walker G.A.H., Yang S., 1987, *ApJ* 321, 425
- Nowak M.A., Juett A., Homan J., et al., 2008, *ApJ* 689, 1199

- Oppenheimer J.R., Volkoff G.M., 1939, *Phys. Rev.* 55, 374
- Orofino H., Faria R.B., 2010, *J. Chem. Edu.* 87, 1451
- Orosz J.A., McClintock J.E., Aufdenberg J.P., et al., 2011, *ApJ* 742, 84
- Owocki S.P., Rybicki G.B., 1984, *ApJ* 284, 337
- Palmer C., Loewen E., 2005, *Diffraction Grating Handbook*, Newport Corporation, 6<sup>th</sup> edition
- Palmeri P., Quinet P., Mendoza C., et al., 2008, *ApJS* 177, 408
- Paschen F., Back E., 1912, *Ann. d. Phys.* 39, 897
- Paschen F., Back E., 1913, *Ann. d. Phys.* 40, 960
- Pauldrach A., Puls J., Kudritzki R.P., 1986, *A&A* 164, 86
- Pauli W., 1925, *Z. Physik* 31, 765
- Pauli W., 1927, *Z. Physik* 43, 601
- Pierce J.R., Millburn N.J., 1952, *Electron Gun*, Patent US 2585582
- Planck M., 1900, *Verhandl. der Deutschen Physikalischen Gesellsch.* 2 13, 202
- Planck M., 1901, *Ann. d. Phys.* 309, 553
- Poisson S.D., 1837, *Probabilité des jugements en matière criminelle et en matière civile, précédées des règles générales du calcul des probabilités*, Bachelier, Paris
- Porquet D., Dubau J., 2000, *A&AS* 143, 495
- Porter F.S., Adams J.S., Beiersdorfer P., et al., 2009a, In: B. Young, B. Cabrera, & A. Miller (ed.) *13th International Workshop on Low Temperature Detectors*. American Institute of Physics Conference Series 1185, p.454
- Porter F.S., Beiersdorfer P., Brown G.V., et al., 2008a, *Journal of Low Temperature Physics* 151, 1061
- Porter F.S., Beiersdorfer P., Brown G.V., et al., 2009b, *J. Phys. Conf. Series* 163, 012105
- Porter F.S., Brown G.V., Boyce K.R., et al., 2004, *Rev. Sci. Instrum.* 75, 3772
- Porter F.S., Brown G.V., Cottam J., 2005, *X-ray Astronomy and Astrophysics*. In: Enss C. (ed.) *Cryogenic Particle Detection*. Topics Appl. Phys., 99 Springer-Verlag Berlin Heidelberg, p.359
- Porter F.S., Gygax J., Kelley R.L., et al., 2008b, *Rev. Sci. Instrum.* 79, 307
- Postnov K.A., Yungelson L.R., 2006, *Living Rev. in Rel.* 9, 6
- Pottschmidt K., Nowak M.A., Wilms J., 2006, In: poster at the 207th meeting of the American Astronomical Society, 8-12 Jan 2006.
- Pradhan A.K., Nahar S.N., 2011, *Atomic Astrophysics and Spectroscopy*, Cambridge University Press, New York, 1<sup>st</sup> edition
- Pravdo S.H., White N.E., Becker R.H., et al., 1980, *Astrophys. J., Lett.* 237, L71
- Procopiu S., 1913, *Bulletin scientifique de l'Académie roumaine de sciences*
- Puls J., Vink J.S., Najarro F., 2008, *A&AR* 16, 209
- Ramsay W., Collie J.N., Travers M., 1895, *J. Chem. Soc., Trans.* 67, 684
- Reid M.J., McClintock J.E., Narayan R., et al., 2011, *ApJ* 742, 83
- Remillard R.A., McClintock J.E., 2006, *ARA&A* 44, 49
- Ritz W., 1908, *ApJ* 28, 237

- Roche É., 1849, Académie des sciences de Montpellier: Mémoires de la section des sciences 1, 243
- Roche É., 1850, Académie des sciences de Montpellier: Mémoires de la section des sciences 1, 333
- Roche É., 1851, Académie des sciences de Montpellier: Mémoires de la section des sciences 2, 21
- Röntgen W.C., 1895, Sitzungsber. der Würzburger Physik.-Medic. Gesellsch. 12
- Rowland H.A., 1882, Phil. Mag. 13, 469
- Rubio J., Perez J.J., 1986, J. Chem. Edu. 63, 476
- Russell H.N., Saunders F.A., 1925, ApJ 61, 38
- Rybicki G.B., Lightman A.P., 1979, Radiative Processes in Astrophysics, John Wiley and Sons, Inc.
- Rydberg J.R., 1889, Kungliga Svenska Vetenskapsakademien Handlingar 23
- Rydberg J.R., 1890, Phil. Mag. 29, 331
- Sampson D.H., Zhang H.L., Mohanty A.K., Clark R.E.H., 1989, Phys. Rev. A 40, 604
- Schpolski E.W., 1976, Atomphysik II, VEB Deutscher Verlag der Wissenschaften Berlin
- Schrödinger E., 1926a, Physical Review 28, 1049
- Schrödinger E., 1926b, Ann. d. Phys. 79, 361
- Schwarzschild K., 1916, Pr. Akad. Wiss. 189–196
- Seeds M.A., Backman D.E., 2011, Foundations of Astronomy, Brooks Cole Pub Co, Boston, 11<sup>th</sup> edition
- Shakura N.I., Sunyaev R.A., 1973, A&A 24, 337
- Shapiro S.L., Teukolsky S.A., 1983, Black Holes, White Dwarfs and Neutron Stars: The Physics of Compact Objects, John Wiley & Sons, Inc., Canada
- Shimura T., Takahara F., 1995, ApJ 445, 780
- Siegbahn K.M., 1924, Spektroskopie der Röntgenstrahlen, Springer Berlin
- Smith R.K., Brickhouse N.S., Liedahl D.A., Raymond J.C., 2001, Astrophys. J., Lett. 556, L91
- Sobolev V.V., 1960, Moving envelopes of stars
- Sowers J.W., Gies D.R., Bagnuolo W.G., et al., 1998, ApJ 506, 424
- Spitzer L., 1962, Physics of Fully Ionized Gases
- Stahle C.K., McCammon D., Irwin K.D., 1999, Phys. Today 52, 32
- Stark J., 1913, Sitzungsber. der kön. preuss. Akad. der Wiss. Berlin 47, 932
- Stark J., 1914, Ann. d. Phys. 43, 965
- Stark J., Wendt G., 1914, Ann. d. Phys. 43, 983
- Stefan J., 1879, Sitz.ber. Mathem.-naturw. Cl. Kais. Akad. d. Wissensch. Wien 79, 391
- Stelzer B., Wilms J., Staubert R., et al., 1999, A&A 342, 736
- Tananbaum H., Gursky H., Kellogg E., et al., 1972, ApJ 177, L5
- Thomson J.J., 1903, Conduction of electricity through gases, Cambridge University Press
- Thomson J.J., 1906, Phil. Mag. Ser. 6 11, 769
- Tuttle E.R., 1967, Am. J. Phys. 35, 26
- Tuttle E.R., 1980, Am. J. Phys. 48, 539

- Vainshtein L.A., Safronova U.I., 1985, *Phys. Scr.* 31, 519
- Vicente J., 1983, *J. Chem. Edu.* 60, 560
- Walborn N.R., 1973, *Astrophys. J., Lett.* 179, L123+
- Watanabe S., Sako M., Ishida M., et al., 2006, *ApJ* 651, 421
- Webster B.L., Murdin P., 1972, *Nat* 235, 37
- Weisskopf M.C., Brinkman B., Canizares C., et al., 2002, *PASP* 114, 1
- Wen L., Cui W., Levine A.M., Bradt H.V., 1999, *ApJ* 525, 968
- Wilms J., (Juett) A., Schultz N., Nowak M., 2012, in prep.
- Wilms J., Juett A., Schulz N., Nowak M., 2006a, In: *AAS/High Energy Astrophysics Division #9, Vol. 38. Bulletin of the American Astronomical Society*, p. 376
- Wilms J., Nowak M.A., Pottschmidt K., et al., 2006b, *A&A* 447, 245
- Wolter H., 1952, *Ann. d. Phys.* 10
- Xiang J., Lee J.C., Nowak M.A., Wilms J., 2011, *ApJ* 738, 78
- Zeeman P., 1896a, *Versl. K. Akad. Wet. Amsterdam* 5, 181
- Zeeman P., 1896b, *Versl. K. Akad. Wet. Amsterdam* 5, 242
- Zeeman P., 1897, *Phil. Mag.* 43, 226
- Zhang H.L., Sampson D.H., Mohanty A.K., 1989, *Phys. Rev. A* 40, 616
- Zhang S.N., Cui W., Harmon B.A., et al., 1997, *Astrophys. J., Lett.* 477, L95
- Ziółkowski J., 2005, *MNRAS* 358, 851

# Acknowledgements

There are a few people I want to thank for their support during the last year and whose contribution to this work shall not be left unmentioned. First I want to thank my advisor Jörn Wilms for his openness to almost any suggestion of possible research topics. When I first asked him about setting up a collaboration with the EBIT group he was hooked right away, although later he became his fair share of all the paperwork. Jörn was even almost more excited about this project than myself.

Thanks to Greg V. Brown for introducing me to the amazing field of laboratory astrophysics during my internship at LLNL in the summer of 2010 and for his kind offer to return to the lab and write my theses under his supervision. Through his commitment I learned that the world of atomic physics is much more fascinating than school tries to teach us.

The German Academic Exchange Service (DAAD) is to be blamed for setting up the first contact to Greg and the laboratory via their RISE in North America (now RISE world wide) program. Special thanks to Thomas Eberl who kept contact after I had the pleasure to do my first research project under his advise and who informed me about the DAAD program.

The observatory with all the great people there (too numerous to name them all) is a place not only to learn and work, but also for joy and lots of fun. Here, events like the Messier Marathon with  $-5^{\circ}\text{C}$  in the domes and a broken telescope mount are no curiosity. Michael Wille, my walking Linux reference, was the one who found a way to keep up our not always sane appearing conversations without a chat program and therefore without braking lab computer security rules. Sorry for my bad influence on your sleep schedule. Manfred Hanke, although he left shortly after I had started with my thesis, kept his interest in our work and happily answers all sorts of questions to help out where possible. With Ivica Miškovičová I had fun discussions about our friend Cyg X-1 and really enjoyed our joint hacking of Manfred's scripts. Victoria Grinberg tested the atomic physics chapter for understandability under hampered conditions of jetlag. With her comments she triggered the hobby of referencing every single ancient piece of physics with its original publication. Because of her I spent many hours cursing my way through the internet on the track of physics history, but it was worth it. Thanks to Norbert Przybilla for not dissolving into a pile of ash when the topic of atomic physics comes up. Being able to have a discussion about some details of the physics is very helpful during the process of writing. Thanks to all our admins for making the Remeis Cluster such a powerful computing environment without becoming tired of answering the thousandth iteration of the same stupid questions over and over again.

The lab with it's security measures is a less homely place but the people there make it no less enjoyable to work there than in the observatory. Joel Clementson took care of the lunch breaks and answered lots of questions about FAC and atomic physics. He also saved

me on short notice when the room I was going to rent turned out to be a fleabag. Peter Beiersdorfer, the head of the group, Alex Graf, who spent some hours with me in the lab, Ed Magee (you have to try his fabulous white peaches!) and David Layne, who are amazing at keeping EBIT running, and Donna Vercelli with her nerd sniping<sup>1</sup> *Bucky Balls* are always good to have a nice discussion about physics, life, the Universe and everything. I also want to thank the Anderson family for providing me with such a nice shelter during my stays in Livermore. It is nice to have a place to call home so far away, where I am also allowed to ‘torture’ somebody else’s kids as a substitute for my own siblings.

Thanks to all of my friends for being such good pen pals when the large distance (in space and time) does not allow for much more.

Last but not least I want to thank my parents for their support in everything I do, even if it means that they won’t even see me on weekends. Without their help it would be much more complicated to leave the country for a couple of months.

---

<sup>1</sup><http://xkcd.com/356/>

# Erklärung

Hiermit bestätige ich, dass ich diese Arbeit selbstständig und nur unter Verwendung der angegebenen Hilfsmittel angefertigt habe.

Bamberg,

Natalie Hell